Experimental Measurement and Phenomenological Study of Positive Pion Production in Nuclear Media

A thesis presented for the degree of

Master in Physics

Esteban Felipe Molina Cárdenas

Evaluating Committee:

Dr. Hayk Hakobyan (Advisor)

Dr. Benjamin Guiot (Co-advisor)

Dr. William Brooks

Dr. Orlando Soto

UNIVERSIDAD TECNICA
FEDERICO SANTA MARIA

Department of Physics

Chile

Dedicado a Alejandra, Esteban, y el resto de mi familia.

Gracias por su infinito amor y por su apoyo incondicional.

Sin ustedes no estaría acá.

Agradecimientos

Me gustaría partir con las personas que hicieron posible que yo trabajará en este tema de tesis: Hayk, gracias por toda tu ayuda, guía y consejo. Yo sabía que eras un gran físico, pero despues de estos tres años bajo tu tutela me he dado cuenta que tambien eres una gran persona. Tu ayuda desinteresada siempre la valoraré. Y gracias tambien por todos los datos de cine poco convencional que mencionas. Benjamin, gracias por toda tu guía, tus ganas de enseñar y por empujarme siempre que fue necesario. Sin lugar a dudas soy un mejor cientifico gracias a ti. Professor Will, I believe that there are very few physicists that really know physics. Undoubtedly, you are one of them. Your wisdom and knowledge is unparalleled and I'm honored to have shared classes, meetings and conversation with you. By the way, I think that you would really like *Plini*, he is a very good guitarist. Taya, Jorge, Orlando, tienen mi gratitud por haberme ayudado con la mejor de las disposiciones siempre que lo necesité.

Karyn, gracias por todo.

Para la gente que me acompaña: Andy, mi hermano, aparte de ser el conocedor de futbol más grande que he conocido, eres el más grande en todo. Gracias por tu amistad, por la hermandad y por estar siempre. Creo que si la gente fuera más como tú el mundo sería un lugar mejor (y eso va en serio). David A., gracias por la amistad, por nuestras conversas eternas, por compartir, por envalentonarme, y por enseñarme a vivir más y preocuparme menos. David K., A.K.A. "Lázaro". Gracias por las risas con apretón de güata, las sesiones de "El Archivo", y por una linda amistad que espero se extienda hasta el momento en que genuinamente pienses que *Mass Effect 2* es el mejor de la franquicia. Sebastián, gracias por la amistad y por enseñarme, mediante el ejemplo propio, que un huaso puede sacar un magister. Por supuesto que tambien quiero agradecer a los Ks del CCTVal: José, Antonio, excelentes personas y aun mejores amigos. Bruno (el androide más cariñoso que conozco), Jairo, Laleins, Javier, gracias por haberme recibido tan bien en el grupo y por su creciente amistad.

Thelma, gracias infinitas por colorear mi mundo, por revivirme y por tu amor.

Gente va, gente viene y todos dejan algo. Así que si no mencioné a alguien, lo siento, pero sepán que tienen mi agradecimiento.

Por ultimo quería agradecer a la gente que ha creado mis obras favoritas, las cuales me han acompañado y ayudado cuando lo necesité: Kentaro Miura, J.R.R. Tolkien, Isaac Asimov, Hideo Kojima, Bioware Team, FFXV Team.

Introduction

In the last decades, experimental physics has developed immensely. The rapid evolution of technology allowed the construction of complex experiments to probe, and in some cases extend, the boundaries of known physics. In the case of particle physics, scattering experiments evolved from simple setups such as The Geiger-Marsden experiment -also known as The Golden Foil Experiment- to much more complex like those present in the modern colliders or modern fixed-target experiments.

In this spirit it is that we studied the *hadronization* phenomenon via the data acquired from the Eg2 experiment performed at Jefferson Lab (JLAB). Specifically, the study was based on positive pions electro-production.

This thesis is divided in two, where we provide experimental and phenomenological work. We will show the influence of nuclear media on hadronization through observables calculated directly from data, and we will use theoretical models to extract theoretical parameters of interest.

Contents

Chapter 1

Theoretical Description of Lepton-Nucleon Scatterings

The collision of high-energy particles is the main method to study the internal structure of composite particles and for this type of collisions the analysis of deep inelastic scattering (DIS) events, between a lepton and a nucleon, plays a central role in understanding the latter's structure.

In this chapter we will present the relevant theoretical background and terminology to have a clear picture of the lepton-nuclei scattering process. The sources used for this chapter were [1, 2, 3].

1.1 Deep Inelastic Scattering

In Deep Inelastic Scattering (DIS)

$$l + N \rightarrow l' + X, \tag{1.1}$$

a lepton l scatters off a nucleon N. The final products of the reaction are the detected scattered lepton and an unknown final state which are denoted as l' and X, respectively (see Fig.1.1).

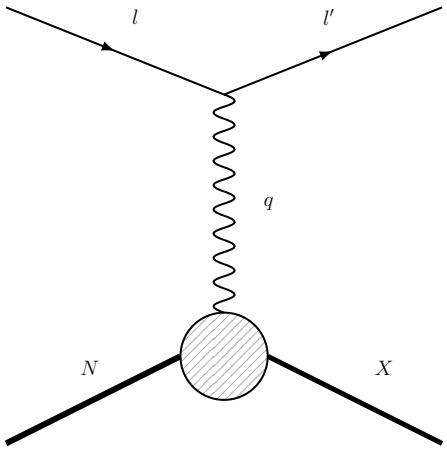

Figure 1.1: N is the targeted nucleon and X is an unknown final state.

This process is characterized by two independent kinematical variables associated with the virtual photon. Usually, these variables are:

$$Q^2 = -(l' - l)^2 = -q^2 = -(\nu^2 - |\mathbf{q}|^2) \quad ; \quad x_b = \frac{Q^2}{2p_N \cdot q}, \tag{1.2}$$

where ν is the energy of the virtual photon, $\mathbf{q}$ its spatial momentum, and x_b is the *Bjorken Scaling Variable* or *Bjorken x*.
Q^2 is associated with the virtual photon's capacity to probe the constituents of the targeted nucleon. With Q much larger than the nucleon mass, M_N, the virtual photon is able to resolve the internal structure of the nucleon.

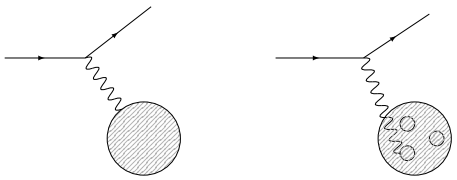

Figure 1.2: (Left) The interaction is with the whole nucleon -$Q^2 \approx M_N^2$-. (Right) The interaction is with one of the constituents -$Q^2 >> M_N^2$-.

To understand x_b it is useful to define the squared invariant mass of the final state:

$$W^2 = (q + p_N)^2. \tag{1.3}$$

To have *inelastic* collisions it is required that $W^2 > M_N^2$. Then, the Bjorken variable

can be re-written as:

$$x_b = \frac{Q^2}{Q^2 + W^2 - M_N^2}. \tag{1.4}$$

Hence, we can associate x_b with the elasticity of the reaction:

- For $W^2 >> M_N^2$, the reaction is inelastic and $x_b \to 0$.
- For $W^2 = M_N^2$, the reaction is elastic and $x_b = 1$.

After the presentation of the adequate variables, we can state the unpolarized DIS differential cross-section as:

$$\frac{\mathrm{d}^2\sigma}{\mathrm{d}x\ \mathrm{d}Q^2} = \frac{4\pi\alpha^2}{Q^4}\left[(1-y)\frac{F_2\left(x,Q^2\right)}{x} + y^2 F_1\left(x,Q^2\right)\right], \tag{1.5}$$

where y is a Lorentz-invariant kinematical variable which, in the nucleon's rest frame, can be interpreted as the fraction of energy lost by the scattered lepton:

$$y = \frac{p_N \cdot q}{p_N \cdot l} = \frac{\nu}{E_e}. \tag{1.6}$$

F_1 and F_2 are known as Structure Functions (SFs) and they have encoded the nucleon structure probed by the virtual photon.

The Stanford Linear Accelerator (SLAC) was the first place where the SF were experimentally studied in the decade of the 70s. The experiment collided electrons with protons. Two important phenomena were observed at the time (see Figure 1.3):

1. The SF did not depend on Q^2. This phenomenon was called *Bjorken Scaling* and it indicated that the nucleon is made of pointlike objects.
2. The SF are not independent and are related by the Callan-Gross relation:

$$F_2(x) \sim 2xF_1(x). \tag{1.7}$$

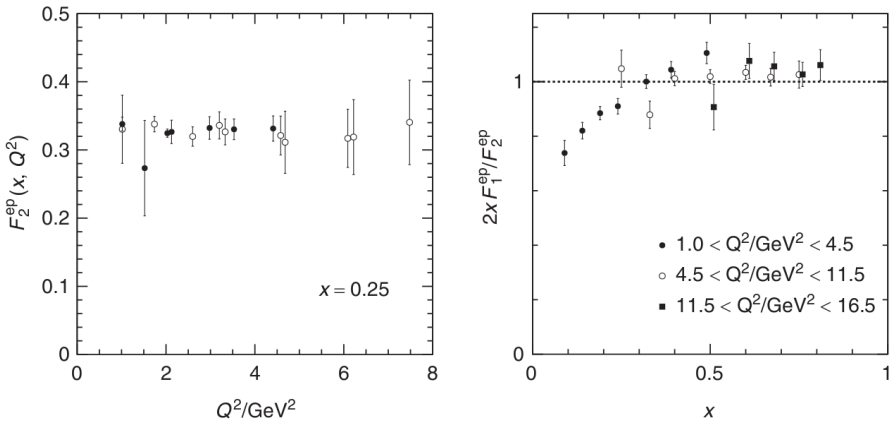

Figure 1.3: (Left) Manifestation of Bjorken Scaling. (Right) Manifestation of the Callan-Gross relation. Plots obtained from [1]

Then, under the wing of experimental observations, the DIS cross-section can be rewritten:

$$\frac{d\sigma}{dxdQ^2} = \frac{4\pi\alpha^2}{Q^4 x}\left[(1-y) + \frac{y^2}{2}\right] F_2(x). \tag{1.8}$$

This equation does provide some insight on DIS. However, the introduction of the Parton Model would provide more physical interpretation about DIS.

1.1.1 Parton Model (PM)

This model was presented by Richard Feynman in the decade of the $60s$[4] to explain the experimental results obtained at SLAC. He stated that hadrons were constituted by quasi-free, pointlike particles called *partons*. These, to be quasi-free, had to be analyzed through a reference frame where the elements of a collision were traveling at high energies; therefore, due to time dilation, the timescale of the parton-parton interaction would be larger than the timescale of the lepton-parton interactions. Thus, the DIS cross-section can be stated as a sum of probabilities of incoherent[1] lepton-parton ($lq \to lq$) scattering cross-sections:

$$\frac{d\sigma}{dQ^2dx} = \sum_q \int_0^1 d\xi f_q(\xi) \times \frac{d\sigma^{lq\to lq}}{dQ^2dx}, \tag{1.9}$$

where ξ is the hadron's fraction of longitudinal momentum carried by the parton, $f_q(\xi)$ is the Parton Distribution Function (PDF) and $f_q(\xi)d\xi$ represents the probability to scatter a parton q with momentum fraction ξ.

Also, ξ can be related to the Bjorken variable through energy conservation. Let p_{q_i} and p_{q_f} be the initial and final four-momentum of the scattered parton, respectively. Then, squaring the energy conservation equation, we obtain

$$m_q^2 = m_q^2 - Q^2 + 2q \cdot p_{q_i}. \tag{1.10}$$

Considering $p_{q_i} = \xi p_N$, the previous equation reads:

$$\xi = \frac{Q^2}{2q \cdot p_N} = x_b. \tag{1.11}$$

Thus, in the PM, x_b is interpreted as the hadron's fraction of momentum carried by the parton.

The lepton-parton cross section is the same as two fermions t-channel scattering. At leading order (LO) in QED[2] it reads:

$$\frac{d\sigma^{lq\to lq}}{dQ^2dx} = \frac{4\pi\alpha^2 e_q^2}{Q^4}\left[(1-y) + \frac{y^2}{2}\right]\delta(x-\xi). \tag{1.12}$$

Then, using eqs. (1.11) and (1.12) in eq. (1.9), the differential cross-section can be rewritten as:

$$\frac{d\sigma}{dxdQ^2} = \frac{4\pi\alpha^2}{Q^4}\left[(1-y) + \frac{y^2}{2}\right]\sum_q e_q^2 f_q(x). \tag{1.13}$$

If we compare it with eq. (1.8), then:

$$F_2(x) = x\sum_q e_q^2 f_q(x). \tag{1.14}$$

[1]Incoherent is another form of saying *independent*.

[2]In this case, leading order means we are considering the Feynman diagram with the lowest power of the coupling constant.

From the independence of Q^2, we can conclude that, in this model, the nucleon is made of pointlike particles.

This model provides a basic foundation to understand the inner structure of hadrons, despite the fact that this interpretation relies on a particular reference frame. Later, with the QCD formalism, this subject would be improved.

1.2 Quantum Chromodynamics

QCD is the field theory that describes the strong interaction, and it formalizes the concept of partons through *quarks* and *gluons*. QCD is a non-abelian gauge theory based on the SU(3) symmetry group. Its Lagrangian density reads:

$$\mathcal{L} = -\frac{1}{4}F^A_{\alpha\beta}F^{\alpha\beta}_A + \sum_{\text{flav}} \bar{q}_a(i\gamma^\alpha D_\alpha - m_q\delta_{ab})_{ab}q_b \tag{1.15}$$

Where q_a are the *quark fields* of color a and flavor q, $\gamma^\mu D_\mu$ is the contraction of the gamma matrices with the covariant derivative, m_q is the mass of the quark q, and $F^A_{\alpha\beta}$ is the gluon field strength tensor defined as:

$$F^A_{\alpha\beta} = (\partial_\alpha A^A_\beta - \partial_\beta A^A_\alpha - g f^{ABC} A^B_\alpha A^C_\beta) \tag{1.16}$$

Where A^A_α are the gluon fields, g is the coupling constant of QCD, and f^{ABC} is the structure constant of the $SU(3)$ group. The term $-gf^{ABC}A^B_\alpha A^C_\beta$ originates from the requirement of gauge invariance in the SU(3) group.

Besides the color inclusion, the Lagrangian of QCD is similar to that of QED. Nonetheless, there is a fundamental difference: QCD's field strength tensor has a term that allows interactions between the interaction carriers -gluons- which increases the complexity of Feynman diagrams for QCD-related processes. This term is:

$$gf^{ABC}A^B_\alpha A^C_\beta. \tag{1.17}$$

Then, the gauge invariance requirement yields the gluon self-interaction.

Quantum field theories allow to calculate cross-sections and decay rates through *Feynman Rules*. In QED, perturbation theory can be used to obtain expressions for the aforementioned observables. However, in QCD, the use of perturbation theory is not straightforward due to its coupling constant behavior.

1.2.1 The Running Coupling

Coupling constants[3] are quantities that indicate how intense is an interaction, and in perturbative calculations they are proportional to the number of vertexes in a reaction's Feynman Diagram. For instance, in QED, the coupling constant α is less than one and positive, given a finite energy scale[4] Q, meaning that if a reaction has a higher number of vertexes it is more unlikely.

In the case of QCD's coupling constant α_s it is not always possible to use perturbation theory. If the energy scale is low the α_s reaches values near unity and above.

The running[5] of the coupling constant can be described as a function of Q^2:

$$Q^2 \frac{\partial \alpha_s}{\partial Q^2} = \beta(\alpha_s), \tag{1.18}$$

where the *beta function* is arbitrary and can be expanded in powers of α_s:

$$\beta(\alpha_s) = -b\alpha_s^2[1 + b'\alpha_s + b''\alpha_s^2 + O(\alpha_s^3)]. \tag{1.19}$$

The $b^{(n)}$ is given by QCD calculations and depends on the number of active flavours n_f. If this number is less than 16, the β function is negative, which contrasts with the case of QED, where its β function is positive.

[3] The name coupling *constant* is debatable because, strictly speaking, these are not constants. Nevertheless, the name remained in time.

[4] In this section we will use Q to refer to the energy scale of the processes since it is widely used in the literature. Do not mistake with the virtuality of the virtual photon in DIS.

[5] *runs* means that it evolves with a certain kinematical variable

If we truncate the expansion to its lowest order we obtain:

$$\alpha_s(Q^2) = \frac{\alpha_s(\mu^2)}{1 + \alpha_s(\mu^2) b \cdot t} \quad ; \quad t = \ln\left(\frac{Q^2}{\mu^2}\right) \quad ; \quad b = \frac{33 - 2n_f}{12\pi}, \tag{1.20}$$

where μ is a *mass scale* introduced to deal with UV divergences when we use α_s to describe an observable. Then, it is noticeable that:

$$\alpha_s(Q^2) \to 0 \quad ; Q^2 \to \infty. \tag{1.21}$$

This result is called *asymptotic freedom* and it is also obtainable if we truncate the β function at higher order. It is essential since it allows to use perturbative calculations in QCD. Having said this, it is useful to define a constant that delimits the border between the use of perturbative and non-perturbative calculations. For this matter it is defined a dimensionful constant parameter:

$$\Lambda^2_{QCD} = Q^2 e^{\frac{-1}{b\alpha_s(Q^2)}}. \tag{1.22}$$

Then, from this equation and the previous ones:

$$\alpha_s(Q^2) = \frac{1}{b \cdot ln(Q^2/\Lambda_{QCD})}. \tag{1.23}$$

Notice that if the energy scale Q is equal to Λ_{QCD} the coupling constant blows up; hence, not allowing the use of perturbative calculations.

1.2.2 QCD Description of DIS

In QCD, the cross-section of neutral current DIS is given by the contraction of the hadronic tensor $W_{\mu\nu}$ and the leptonic tensor $L^{\mu\nu}$:

$$\frac{\mathrm{d}^2\sigma}{\mathrm{d}x\ \mathrm{d}Q^2} \propto L^{\mu\nu} W_{\mu\nu}. \tag{1.24}$$

The leptonic tensor is given by electromagnetic interactions between the incoming lepton and the quarks inside the nucleon. The hadronic tensor is harder to express because it represents whatever is inside the targeted nucleon and its interactions; therefore, it contains the SFs. The leptonic tensor is defined as:

$$L_{\mu\nu} = 2\left(l_\mu l'_\nu + l'_\mu l_\nu - g_{\mu\nu} l \cdot l'\right), \tag{1.25}$$

and the hadronic tensor is defined as:

$$\begin{aligned} W^{\mu\nu} =& F_1\left(x, Q^2\right)\left(-g^{\mu\nu} + \frac{q^\mu q^\nu}{q^2}\right) \\ &+ F_2\left(x, Q^2\right)\frac{\left(p_N^\mu - q^\mu p_N \cdot q/q^2\right)\left(p_N^\nu - q^\nu p_N \cdot q/q^2\right)}{p_N \cdot q} \end{aligned} \tag{1.26}$$

QCD gives the framework to derive mathematical expressions for the SF in terms of non-perturbative objects, which, at this point, were described by experimental observables and PM approximations. To obtain SFs mathematical expressions the *factorization* procedure is used.

1.2.2.1 Collinear Factorization

Collinear factorization is a process where the physical cross-section is factorized into non-perturbative (long distance) functions -the parton densities- and a hard cross-section calculable in perturbation theory:

$$\frac{d\sigma}{dQ^2 dx} = \sum_q \int_x^1 \frac{dy}{y} f_q(y, \mu) \times \frac{d\hat{\sigma}}{dQ^2 dx}\left(\frac{x}{y}, \frac{Q^2}{\mu^2}\right) + O\left(\frac{\Lambda^2_{QCD}}{Q^2}\right). \tag{1.27}$$

The main difference between this equation and eq. (1.9) is the dependence on μ by the parton density and the hard cross-section. However, this dependence is canceled inside the integral such that the physical cross-section is independent of μ. This is the general idea of the renormalization group equations which in this case leads to the DGLAP equations [5, 6, 7] for the parton densities.

At leading order $\hat{\sigma}$ is given by eq. (1.12) obtained in the PM. Nonetheless, in the

present case the structure function depends on the energy scale:

$$F_2(Q^2, x) = x \sum_q e_q^2 f_q(x, Q^2), \tag{1.28}$$

where we chose $\mu = Q$. Given these results, regarding the structure functions, the nucleon does have a structure and it is not made only of pointlike particles.

1.3 Semi-Inclusive Deep Inelastic Scattering

DIS events can be classified according to the number of detected particles in the final state. This classification can be stated as:

- Inclusive events: only the out-coming lepton l' is detected. X can be anything.

$$l + N \to l' + X \tag{1.29}$$

- Semi-Inclusive events: the out-coming lepton l' and a hadron h are detected

$$l + N \to l' + h + X \tag{1.30}$$

- Exclusive events: all the particles from the final state are detected.

In this thesis we studied the Semi-Inclusive Deep Inelastic Scattering (SIDIS) regime with a positive pion as the detected hadron:

$$e\,(\ell) + N\,(p_N) \to e'\,(\ell') + \pi^+\,(p_h) + X(p_X). \tag{1.31}$$

To describe this process it is necessary to define additional kinematical variables:

- s: The squared invariant mass of the initial state.

$$s = (\ell + p_N)^2 \tag{1.32}$$

- z_h: In the rest frame of the target can be interpreted as the fraction of energy passed from the virtual photon to the detected hadron.

$$z_h = \frac{p_N \cdot p_h}{p_N \cdot q} = \frac{E_h}{\nu} \tag{1.33}$$

- P_T^2: The squared transverse momentum of the detected hadron w.r.t. the virtual photon's direction (see Fig.1.4).

- ϕ_h: The azimuthal angle between the hadronic and the leptonic plane (see Fig.1.4).

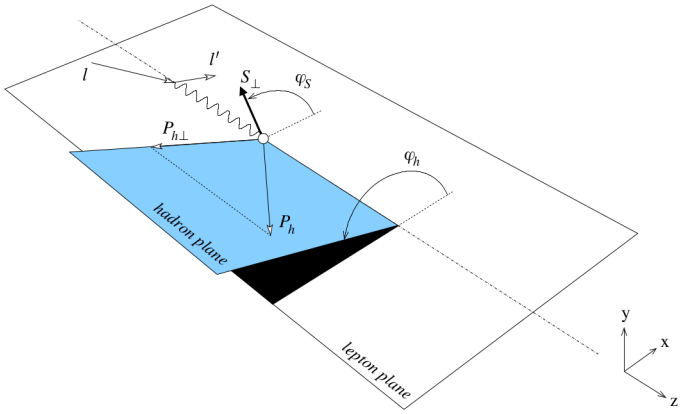

Figure 1.4: SIDIS schematic representation.

The SIDIS differential cross-section can be written in a model-independent format where we can find several SFs that describe the internal properties of the nucleon[8]. The differential cross-section has 18 SF but this number will be reduced since we are studying an unpolarized target [6]. The cross-section, assuming single virtual photon exchange, reads [9]:

$$\begin{aligned}\frac{\mathrm{d}\sigma}{\mathrm{d}x_B\,\mathrm{d}y\,\mathrm{d}z_h\,\mathrm{d}P_T^2\,\mathrm{d}\phi} = &\frac{\pi\alpha^2}{Q^2xy}\Big\{\left(1+(1-y)^2\right)F_{UU} + 2(2-y)\sqrt{1-y}F_{UU}^{\cos\phi}\cos\phi \\ &+2(1-y)F_{UU}^{\cos(2\phi)}\cos(2\phi)\Big\}\end{aligned} \tag{1.34}$$

Notice that unpolarized SIDIS has three structure functions in comparison to DIS which has two that are inter-dependent.

[6] Unpolarized target: Nucleon target in which the total spin of averages to zero.

1.3.1 TMD Factorization

Collinear factorization is not applicable in problems with two energy scales, for instance, when $P_T << Q$[7]. In this case, we can use the *TMD factorization*. As an example, we can state the general factorization expression for F_{UU} as:

$$\begin{aligned} F_{UU} =& \mathcal{H}_{q\bar{q}}(Q) \\ & \int d^2\mathbf{p}_\perp d^2\mathbf{k}_\perp \delta(\mathbf{P}_T - \mathbf{p}_\perp - z_h\mathbf{k}_\perp) f_q(x_b, k_\perp; Q) \times D_{\bar{q}}^h(z_h, p_\perp; Q) \\ & + \mathcal{O}(\frac{P_T}{Q}), \end{aligned} \tag{1.35}$$

where $\mathcal{H}_{q\bar{q}}$ is a hard factor calculable in perturbation theory, f_q is the transverse momentum dependent PDF, D_q^h is the transverse momentum dependent Fragmentation Function (FF). In this scheme, different transverse momenta (see Fig.1.5) are fundamental to describe the cross-section.

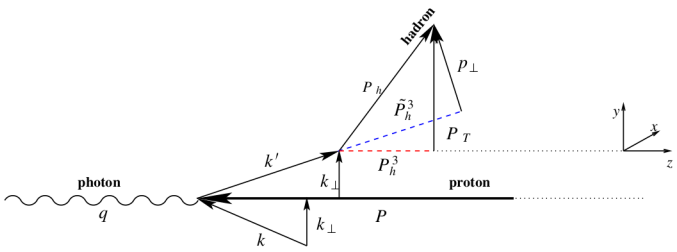

Figure 1.5: $k_\perp$ is the parton's intrinsic transverse momentum. $k'_\perp$ is the parton's intrinsic transverse momentum post-scattering. $p_\perp$ is the transverse momentum of the hadronized quark w.r.t. $k'_\perp$

This factorization provides a three dimensional representation of the nucleon. To use it, the following kinematical condition is required[10]:

$$k_\perp^2 \sim P_T^2 << Q^2. \tag{1.36}$$

[7]The number of scales used is related to how similar are the energy variables. For instance, $P_T \sim Q$ is a one scale problem.

At LO the relation between collinear and TMD PDF is:

$$f_q(x_b) = \int d^2\mathbf{k}_\perp f_q(k_\perp, x_b). \tag{1.37}$$

From now on, we will omit the Q^2 dependence of partonic and fragmentation functions. The integration is performed in all of $k_\perp$'s phase space such that we retrieve the collinear PDF.

A usual model to represent the TMD PDF is

$$f_q(x_b, k_\perp) = f_q(x_b)\frac{e^{-k_\perp^2/\langle k_\perp^2\rangle}}{\pi\langle k_\perp^2\rangle}. \tag{1.38}$$

This model can be used with other distributions. For instance, the Fragmentation Function (FF) reads:

$$D_{h/q}(z_h, p_\perp) = D_{h/q}(z_h)\frac{e^{-p_\perp^2/\langle p_\perp^2\rangle}}{\pi\langle p_\perp^2\rangle}. \tag{1.39}$$

Then, the SFs with the TMD factorization can be represented as convolutions of certain transverse momentum-dependent partonic/hadronic distributions. At LO, these convolutions read as [11]:

- Convolution of the unpolarized distributions. This term is associated with the phi-independent term of the cross-section.

$$F_{UU} = \sum_q e_q^2 \int d^2\boldsymbol{k}_\perp f_{q/p}\left(x, k_\perp\right) D_{h/q}\left(z, p_\perp\right). \tag{1.40}$$

- Convolution with two separate contributions: unpolarized and polarized. This

term is associated with the $\cos\phi$ term (Cahn term).

$$\begin{aligned} F_{UU}^{\cos\phi_h} =& 2\sum_q e_q^2 \int d^2\boldsymbol{k}_\perp \frac{k_\perp}{Q} \left[\left(\hat{\boldsymbol{P}}_T \cdot \hat{\boldsymbol{k}}_\perp \right) f_{q/p}\left(x, k_\perp\right) D_{h/q}\left(z, p_\perp\right) \right. \\ &+ \frac{P_T - z_h k_\perp \left(\hat{\boldsymbol{P}}_T \cdot \hat{\boldsymbol{k}}_\perp \right)}{2p_\perp} \Delta f_{q^\dagger/p}\left(x, k_\perp\right) \\ &\left. \times \Delta^N D_{h/q^\dagger}\left(z, p_\perp\right) \right] . \end{aligned} \tag{1.41}$$

- Convolution of the polarized distributions. This term is associated with $\cos 2\phi$ term.

$$\begin{aligned} F_{UU}^{\cos 2\phi_h} =& -\sum_q e_q^2 \\ &\times \int d^2\boldsymbol{k}_\perp \left[\frac{P_T \left(\hat{\boldsymbol{P}}_T \cdot \hat{\boldsymbol{k}}_\perp \right) - 2 z_h k_\perp \left(\hat{\boldsymbol{P}}_T \cdot \hat{\boldsymbol{k}}_\perp \right)^2 + z_h k_\perp}{2p_\perp} \right] \\ &\times \Delta f_{q^\dagger/p}\left(x, k_\perp\right) \Delta^N D_{h/q'}\left(z, p_\perp\right) . \end{aligned} \tag{1.42}$$

Here we give the definitions of the distributions without the transverse momentum dependent term:

- $f(x_b)_{q/p}$: Parton Distribution Function
- $D(z_h)_{h/q}$: Fragmentation Function. It represent the distribution of a hadron h, originated from the fragmentation of a quark q, with z_h.
- $\Delta f(x_b)_{q^\dagger/p}$: Boer-Mulders Distribution Function. It is the polarized analogous of the PDFs, i.e. the distribution of a polarized parton with a certain fraction x_b of nucleon momentum.
- $\Delta^N D(z_h)_{h/q^\dagger}$: Collins Fragmentation Function. It represents the distribution of a hadron h, originated from the fragmentation of a polarized quark q, with z_h.

With the Gaussian model, the convolutions that compose the SF can be integrated analytically if the integration is in all the phase space. Assuming that the widths of

the Gaussians are flavour independent, then:

$$
\begin{aligned}
F_{UU} =& \sum_q e_q^2 f_{q/p}\left(x_B\right) D_{h/q}\left(z_h\right) \frac{e^{-P_T^2/\left\langle P_T^2\right\rangle_G}}{\pi \left\langle P_T^2\right\rangle_G} \\
F_{UU}^{\cos 2\phi_h} =& -eP_T^2 \sum_q e_q^2 \frac{\Delta f_{q^\dagger/p}\left(x_B\right)}{M_{\mathrm{BM}}} \frac{\Delta^N D_{h/q^\dagger}\left(z_h\right)}{M_h} \frac{e^{-P_T^2/\left\langle P_T^2\right\rangle_{\mathrm{BM}}}}{\pi \left\langle P_T^2\right\rangle_{\mathrm{BM}}^3} \\
&\times \frac{z_h \left\langle k_\perp^2\right\rangle_{\mathrm{BM}}^2 \left\langle p_\perp^2\right\rangle_C^2}{\left\langle k_\perp^2\right\rangle \left\langle p_\perp^2\right\rangle}. \\
F_{UU}^{\cos \phi_h} =& -2\frac{P_T}{Q} \sum_q e_q^2 f_{q/p}\left(x_B\right) D_{h/q}\left(z_h\right) \frac{e^{-P_T^2/\left\langle P_T^2\right\rangle_G}}{\pi \left\langle P_T^2\right\rangle_G^2} z_h \left\langle k_\perp^2\right\rangle \\
&+ 2e\frac{P_T}{Q} \sum_q e_q^2 \frac{\Delta f_{q^\dagger/p}\left(x_B\right)}{M_{\mathrm{BM}}} \frac{\Delta^N D_{h/q}^\dagger\left(z_h\right)}{M_h} \frac{e^{-P_T^2/\left\langle P_T^2\right\rangle_{\mathrm{BM}}}}{\pi \left(P_T^2\right\rangle_{\mathrm{BM}}^4} \\
&\times \frac{\left\langle k_\perp^2\right\rangle_{\mathrm{BM}}^2 \left\langle p_\perp^2\right\rangle_C^2}{\left\langle k_\perp^2\right\rangle \left\langle p_\perp^2\right\rangle} \left[z_h^2 \left\langle k_\perp^2\right\rangle_{\mathrm{BM}} \left(P_T^2 - \left\langle P_T^2\right\rangle_{\mathrm{BM}}\right)\right. \\
&\left. + \left\langle p_\perp^2\right\rangle_C \left\langle P_T^2\right\rangle_{\mathrm{BM}}\right],
\end{aligned}
\tag{1.43}
$$

where M_{BM}, M_h are parameters of the polarized distributions (Collins, Boer-Mulders), and

$$
\langle P_T^2\rangle_G = \langle p_\perp^2\rangle + z_h^2\langle k_\perp^2\rangle, \quad \left\langle k_\perp^2\right\rangle_{\mathrm{BM}} = \frac{\langle k_\perp^2\rangle M_{\mathrm{BM}}^2}{\langle k_\perp^2\rangle + M_{\mathrm{BM}}^2}, \quad \left\langle p_\perp^2\right\rangle_C = \frac{\langle p_\perp^2\rangle M_h^2}{\langle p_\perp^2\rangle + M_h^2}. \tag{1.44}
$$

A noteworthy result, considering all the assumptions made so far, is that

$$
\langle P_T^2\rangle = \frac{\int_0^\infty d^2\mathbf{P}_T P_T^2 d\sigma}{\int_0^\infty d^2\mathbf{P}_T d\sigma} = \langle P_T^2\rangle_G. \tag{1.45}
$$

Hence, within the TMD factorization scheme, the average of the squared transverse momentum is related to two contributions of different nature: one coming from the intrinsic parton momentum ($k_\perp$) and the other coming from the *hadronization* process ($p_\perp$).

At the moment, the fundamental descriptions are solid enough. Nonetheless, there is a concept that we haven't explained too much: *hadronization*. This is key in what the struck quark will do once it is freed from its bound state with the nucleon.

1.4 Hadronization

In physics, *Confinement* is an unsolved problem where a parton cannot propagate as a free particle; hence, it has to transform into a hadron. This transformation is known as *Hadronization*.

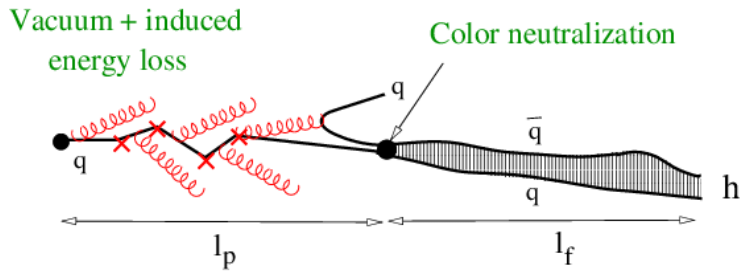

Figure 1.6: Space-time development process of hadronization[12]. l_p and l_f are the production length/time and the formation length/time, respectively.

This process can be characterized by two timescales [13]: the production time and the formation time (see Fig.1.6). The former ranges from when the quark is knocked-out off the nucleon to when its color field is neutralized. The latter ranges from when color neutralization happens to when the hadron fully forms.

In the production time, the free quark loses energy according to its environment and its energy. In *vacuum*, the quark will produce a jet of hadrons with which it will share its energy. At this point, a non-perturbative model to describe the energy loss is the *Lund string model*[14]; thus, the energy loss is given by:

$$\Delta E_{vac} = \kappa L, \tag{1.46}$$

where κ is known as *string tension* and is usually assigned the value $1[GeV/fm]$, and L is the distance traveled by the quark. In DIS, *gluon bremmstrahlung* becomes an additional or even the principal source of energy loss; hence, we can use a perturbative approach to describe the energy loss[13]:

$$\Delta E_{vac} = \frac{2}{3\pi}\alpha_s(Q^2)Q^2 L. \tag{1.47}$$

When the quark travels through nuclear media, an additional source of energy loss is the *induced energy loss*. It is given by the elastic collisions between the quark and the nucleons inside the nucleus. The former gains transverse momentum due to these collisions. Induced energy loss reads[13]:

$$\Delta E_{ind} = \frac{3}{8}\alpha_s \Delta p_T^2 L = \frac{3}{4}\alpha_s C(E)\rho_A L^2, \tag{1.48}$$

where ρ_A is the nuclear density, Δp_T^2 is the transverse momentum acquired by the quark, and $C(E)$ is the derivative of the nucleon-dipole cross-section w.r.t. the separation between the dipole components, where this separation is evaluated at zero after the derivation[15].

In the formation time (see Fig.1.6), the prehadron has an uneventful trip if it is in vacuum. However, in nuclear media, the prehadron can elastically and inelastically scatter with nucleons. The latter leads to *nuclear absorption*. The former is measured experimentally and is parameterized as a fraction of the hadron-nucleon elastic cross section (see next section).

1.4.1 Transverse Momentum Broadening

Induced energy loss and transverse momentum broadening are conceptually tied as we previously saw. There are models to obtain expressions for the broadening. In this section we will show a model in which the broadening is given by [15]:

$$\left\langle \Delta p_\perp^2 \right\rangle_q = \left\langle \sigma q_\perp^2 \right\rangle \frac{1}{\langle S_* \rangle} \times \int_{-\infty}^{\infty} d^2b dz \rho_A(\vec{b}, z) \int_z^{z+l_p} dz' \rho_A\left(\vec{b}, z'\right) \exp\left(-\sigma_* \int_{z+lp}^{\infty} dz'' \rho_A\left(\vec{b}, z''\right)\right), \tag{1.49}$$

which is based on the *hard-sphere approximation*. The terms of the equation are:

- $\langle \sigma q_\perp^2 \rangle$ is the mean transverse momentum acquired by the quark in one collision:

$$\langle \sigma q_\perp^2 \rangle = \int d^2 q_\perp \frac{d\sigma}{d^2 q_\perp} q_\perp^2, \tag{1.50}$$

where σ is the quark-nucleon cross section.

- S^* represents the pre-hadron survival probability, i.e., the probability that the pre-hadron is not absorbed by the medium. Assuming that the shape of the prehadron does not change substantially over space-time, the mean of S^* is defined as:

$$\langle S^* \rangle = \int_{-\infty}^{\infty} d^2b dz \rho_A(\vec{b}, z) \exp\left(-\sigma_* \int_{z+l_p}^{\infty} dz' \rho_A(\vec{b}, z') \right), \tag{1.51}$$

where σ_* is the prehadron-nucleon inelastic cross section. It is experimentally determined as a fraction of the hadron-nucleon cross section:

$$\sigma_* \approx \frac{2}{3} \sigma_{hN}. \tag{1.52}$$

It is worth remarking that eq. (1.51) it is not the proper survival probability. The survival probability of a prehadron is called *Nuclear Transparency* and, for prehadrons with quasi non-changing size, is defined as [13]:

$$Tr = \left| \frac{\left\langle \Psi_h(r_T) \left| \exp\left[-\frac{1}{2} \sigma^N_{\bar{q}q}(r_T) T_A \right] \right| \Psi_{\bar{q}q}(r_T) \right\rangle}{\langle \Psi_h(r_T) \mid \Psi_{\bar{q}q}(r_T) \rangle} \right|^2, \tag{1.53}$$

where the $q\bar{q}$ subscript references to a dipole which is a common picture referencing the prehadron, r_T represents the transverse distance between the dipole components, and T_A is the nuclear thickness function:

$$T_A = \int dz \rho_A(b, z). \tag{1.54}$$

The nuclear density ρ_A can be determined in the hard-sphere approximation. This is reasonable when the size of the boundary of the nucleus is smaller in comparison to its whole body. Then, the nuclear density can be expressed as:

$$\rho_A(b, z) = \rho_0 \Theta(R_A - b) \Theta(R(b) - |z|); \quad R(b) = \sqrt{R_A^2 - b^2}, \tag{1.55}$$

where the homogeneous nuclear density ρ_0 is $0.16[fm^{-3}]$ (experimental value), and R_A is the nuclear radius which is proportional to $A^{1/3}$.

Finally, an analytical expression of eq. (1.49) can be obtained considering a non-changing size dipole[15]:

$$\begin{aligned}\left\langle \Delta p_\perp^2 \right\rangle_q = \left\langle \sigma q_\perp^2 \right\rangle \rho_0 \Bigg\{ l_p \left[1 - \frac{1}{\langle S_* \rangle} \cdot \left(\frac{3}{8} \frac{l_p}{R_A} - \frac{1}{64} \left(\frac{l_p}{R_A} \right)^3 \right) \right] \Theta \left(2R_A - l_p \right) \\ + \frac{3}{4} R_A \Theta \left(l_p - 2R_A \right) \Bigg\}.\end{aligned} \tag{1.56}$$

The importance of eq. (1.56) lies in the behavior of the broadening according to variables such as l_p and R_A.

The term accompanied by $\Theta \left(l_p - 2R_A \right)$ refers to when the hadronization happens outside the nucleus. If that is the case, the usual proportion $\Delta P_T^2 \propto A^{1/3}$ is recovered. The term accompanied by $\Theta \left(2R_A - l_p \right)$ addresses the case in which the production length is smaller than the nucleus, in which the l_p/R_A terms are corrections introduced due to the finite size of the nucleus.

Chapter 2

Experimental setup

2.1 CEBAF Accelerator

The Continuous Electron Beam Accelerator Facility (CEBAF) accelerator (see Fig.2.1) is located at the Thomas Jefferson National Accelerator Facility (JLAB) in Newport News, Virginia, USA; and the main lines of investigation is nuclear physics and elementary particle physics.

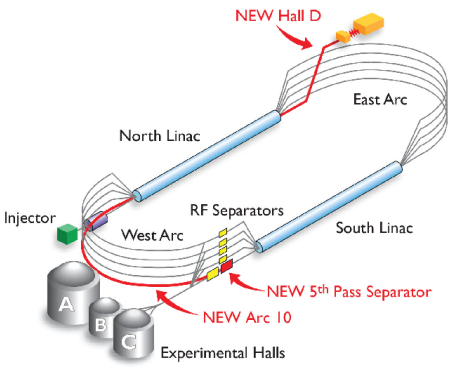

Figure 2.1: CEBAF map

The accelerator functioning can be summarized in the following steps:

1. The injector delivers 45$[MeV]$ polarized or unpolarized electrons with a frequency of 1.4791$[GHz]$.

2. The electrons enter the north linear accelerator (LINAC) which is composed of 20 cryo-modules. Each cryo-module (see Fig.2.2) is composed of eight niobium

cavities kept at $2[K]$ due to the constant supply of liquid hydrogen, work of the Central Helium Liquefier. In these cavities, an electric field accelerates the electrons. At the end of the linear accelerator (LINAC) the electrons' energy should increase in $0.6[GeV]$.

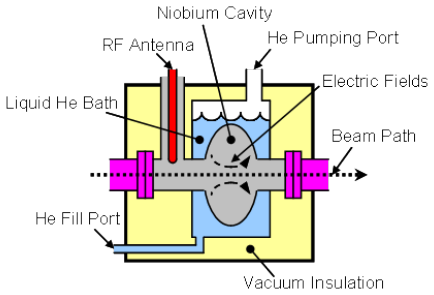

Figure 2.2: Reference image of the structure of a cryo-module

3. After the LINAC, the electrons go to the recirculating arc. This is a semi-circular track that brings electrons from one LINAC to the other. The arcs are a solution to the acceleration procedure given the space availability of the facility.

4. In the southern LINAC occurs the same process as in the first. However, there is a difference in the possible outcome:

   - The electrons can exit the acceleration process and enter one of the halls.
   - The electrons can keep going with the acceleration process entering the northern LINAC once again, then the south, and so forth so on.

Recently, the facility was updated to perform with a $12[GeV]$ beam, and also with the construction of Hall D.

As of now, there are four halls: A, B, C, and D. Hall A and C reaches luminosities of $10^{38}[cm^{-2}s^{-1}]$, with very small acceptance, meanwhile Hall B reaches luminosities of $2 * 10^{34}[cm^{-2}s^{-1}]$ with large acceptance.

2.2 CLAS Detector

Inside Hall B it is located the CEBAF Large Acceptance Spectrometer (CLAS) detector (see Fig.2.3). One of its main characteristics is that it has a near 4π solid angle detection coverage. Considering the z axis as the beamline (see Fig.2.4), the coverage in the polar coordinate θ is from 8° to 142°. In the azimuthal coordinate, it is from 0° to 360°, with six gaps due to the magnetic coils. These gaps divide the detextor in six sectors.

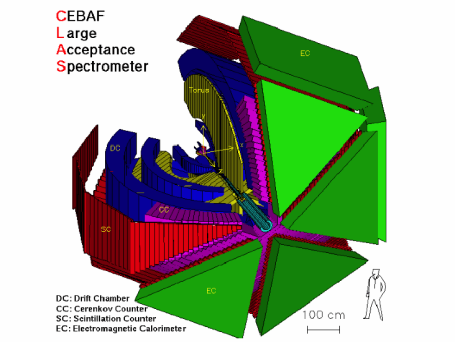

Figure 2.3: CLAS detector general view.

The plane perpendicular to the beamline is divided in six *sectors* due to the presence of superconducting coils (see Fig. 2.4). These form a torus shaped magnetic field around the beamline:

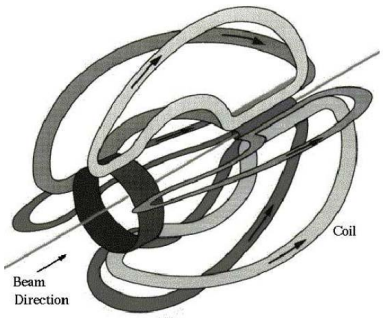

Figure 2.4: CLAS detector division by the coils

The particles involved in the scattering processes are affected by this magnetic field, hence, they are deviated from their original paths. In the case of positively charged particles, these tend to have an out-bending trajectory deviation. Meanwhile, the negatively charged particles tend to have an in-bending trajectory de-

viation. In the case of the target and the non-scattered electrons, the magnetic field won't affect them because the design contemplates a null magnetic field in the beamline. This allows the usage of a polarized target.

Additionally, around the target zone, we can find a smaller version of the large torus, and it applies a small magnetic field that deviates low energy electrons, produced by Moller scattering, from reaching the innermost drift chambers. In other words, the smaller torus greatly reduces background.

All the non-scattered electrons are collected in a Faraday Cup (FC) at the end of their route.

CLAS is composed of[16]:

- Drift chambers
- Cherenkov counters
- Time of Flight counters
- Electromagnetic calorimeters

2.2.1 Drift Chambers

Drift chambers (DC) are detectors filled with inert gas or a mixture of gases. In CLAS case this mixture is $90\%Ar$ and $10\%CO_2$. Additionally, they have conducting wires subject to a certain electric potential. Then, when a charged particle passes, the gas ionizes and the electrons produced by this process goes to the wires due to the electric force exerted by their electric field. This generates an electric pulse that allows to detect where the original particle passed. Hence, DC are used to measure particle trajectories and momentum.

CLAS has 18 multi-wire DC. Three per sector, and each one of them in a different radial position or *region* (see Fig.2.5).

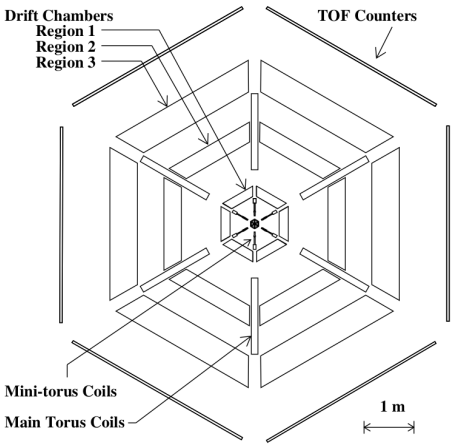

Figure 2.5: CLAS point of view facing the beamline

The DC has a $8° \leq \theta \leq 142°$ and 80% ϕ coverage [17]. Track resolution for 1[GeV] charged particles were:

- Relative resolution ($\delta p/p \leq 0.5\%$)
- $\delta\theta$,$\delta\phi \leq 2[mrad]$.

2.2.2 Cherenkov Counters

The Cherenkov effect is a physical phenomenon where a charged particle induces to the traversed medium to radiate. This happens whenever the charged particle has a speed greater than the speed of light in the medium. The essential condition being:

$$\beta \cdot n > 1 \tag{2.1}$$

Where n is the medium's refractive index.

In CLAS, the Cherenkov counters (CC) are used to identify, or discriminate, charged particles, specifically electrons and pions. With a coverage in the θ angle up to 45°[18], the structure is divided by the *sectors* of CLAS. The CC are composed of several mirrors to reflect the Cherenkov radiation into *Winston Cones* (see Fig.2.6) where the latter conducts the light to photo-multiplier tubes.

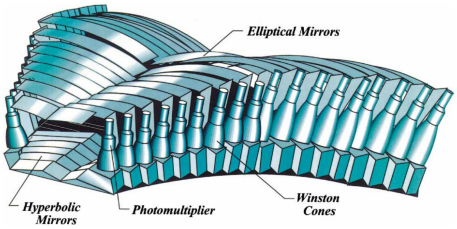

Figure 2.6: Cherenkov detector of one CLAS sector

These tubes are filled with Perfluorobutane -C_4F_{10}-, which has a refractive index $n = 1.00153$. This allows a high photon yield and a pion momentum threshold of $p_{th} = 2.5[GeV/c]$[16].

2.2.3 TOF Counters

The Time Of Flight (TOF) counters correspond to a family of detectors know as *Scintillator Counters*. How these work is simple:

1. A charged particle interacts with the surrounding atoms.

2. Excited atomic electrons re-emit energy through photons.

3. The emitted photons travel through the scintillator and reach a photo-multiplier tube. In other cases, if the frequency of the light is out of the detector sensibility, it reach a wavelength shifter first and then a photo-multiplier tube.

4. The photo-multiplier converts the light into an electric signal.

In CLAS, there are 57 scintillators per sector, with a $8° \leq \theta \leq 142°$ and full active ϕ coverage. The thickness of every scintillator is $5.08[cm]$, and its length stretches from $15[cm]$ in the front to $4.22[m]$ in the middle. Also, their widths stretch from $15[cm]$ to $22[cm]$ [19]. At both ends of every scintillator there is a photo-multiplier tube (see Fig.2.7).

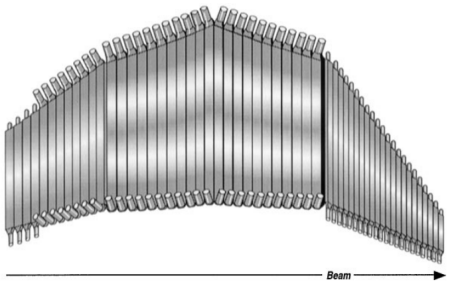

Figure 2.7: Scintillator system of one CLAS' sector

The timing resolution of the scintillators was parameterized with the following formula[16]:

$$\sigma_{TOF} = \sqrt{\sigma_0^2 + \frac{\sigma_1^2 + (\sigma_P \cdot L/2)^2}{N_{pe} \cdot e^{-L/2\lambda}}} \tag{2.2}$$

Where:

- $\sigma_0 = 0.062[ns]$ is the natural timing resolution of the scintillator.
- $\sigma_1 = 2.1[ns]$ is the combined single photo-electron response of the scintillator and the photo-multiplier tube.
- $\sigma_P = 0.0118[ns/cm]$ accounts for path-length variations in the light collection.
- $N_{pe} = 1043$ is the average number of photo-electrons that the photo-multiplier tube would receive if there was no attenuation in the scintillator.
- L is the scintillator length.
- λ is the light wavelength.

2.2.4 Calorimeters

Calorimeters are detectors used to detect charged and neutral particles. The detection works via deposition of energy. Showers of secondary particles are produced and this generates signals in a contained region of the detector. The type of calorimeters used in CLAS are called *sampling calorimeters* and are composed of various layers of scintillators and *absorbers*.

CLAS possesses two types of sampling calorimeters: the forward calorimeters and

the large angle calorimeter.

The forward calorimeters have a projective geometry where the polar angle coverage extends up to 45°. They are divided in modules and are located in the sectors of the detector. Each triangle-shaped module consists of 39 layers, with each one of them increasing its area linearly w.r.t. the distance from the target. The layers are composed of a 22$[mm]$ thick lead sheet and a 10$[mm]$ thick BC142 scintillator, the latter is aligned parallel to one of the sides of the triangle shaped module. Layer-by-layer, this orientation changes. These are denoted as U, V and W (see Fig.2.8).

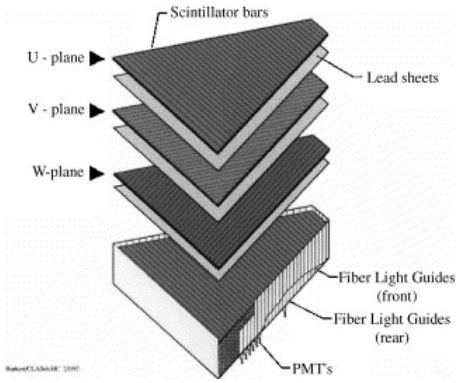

Figure 2.8: Calorimeters modules

There is an exclusion zone within 10$[cm]$ from the edges of the module. This is to contain completely the showers produced by the traversing particle. The detection is made through a triangulation of the shower's position. The scintillators are the devices in charge of giving the signal of the shower.

The relative resolution of the forward calorimeter is:

$$\frac{\Delta E}{E} = \frac{10.3\%}{\sqrt{E[GeV]}} \tag{2.3}$$

The large angle calorimeter (LAC) is used to detect neutral particles and scattered electrons. It covers up to 120° in the azimuthal coordinate, hence it covers two sectors. In the polar coordinate goes from 45° to 75°. The modules are comprised of 33 layers of lead foil and scintillators.

2.3 Eg2 Experiment

The Eg2 experiment had its experimental runs through 2004 at Jefferson Lab's Hall B. The motivation of this experiment was to study phenomena such as the hadronization process and color transparency. These would be analyzed in nuclear media through specific observables like the hadronic multiplicity ratios or the hadronic transverse momentum broadening.

For this experiment, a double target system [20] was designed in which a liquid (hydrogen, deuterium) and a solid (carbon, iron, lead, tin, aluminum) target would be exposed simultaneously to JLAB's electron beam (see Fig.2.9). In this thesis we used the results from the carbon, iron and lead targets with its liquid results associated.

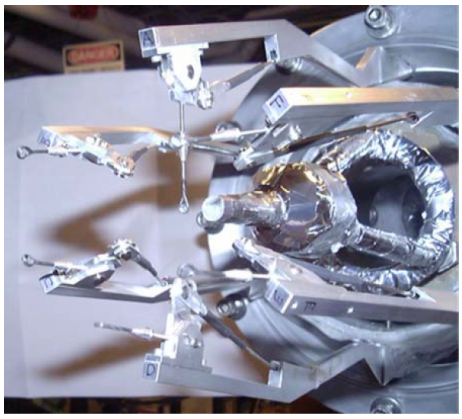

Figure 2.9: Eg2's double target system. The *claws* holds the interchangeable solid targets. The cylinder-shaped object wrapped in foil is the liquid target.

The spatial dimensions of the target were designed such that both solid and liquid targets provide the same luminosity, except in the case of Pb. The specific lengths and areal densities (A.D.) are given in Table 2.1[20].

To perform acceptance correction on the data a GEANT package called GSIM was

Target	Length $[mm]$	Longitudinal A.D. $[g/cm^2]$	Transverse A.D. $[g/cm^2]$
C	1.7	0.38	0.33
Fe	0.40	0.31	1.2
Pb	0.14	0.16	1.7

Table 2.1: Eg2's solid target dimensions.

developed in which the target geometry was implemented by Hayk Hakobyan [20] to realistically simulate the experiment (see Fig.2.10).

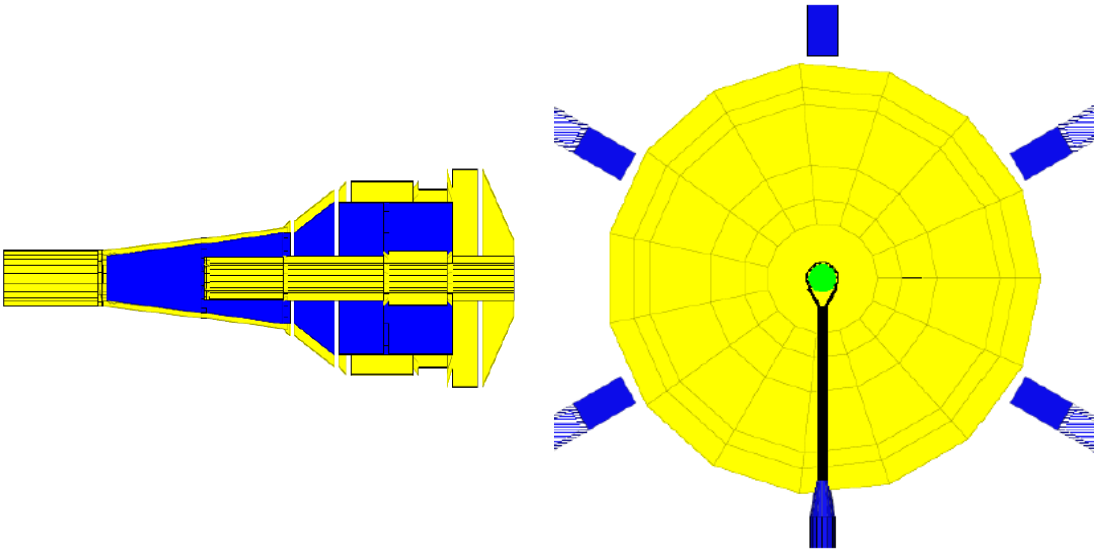

Figure 2.10: GSIM representation of the liquid target cross-section looked from the side (left).GSIM representation of the solid target (green) and the liquid target (yellow) looked from the front (right).

Chapter 3

Data analysis

3.1 Particle Identification and Vertex Determination

The data acquired is reconstructed with *RECSIS* in a process that is known as *cooking*. Then, the data is stored in a BOS (Bank Object System) format database. The files that contain the events is in *CLASTool* format, which is a C++ package developed to analyse CLAS data. Finally, *Analyser* is used to filter these events and calculate its respective variables.

To select an event, first, we need to identify an electron. Afterwards, the rest of the particles can be identified. In this analysis those particles were positive pions. These were stored in TNtuples on ROOT files with all its relevant kinematical variables.

The data set and the particle identification scheme used in the approved analysis note of charged pions [21] were used in this analysis.

3.1.1 Electrons

The following criteria was used to identify a particle candidate as an electron:

- A negatively charged signal must be recorded in the Drift Chambers (DC),

the Cherenkov Counters (CC), the Electromagnetic Calorimeters (EC), and the Scintillator Counters (SC, TOF).

- It is required a minimum number of photo-electrons ($Nphe$), which are emitted by the passage of a candidate in the CC, to reduce negative pion contamination. The $Nphe$ requirement depends on the CLAS's sector where a candidate was detected:

$$Nphe = \begin{cases} > 25; \text{ Sector 1} \\ > 25; \text{ Sector 2} \\ > 26; \text{ Sector 3} \\ > 21; \text{ Sector 4} \\ > 28; \text{ Sector 5} \\ > 28; \text{ Sector 6} \end{cases} \tag{3.1}$$

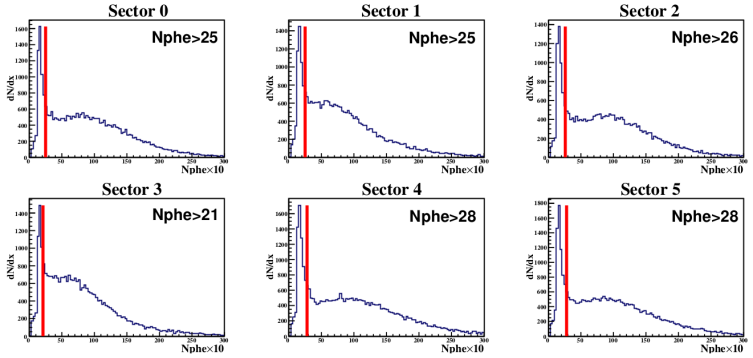

Figure 3.1: $Nphe$ distributions for different CLAS's sectors. The red lines represent where the cut was applied. The regions of low $Nphe$ are associated with negative pion contamination. Plot from [21].

- A coincidence time between the EC and SC was required. This time is defined as:

$$\Delta T = (\text{Time(EC)} - \text{Time(SC)}) - \left(\frac{Path(EC)}{vel} - \frac{Path(SC)}{vel} \right) \tag{3.2}$$

Where:

  - Time(EC/SC) is the time a candidate takes from the vertex to the EC/SC

and it is measured with the TOF detector.

- Path(EC/SC) is the distance traveled by the candidate from the vertex to the EC/SC.
- *vel* is the velocity of a candidate measured through its momentum which is obtained with the DC.

From eq.(3.2) is obtained a Gaussian-like distribution centered at zero (see Fig.3.2).

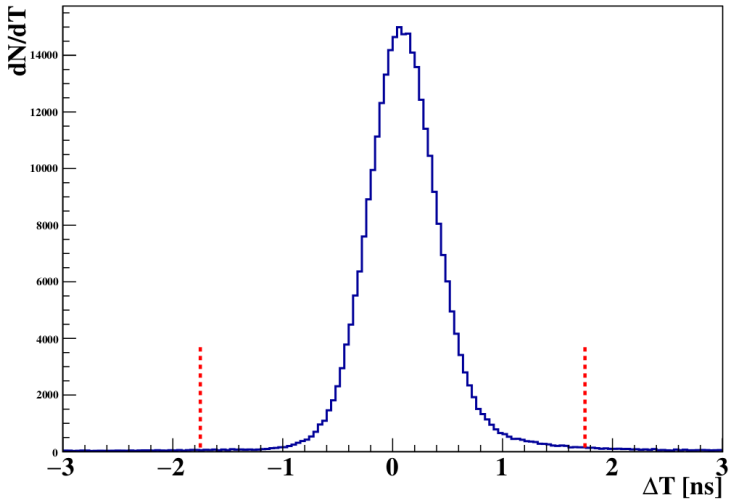

Figure 3.2: Coincidence time distribution of electron candidates. The dashed red lines represent the points where the cut was applied. Plot from [21].

The cut imposed on ΔT is given by the standard deviation σ obtained from a fit to the variable with a Gaussian function:

$$|\Delta T| < 5 * 0.35 = 5 * \sigma \tag{3.3}$$

- A set of cuts was applied to the candidates in the EC based on the energy deposited in it. This energy can be treated twofold: total energy deposited in the 13 layers of the EC (E_{tot}) or energy deposited in the outer (E_{out}) and inner (E_{int}) part of the EC. The inner part is the closest set of five layers to the vertex. Meanwhile, the outer part is the farthest set of eight layers to the vertex.

Therefore, the following cut was applied:

$$E_{out} > 0[GeV] \tag{3.4}$$

To reduce negative pions contamination it is imposed:

$$E_{in} > 0.06[GeV] \tag{3.5}$$

To further reduce this contamination two more sets of cuts were applied. The first involved E_{tot} and it is applied under the assumption that negative pion's energy deposition in the EC is independent of their momentum (see Fig.3.3).

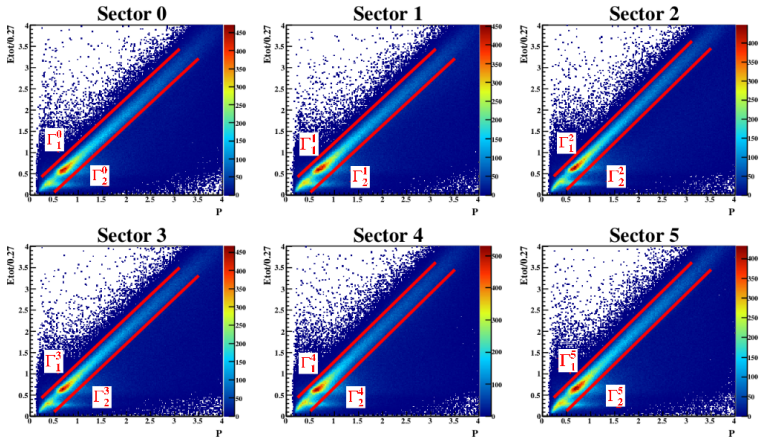

Figure 3.3: Candidates' normalized E_{tot} versus their momentum for all sectors of CLAS. Events between the red lines are the ones selected in the analysis. Plot from [21].

Thus, the cuts applied were:

$$\begin{aligned}
\Gamma_1^0: &\quad \mathrm{E'_{tot}} < 1.05 \times \mathrm{P} + 0.18 \quad ; \quad \Gamma_2^0: \quad \mathrm{E'_{tot}} > 1.05 \times \mathrm{P} - 0.46 \\
\Gamma_1^1: &\quad \mathrm{E'_{tot}} < 1.05 \times \mathrm{P} + 0.18 \quad ; \quad \Gamma_2^1: \quad \mathrm{E'_{tot}} > 1.05 \times \mathrm{P} - 0.46 \\
\Gamma_1^2: &\quad \mathrm{E'_{tot}} < 1.11 \times \mathrm{P} + 0.18 \quad ; \quad \Gamma_2^2: \quad \mathrm{E'_{tot}} > 1.11 \times \mathrm{P} - 0.43 \\
\Gamma_1^3: &\quad \mathrm{E'_{tot}} < 1.07 \times \mathrm{P} + 0.18 \quad ; \quad \Gamma_2^3: \quad \mathrm{E'_{tot}} > 1.07 \times \mathrm{P} - 0.43 \\
\Gamma_1^4: &\quad \mathrm{E'_{tot}} < 1.11 \times \mathrm{P} + 0.18 \quad ; \quad \Gamma_2^4: \quad \mathrm{E'_{tot}} > 1.11 \times \mathrm{P} - 0.43 \\
\Gamma_1^5: &\quad \mathrm{E'_{tot}} < 1.11 \times \mathrm{P} + 0.18 \quad ; \quad \Gamma_2^5: \quad \mathrm{E'_{tot}} > 1.11 \times \mathrm{P} - 0.43
\end{aligned} \tag{3.6}$$

Where E'_{tot} is the normalized energy $E'_{tot} = E_{tot}/0.27$.

The second set of cuts involved E_{in} and E_{out} (see Fig.3.4). The cuts are based on the same assumption in regards to the previous set.

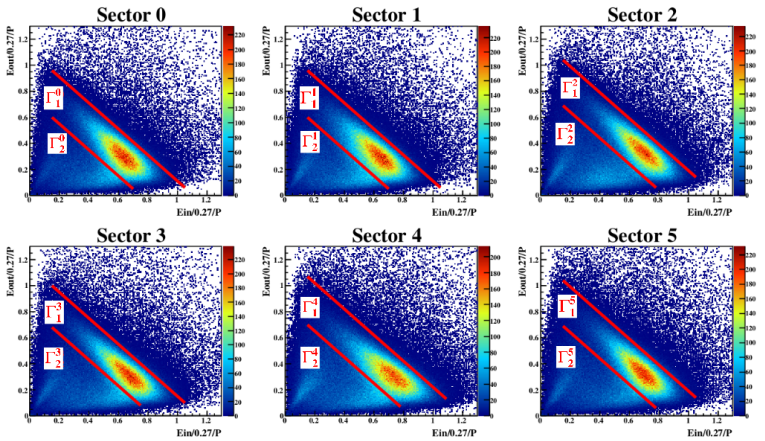

Figure 3.4: Candidates' normalized E_{in} versus normalized E_{out} for all sectors of CLAS. Events between the red lines are the ones selected in the analysis. Plot from [21].

Thus, the cuts applied were:

$$\begin{aligned}
\Gamma_1^0: &\ \mathrm{E'_{in}} + \mathrm{E'_{out}} < 1.11 \times \mathrm{P} \quad ; \quad \Gamma_2^0: \ \mathrm{E'_{in}} + \mathrm{E'_{out}} > 0.75 \times \mathrm{P} \\
\Gamma_1^1: &\ \mathrm{E'_{in}} + \mathrm{E'_{out}} < 1.11 \times \mathrm{P} \quad ; \quad \Gamma_2^1: \ \mathrm{E'_{in}} + \mathrm{E'_{out}} > 0.75 \times \mathrm{P} \\
\Gamma_1^2: &\ \mathrm{E'_{in}} + \mathrm{E'_{out}} < 1.19 \times \mathrm{P} \quad ; \quad \Gamma_2^2: \ \mathrm{E'_{in}} + \mathrm{E'_{out}} > 0.84 \times \mathrm{P} \\
\Gamma_1^3: &\ \mathrm{E'_{in}} + \mathrm{E'_{out}} < 1.15 \times \mathrm{P} \quad ; \quad \Gamma_2^3: \ \mathrm{E'_{in}} + \mathrm{E'_{out}} > 0.83 \times \mathrm{P} \\
\Gamma_1^4: &\ \mathrm{E'_{in}} + \mathrm{E'_{out}} < 1.22 \times \mathrm{P} \quad ; \quad \Gamma_2^4: \ \mathrm{E'_{in}} + \mathrm{E'_{out}} > 0.85 \times \mathrm{P} \\
\Gamma_1^5: &\ \mathrm{E'_{in}} + \mathrm{E'_{out}} < 1.19 \times \mathrm{P} \quad ; \quad \Gamma_2^5: \ \mathrm{E'_{in}} + \mathrm{E'_{out}} > 0.84 \times \mathrm{P}
\end{aligned} \tag{3.7}$$

- This requirement, developed by Taisiya Mineeva [22], is based on positive pions energy deposition. This is approximately 27% of their energy on the EC (see Fig.3.5).

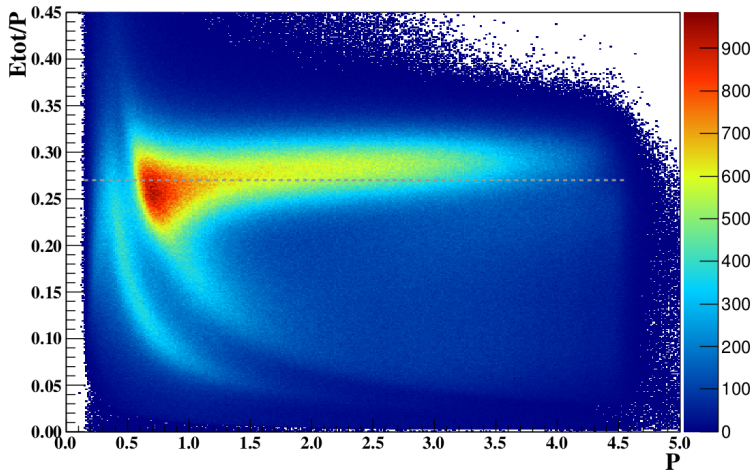

Figure 3.5: Candidates' total energy deposited normalized to its momentum vs its momentum. The dashed line represents the approximate value of the E_{tot}/P ratio expected for electrons.

Therefore, a fit is performed on every sector's E/P vs P distribution (see Fig.3.6). A second degree polynomial is used:

$$\begin{aligned} \mu(P) &= a_1 + a_2 \times P + a_3 \times P^2 \\ \sigma(P) &= \sqrt{a_4^2 + \frac{a_5^2}{P}} \end{aligned} \tag{3.8}$$

Then the cut is stated as:

$$\left| \frac{E}{P} - \mu \right| < 2.5 \times \sigma; \quad E = Max(E_{tot}, E_{in} + E_{max}) \tag{3.9}$$

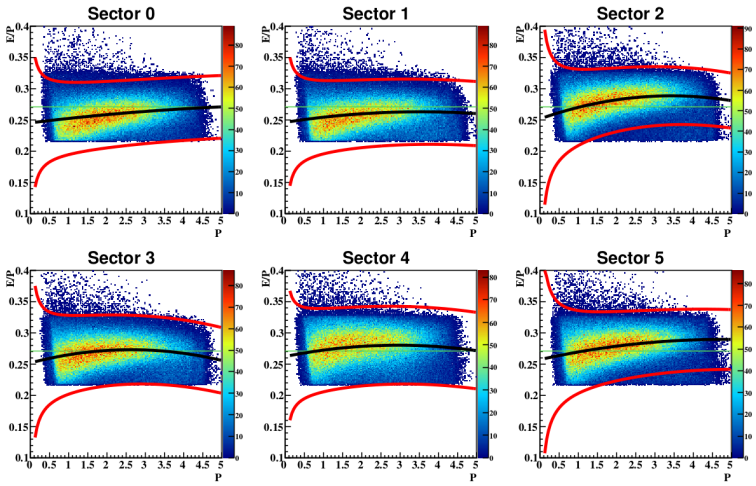

Figure 3.6: The black line corresponds to ν, and the red lines correspond to $\nu \pm \sigma$. The events between the red lines were selected for the analysis. These plots show electron candidates with some cuts already applied as can be observed from the drastic cutoff near $E/P = 0.21$.

- Fiducial cuts were applied to exclude regions of the detectors that did not have a good reconstruction in the simulations. These requirements were imposed in the DC and EC.

  The DC fiducial cuts were developed by Lorenzo Zana [23] and were applied to exclude regions where the simulation did not represent the detector optimally (see Fig.3.7).

  The EC fiducial cuts exclude its edges. Hits detected there had the issue that

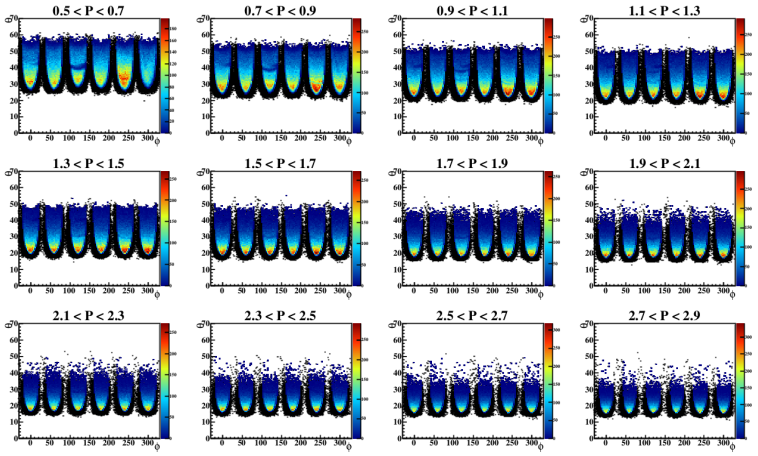

Figure 3.7: Superimposed plots of lab angles. The events in black are those removed due to the DC fiducial cuts.

showers wouldn't be entirely contained in the detector. The cuts were applied in the coordinates of the different layers of the EC[1].

The cuts were the following:

$$40 < U < 410 \quad V < 370 \quad W < 405 \tag{3.10}$$

The effect is best observed in the plane perpendicular to the beam line (see Fig.3.8).

[1]The layers of the EC had certain orientations with the purpose of a precise triangulation procedure of the shower. The orientations are denoted with the letters U, V and W.

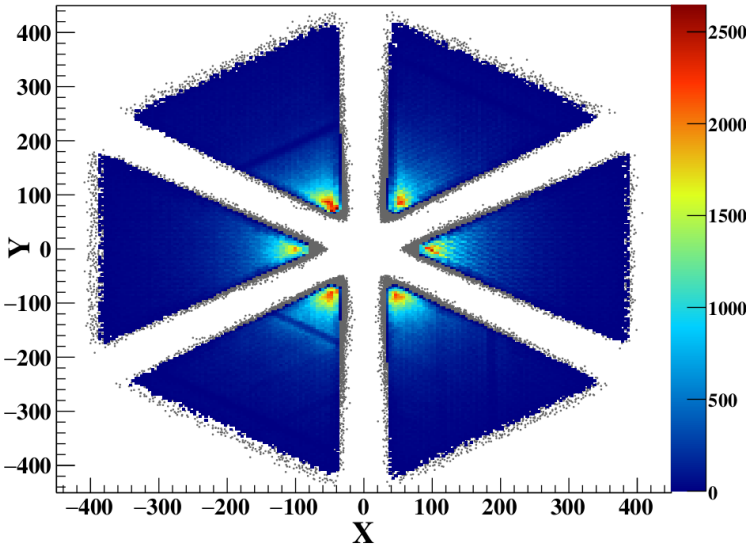

Figure 3.8: Superimposed plots of X-Y coordinate. The events in gray are those removed due to the EC fiducial cuts. Plot from [21].

3.1.2 DIS Cuts

After electrons have been selected we isolate DIS events. The following cuts were applied:

- $Q^2 > 1[GeV^2]$ to ensure that the energy of the virtual photon is enough to resolve the elemental constituents of the targeted nucleon.
- $W > 2[GeV]$ to avoid the resonance region and to select inelastic events.
- $y < 0.85$ to reduce the number of events with a high radiation of photons.

3.1.3 Positive Pions

To select positive pions with $P < 2.7[GeV]$ a TOF-based method was used. In this case was defined a variable similar to the coincidence time of the electron. It reads:

$$\Delta T = \left(\frac{L^{e^-}_{flight}}{c} - \frac{L^{\pi^+}_{flight}}{v_{\pi^+}} \right) - (t_{e^-} - t_{\pi^+}) \tag{3.11}$$

Where the L's are the distances from the vertex point to the location of the SC for the indicated particle, v is the velocity of the particle, and t's are the measured

times from the vertex point to the SC. Similarly to the electron coincidence time, we expect that this variable should be centered in zero. The cuts were applied in different bins of momentum (see Table 3.1).

P[GeV/c]	Lower Limit	Upper Limit
[0.00-0.25]	-0.70	0.70
] 0.25-0.50]	-0.70	0.65
] 0.50-0.75]	-0.70	0.65
] 0.75-1.00]	-0.70	0.65
] 1.00-1.25]	-0.55	0.55
] 1.25-1.50]	-0.50	0.55
] 1.50-1.75]	-0.50	0.40
] 1.75-2.00]	-0.48	0.40
] 2.00-2.25]	-0.50	0.40
] 2.25-2.50]	-0.50	0.40
] 2.50-2.70]	-0.50	0.40

Table 3.1: ΔT cuts in different momentum ranges.

3.1.4 High Energy Positive Pions

Methods that only use TOF variables to identify positive pions at high momentum ($P > 2.7[GeV]$) are not reliable. Therefore, CC cuts are added.

The requirements were the following:

- Entries in the CC and a positive status in the CC bank.
- To reduce heavy hadron contamination it was imposed:

$$Nphe > 1.5 \tag{3.12}$$

To further reduce heavy hadron contamination a TOF cut is applied (see Table 3.2).

P[GeV/c]	Lower Limit	Upper Limit
]2.7-3.3]	-0.60	0.45
]3.3-6.0]	-0.60	0.50

Table 3.2: ΔT cuts in different momentum ranges.

- A geometrical matching cut between the SC and CC hit:

$$\text{Geo.Match} < 5^{\circ} \tag{3.13}$$

3.1.5 Vertex Determination

Taisiya Mineeva developed these cuts in her neutral pion approved analysis note [24]. The CLAS's track reconstruction determined the location where the particles were coming. The previous procedure assumed that the beam position, in an x,y plane -perpendicular to the beamline-, is $(x, y) = (0[cm], 0[cm])$. Nevertheless, using proton elastic scattering, an offset was determined. Then, the *real* beam position was $(x, y) = (-0.043[cm], 0.33[cm])$. This offset implied that the real position of the vertex had to be obtained after the application of a sector-dependent correction to its coordinates. The set of corrected coordinates obtained were named: XC, YC, ZC.

After this procedure, the ZC coordinate becomes sector-independent, meaning that the longitudinal vertex cut selection also acquires this feature . The solid targets cut were determined through a Gaussian fit to ZC. Then, the cuts (see Table 3.3) are given by the parameters obtained from the fit:

$$\langle ZC \rangle - 3\sigma < ZC < \langle ZC \rangle + 3\sigma \tag{3.14}$$

Where $\langle ZC \rangle$ is the mean, and σ is the standard deviation.

Target	$ZC_{min}[cm]$	$ZC_{max}[cm]$
D	-31.80	-28.40
C	-25.33	-24.10
Fe	-25.65	-24.26
Pb	-25.54	-24.36

Table 3.3: ZC cuts for different targets.

3.1.6 Additional Cuts

The following cuts were applied to further improve the quality of data:

- To reduce background, a YC cut was applied. A study by Orlando Soto, Raphael Dupré, and William Brooks [24], determined that $|YC| < 1.4[cm]$ reduced the amount of events in 22%, approximately. With this cut, background is subtracted such that it can be negligible in some regions (see Fig.3.9).

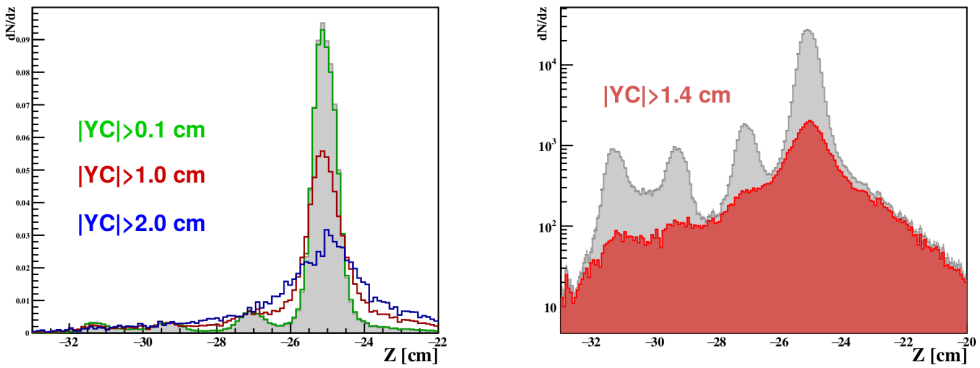

Figure 3.9: YC cut effect looking at the longitudinal coordinate Z. Notice that in the right plot the background is almost completely removed by the $|YC| < 1.4[cm]$ cut. Plot from [21].

Therefore, the cut applied on YC was:

$$|YC| < 1.4[cm] \tag{3.15}$$

- Simulation-based studies determined that $\sim$ 18% of positive pions decay in flight into muon-neutrino pairs [25]. The muon takes most of the energy of the pion, and the former is often misreconstructed as a pion with different momentum. To reduce the number of these events, first, the difference of Z coordinate was defined as:

$$\Delta Z = Z_{\pi^+} - Z_{e^-} \tag{3.16}$$

Then, based on [26], the cut applied was:

$$|\Delta Z| < 3[cm] \tag{3.17}$$

3.2 Binning

The following criteria was used to determine the binning:

- Every (Q^2, ν) bin has, approximately, the same number of events.
- Bigger bins are to be used at high z_h to reduce the statistical uncertainties in that region.
- The (Q^2, ν) bins are large such that we have enough events to provide a detailed description of P_T^2 distributions' tails.

The binning is given by:

Variable	Number of Bins	Limits
$Q^2[GeV^2]$	3	1 - 1.3 - 1.8 - 4
$\nu[GeV]$	3	2.2 - 3.2 - 3.7 - 4.26
z_h	8	0 - 0.1 - 0.2 - 0.3 - 0.4 - 0.5 - 0.6 - 0.8 - 1
$P_T^2[GeV^2]$	90	[0,3]
$\phi_{PQ}[Deg.]$	12	[-180,180]

Table 3.4: Binning used in this analysis

3.3 Experimental Corrections of the Data

3.3.1 Acceptance Correction

Pions that were not detected due to geometrical or efficiency reasons are included in the analysis via the application of the acceptance correction. This is calculated in a five-dimensional phase space. For every five-dimensional bin i, the acceptance factor was calculated as:

$$\mathrm{Acc}_i = \frac{N_{\mathrm{accept}_i}}{N_{\mathrm{thrown}_i}} \tag{3.18}$$

Where N_{accept_i} is the number of detected events in the realistic detector simulation, given by the GEANT simulation, and N_{thrown_i} is the number of generated events by the PYTHIA simulation. These simulations were generated by Hayk Hakobyan [27]. Then, the factors were applied to data as:

$$(\mathrm{Acc.\ Corr.\ Data})_i = \frac{(Data)_i}{\mathrm{Acc}_i} \tag{3.19}$$

The statistical error of this factor was calculated with error propagation and under the assumption that there is no correlation between N_{accept} and N_{thrown}:

$$\delta\mathrm{Acc} = \mathrm{Acc} * \sqrt{\left(\frac{\delta N_{\mathrm{accept}_i}}{N_{\mathrm{accept}_i}}\right)^2 + \left(\frac{\delta N_{\mathrm{thrown}_i}}{N_{\mathrm{thrown}_i}}\right)^2} \tag{3.20}$$

The statistical error of the thrown events is zero since these were generated from a theoretical model encoded in PYTHIA. Hence, the acceptance statistical error reads:

$$\delta\mathrm{Acc} = \mathrm{Acc} * \sqrt{\left(\frac{\delta N_{\mathrm{accept}_i}}{N_{\mathrm{accept}_i}}\right)^2} \tag{3.21}$$

To estimate δN_{accept_i}, we used the binomial distribution to characterize the behavior of the number of accepted events. The previous distribution is given by an n number of independent trials with a p probability of success in each trial. This is an analog to the acceptance in which $n = N_{\mathrm{thrown}}$, and p can be estimated as $p \sim \mathrm{Acc}$. Therefore,

the error of the acceptance factor is:

$$\delta \mathrm{Acc} = \pm \left| \sqrt{\frac{\mathrm{Acc}(1-\mathrm{Acc})}{N_{\mathrm{thrown}}}} \right| \tag{3.22}$$

We followed a conservative approach regarding the requirements to the acceptance factors since we explored the variations to these requirements in the systematic errors chapter. Hence, the acceptance factors were filtered by:

$$N_{\mathrm{accept}} > 1 \tag{3.23}$$

The effects of the acceptance correction on the integrated $\langle P_T^2 \rangle$ results without the x_f cut and with the x_f cut are displayed in Figs.3.10 and 3.11, respectively.

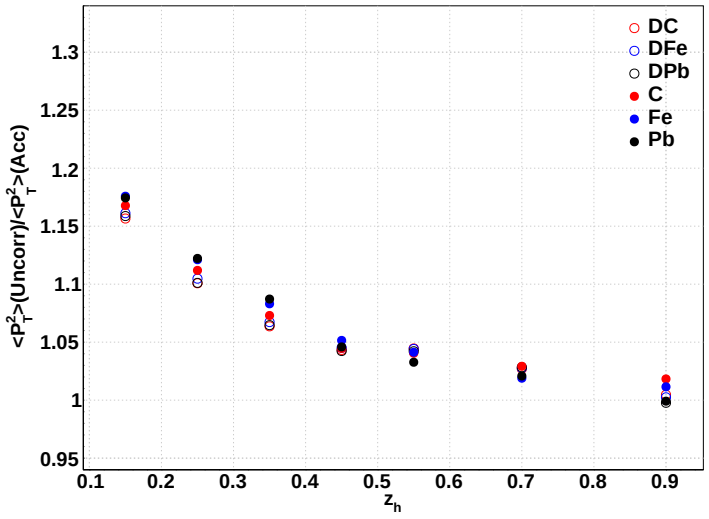

Figure 3.10: Ratio between the uncorrected and the acceptance corrected integrated results of $\langle P_T^2 \rangle$. The hollow points correspond to the liquid targets results, and the full points correspond to the solid targets results.

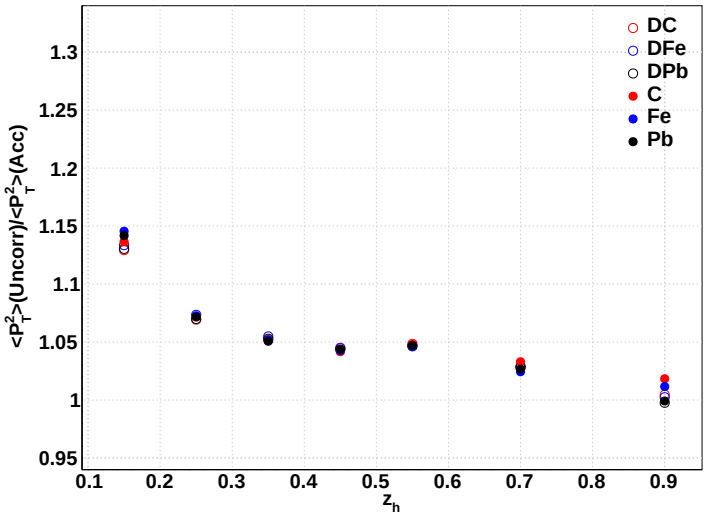

Figure 3.11: Ratio between the uncorrected and the acceptance corrected integrated results of $\langle P_T^2 \rangle$ with $x_f > 0$. The hollow points correspond to the liquid targets results, and the full points correspond to the solid targets results.

The effects of the acceptance correction on the integrated ΔP_T^2 results without the x_f cut and with the x_f cut are displayed in Figs.3.12 and 3.13, respectively.

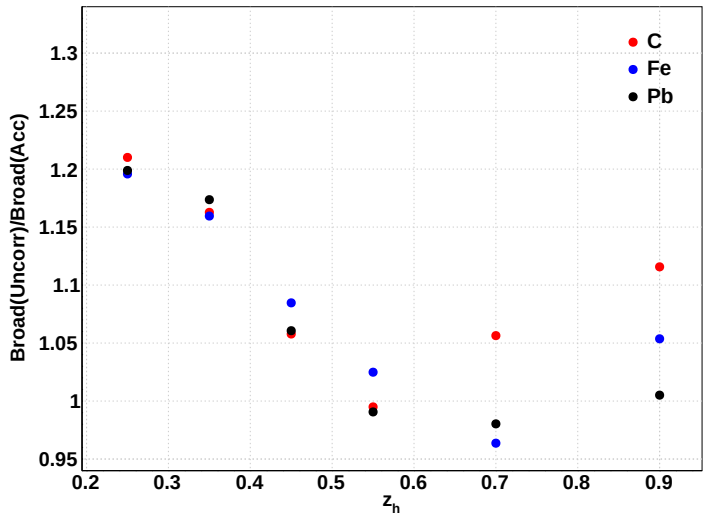

Figure 3.12: Ratio between the uncorrected and the acceptance corrected integrated results of ΔP_T^2.

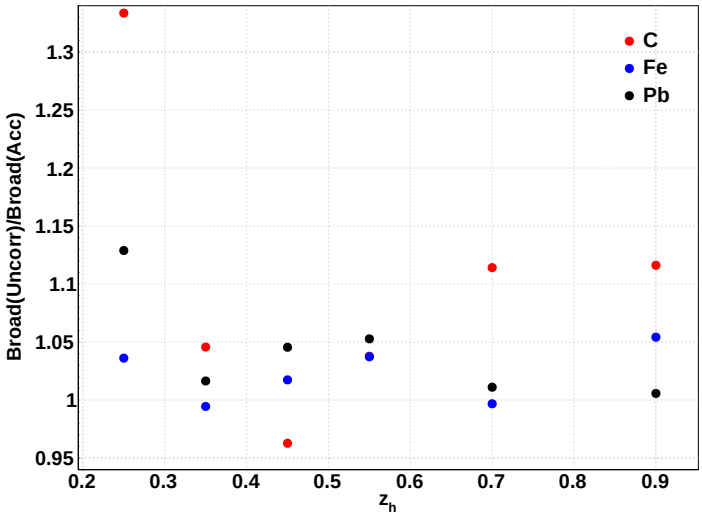

Figure 3.13: Ratio between the uncorrected and the acceptance corrected integrated results of ΔP_T^2 with x_f cut.

We observed a non-negligible influence of the acceptance correction on the squared transverse momentum. The region that is most affected is low z_h.

In the case of the transverse momentum broadening, the effect is amplified. Also, high z_h is affected reaching up to 12% of effect in the case of Carbon.

3.3.2 Radiative Correction

To correct the cross section that contains real photon emission and internal loops (see Fig.3.14) we used a SIDIS radiative correction package called HAPRAD.

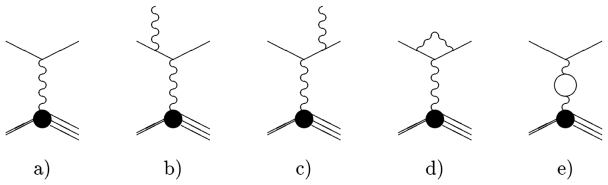

Figure 3.14: Born cross-section diagram (a) and diagrams with different radiative contributions (b,c,d,e).

The calculations in [28, 29] were used as the main reference to obtain the Radiative Correction (RC) factors. These are defined as the ratio between the radiatively corrected cross section and the Born cross section:

$$\delta_{RC} = \frac{\sigma_{\text{rad}}}{\sigma_{\text{Born}}} \tag{3.24}$$

The σ_{rad} reads [28]:

$$\sigma_{\text{rad}} = \sigma_{\text{Born}} e^{\delta_{\text{inf}}}(1 + \delta_{VR} + \delta_{\text{vac}}) + \sigma_F \tag{3.25}$$

Where σ_F is the contribution of the radiative tail, δ_{inf} and δ_{vac} are corrections related to radiation of soft photons and effects of vacuum polarization, and δ_{VR} is an infra-red sum of factorized parts of real and virtual photon radiation. The previous terms are given in [28].

The procedure to obtain the RC factors is based on a data-driven structure function extraction method where the acceptance corrected ϕ distributions, given by (Q^2, x, z, P_T) bins, are fitted with the following function:

$$f(\phi) = A + B \cdot Cos(\phi) + C \cdot Cos(2\phi) \tag{3.26}$$

The quality of the fits can be observed in Figs.(3.15, 3.16)

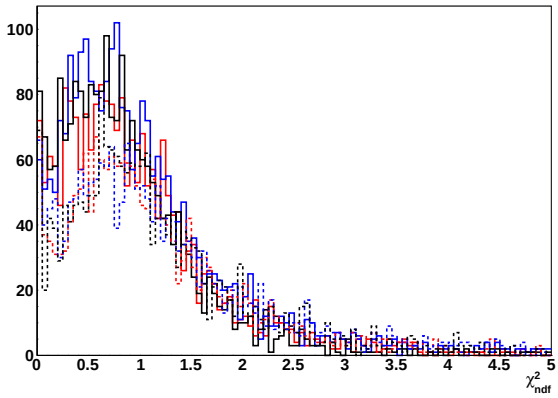

Figure 3.15: Distribution of the *goodness of fit*. The dashed lines correspond to the liquid targets results. The red corresponds to C-related results, the blue corresponds to Fe-related results, and the black corresponds to Pb-related results.

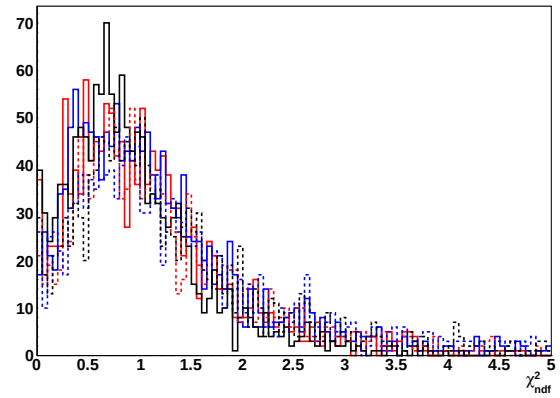

Figure 3.16: Distribution of the *goodness of fit* for $x_f > 0$ results. The dashed lines correspond to the liquid targets results. The red corresponds to C-related results, the blue corresponds to Fe-related results, and the black corresponds to Pb-related results.

The RC factors were calculated in a five-dimensional phase space; then, they were applied to the data as:

$$(\text{Rad. Corr. Data})_i = \frac{(\text{Data})_i}{\delta_{RC}} \tag{3.27}$$

We estimated the effect of the radiative corrections over the acceptance corrected results due to the use of the latter by HAPRAD. Thus, the effects of the radiative correction on the integrated $\langle P_T^2 \rangle$ results without the x_f cut and with the x_f cut are displayed in Figs.3.17 and 3.18, respectively.

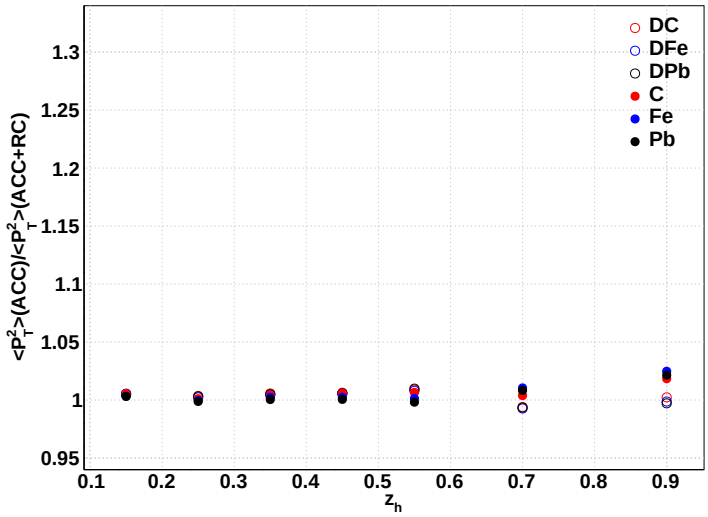

Figure 3.17: Ratio between the acceptance and the acceptance+radiative corrected integrated results of $\langle P_T^2 \rangle$. The hollow points correspond to the liquid targets results, and the full points correspond to the solid targets results.

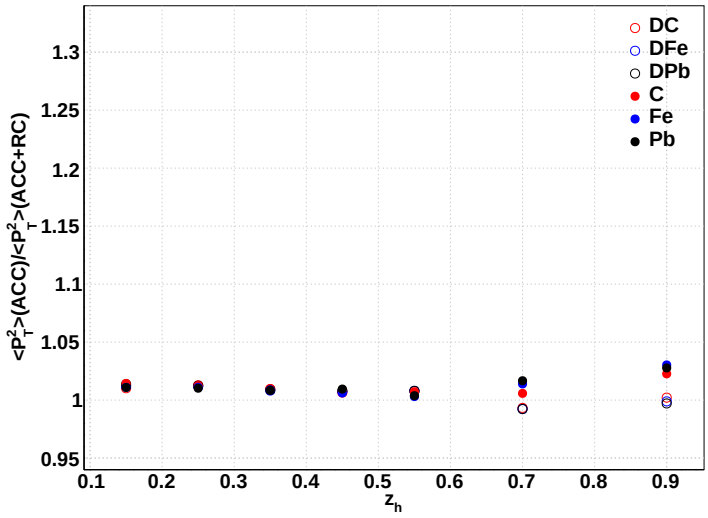

Figure 3.18: Ratio between the acceptance and the acceptance+radiative corrected integrated results of $\langle P_T^2 \rangle$ with $x_f > 0$. The hollow points correspond to the liquid targets results, and the full points correspond to the solid targets results.

The effects of the radiative corrections on the integrated ΔP_T^2 results without the x_f cut and with the x_f cut are displayed in Figs.3.19 and 3.20, respectively.

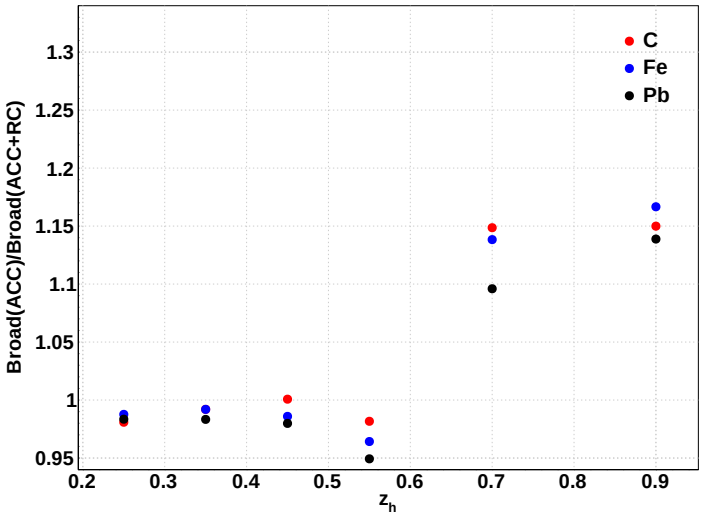

Figure 3.19: Ratio between the acceptance and the acceptance+radiative corrected integrated results of ΔP_T^2.

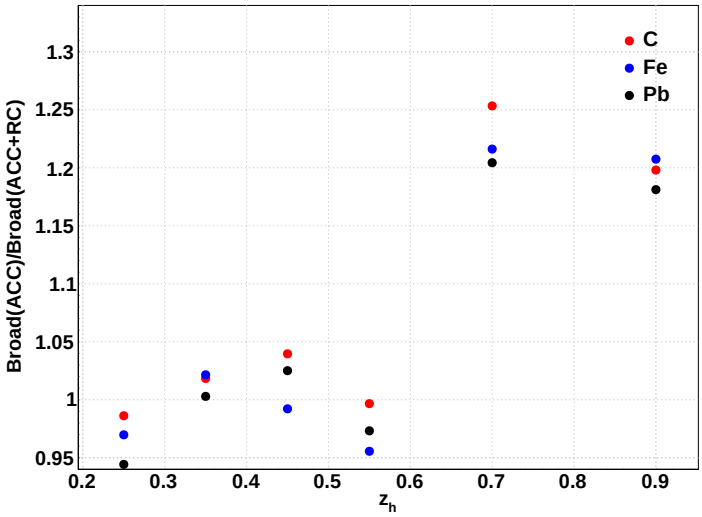

Figure 3.20: Ratio between the acceptance and the acceptance+radiative corrected integrated results of ΔP_T^2 with $x_f > 0$.

The radiative corrections do not present a big effect (such as the acceptance correction) on the averaged squared transverse momentum. The biggest effects are in the order of 3%.

For the transverse momentum broadening the effect is also amplified. However, in $z_h < 0.6$ the effect is only about 5%. The region where the correction has its biggest effect is in $z_h > 0.6$.

Due to the small effect of the radiative corrections, in comparison to the acceptance

correction, this is considered as a systematic uncertainty source.

3.4 Background Subtraction

Due to the observables we chose to analyze, P_T^2 distributions are fundamental. Therefore, to ensure a good quality of these the following two-step process was implemented.

3.4.1 Distributions' Cutoff Value

We called *scattered events* to those that had high P_T^2 values and did not followed an exponential trend (see Fig.3.21). These events were a minor fraction of the total and, in consequence, considered as background.

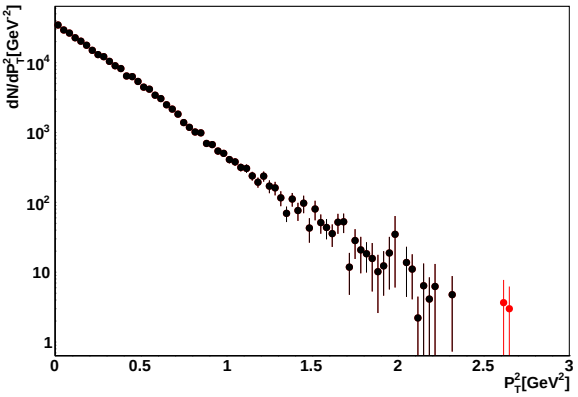

Figure 3.21: P_T^2 distribution for Fe target and within $1.3 < Q^2[GeV^2] < 1.8$, $2.2 < \nu[GeV] < 3.2$, $0.6 < z_h < 0.8$. The red points indicates which bins were considered as scattered points.

The method, in summary, consisted in the calculation of a cutoff based on multiple fits. The advantage is that it reduces the bias in the cutoff estimation. Usually, one fit per distribution for these endeavours is used. Instead, multiple fits weighted by the quality of the fit is a less biased form to obtain a cutoff.
The procedure is detailed next for a given distribution in a three-dimensional bin:

1. The distribution is fitted from the first to the last bin of P_T^2 with an exponential distribution (see Fig.3.22):

$$f(P_T^2) = a \cdot e^{-P_T^2/b} \tag{3.28}$$

Where a is a normalization parameter, and b is associated with the width of the distribution.

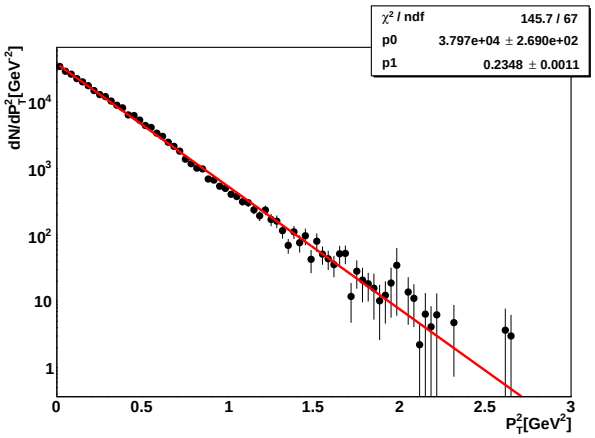

Figure 3.22: P_T^2 distribution for Fe target and within $1.3 < Q^2[GeV^2] < 1.8$, $2.2 < \nu[GeV] < 3.2$, $0.6 < z_h < 0.8$. The black line corresponds to the fit with the function described in equation (3.28).

2. The cutoff for that fit is determined as the P_T^2 value where the fit function is equal to 1.

3. Then we repeat (1) and (2) but with a change in the first step: the beginning of the fit is pushed to the next bin of P_T^2 (see Fig.3.23).

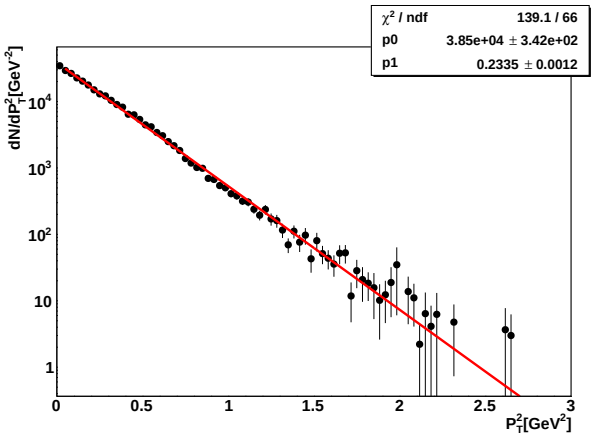

Figure 3.23: P_T^2 distribution for Fe target and within $1.3 < Q^2[GeV^2] < 1.8$, $2.2 < \nu[GeV] < 3.2$, $0.6 < z_h < 0.8$. The black line corresponds to the fit with the function described in equation (3.28).

To corroborate the exponential behavior of data we repeated this step 15 times. Two reasons are behind this decision:

- If this number was increased, to a certain extent, we observed no difference in the cutoff calculated (see next steps).
- If the fit starts near the end of the distribution the curve adjusts perfectly to the last points -scattered points-. Therefore, we obtain an overestimated cutoff where this overestimation is transferred to the final cutoff -the explanation of the final cutoff's estimation is in the following steps-.

After some repetitions, the fits look like Fig.3.24.

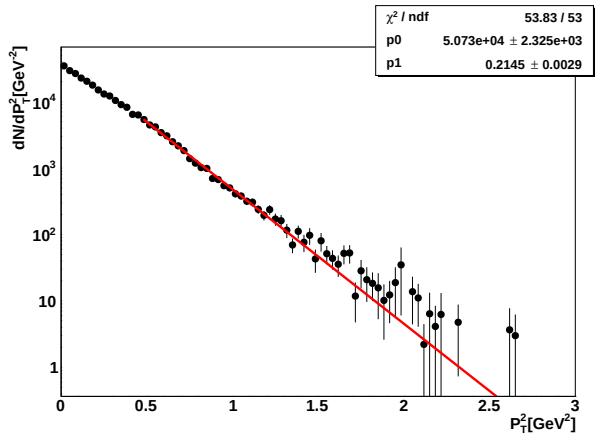

Figure 3.24: P_T^2 distribution for Fe target and within $1.3 < Q^2[GeV^2] < 1.8$, $2.2 < \nu[GeV] < 3.2$, $0.6 < z_h < 0.8$. The black line corresponds to the fit with the function described in equation (3.28).

4. After we applied the fits a weight was assigned to every cutoff value. That weight considered two attributes: χ^2_{ndf} and ndf. The functions that processed these attributes were:

   - $\chi^2_{ndf} \rightarrow$ a Gaussian distribution given by:

$$G(\chi^2_{ndf_i}) = \frac{e^{\frac{-(\chi^2_{ndf_i}-1)^2}{2\cdot 0.2}}}{\sqrt{2\pi}0.2} \tag{3.29}$$

   Therefore, fits that described well the data ($\chi^2_{ndf_i} \rightarrow 1$) were given a higher value of this function. The standard deviation value 0.2 is arbitrary but was selected in such manner that fits outside the $1 \pm 2\sigma$ range would practically have a null contribution to the final weight (see Fig.3.25).

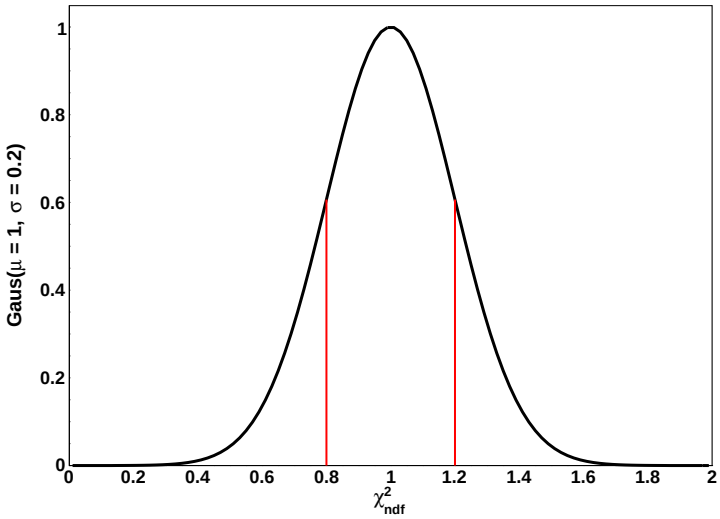

Figure 3.25: Red lines denote the $\pm\sigma$ values.

- $ndf \rightarrow$ a linear function where higher values of ndf give a higher value of the function:

$$L(ndf_i) = \frac{ndf_i}{ndf_{\text{total}}} = \frac{ndf_i}{\sum_j^N ndf_j} \tag{3.30}$$

  The inclusion of ndf as an attribute is to assign a slightly bigger weight to one of two fits whenever both of them would have an equal χ^2_{ndf}.

Both attributes had weights assigned: $(\alpha, \beta) = (0.95, 0.05)$. Then, the weight assigned to a cutoff value, obtained from a fit i, is defined as:

$$w_i = \frac{\alpha \cdot G(\chi^2_{ndf_i}) + \beta \cdot L(ndf_i)}{\alpha + \beta} \tag{3.31}$$

5. Finally, the cutoff reads:

$$P^2_{T_{\text{cutoff}}} = \frac{\sum_i^N w_i \cdot P^2_{T_{\text{cutoff}_i}}}{\sum_i^N w_i} \tag{3.32}$$

3.4.2 Interpolation Procedure

After the cutoff procedure took place, empty bins are replaced with interpolated values. Therefore, for these points, a value is calculated via linear interpolation between the two nearest non-zero bins:

$$P^2_{T_{\text{interpolated}}} = \frac{P^2_{T_{\text{prev}}} + P^2_{T_{\text{post}}}}{2} \tag{3.33}$$

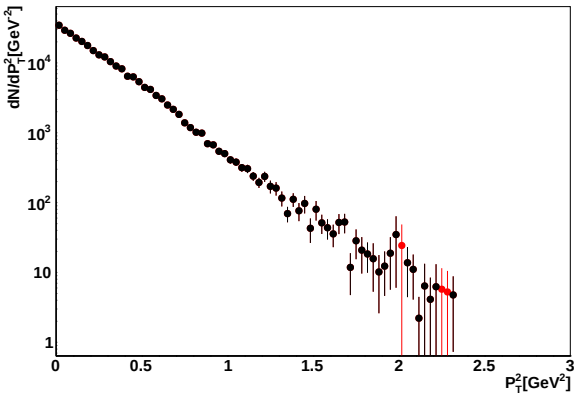

Figure 3.26: P_T^2 distribution for Fe target and within $1.3 < Q^2[GeV^2] < 1.8$, $2.2 < \nu[GeV] < 3.2$, $0.6 < z_h < 0.8$. The red points are the bins which were interpolated.

The errors of the interpolated point have no importance on the observable calculation since they are not considered in the calculation of averages [30]:

$$\langle x \rangle = \frac{\sum_i w_i \cdot x_{\text{center}_i}}{\sum_i w_i} \tag{3.34}$$

Where the index i runs through all bins of the histogram, w_i is the weight of the i^{th} bin, and x_{center_i} is the bin center of bin i.

Chapter 4

Systematic Uncertainties

The sources of systematic uncertainties are based loosely on those selected in the charged pion research [21].

To calculate the deviation percentage between nominal and variation values, we used:

$$\text{Dev.}\% = 100 \times \frac{X_{\text{nominal}} - X_{\text{variation}}}{X_{\text{variation}}} \tag{4.1}$$

The approach [21] to calculate the systematic error was based on the assumption that the nominal value is the center of a uniform distribution. The biggest deviation w.r.t. the nominal value Δ was considered the limit value of that distribution; thus, its length was 2Δ. We estimated the real value of the measurement to be within a 68% confidence interval in the uniform distribution. Thus, the systematic error is:

$$\text{Syst. Error} = \pm\Delta/\sqrt{3}. \tag{4.2}$$

It is worth mentioning that the studied observables have a numerical difference of one order of magnitude. Therefore, single-digit systematic errors in $\langle P_T^2 \rangle$ can be translated to double-digits systematic error in the Broadening.

4.1 Pion Identification

4.1.1 TOF Method

The method used to identify a pion depended on the candidate's momentum. The momentum value that discriminated between methodologies was $2.7[GeV]$. Therefore, two variations were applied to this limiting value: $2.5[GeV]$ and $2.9[GeV]$.

- In the case of $\langle P_T^2 \rangle$, the deviations from the nominal values are negligible until $z_h = 0.6$. At higher z_h values, it is observed that the $P < 2.5[GeV]$ variation has a positive deviation, and the $P < 2.9[GeV]$ variation has a negative deviation (see Figs. B.1,B.2,B.4,B.3)

  For the configurations of liquid target and solid targets, with and without x_f cut, the systematic errors oscillated within the $[0.86, 0.93]\%$ range and $[0.83, 0.97]\%$ range, respectively.

- The ΔP_T^2 deviations did not display behavior as clear as the previous observable. Nonetheless, on $z_h > 0.6$ could be observed the biggest deviations (see Figs.B.5,B.6).

  For all targets' configurations, with and without x_f cut, the systematic errors oscillated within the $[0.79, 4]\%$ range.

4.2 Vertex Selection

4.2.1 Vertex Cut

Two different vertex cuts were tested: one developed by Hayk Hakobyan (HH) [27], and the other developed by Raphael Dupré (RD) [26].

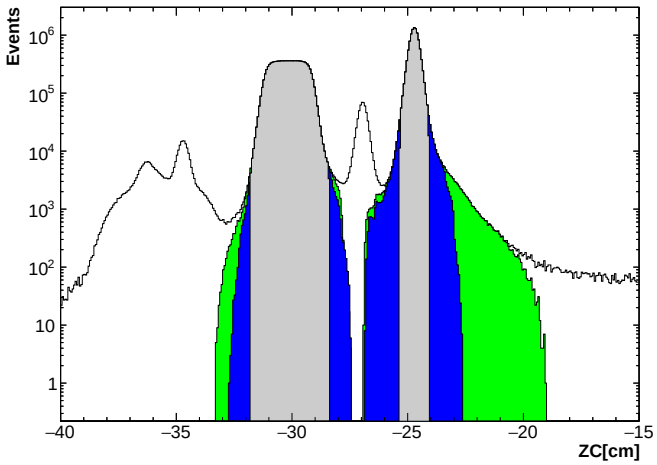

Figure 4.1: In gray the events selected by TM vertex cut. In green the events selected by HH vertex cut. In blue the events selected by RD vertex cut.

HH's vertex selection works with uncorrected coordinates; thus, it is sector-dependent, and its solid target vertex selection is target independent. The cuts are presented in Table 4.1.

Sector	$Z_{liquid_{min}}[cm]$	$Z_{liquid_{max}}[cm]$	$Z_{solid_{min}}[cm]$	$Z_{solid_{max}}[cm]$
0	-32.50	-28.00	-26.50	-20.00
1	-32.50	-27.50	-26.00	-20.00
2	-32.00	-27.75	-25.65	-20.00
3	-32.00	-27.75	-25.85	-20.00
4	-32.50	-28.35	-26.65	-20.00
5	-32.50	-28.75	-27.15	-20.00

Table 4.1: HH longitudinal coordinate Z cut per Sector.

RD's vertex selection procedure is sector-dependent and target-dependent. It uses a shift in the Z coordinate to correct the offset of the beam (see Table 4.2).

Sector	Shift$[cm]$
0	$+0.1$
1	-0.4
2	-0.6
3	-0.1
4	$+0.4$
5	$+0.6$

Table 4.2: RDs Z coordinate shift.

The shifts were determined through a fit to the solid target position in all sectors of CLAS. The cuts are presented in Table 4.3.

Target	$Z_{liquid_{min}}[cm]$	$Z_{liquid_{max}}[cm]$	$Z_{solid_{min}}[cm]$	$Z_{solid_{max}}[cm]$
D-C setup	-32.1	-28.1	-26.2	-23.2
D-Fe setup	-32.2	-28.2	-26.4	-23.4
D-Pb setup	-32.1	-28.1	-26.2	-23.2

Table 4.3: RD longitudinal coordinate Z cut.

- In the case of $\langle P_T^2 \rangle$, the deviations from the nominal value are negligible in the liquid targets results. However, the solid targets' deviations were non-negligible in the last bin (see Figs.B.7,B.8,B.9,B.10).

  With and without x_f cut, the liquid configurations' systematic errors were of the 10^{-2} order. The solid targets' deviations oscillated within the $[0.1, 0.4]\%$ range.

- The ΔP_T^2 deviations do not have a clear pattern, and the x_f cut results seems to have been have bigger deviations at low z_h in comparison to the results without the x_f cut (see Figs.B.11,B.12). In general, the biggest deviations gives systematic errors around 1% and 2%.

4.2.2 $|\Delta Z|$ Variation

In this systematic uncertainty we tested two variations: $|\Delta Z| < 3.5[cm]$ and $|\Delta Z| < 2.5[cm]$.

- The deviations of $\langle P_T^2 \rangle$ are uniform through z_h. Also, no significant difference was observed between the results with and without x_f cut (see Figs. B.13,B.14,B.15,B.16). For the different configurations of targets, the systematic errors fluctuated between $[0.3 - 0.7]\%$.

- The ΔP_t^2 variations vaguely resembled the behavior of the previous variations (see Figs.B.17,B.18). For the different configurations of targets, the values of the systematic errors ranged from 0.1% to 4%.

4.3 Acceptance

4.3.1 Minimum N_{accept} Value

The nominal cut applied to the acceptance factors was $N_{\text{accept}} > 1$. Therefore, we tested two variations: $N_{\text{accept}} > 0$ and $N_{\text{accept}} > 2$.

- In the case of $\langle P_T^2 \rangle$, the liquid targets' deviations are uniform through z_h; however, the solid targets' deviations, from $z_h > 0.5$, presented a separation between both variations (see Figs.B.19,B.20,B.21,B.22). Between the results with x_f cut and the results without x_f cut, there was not a noticeable difference. The systematic errors associated with the liquid targets' deviations and the solid targets' deviations can go up to 0.17% and 0.56%, respectively.

- The ΔP_T^2 deviations presented a similar behavior to the previous observables' deviations(see Figs.B.23,B.24). In most cases, the values of the systematic errors can go up to 4%. Nonetheless, the behavior depended on the target and if the x_f cut was applied or not.

4.3.2 Minimum Acceptance Value

An explicit cut on the acceptance factor was not applied; therefore, we tested two variations: Acc > 0.005 and Acc > 0.01.

- In the case of $\langle P_T^2 \rangle$, the deviations are all negatives (see Figs.B.25,B.26,B.27,B.28). The systematic errors can go up to 0.9% in the liquid targets case and up to 1.2% in the solid targets case.

- The behavior of the previous deviations is inherited by those of ΔP_T^2. In the x_f cut case, the low z_h region acquires more deviations in comparison with its no x_f cut pair (see Figs.B.29,B.30). Then, the systematic errors varied between 0.2% and 3.5% when the x_f cut was not applied. When this cut was applied the systematic errors varied between 0.6% and 3.5%.

4.3.3 Different P_T^2 Binning

The nominal number of bins chose for P_T^2 was 90. Then, we tested the following two variations: 70 and 110 bins in P_T^2.

- In the case of $\langle P_T^2 \rangle$, it was noticed that the deviations were mostly uniform through z_h except when $z_h < 0.2$ along with $x_f > 0$ (see Figs.B.31,B.32,B.33,B.34). The systematic errors for liquid targets could go up to 0.25% and for solid targets could go up to 0.48%. In the case of $x_f > 0$ results we obtained similar results except at $z_h < 0.2$ where the systematic errors for the liquid targets could go up to 2% and for the solid targets could go up to 2.45%.

- In the case of ΔP_T^2 (see Figs.B.35,B.36) the systematic errors varied between 0.22% and 3.8%. This depended on the target and the if the x_f cut was applied.

4.3.4 Closure Test (CT)

The CT is a procedure that evaluates the acceptance correction algorithm's quality and it was performed via the next steps:

1. Simulations were divided into:

   - Reconstructed Events: one half was considered pseudo-data and the other half was used to calculate acceptance factors.
   - Thrown Events: one half was considered the true data (Thrown') and the other half was used to calculate acceptance factors.

2. With the acceptance factors calculated from the previous step -Acc'- we applied them to the pseudo-data.

$$\text{Corr.Pseudo-data} = \frac{\text{Pseudo-data}}{\text{Acc'}} \tag{4.3}$$

3. The following ratio was evaluated:

$$w = \frac{\text{Corr.Pseudo-data}}{\text{Thrown'}} \tag{4.4}$$

Thus if:

$$\frac{\text{Corr.Pseudo-data}}{\text{Thrown'}} \sim 1 \tag{4.5}$$

Then, we can say the CT *closes*, and the correction algorithm is *healthy*. However, if that is not the case then we might be under/over correcting data. To compensate this, a scale factor can be applied to the nominal acceptance factor Acc. Thus, the compensated acceptance factor Acc_{corr} reads:

$$\text{Acc}_{corr} = w * \text{Acc} \tag{4.6}$$

Then, the corrected data in the analysis is:

$$\text{Corr.Data} = \frac{\text{Data}}{\text{Acc}_{corr}} \tag{4.7}$$

The w factors are calculated in a five-dimensional phase space. Ideally, the same binning as the nominal acceptance factors should be used, though it is not mandatory. In our case, the nominal P_T^2 binning was too thin to observe any noticeable trend in the w factors . Therefore, these were calculated with less P_T^2 bins, namely 70 and 50 bins were used.

To assign a w factor, a revision was done in all the bins of the nominal P_T^2 distribution:

1. Get the center value of the P_T^2 bin.
2. Search in the w distribution the bin in which the value of step (1) fits.
3. The bin found in step 2 will be assigned to the nominal P_T^2 bin being analyzed.

- In the case of $\langle P_T^2 \rangle$, with and without x_f cut, the impact of the Scale Factors was visible in medium to high z_h(see Figs.B.37,B.38,B.39,B.40). The systematic error values could go up to 0.8% in the case of the liquid targets and could go up to 1.3% in the case of solid targets. These numbers were independent of the x_f cut.

- The ΔP_T^2 deviations, without x_f cut, inherited the behavior from the previous observables. The biggest deviations are located at medium to high z_h (see Fig.B.41). When we analyzed the deviations of the results without x_f cut, was observed that in $z_h < 0.3$ there were big deviations. This can be explained looking at the $\langle P_T^2 \rangle$ deviations with x_f cut, where the solid results are enhanced (negative deviation) and the liquid results are suppressed (positive deviation). This provoked the enhancement in the broadening's deviations that resulted in a large negative deviation (see Fig.B.42). The systematic errors could go

up to 4.5% when the x_f was not applied. Also, the systematic errors could go up to 20% when the x_f was applied. Nevertheless, the general value of the systematic error ranges from 7% to 8%.

4.4 Background Subtraction

The background subtraction consisted of two procedures: the P_T^2 cutoff calculation and the interpolation of missing bins. Therefore, we tested two variations: no background subtraction on data and only P_T^2 cutoff on data.

- In the case of $\langle P_T^2 \rangle$, the deviations for both liquid targets and solid targets are uniform through z_h, except in the last bin of z_h where solid targets' deviations are bigger w.r.t. the deviations in $z_h < 0.8$ (see Figs.B.43,B.44,B.45,B.46).The systematic errors associated to liquid targets reached up to 0.23% and to solid targets reached up to 0.64%. This was independent of the x_f cut application.

- The ΔP_T^2 has a similar deviation pattern to the previous observable (see Fig.B.47,B.48). The systematic errors reaches up to 2.8% at high z_h. This was dependent on the target, but independent of the x_f cut application.

4.5 Radiative Corrections

The radiative corrections were included in two different forms. *Not treated* refers to radiative corrections that were applied without any type of interpolation; therefore, any bin where the RC factor would be evaluated as one. *Treated* refers to RC factors that could not be calculated and they where replaced by an interpolation between all non-zero neighbouring factors. The factors that weren't calculated are located in the high P_T^2 region.

- In the case of $\langle P_T^2 \rangle$, the deviations followed a similar pattern between them where high z_h deviations are the biggest and the rest are small. The x_f cut accentuated the deviations at low and medium z_h. Also, it was noticed that the biggest deviations happened in the solid targets (see Figs.B.49,B.50,B.51,B.52). The deviations' values are well bounded in the 1% region, except for the last bin of z_h where in the liquid targets results it could go up to 3% and in the solid targets results it could go up to 7%.

- The broadening deviations inherited the same behavior from the previous observables and also enhances them (see Figs.B.53,B.54). In $z_h < 0.6$ the deviations are relatively small and contained within the statistical fluctuations. At $z_h > 0.6$ deviations can reach up to 23%.

4.6 Summary

To have a detailed outlook of the systematic errors an interval description was used instead of a single number characterization. The intervals are determined by:

$$[Min(Syst.Err(z_h)), Max(Syst.Err(z_h))] \tag{4.8}$$

We used the codes that plotted the deviations to obtain the intervals that are presented next. Finally, the total systematic errors intervals were calculated directly from the codes that plotted the final results with these errors included. The total systematic error reads:

$$\sigma^2_{syst}(z_h) = \sum_i^N \sigma^2_i(z_h) \tag{4.9}$$

Where N is the number of systematic uncertainties sources and the index i runs through all the systematic uncertainties sources.

Source	$\langle P_T^2 \rangle_{DC}$	$\langle P_T^2 \rangle_{DFe}$	$\langle P_T^2 \rangle_{DPb}$
TOF	$< 0.33\%$	$< 0.93\%$	$< 0.86\%$
VC	$< 0.02\%$	$< 0.02\%$	$< 0.02\%$
$\lvert\Delta Z\rvert$	$[0.37, 1.20]\%$	$[0.34, 1.02]\%$	$[0.38, 1.13]\%$
N_{accept}	$< 0.17\%$	$< 0.09\%$	$< 0.12\%$
Acc_{min}	$< 0.86\%$	$< 0.70\%$	$< 0.76\%$
P_T^2 bins	$[0.05, 0.28]\%$	$[0.06, 0.20]\%$	$[0.08, 0.25]\%$
CT	$[0.12, 1.15]\%$	$[0.15, 1.11]\%$	$[0.15, 1.11]\%$
Tail	$< 0.29\%$	$< 0.11\%$	$< 0.12\%$
Rad	$[0.05, 1.77]\%$	$[0.04, 1.57]\%$	$[0.02, 1.43]\%$
Total	$[0.61, 2.5]\%$	$[0.59, 2.22]\%$	$[0.61, 2.16]\%$

Table 4.4: Systematic errors for $\langle P_T^2 \rangle$ liquid targets results without x_f cut.

Source	$\langle P_T^2 \rangle_C$	$\langle P_T^2 \rangle_{Fe}$	$\langle P_T^2 \rangle_{Pb}$
TOF	$< 0.88\%$	$< 0.9\%$	$< 0.97\%$
VC	$[0.03, 0.1]\%$	$[0.03, 0.19]\%$	$< 0.4\%$
$\lvert\Delta Z\rvert$	$[0.36, 1.43]\%$	$[0.32, 1.21]\%$	$[0.35, 1.54]\%$
N_{accept}	$< 0.54\%$	$< 0.56\%$	$< 0.59\%$
Acc_{min}	$< 1.18\%$	$< 0.85\%$	$< 1.24\%$
P_T^2 bins	$[0.14, 0.48]\%$	$[0.09, 0.25]\%$	$[0.16, 0.37]\%$
CT	$[0.15, 1.13]\%$	$[0.03, 1.29]\%$	$[0.04, 1.25]\%$
Tail	$< 0.39\%$	$< 0.25\%$	$< 0.64\%$
Rad	$[0.07, 2.88]\%$	$[0.02, 3.64]\%$	$[0.11, 3.67]\%$
Total	$[0.64, 3.63]\%$	$[0.53, 4.11]\%$	$[0.57, 4.37]\%$

Table 4.5: Systematic errors for $\langle P_T^2 \rangle$ solid targets results without x_f cut.

Source	$\langle P_T^2 \rangle_{DC}$	$\langle P_T^2 \rangle_{DFe}$	$\langle P_T^2 \rangle_{DPb}$
TOF	$< 0.89\%$	$< 0.93\%$	0.85%
VC	$< 0.02\%$	$< 0.02\%$	$< 0.02\%$
$\lvert\Delta Z\rvert$	$[0.34, 1.20]\%$	$[0.31, 1.02]\%$	$[0.35, 1.12]\%$
N_{accept}	$< 0.15\%$	$< 0.09\%$	$< 0.12\%$
Acc_{min}	$< 0.86\%$	$< 0.70\%$	$< 0.76\%$
P_T^2 bins	$[0.04, 1.85]\%$	$[0.06, 2.05]\%$	$[0.03, 1.9]\%$
CT	$[0.28, 0.82]\%$	$[0.28, 0.80]\%$	$[0.23, 0.8]\%$
Tail	$< 0.29\%$	$< 0.08\%$	$< 0.13\%$
Rad	$[0.05, 1.77]\%$	$[0.07, 1.57]\%$	$[0.06, 1.43]\%$
Total	$[1, 2.53]\%$	$[0.95, 2.26]\%$	$[1.02, 2.17]\%$

Table 4.6: Systematic errors for $\langle P_T^2 \rangle$ liquid targets results with x_f cut.

Source	$\langle P_T^2 \rangle_C$	$\langle P_T^2 \rangle_{Fe}$	$\langle P_T^2 \rangle_{Pb}$
TOF	$< 0.83\%$	0.89%	0.97%
VC	$[0.01, 0.15]\%$	$< 0.2\%$	$< 0.4\%$
$\lvert\Delta Z\rvert$	$[0.33, 1.43]\%$	$[0.35, 1.54]\%$	$[0.35, 1.54]\%$
N_{accept}	$< 0.52\%$	$< 0.52\%$	$< 0.31\%$
Acc_{min}	$< 1.13\%$	$< 0.83\%$	$< 1.24\%$
P_T^2 bins	$[0.12, 2.11]\%$	$[0.05, 2.45]\%$	$[0.13, 2.36]\%$
CT	$[0.38, 1.28]\%$	$[0.01, 1.00]\%$	$[0.05, 1.26]\%$
Tail	$< 0.39\%$	$< 0.26\%$	$< 0.64\%$
Rad	$[0.33, 2.92]\%$	$[0.175, 3.64]\%$	$[0.22, 3.67]\%$
Total	$[0.96, 3.66]\%$	$[0.9, 4.12]\%$	$[0.91, 4.45]\%$

Table 4.7: Systematic errors for $\langle P_T^2 \rangle$ solid targets results with x_f cut.

Source	$(\Delta P_T^2)_C$	$(\Delta P_T^2)_{Fe}$	$(\Delta P_T^2)_{Pb}$
TOF	$< 2.7\%$	$< 0.79\%$	$< 4\%$
VC	$[0.35, 0.77]\%$	$[0.18, 1]\%$	$< 2.1\%$
$\lvert\Delta Z\rvert$	$[0.15, 3.07]\%$	$[0.17, 2.18]\%$	$[0.19, 3.26]\%$
N_{accept}	$< 3.98\%$	$[0.03, 2.73]\%$	$< 3.58\%$
Acc_{min}	$[0.17, 3.43]\%$	$[0.20, 1.54]\%$	$[0.27, 3.30]\%$
P_T^2 bins	$[0.82, 3.78]\%$	$[0.24, 0.82]\%$	$[0.22, 1.66]\%$
CT	$[1.36, 4.56]\%$	$[0.34, 3.55]\%$	$[0.05, 3.40]\%$
Tail	$[0.19, 1.15]\%$	$[0.04, 1.12]\%$	$< 2.85\%$
Rad	$[0.07, 10.8]\%$	$[0.01, 13.3]\%$	$[0.15, 13.1]\%$
Total	$[1.97, 13.51]\%$	$[0.95, 14.09]\%$	$[0.95, 15.05]\%$

Table 4.8: Systematic errors for ΔP_T^2 without x_f cut.

Source	$(\Delta P_T^2)_C$	$(\Delta P_T^2)_{Fe}$	$(\Delta P_T^2)_{Pb}$
TOF	$< 2.7\%$	$< 0.9\%$	$< 4\%$
VC	$[0.36, 1.6]\%$	$[0.09, 0.94]\%$	$< 2.1\%$
$\lvert\Delta Z\rvert$	$[0.15, 3.90]\%$	$[0.05, 2.37]\%$	$[0.19, 3.30]\%$
N_{accept}	$[0.06, 3.82]\%$	$[0.33, 2.51]\%$	$[0.05, 1.97]\%$
Acc_{min}	$[0.59, 3.49]\%$	$[1.14, 2.26]\%$	$[0.62, 3.30]\%$
P_T^2 bins	$[0.08, 3.72]\%$	$[0.18, 2.83]\%$	$[0.69, 2.14]\%$
CT	$[11, 20.8]\%$	$[4.92, 8.19]\%$	$[4.94, 6.88]\%$
Tail	$[0.24, 1.14]\%$	$[0.03, 1.19]\%$	$< 2.83\%$
Rad	$[0.8, 11.7]\%$	$[2.18, 13.3]\%$	$[2.71, 13.1]\%$
Total	$[5.52, 21]\%$	$[5.12, 14.72]\%$	$[2.61, 16.05]\%$

Table 4.9: Systematic errors for ΔP_T^2 with x_f cut.

Chapter 5

Results

5.1 Experimental Measurements

The results are shown in a common format where:

- Statistical errors were represented by vertical bars.
- Total errors ($\sqrt{\sigma^2_{syst} + \sigma^2_{stat}}$) were represented by an horizontal line at the end of every point.
- All the plots, except the differential ΔP_T^2 vs z_h, followed the color convention: red (C), blue (Fe) and black (Pb).
- In the $\langle P_T^2 \rangle$ plots, the colored hollow points represented the deuterium data associated with the solid target data given by the color.
- All the plots, except the integrated ΔP_T^2 vs $A^{1/3}$, had points with small shifts to improve readability.

5.1.1 Average Transverse Momentum

In the integrated results we observed:

1. The liquid targets results had small variations between them. Nonetheless, the fluctuations compensated these variations.

2. The solid targets results were bigger than the liquid targets' and there was a correlation between the mass of the solid targets and their P_T^2 values.

3. The x_f cut removed a non-negligible portion of the P_T^2 tail at $z_h < 0.6$ - specially in the solid targets results- since the values of $\langle P_T^2 \rangle$ decrease in that region (see Figs.B.55,B.56). This decrease is estimated to be between 10% to 20%.

In the differential results we observed:

1. All the observations stated for the integrated results.

2. An increase in the $\langle P_T^2 \rangle$ values with ν (see Figs.B.57,B.56).

5.1.2 Transverse Momentum Broadening

In the transverse momentum broadening w.r.t. $A^{1/3}$ results we observed:

1. Integrated results

   - A positive non-linear correlation between the transverse momentum broadening and the mass of the target (see Figs.B.59,B.60).
   - The x_f cut application roughly reduced the magnitude of the transverse momentum broadening in 30% (see Fig.B.60).

2. Differential results

   - The results without the x_f cut presented a correlation between the transverse momentum broadening and the mass of the target. However, there was not a clear correlation between the former and the z_h interval (see Fig.B.61).
   - The results with the x_f cut presented a correlation between the transverse momentum broadening and the mass of the target. In this case, there was a clearer correlation between the former and the z_h interval (see Fig.B.62) where the magnitude of the transverse momentum broadening increased w.r.t. z_h.

In the transverse momentum broadening w.r.t. z_h results we observed:

1. Integrated results

   - The transverse momentum broadening was not zero at $z_h \to 1$. This could imply a contribution of the intrinsic parton momentum to the broadening since the hadronization-related contribution would be zero, due to energy conservation; or a contribution from hadronic elastic scattering with the nuclear medium.
   - The results with the x_f cut applied presented a positive correlation between the broadening and the value of z_h. The C-related broadening

presented a linear behavior; meanwhile, the other targets presented a non-linear behavior.

Also, these results show that the x_f cut has an effect in every bin except the last one.

2. Differential results

   - Again, the results presented non-zero values at $z_h \to 1$.
   - The application of the x_f cut delivered the same outcome as in the integrated results. Nonetheless, the bins where $3.7 < \nu[GeV] < 4.3$ show some deviation, from a monotonic increase, in the C-related results and the Pb-related results.

For the other variables:

- A weak dependence on ν is observed. This is clearer in the results where the x_f cut was applied.
- No visible Q^2 dependence was observed

5.2 Intrinsic Parton Momentum

The previous broadening results have an interesting behavior at $z_h \to 1$ and is its non-zero value. This, is something not observed in HERMES' results (see Fig.5.1).

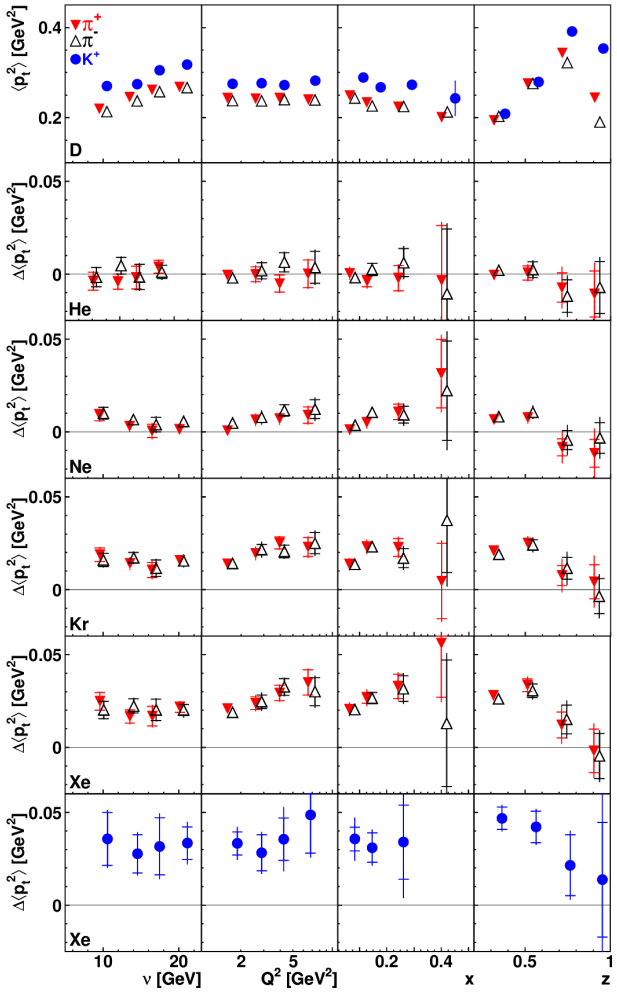

Figure 5.1: HERMES transverse momentum broadening measurements in function of different kinematical variables. Notice that for the z_h dependence the broadening vanishes at $z_h \to 1$.

Due to energy conservation the broadening should be zero in that kinematical region, since:

$$\Delta P_T^2 = (\text{Quark Broadening}) \propto l_p, \tag{5.1}$$

where the production length is directly related to the energy loss of the traversing quark; hence, if $l_p \to 0$ then the quark does not lose energy because it transforms directly into a pre-hadron.

Eq. (5.1) works under the assumption that the $\langle k_\perp^2 \rangle$ is the same in every target,

given that a more general expression yields

$$\Delta P_T^2 = (\text{Quark Broadening}) + z_h^2(\langle k_\perp^2\rangle_A - \langle k_\perp^2\rangle_D). \tag{5.2}$$

Therefore, a possible explanation of CLAS broadening's behavior at $z_h \to 1$ is $\langle k_\perp^2\rangle$'s variation between the different targets. A recent research conducted by Brooks and Lopez [31] concluded that for HERMES' measurements the contribution of the intrinsic parton momentum to the broadening was:

$$z_h^2(\langle k_\perp^2\rangle_A - \langle k_\perp^2\rangle_D) \approx -0.002 \pm 0.001[GeV^2], \tag{5.3}$$

in all the considered bins of z_h. In CLAS case we propose that this contribution is positive.

In this section, we extract the values of $\langle k_\perp^2\rangle$ via fitting of $\langle P_T^2\rangle(Q^2, \nu, z_h)$ and analyze if $\langle k_\perp^2\rangle$ is dependent of the nuclear environment. The fitting function depends on:

- $\langle k_\perp^2\rangle$ as a free parameter.

- $\langle p_\perp^2\rangle(z_h)$ which is described by a beta distribution and a normalization constant.

  $$\langle p_\perp^2\rangle(z_h) = (\text{Norm.}) \times Beta(z_h; \alpha, \beta) \tag{5.4}$$

  The beta distribution was chose because:

  - Under certain parameters (α,β) values, it vanishes at $z_h = 1$.

  - Given that $\langle P_T^2\rangle \geq \langle p_\perp^2\rangle$ we expect a similar asymmetric behavior between both variables. The beta distribution has a convenient asymmetric shape (see Fig.5.2).

  Then, to a good approximation, it describes the behavior of $\langle p_\perp^2\rangle(z_h)$.

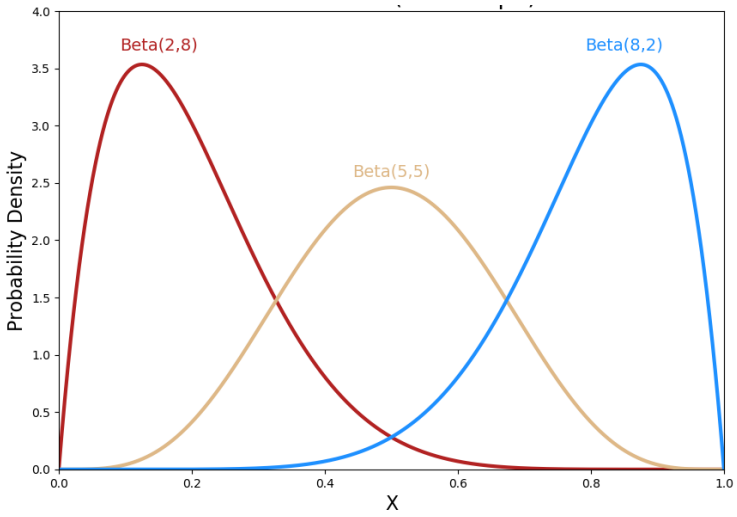

Figure 5.2: Beta distributions with different parameter configurations. Notice that the blue plot has the behavior that is expected from $\langle p_\perp^2 \rangle$.

In consequence, the hadronization-related term is described by three free parameters.

We tested two fitting functions:

1. The expression of the averaged squared transverse momentum given by eq.(1.45).

2. The eq.(1.45), but without the integration to infinity (see following section for more detail).

Additionally, we tried different global fits based on the following hypotheses:

1. $\langle p_\perp^2 \rangle$ is independent of Q^2 and ν; and dependent of z_h. $\langle k_\perp^2 \rangle$ depends on Q^2 and ν.

2. $\langle p_\perp^2 \rangle$ is independent of Q^2 and ν; and dependent of z_h. $\langle k_\perp^2 \rangle$ depends on ν.

5.2.1 Fit With Analytic Function

The function to fit the averaged squared transverse momentum is given by;

$$\langle P_T^2 \rangle = \langle p_\perp^2 \rangle + z_h^2 \langle k_\perp^2 \rangle \tag{5.5}$$

This, is the same equation called $\langle P_t^2 \rangle_G$ in chapter (1). Thus, we assumed that:

$$\langle P_T^2 \rangle = \langle P_T^2 \rangle_G \tag{5.6}$$

The results of the intrinsic parton momentum extraction are in chap. (C.3), and the plots of the global fits are in chap.(B.4).

In table (5.1) can be found the quality of the fits.

x_f	Target	χ^2_{ndf}	Target	χ^2_{ndf}	Hypothesis
$[0,1]$	DC	12.9	C	12.6	1
$[0,1]$	DFe	11.2	Fe	15.2	1
$[0,1]$	DPb	14.9	Pb	9.93	1
$[-1,1]$	DC	7.6	C	3.53	1
$[-1,1]$	DFe	6.17	Fe	3.71	1
$[-1,1]$	DPb	7.55	Pb	2.54	1
$[0,1]$	DC	18	C	18.5	2
$[0,1]$	DFe	17.7	Fe	22.9	2
$[0,1]$	DPb	20.9	Pb	13.5	2
$[-1,1]$	DC	12.7	C	8.05	2
$[-1,1]$	DFe	12.4	Fe	8.05	2
$[-1,1]$	DPb	13.8	Pb	3.77	2

Table 5.1: Table that contains the quality of the global fits with the analytical fit function.

The results in the tables of chapter (C.3) lead to the following observations:

- Hypothesis 1 described the data better than hypothesis 2. Hence, $\langle k_\perp^2 \rangle$ does depend on both Q^2 and ν.
- When the x_f cut was not applied we obtained a better description of data. This happened with both hypothesis.
- Hypothesis 1, with no x_f cut, showed that $\langle k_\perp^2 \rangle$ increases with ν and with Q^2. Nonetheless, the dependence is stronger for ν. This makes sense since the experimental results show that $\langle P_T^2 \rangle (z_h \to 1)$ values increases with ν.

In summary, the analytic function describes the results optimally when the results do not have the x_f cut applied and when the fits consider the intrinsic parton mo-

mentum dependent on Q^2 and ν.

5.2.2 Fit With Integral

The fit function used for $\langle P_T^2 \rangle$ is a modified version of the integral presented in eq.(1.45). The experimental extension of the P_T^2 distributions were taken into account to fix an upper limit ($P_{T_{MAX}}^2$) in the previously mentioned integral. To determine this, we selected the maximum value of the P_T^2 distribution with the longest tail which is usually located in $0.4 < z_h < 0.5$. This is done for every target and every (Q^2,ν) bin. It is worth mentioning that $P_{T_{MAX}}^2$ depends continuously on z_h, but we will study that dependence in future works.

The fit function used normalized TMDs and the mathematical definition of $\langle P_T^2 \rangle$. Then:

$$\langle P_T^2 \rangle = \int_0^{P_{T_{MAX}}^2} dP_T^2 \int_0^{k_{\perp_{MAX}}^2} dk_\perp^2 \int_0^{2\pi} d\theta \frac{e^{k_\perp^2/\langle k_\perp^2 \rangle}}{\pi \langle k_\perp^2 \rangle (1 - e^{-k_{\perp_{MAX}}^2/\langle k_\perp^2 \rangle})} \times \frac{e^{p_\perp^2/\langle p_\perp^2 \rangle}}{\pi \langle p_\perp^2 \rangle} \times P_T^2 \tag{5.7}$$

Regarding the previous equation there are various points to address:

- That maximum value of $k_{\perp_{MAX}}^2$ is given by [11]:

$$\begin{aligned} k_{\perp_{MAX}}^2 &= \frac{x_b(1-x_b)}{(1-2x_b)^2} Q^2; \quad x_b < 0.5 \\ k_{\perp_{MAX}}^2 &= (2-x_b)(1-x_b) Q^2; \quad x_b > 0.5 \end{aligned} \tag{5.8}$$

  This choice has a direct influence in the representation of the transverse momentum dependent parton distribution.

- Flavour-independent Gaussian widths were used in the transverse momentum dependencies.

The transverse momentum related to the hadronization $p_\perp$ is associated with the intrinsic momentum and the hadronic transverse momentum by the following rela-

tionship[11]:

$$\mathbf{p}_\perp \approx \mathbf{P}_T - z_h \mathbf{k}_\perp \tag{5.9}$$

Thus:

$$p_\perp^2 = P_T^2 + z_h^2 k_\perp^2 - 2 z_h P_T k_\perp cos(\theta) \tag{5.10}$$

Notice that the angle θ also appears in eq. (5.7) as the polar angle of $k_\perp$. In the integration, this angles can be easily associated through a rotation due to them being in the same plane, approximately.

In table (5.2) can be found the quality of the global fits.

x_f	Target	χ^2_{ndf}	Target	χ^2_{ndf}	Hypothesis
$[0,1]$	DC	14.3	C	10.2	1
$[0,1]$	DFe	19.2	Fe	13.9	1
$[0,1]$	DPb	18	Pb	11.8	1
$[-1,1]$	DC	9.63	C	5.67	1
$[-1,1]$	DFe	7.96	Fe	6.33	1
$[-1,1]$	DPb	9.58	Pb	3.57	1
$[0,1]$	DC	17.1	C	13.9	2
$[0,1]$	DFe	24	Fe	21	2
$[0,1]$	DPb	22.6	Pb	15	2
$[-1,1]$	DC	14.8	C	10.1	2
$[-1,1]$	DFe	14.6	Fe	10.6	2
$[-1,1]$	DPb	16.3	Pb	4.93	2

Table 5.2: Table that contains the quality of the global fits with the numerical fit function.

The results in the tables of chapter (C.3) lead to the same observations as in the case where we tested the analytic function in the fit.

5.2.3 Observations

Given the previous results we made the following observations:

- From the two hypotheses, the first described the data better.
- The fit functions described better the results when these were without the x_f cut applied.

- The data was described better by the analytic fit function.
- The fits to Fe-related results yields unexpected low results. Nonetheless, the $\langle k_{\perp}^2 \rangle_{Fe} - \langle k_{\perp}^2 \rangle_{DFe}$ is positive.
- The global fits quality is still far from what is considered a good fit. However, the results of the best fits (analytic function, hypothesis 1) give $(\langle k_{\perp}^2 \rangle_A - \langle k_{\perp}^2 \rangle_D) \geq 0$.

Chapter 6

Conclusion

In this thesis we presented the experimental measurements of the averaged squared transverse momentum and the transverse momentum broadening; and a phenomenological analysis of the intrinsic parton momentum.

Both experimental observables presented a dependence on the x_f cut. This is more noticeable in the transverse momentum broadening, where its shape changes drastically if we are observing it w.r.t. z_h.

A strong dependence on z_h and to A is also observed on both observables. The dependence on z_h bears a behavior unseen in other transverse momentum broadening measures, that being its non-zero values at $z_h \to 1$. The dependence on ν is rather weak and to Q^2 is weaker. However, the ν dependence is more noticeable in the averaged transverse momentum measurements than in the transverse momentum broadening.

The phenomenological analysis was done via global fits. These showed that there might be a contribution of the intrinsic parton momentum on the previously mentioned behavior of the broadening. However, the global fits need to be improved in order to be considered a valid representation of the data since the average value of χ^2_{ndf} for deuterium target results is seven, and for solid target results is three. This is far from unity, which is the value used as standard to consider the quality of a fit as good. Lastly, the Fe-related results presented low values w.r.t. C-related results.

This is something to investigate in the future.

To conclude this section we would like to mention that the works presented in this document will be portrayed in two different scientific articles, that will be connected by the concepts they touch.

Appendix A

Additional Discussions

A.1 Heuristic Approach to Structure Functions

To understand the meaning of these functions it is useful to take some steps back in the theory. Quantum Field Theory (QFT) allow us to calculate probability amplitudes of elementary processes with the Feynman rules of the theory that describes the aforementioned process, but also this probability amplitudes can be calculated with old fashioned perturbation theory. Then, we can write:

$$\sigma \propto |M_{fi}|^2 \propto |\langle \text{final}| H_I |\text{initial}\rangle|^2 \tag{A.1}$$

Where σ is the cross section, $|M_{fi}|^2$ the probability amplitude of the process, and H_I is the interaction term in the Hamiltonian which described the process.
Now the question is: ¿What has to do the previous with the Structure Functions?. There is a well known case that helps to connect the dots: the *Rosenbluth formula*. It is used to describe the differential cross section of the elastic scattering of a charged lepton with a proton, but in the case that the proton is considered to have a certain spatial distribution, i.e., proton is no longer considered a point-like particle. The equation reads as:

$$\frac{\mathrm{d}\sigma}{\mathrm{d}\Omega} = \frac{\alpha^2}{4E_1^2 \sin^4(\theta/2)} \frac{E_3}{E_1} \left(\frac{G_E^2 + \tau G_M^2}{(1+\tau)} \cos^2 \frac{\theta}{2} + 2\tau G_M^2 \sin^2 \frac{\theta}{2} \right) \tag{A.2}$$

The objects of interest in this equation are G_E and G_M, these are known as *Form Factors* and their origin is encoded in (A.1). Say that an electron is the lepton that scatters off the proton, the charged nature of the particles will result in an electromagnetic interaction, thus:

$$\begin{aligned} H_I &\propto H_{electric} + H_{magnetic} \\ H_{electric} &\propto \rho(r) \\ H_{magnetic} &\propto \mu(r) \end{aligned} \tag{A.3}$$

Where $\rho(r)$ and $\mu(r)$ are densities respectively associated with the electric and magnetic properties of the proton. In few words, the elastic Form Factors contain the information about the electric and magnetic distributions of the proton.

Then the Structure Functions can be related to the Form Factors as being more general and complex objects, but in their meaning they are similar: they contain information about the target.

Appendix B

Plots

B.1 Systematic Errors

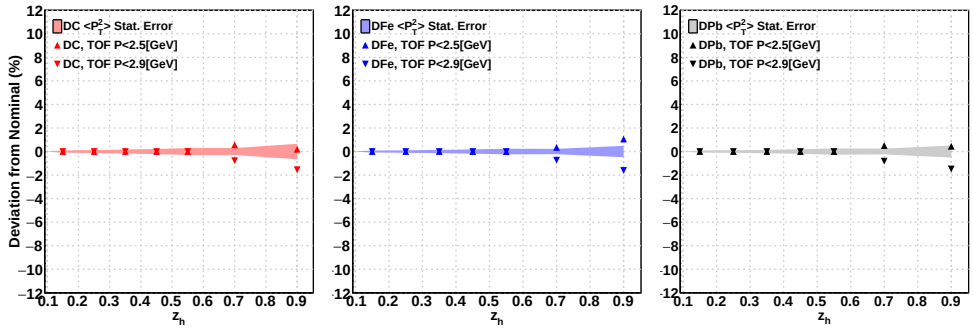

Figure B.1: TOF systematic uncertainty's $\langle P_T^2 \rangle$ deviations from the nominal values for liquid targets

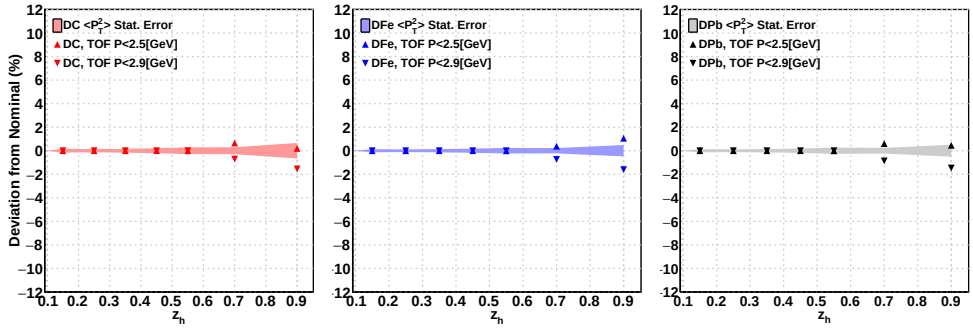

Figure B.2: TOF systematic uncertainty's $\langle P_T^2 \rangle$, with $x_f > 0$, deviations from the nominal values for liquid targets

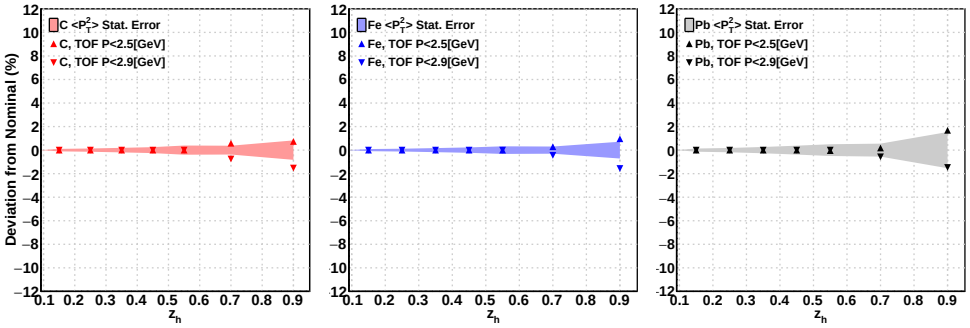

Figure B.3: TOF systematic uncertainty's $\langle P_T^2 \rangle$ deviations from the nominal values for solid targets

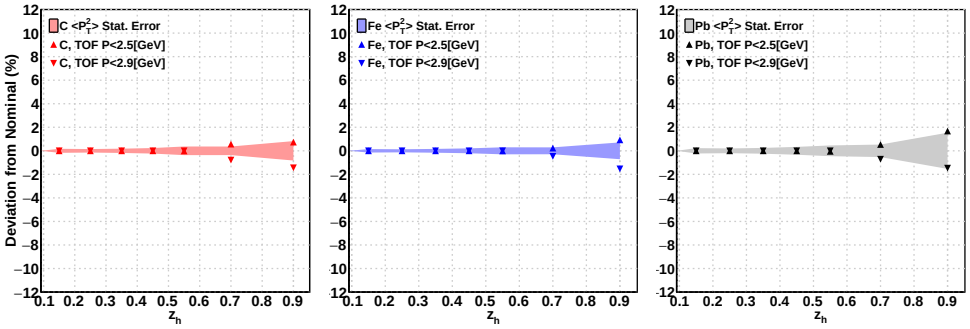

Figure B.4: TOF systematic uncertainty's $\langle P_T^2 \rangle$, with $x_f > 0$, deviations from the nominal values for solid targets

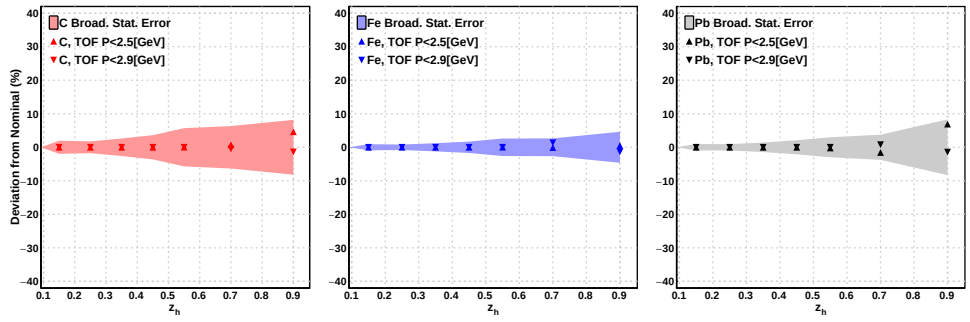

Figure B.5: TOF systematic uncertainty's ΔP_T^2 deviations from the nominal values

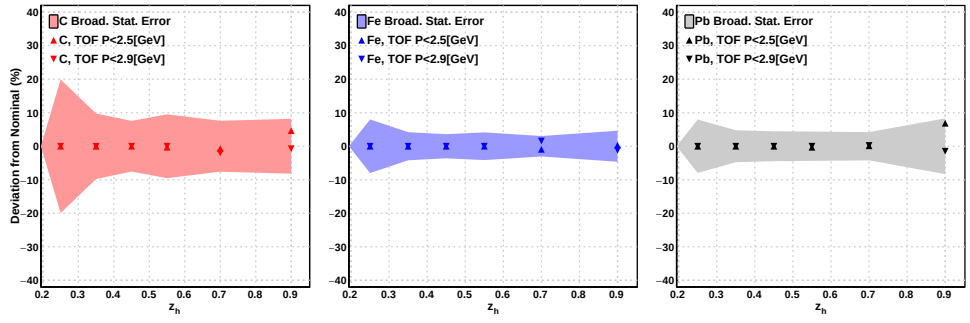

Figure B.6: TOF systematic uncertainty's ΔP_T^2, with $x_f > 0$, deviations from the nominal values

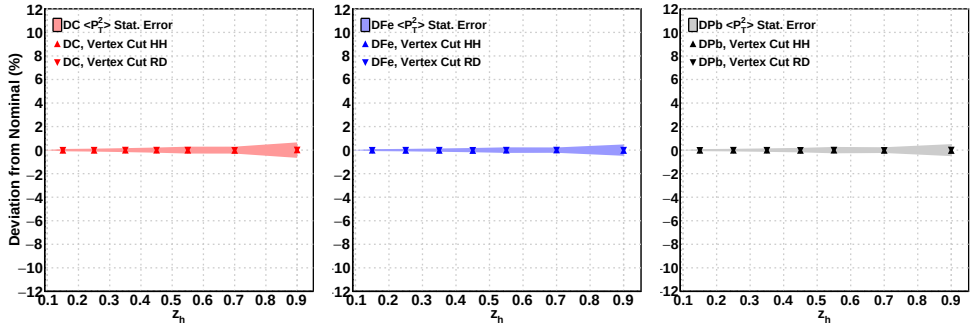

Figure B.7: Vertex cut systematic uncertainty's $\langle P_T^2 \rangle$ deviations from the nominal values for liquid targets

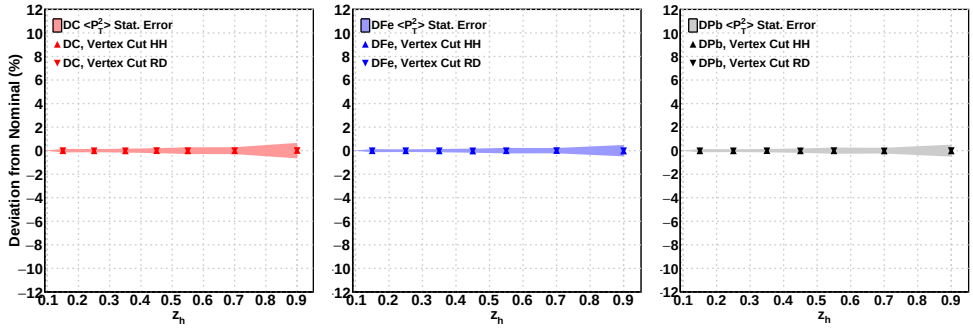

Figure B.8: Vertex cut systematic uncertainty's $\langle P_T^2 \rangle$, with $x_f > 0$, deviations from the nominal values for liquid targets

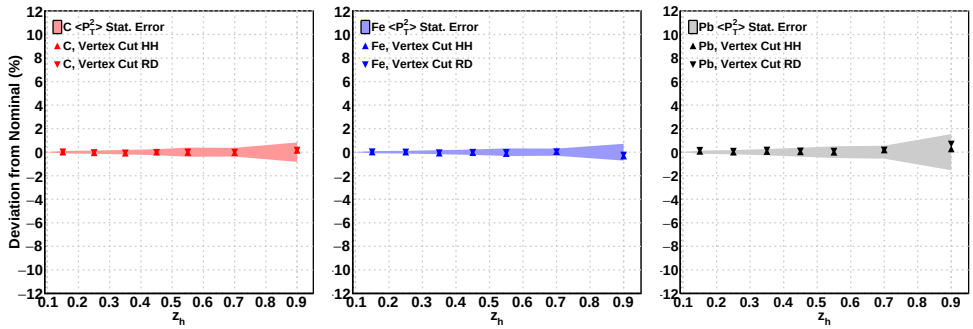

Figure B.9: Vertex cut systematic uncertainty's $\langle P_T^2 \rangle$ deviations from the nominal values for solid targets

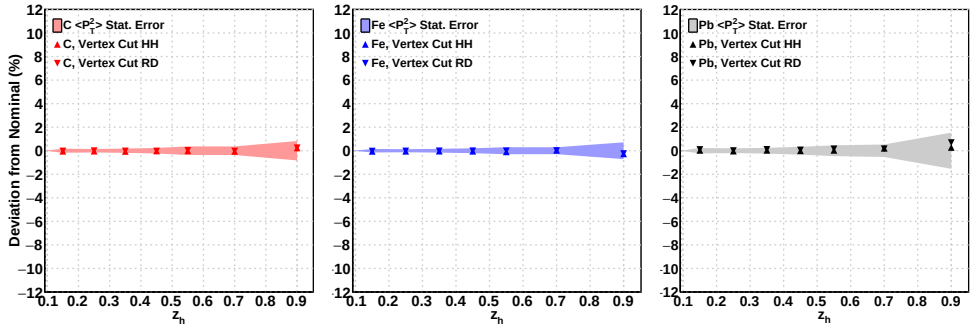

Figure B.10: Vertex cut systematic uncertainty's $\langle P_T^2 \rangle$, with $x_f > 0$, deviations from the nominal values for solid targets

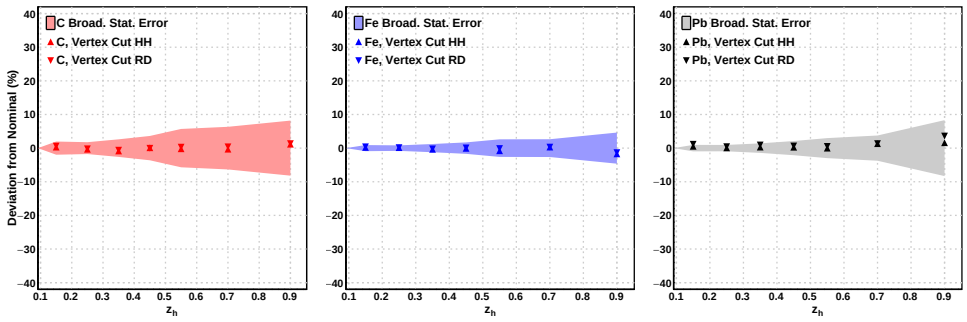

Figure B.11: Vertex cut systematic uncertainty's ΔP_T^2 deviations from the nominal values

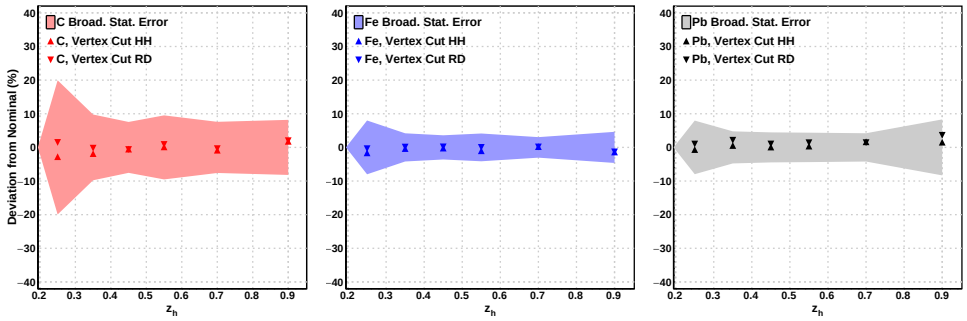

Figure B.12: Vertex cut systematic uncertainty's ΔP_T^2, with $x_f > 0$, deviations from the nominal values

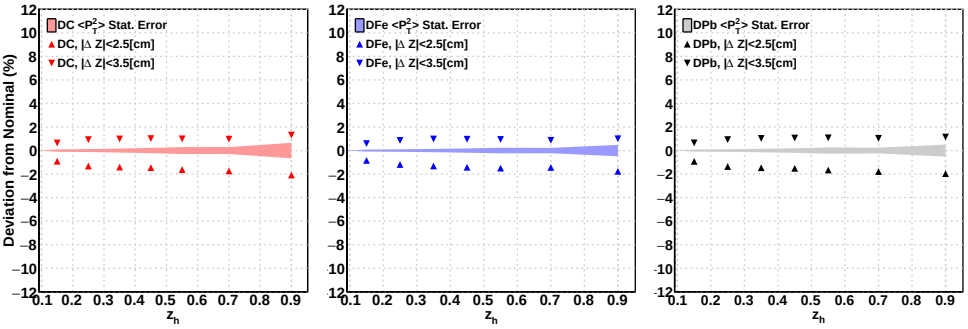

Figure B.13: ΔZ cut systematic uncertainty's $\langle P_T^2 \rangle$ deviations from the nominal values for liquid targets

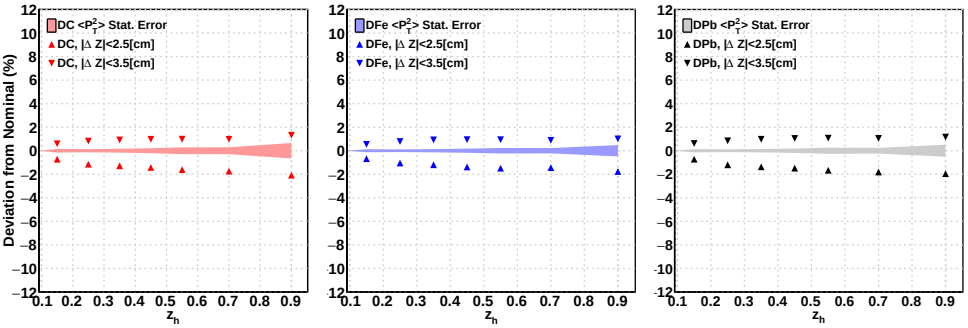

Figure B.14: ΔZ cut systematic uncertainty's $\langle P_T^2 \rangle$, with $x_f > 0$, deviations from the nominal values for liquid targets

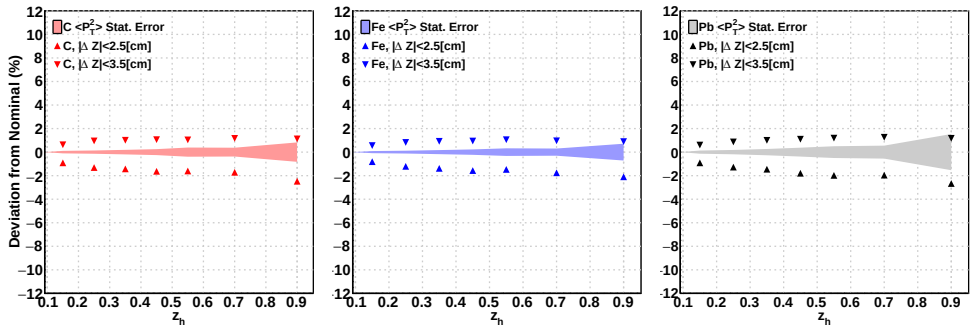

Figure B.15: ΔZ cut systematic uncertainty's $\langle P_T^2 \rangle$ deviations from the nominal values for solid targets

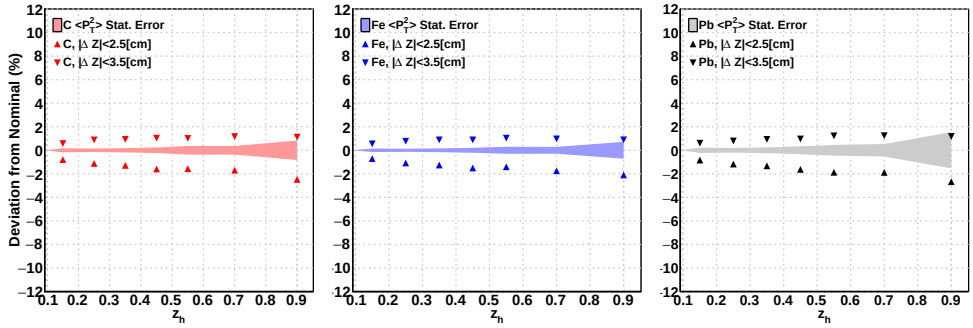

Figure B.16: ΔZ cut systematic uncertainty's $\langle P_T^2 \rangle$, with $x_f > 0$, deviations from the nominal values for solid targets

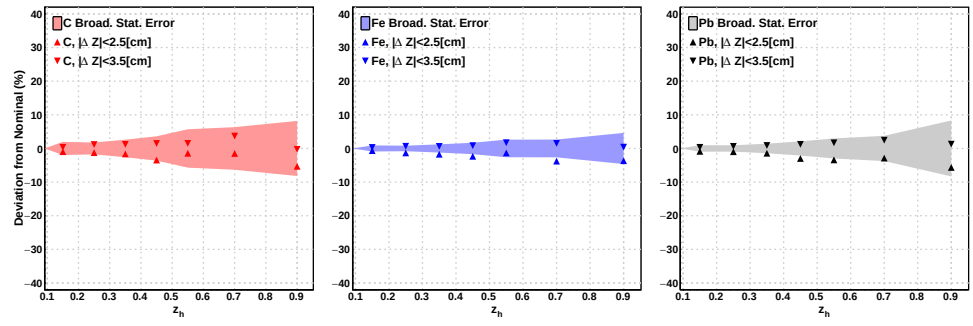

Figure B.17: ΔZ cut systematic uncertainty's ΔP_T^2 deviations from the nominal values

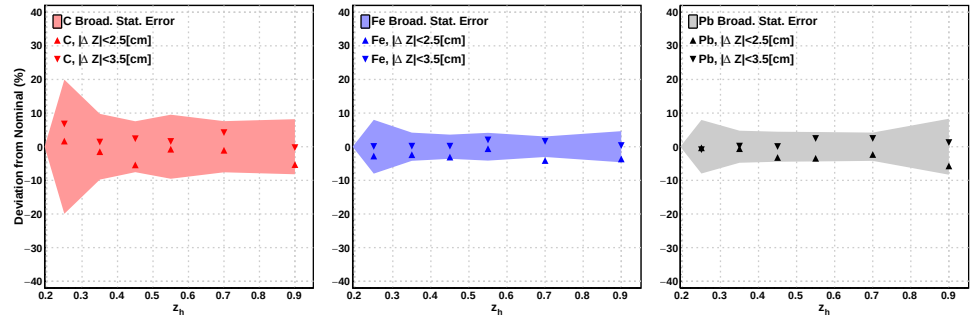

Figure B.18: ΔZ cut systematic uncertainty's ΔP_T^2, with $x_f > 0$, deviations from the nominal values

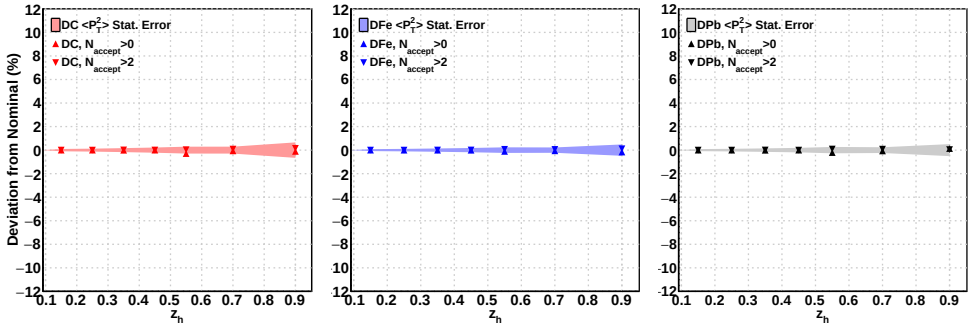

Figure B.19: N_{accept} cut systematic uncertainty's $\langle P_T^2 \rangle$ deviations from the nominal values for liquid targets

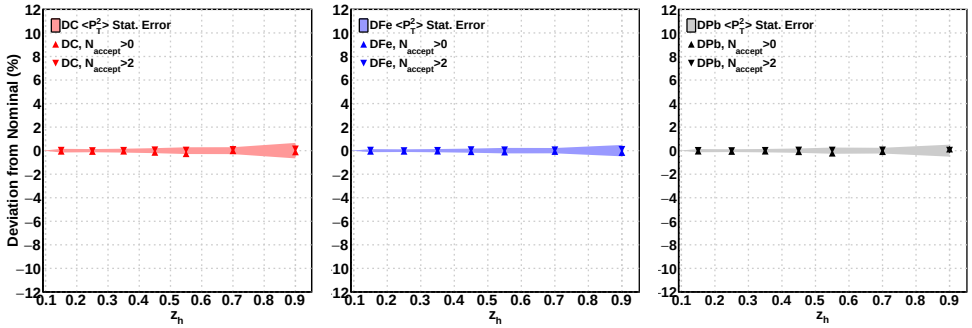

Figure B.20: N_{accept} cut systematic uncertainty's $\langle P_T^2 \rangle$, with $x_f > 0$, deviations from the nominal values for liquid targets

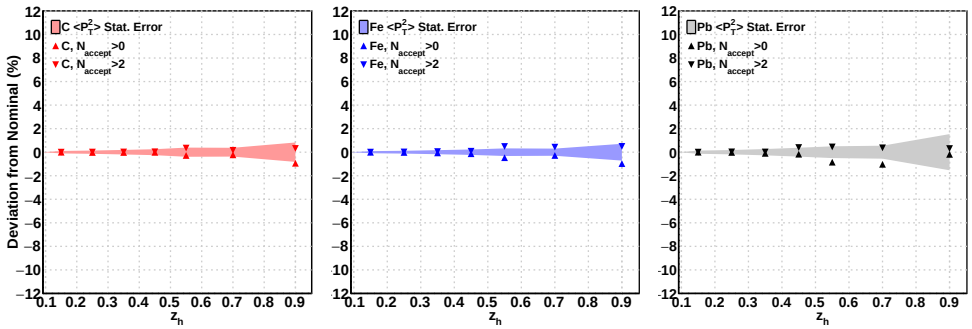

Figure B.21: N_{accept} cut systematic uncertainty's $\langle P_T^2 \rangle$ deviations from the nominal values for solid targets

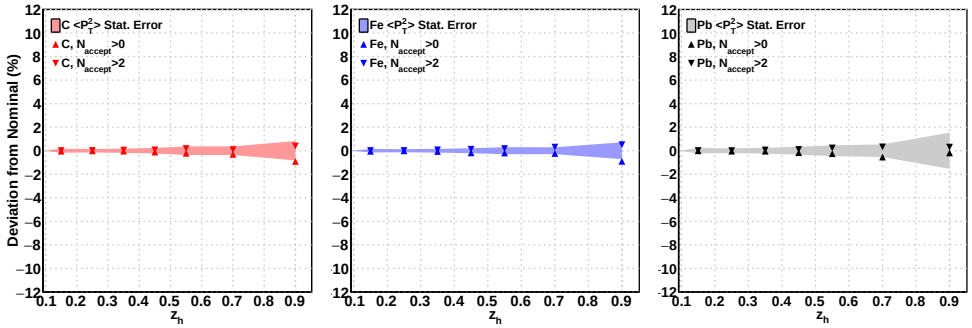

Figure B.22: N_{accept} cut systematic uncertainty's $\langle P_T^2 \rangle$, with $x_f > 0$, deviations from the nominal values for solid targets

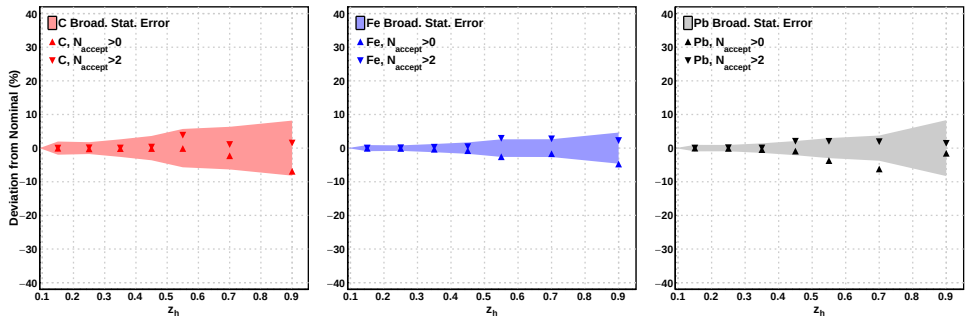

Figure B.23: N_{accept} cut systematic uncertainty's ΔP_T^2 deviations from the nominal values

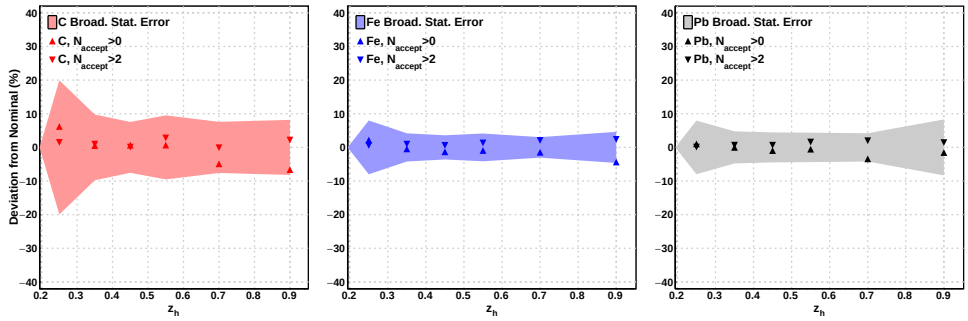

Figure B.24: N_{accept} cut systematic uncertainty's ΔP_T^2, with $x_f > 0$, deviations from the nominal values

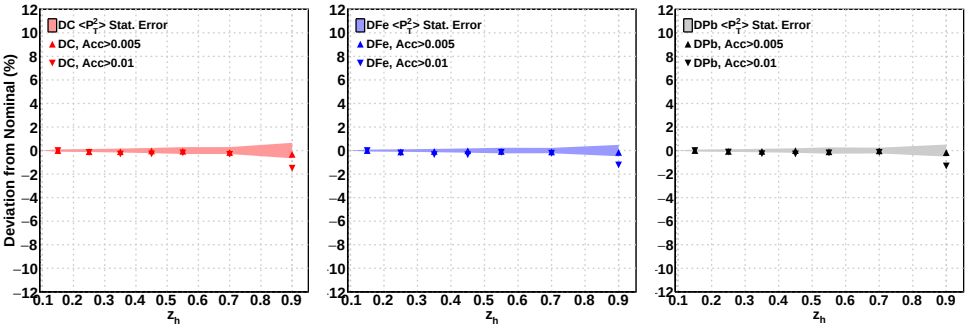

Figure B.25: Minimum *Acc* cut systematic uncertainty's $\langle P_T^2 \rangle$ deviations from the nominal values for liquid targets

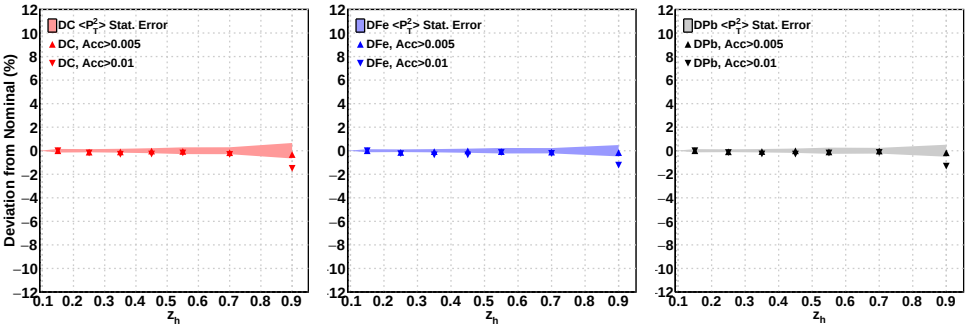

Figure B.26: Minimum *Acc* cut systematic uncertainty's $\langle P_T^2 \rangle$, with $x_f > 0$, deviations from the nominal values for liquid targets

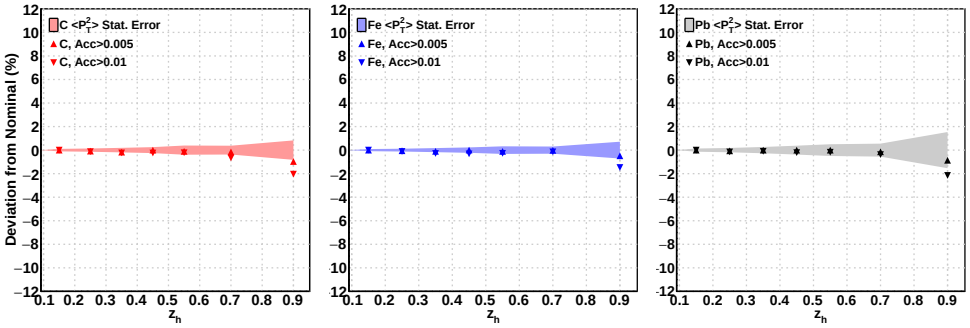

Figure B.27: Minimum *Acc* cut systematic uncertainty's $\langle P_T^2 \rangle$ deviations from the nominal values for solid targets

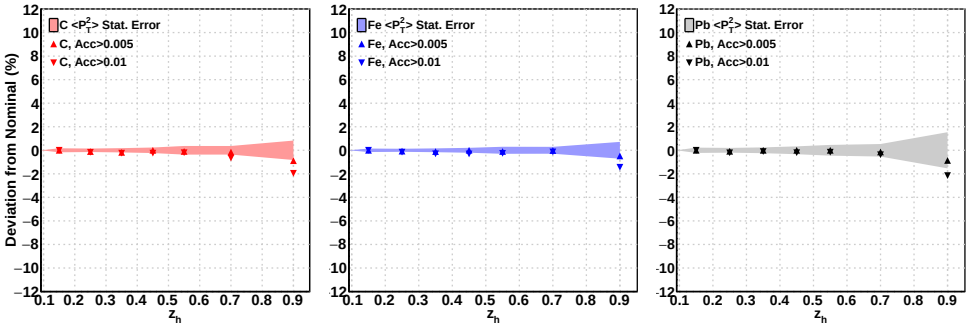

Figure B.28: Minimum *Acc* cut systematic uncertainty's $\langle P_T^2 \rangle$, with $x_f > 0$, deviations from the nominal values for solid targets

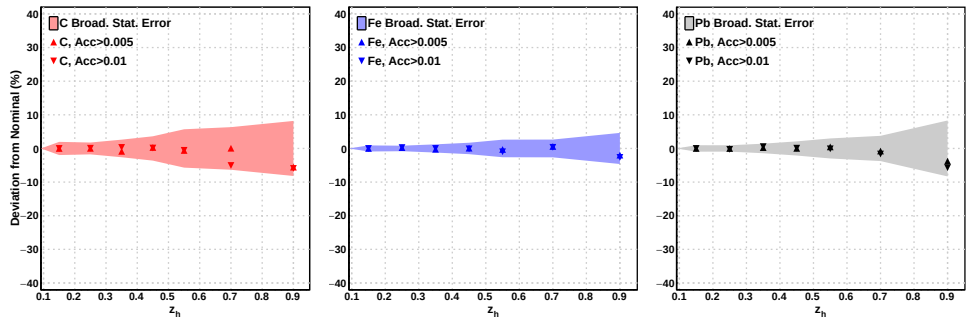

Figure B.29: Minimum *Acc* cut systematic uncertainty's ΔP_T^2 deviations from the nominal values

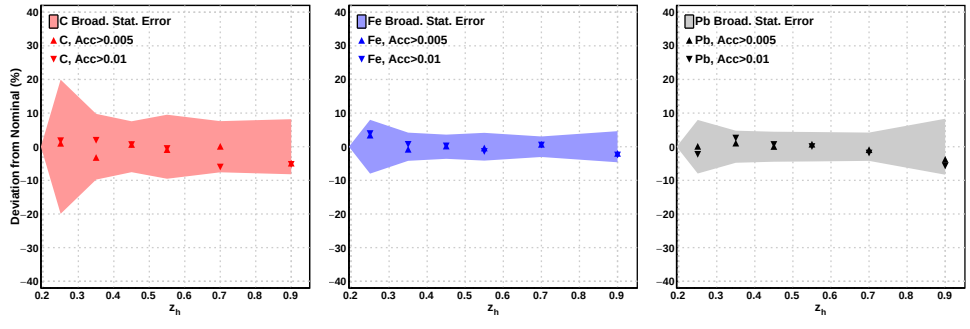

Figure B.30: Minimum *Acc* cut systematic uncertainty's ΔP_T^2, with $x_f > 0$, deviations from the nominal values

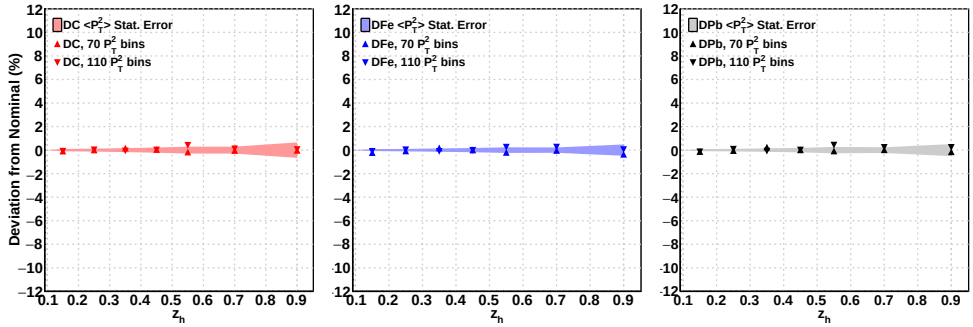

Figure B.31: Number of P_T^2 bins systematic uncertainty's $\langle P_T^2 \rangle$ deviations from the nominal values for liquid targets

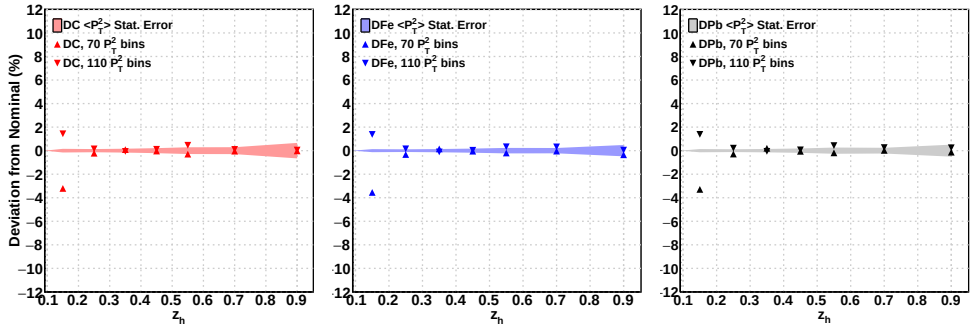

Figure B.32: Number of P_T^2 bins systematic uncertainty's $\langle P_T^2 \rangle$, with $x_f > 0$, deviations from the nominal values for liquid targets

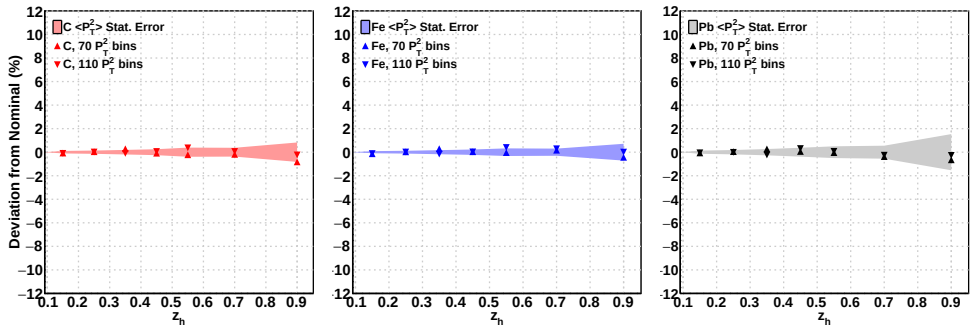

Figure B.33: Number of P_T^2 bins systematic uncertainty's $\langle P_T^2 \rangle$ deviations from the nominal values for solid targets

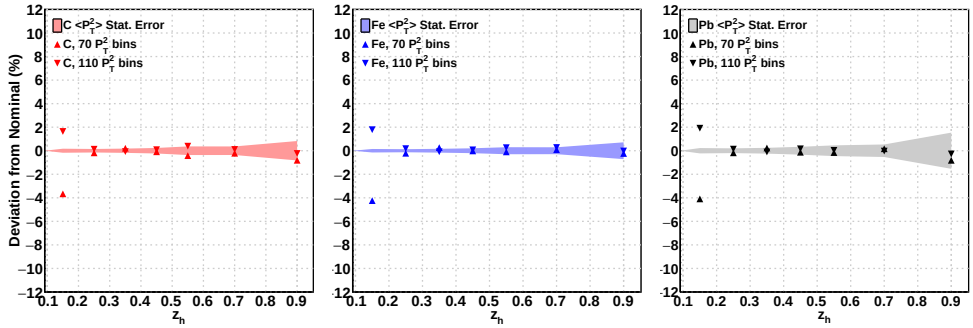

Figure B.34: Number of P_T^2 bins systematic uncertainty's $\langle P_T^2 \rangle$, with $x_f > 0$, deviations from the nominal values for solid targets

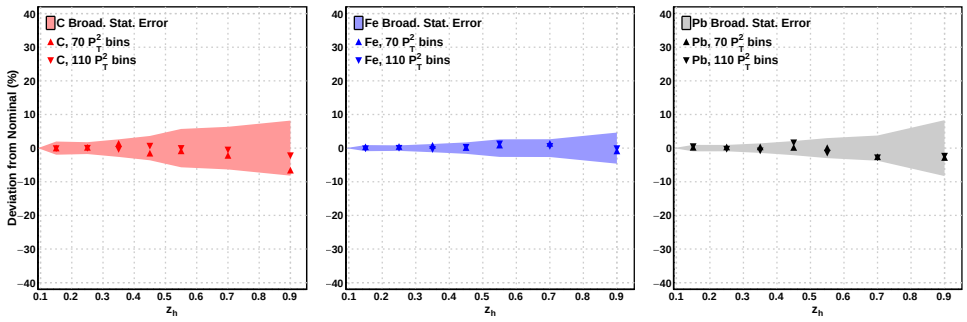

Figure B.35: Number of P_T^2 bins systematic uncertainty's ΔP_T^2 deviations from the nominal values

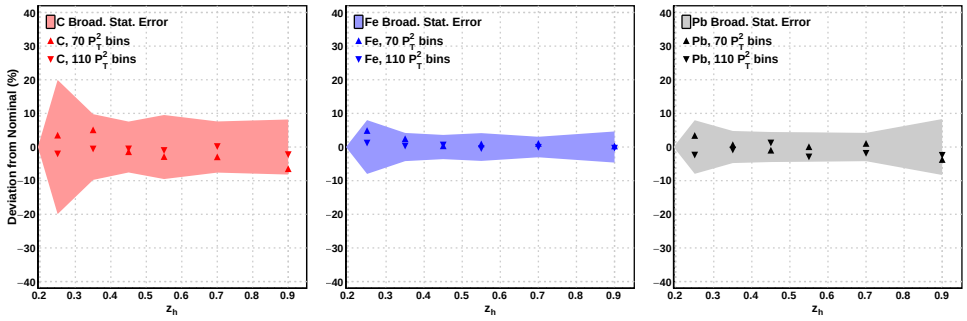

Figure B.36: Number of P_T^2 bins systematic uncertainty's ΔP_T^2, with $x_f > 0$, deviations from the nominal values

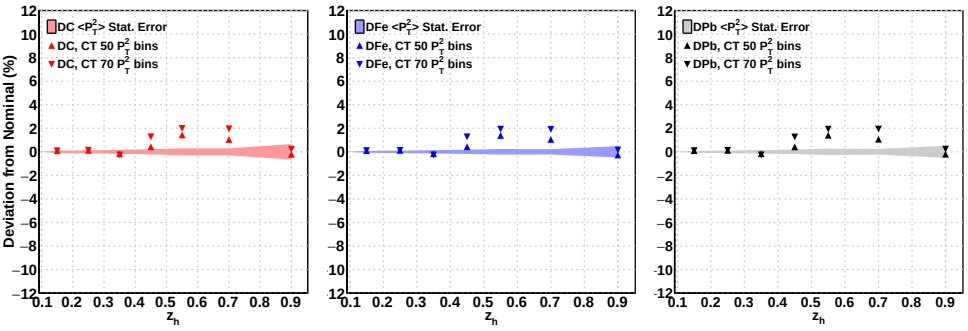

Figure B.37: CT systematic uncertainty's $\langle P_T^2 \rangle$ deviations from the nominal values for liquid targets

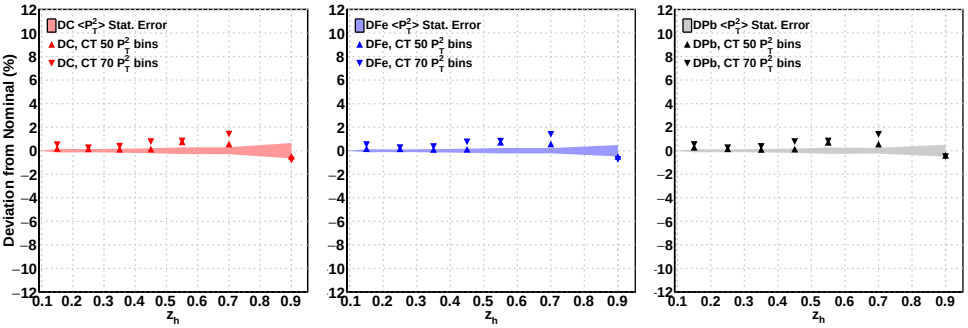

Figure B.38: CT systematic uncertainty's $\langle P_T^2 \rangle$, with $x_f > 0$, deviations from the nominal values for liquid targets

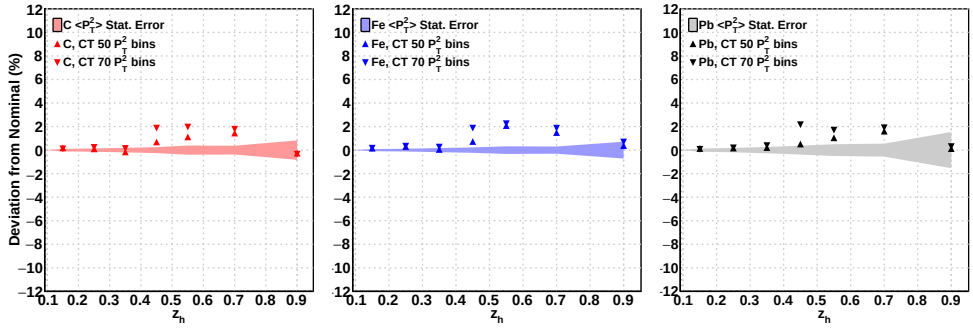

Figure B.39: CT systematic uncertainty's $\langle P_T^2 \rangle$ deviations from the nominal values for solid targets

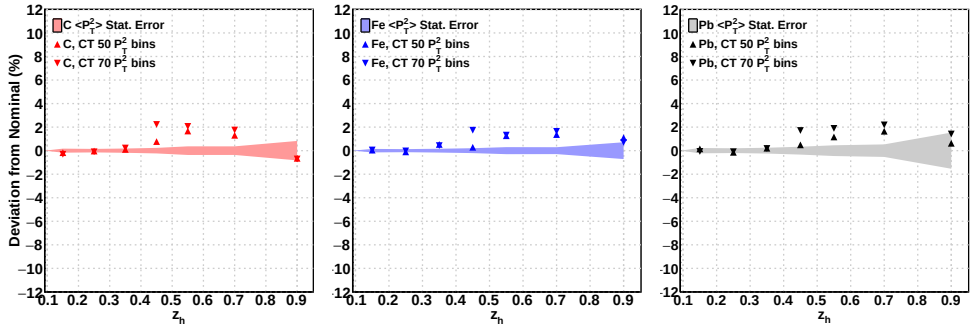

Figure B.40: CT systematic uncertainty's $\langle P_T^2 \rangle$, with $x_f > 0$, deviations from the nominal values for solid targets

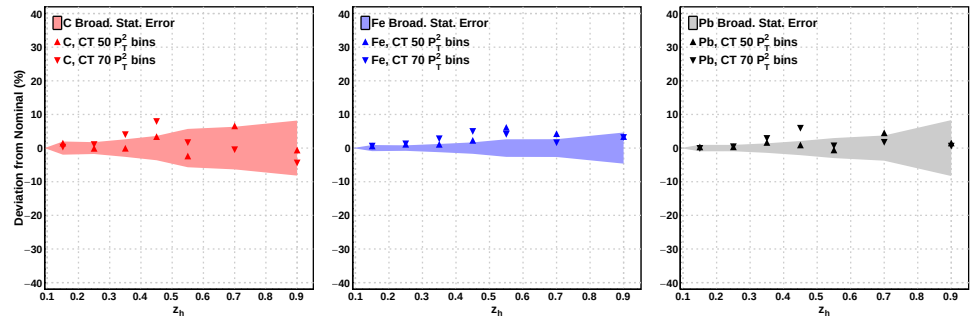

Figure B.41: CT systematic uncertainty's ΔP_T^2 deviations from the nominal values

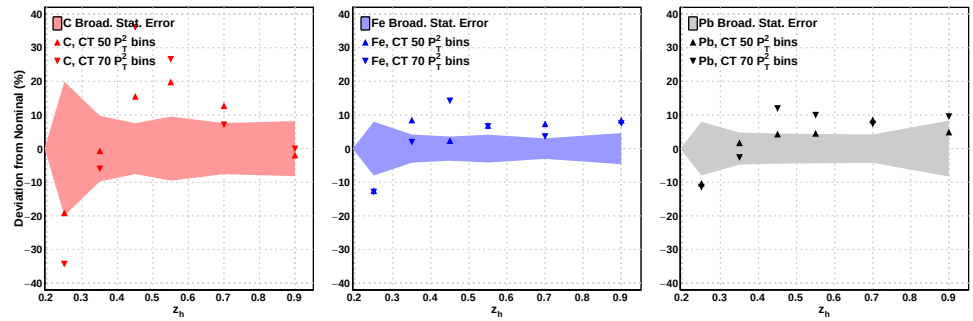

Figure B.42: CT systematic uncertainty's ΔP_T^2, with $x_f > 0$, deviations from the nominal values

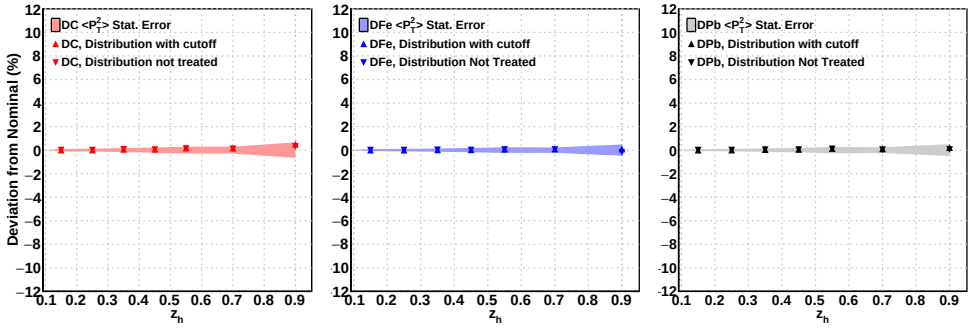

Figure B.43: BG subtraction systematic uncertainty's $\langle P_T^2 \rangle$ deviations from the nominal values for liquid targets

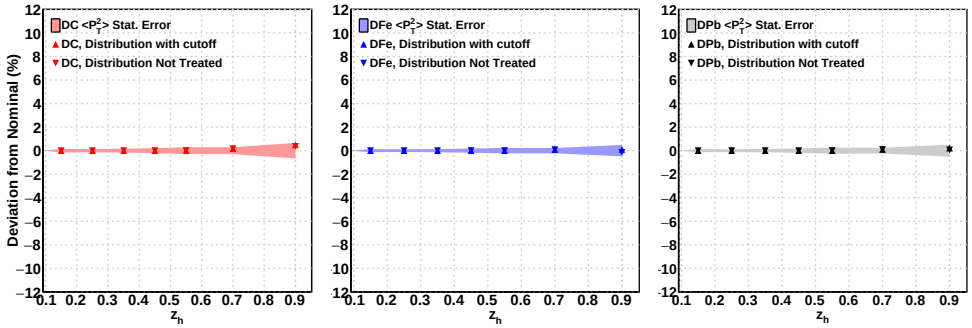

Figure B.44: BG subtraction systematic uncertainty's $\langle P_T^2 \rangle$, with $x_f > 0$, deviations from the nominal values for liquid targets

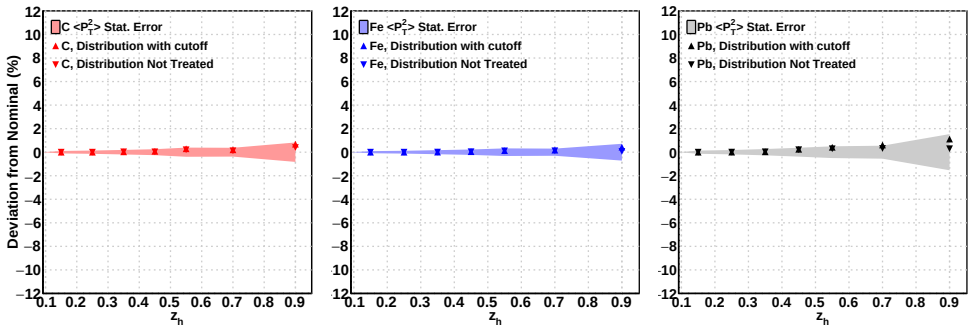

Figure B.45: BG subtraction systematic uncertainty's $\langle P_T^2 \rangle$ deviations from the nominal values for solid targets

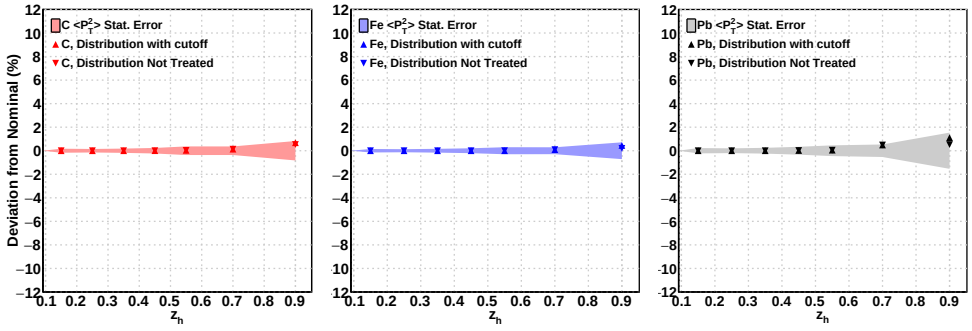

Figure B.46: BG subtraction systematic uncertainty's $\langle P_T^2 \rangle$, with $x_f > 0$, deviations from the nominal values for solid targets

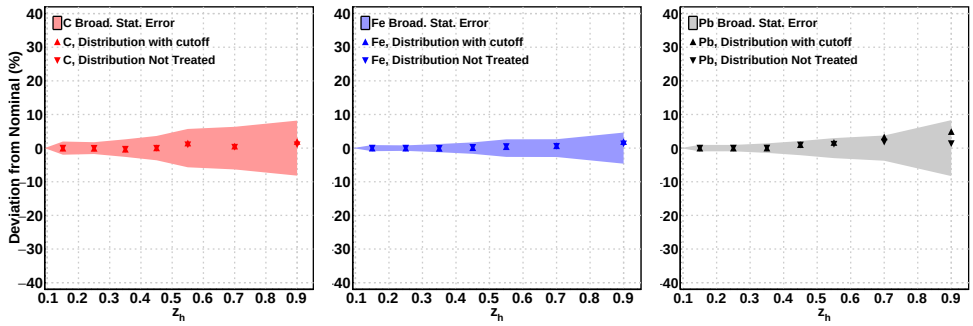

Figure B.47: BG subtraction systematic uncertainty's ΔP_T^2 deviations from the nominal values

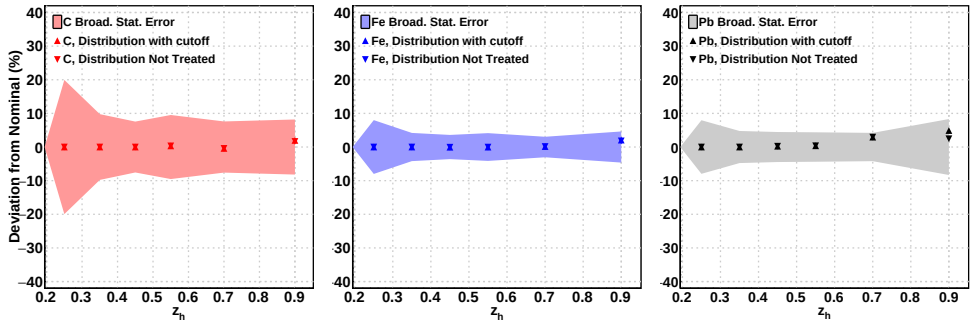

Figure B.48: BG subtraction systematic uncertainty's ΔP_T^2, with $x_f > 0$, deviations from the nominal values

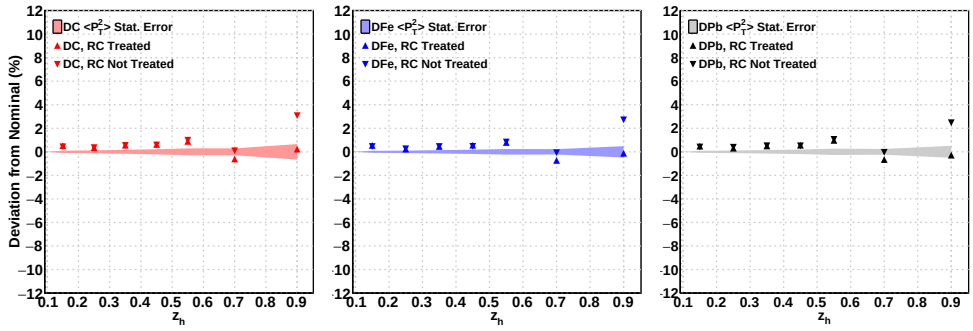

Figure B.49: RC systematic uncertainty's $\langle P_T^2 \rangle$ deviations from the nominal values for liquid targets

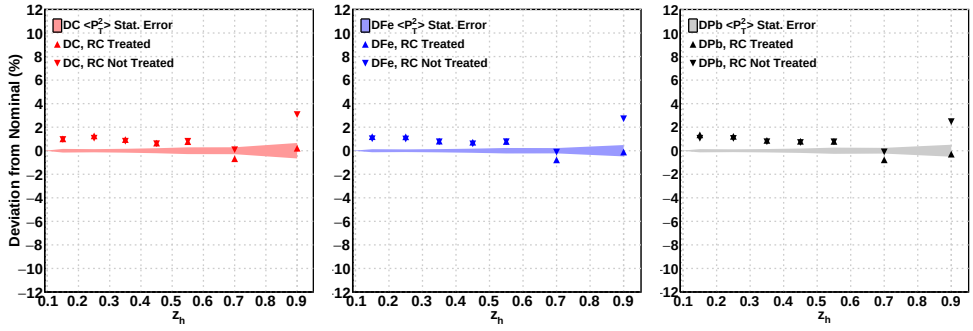

Figure B.50: RC systematic uncertainty's $\langle P_T^2 \rangle$, with $x_f > 0$, deviations from the nominal values for liquid targets

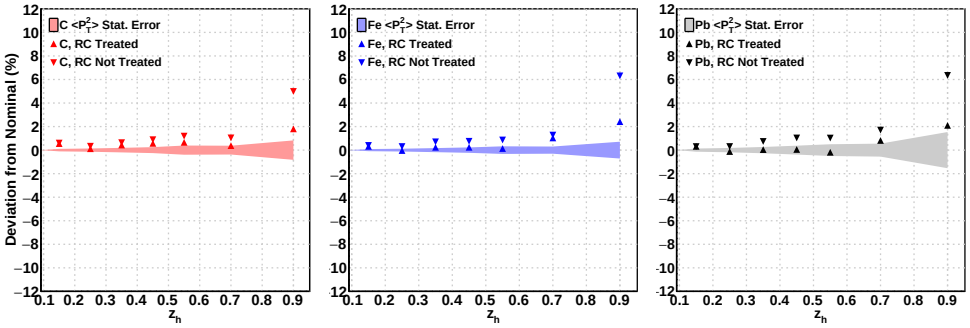

Figure B.51: RC systematic uncertainty's $\langle P_T^2 \rangle$ deviations from the nominal values for solid targets

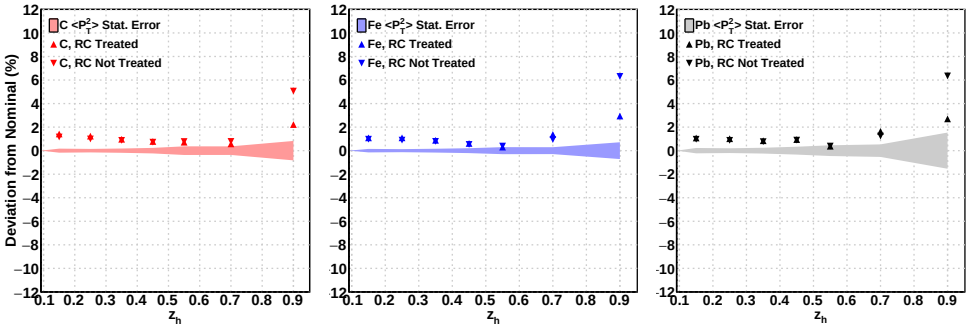

Figure B.52: RC systematic uncertainty's $\langle P_T^2 \rangle$, with $x_f > 0$, deviations from the nominal values for solid targets

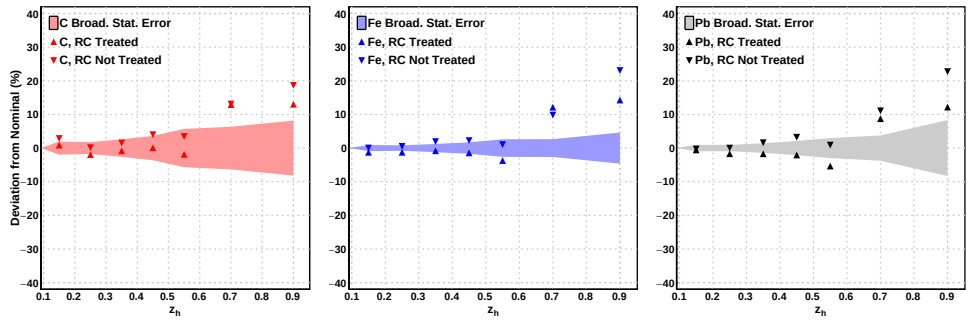

Figure B.53: RC systematic uncertainty's ΔP_T^2 deviations from the nominal values

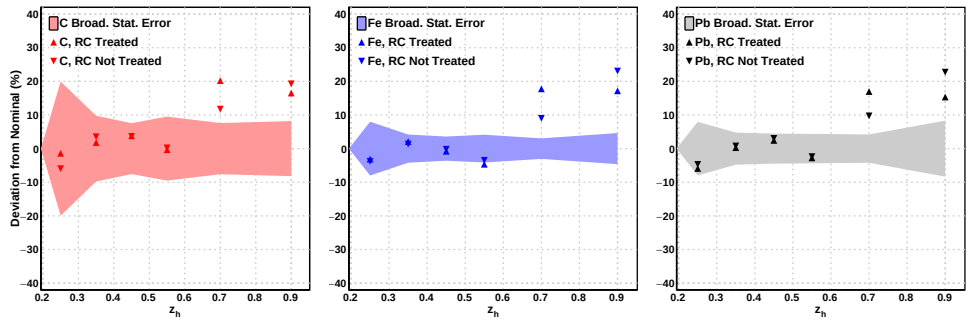

Figure B.54: RC systematic uncertainty's ΔP_T^2, with $x_f > 0$, deviations from the nominal values

B.2 Average Squared Transverse Momentum

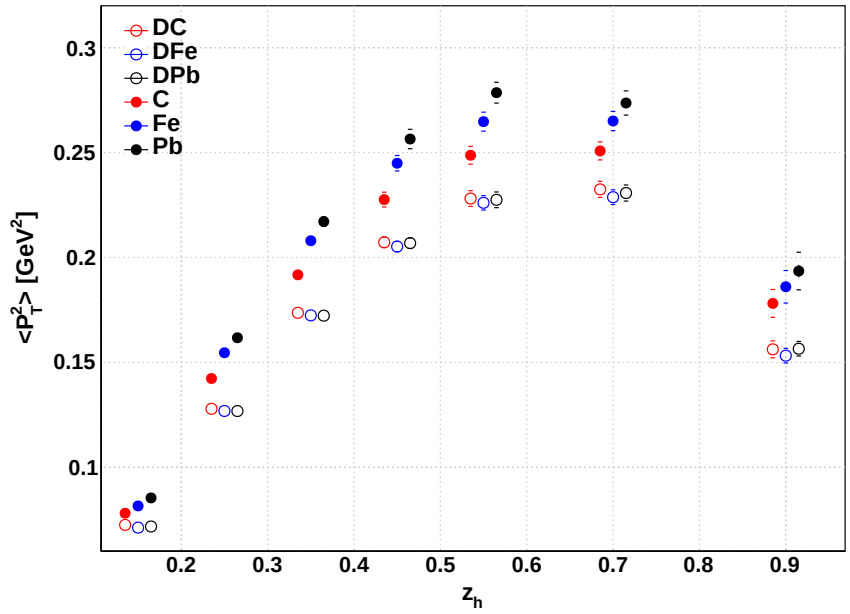

Figure B.55: $\langle P_T^2 \rangle$ with all variables integrated except z_h and no $x_f cut$. Statistical errors are too small to be seen.

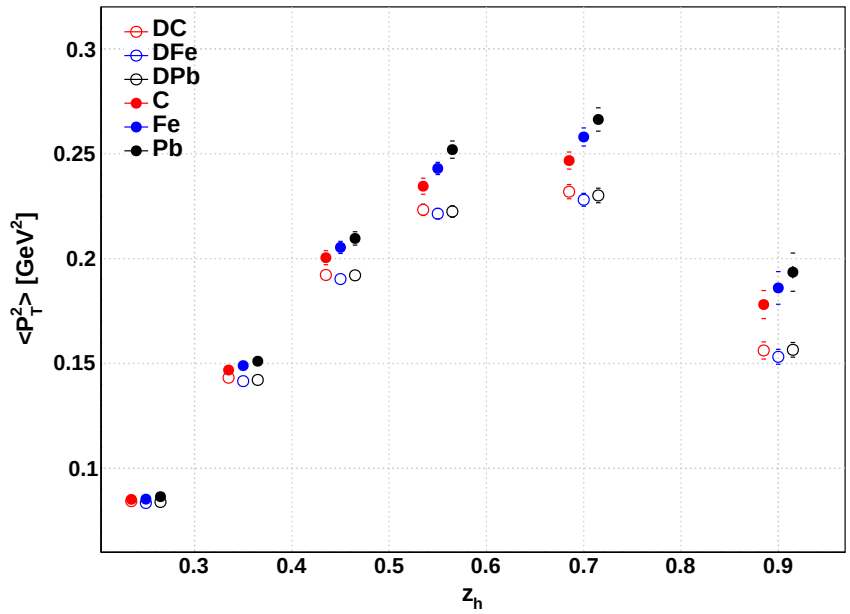

Figure B.56: $\langle P_T^2 \rangle$ with all variables integrated except z_h and $x_f > 0$ cut. Statistical errors are too small to be seen.

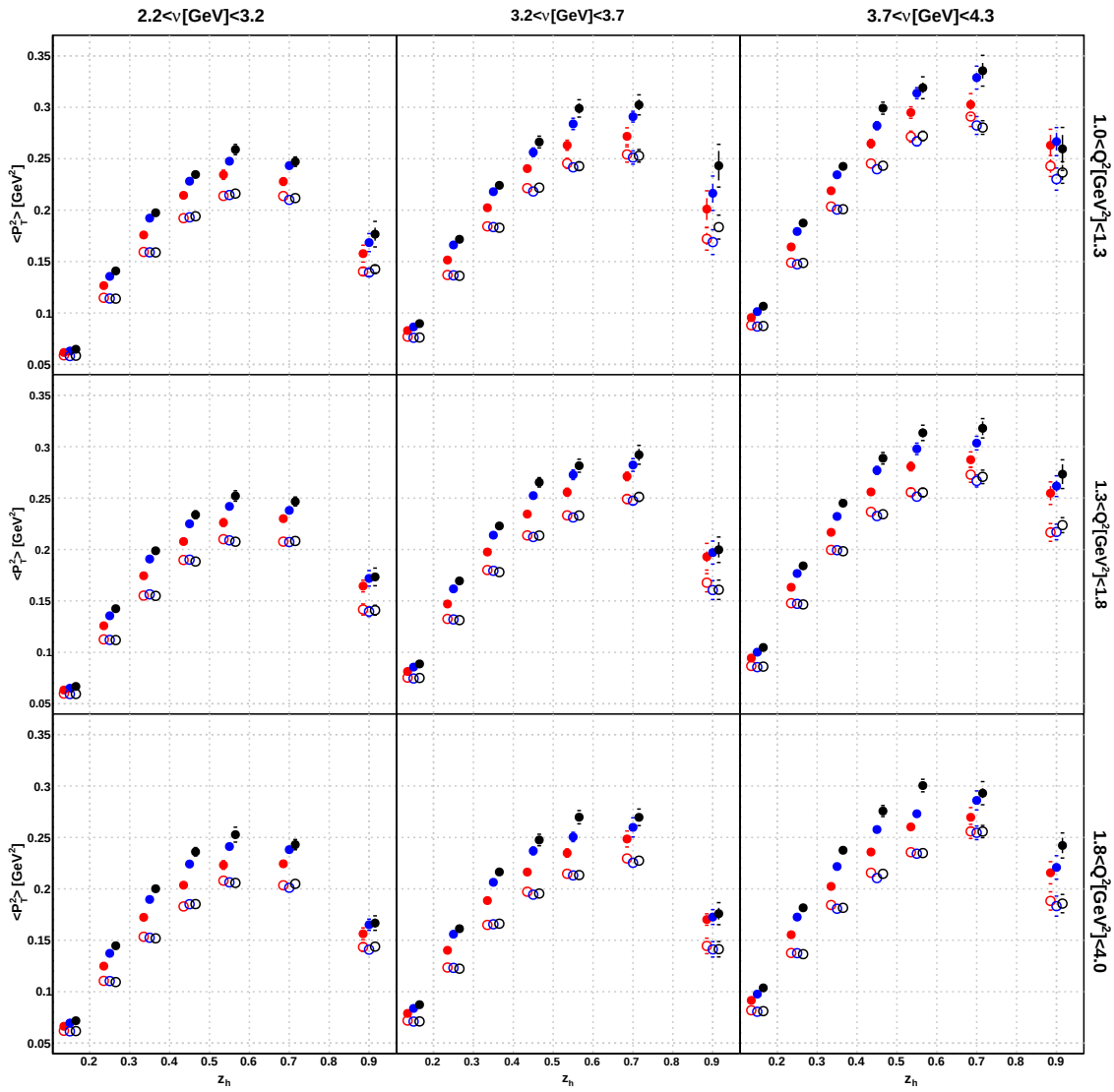

Figure B.57: $\langle P_T^2 \rangle$ differential distributions with no x_f cut.

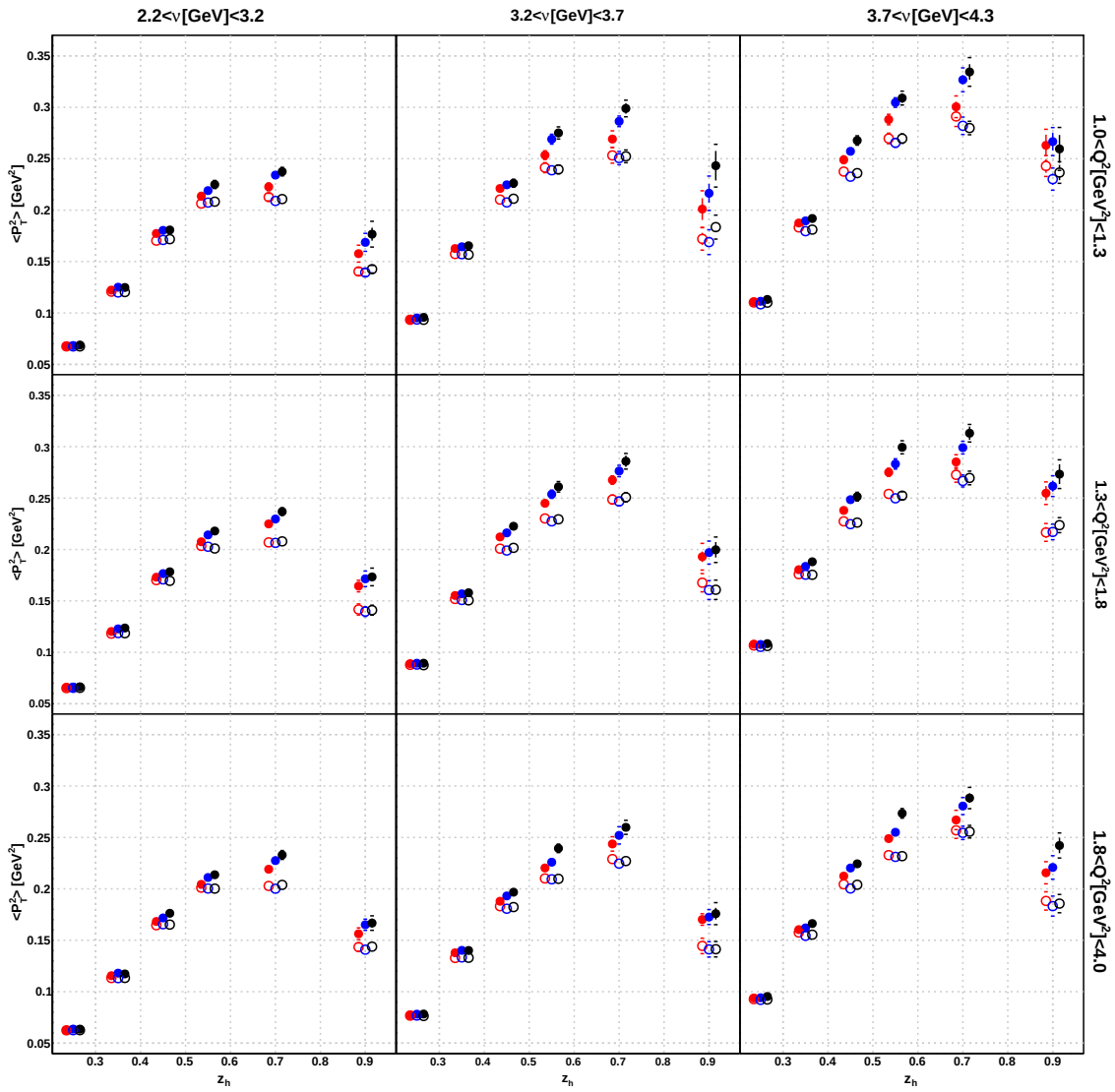

Figure B.58: $\langle P_T^2 \rangle$ differential distributions with $x_f > 0$ cut.

B.3 Transverse Momentum Broadening

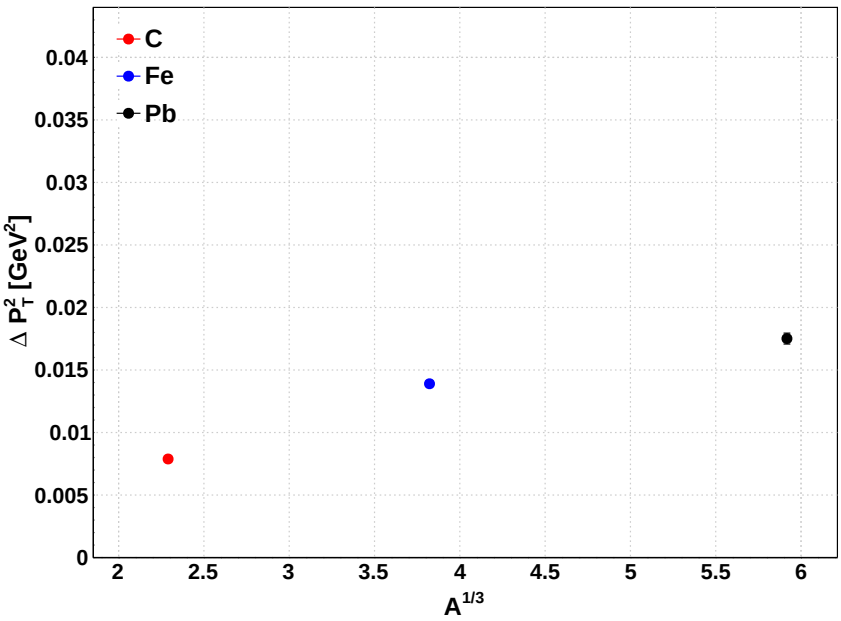

Figure B.59: ΔP_T^2 with all variables integrated and no x_f cut.

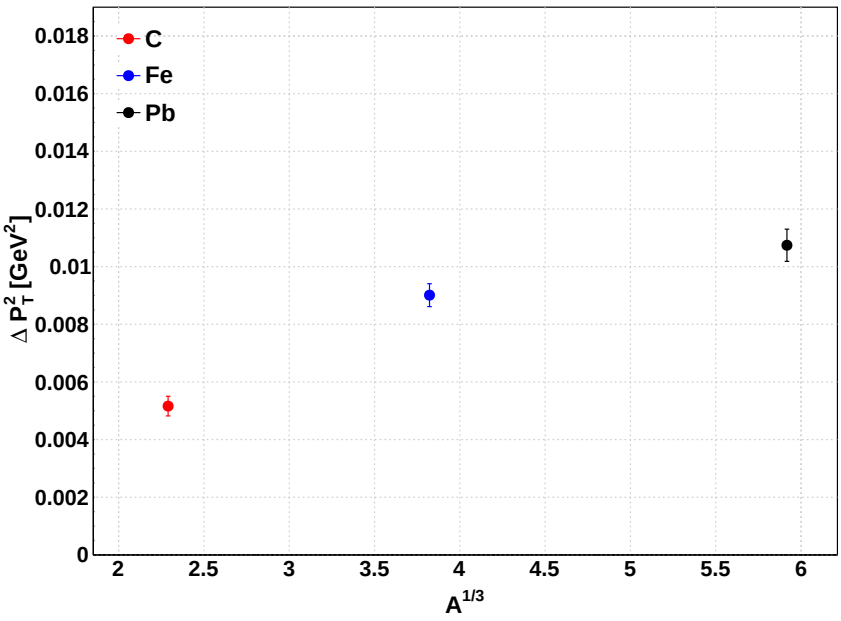

Figure B.60: ΔP_T^2 with all variables integrated and with $x_f > 0$ cut.

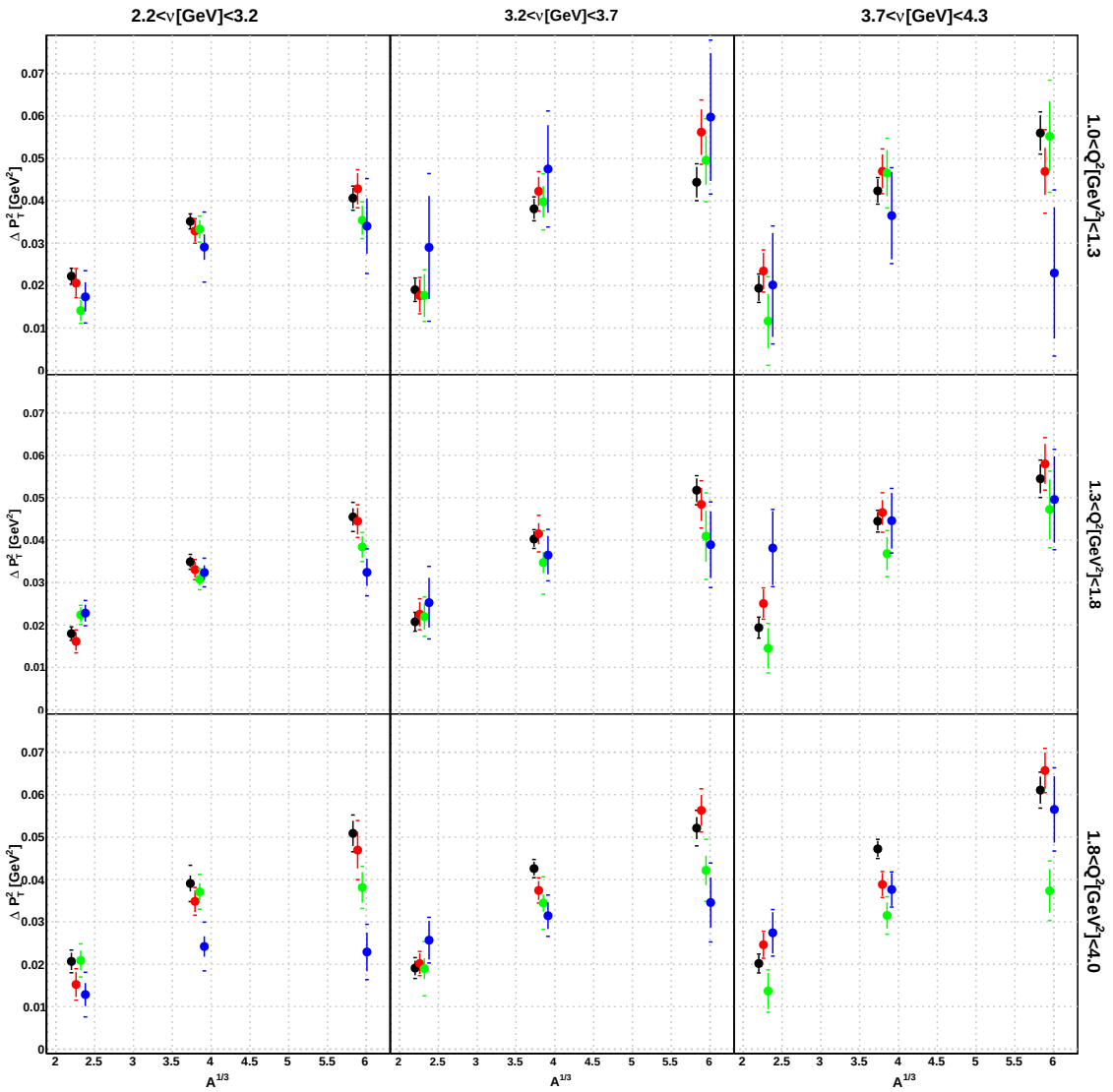

Figure B.61: ΔP_T^2 differential distributions with no x_f cut. Black points ($0.4 < z_h < 0.5$), red points ($0.5 < z_h < 0.6$), green points ($0.6 < z_h < 0.8$), blue points ($0.8 < z_h < 1$).

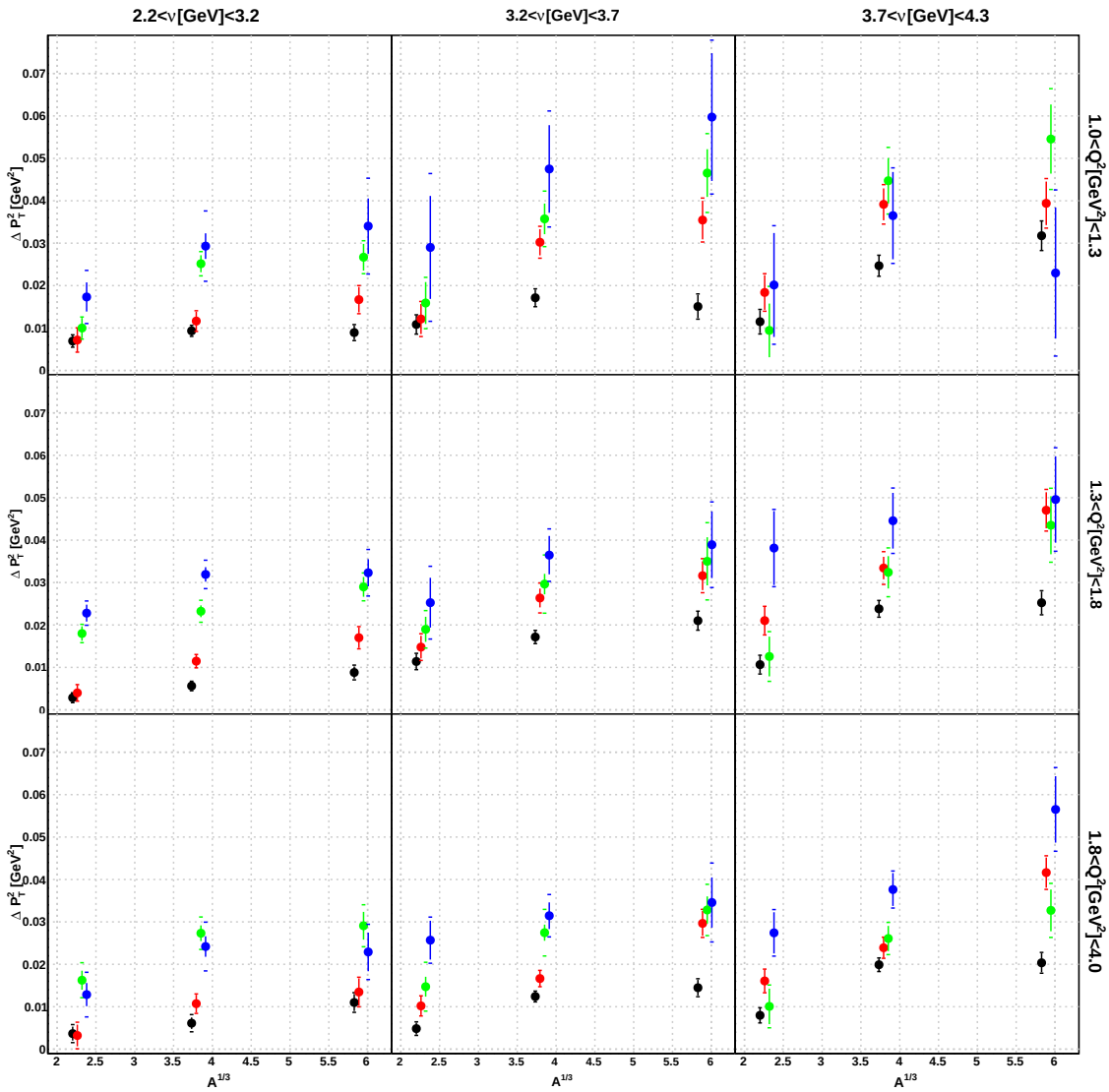

Figure B.62: ΔP_T^2 differential distributions with x_f cut. Black points ($0.4 < z_h < 0.5$), red points ($0.5 < z_h < 0.6$), green points ($0.6 < z_h < 0.8$), blue points ($0.8 < z_h < 1$).

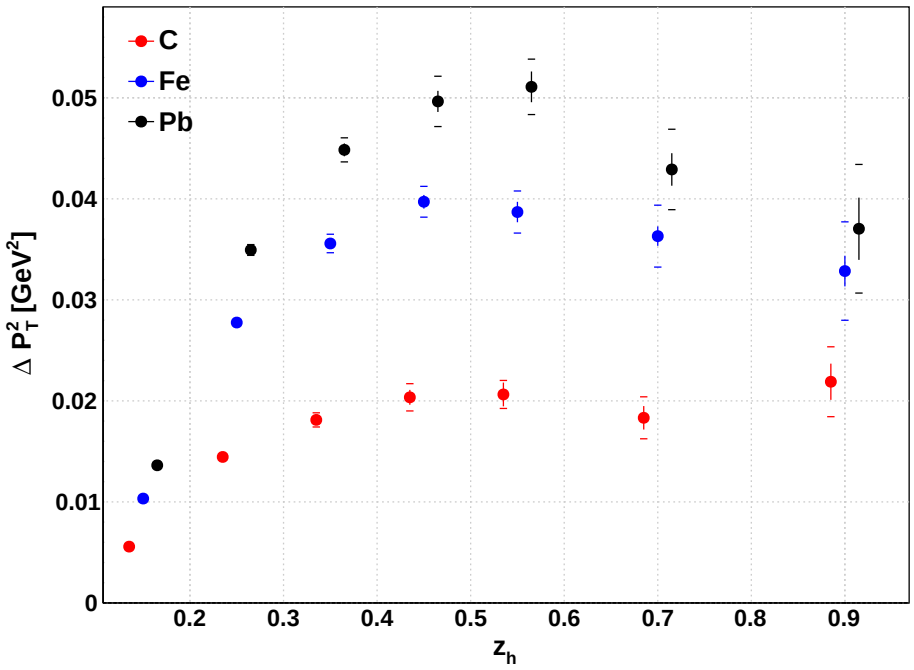

Figure B.63: ΔP_T^2 with all variables integrated except z_h.

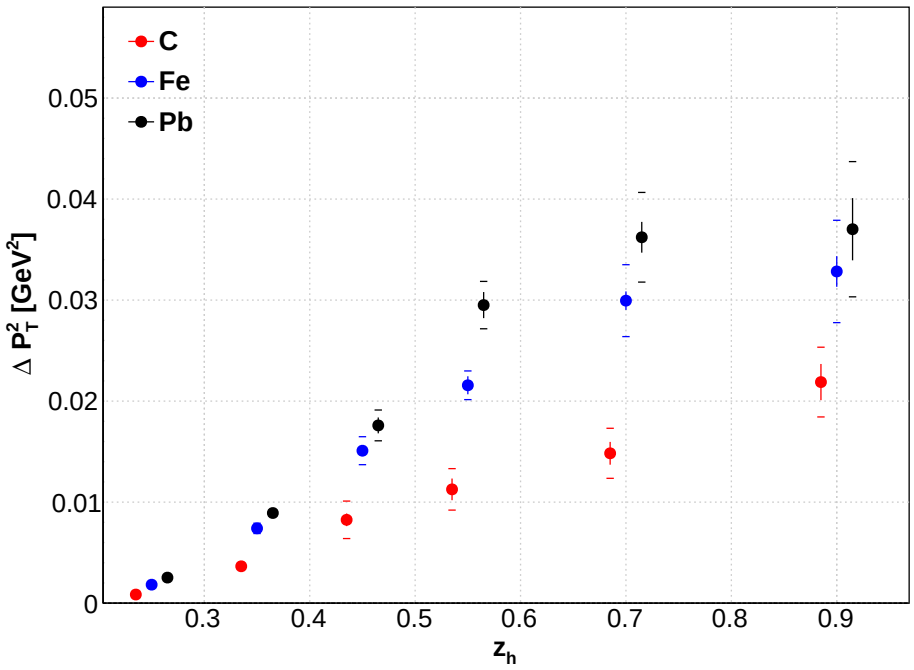

Figure B.64: ΔP_T^2 with all variables integrated except z_h.

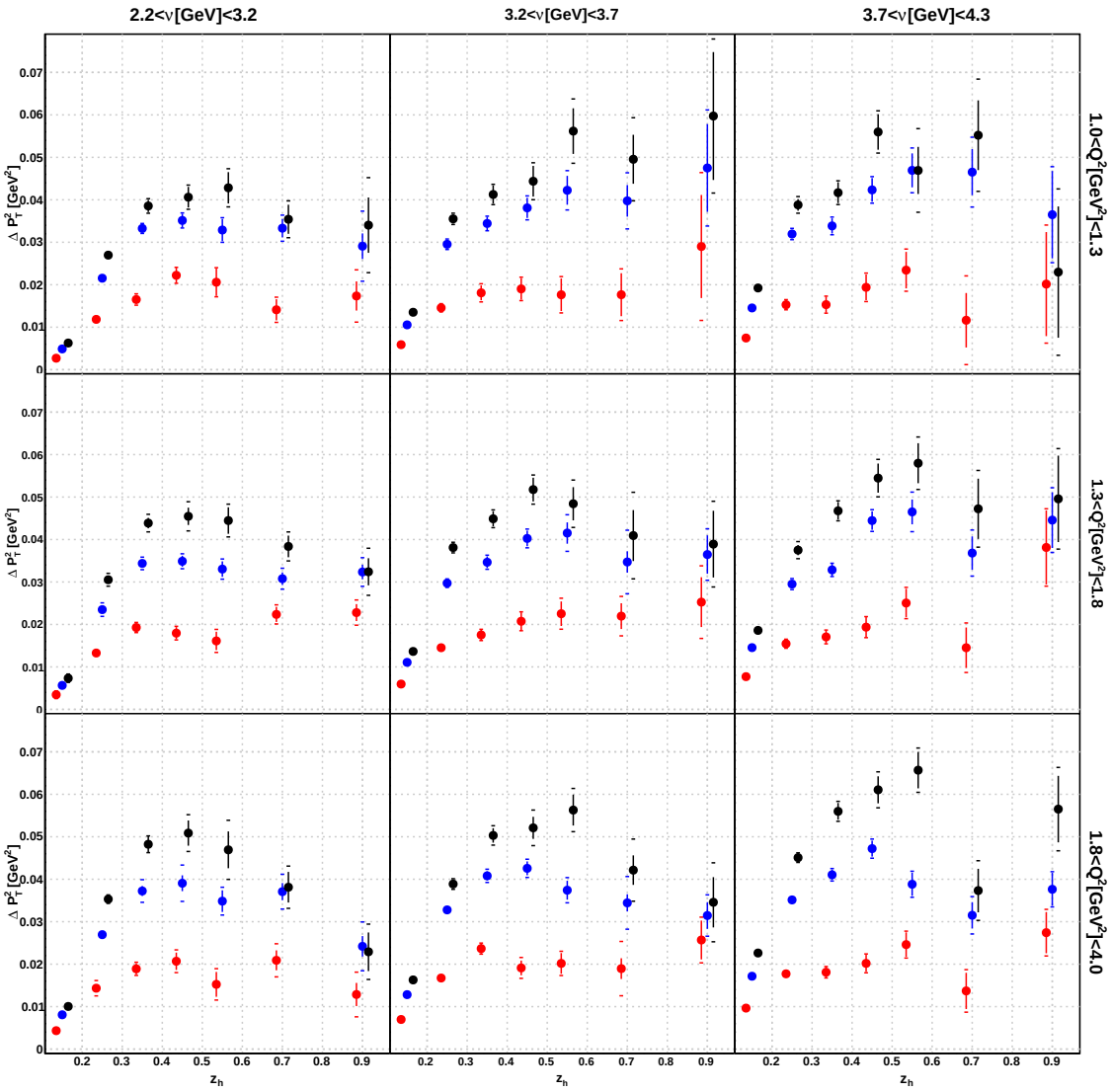

Figure B.65: ΔP_T^2 differential distributions.

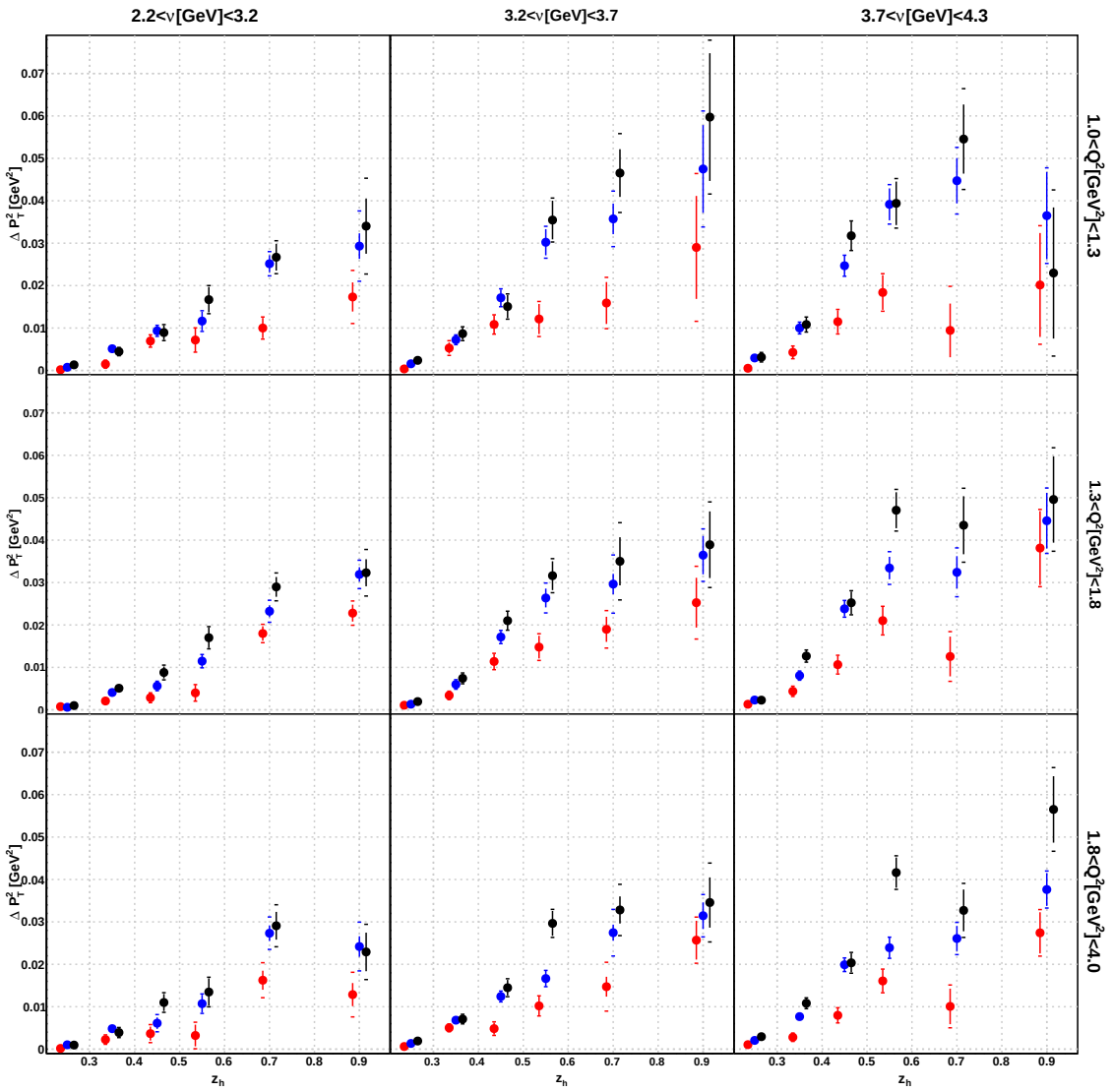

Figure B.66: ΔP_T^2 differential distributions.

B.4 Fits to Averaged Squared Transverse Momentum

B.4.1 Fit With Analytic Function (Hypothesis 1)

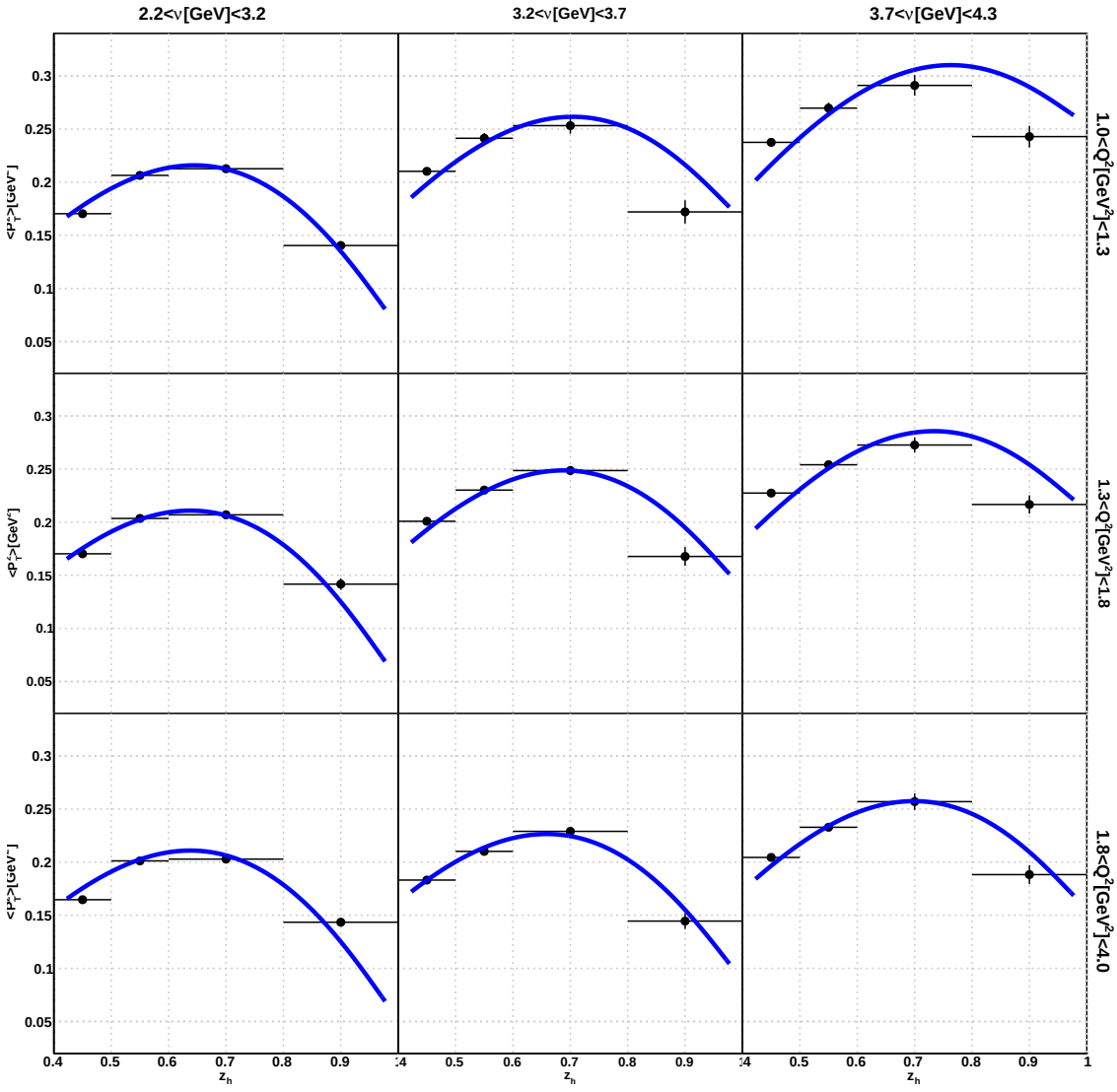

Figure B.67: Fits to Deuterium (C) results with $x_f > 0$ cut applied.

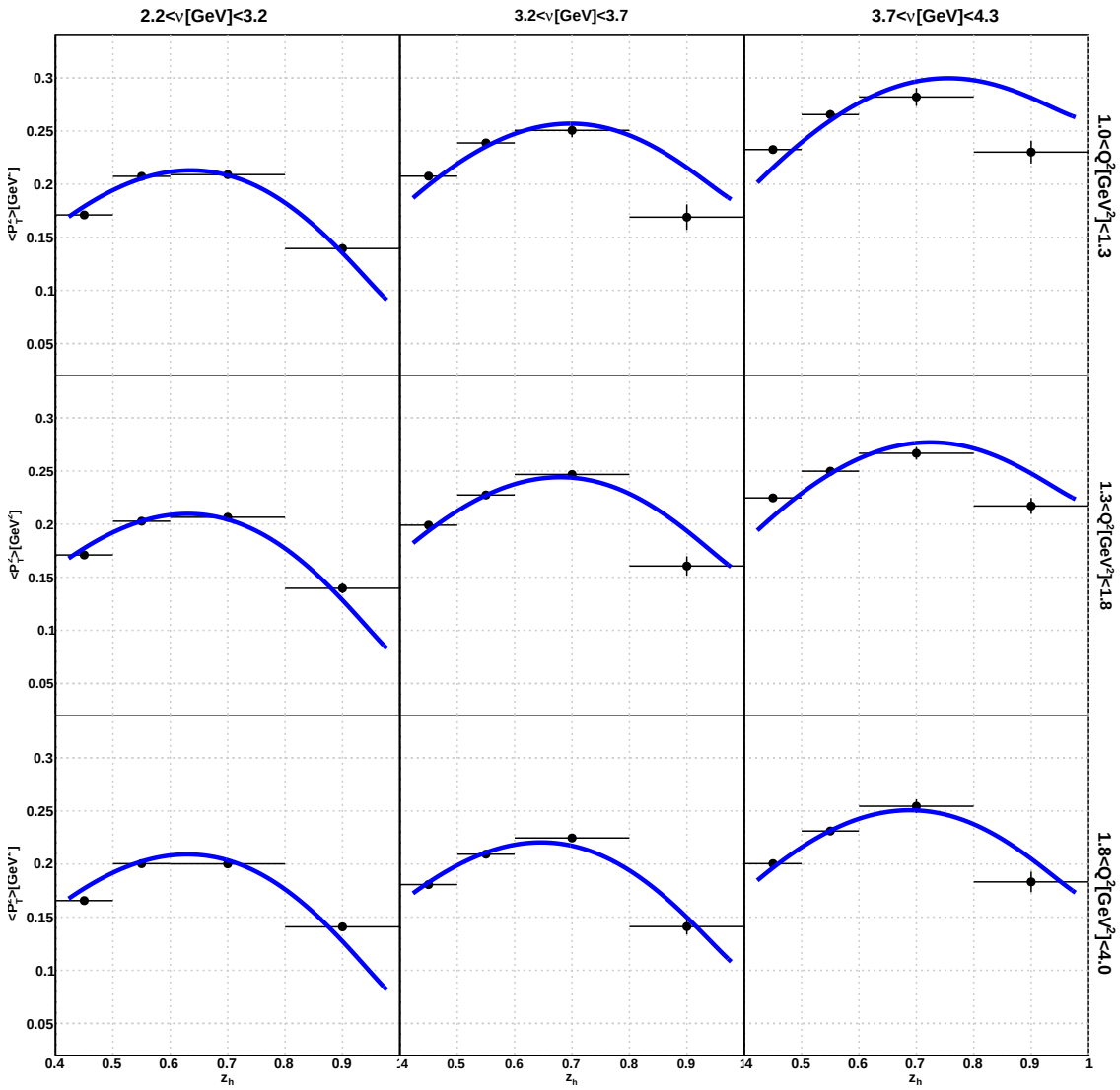

Figure B.68: Fits to Deuterium (Fe) results with $x_f > 0$ cut applied.

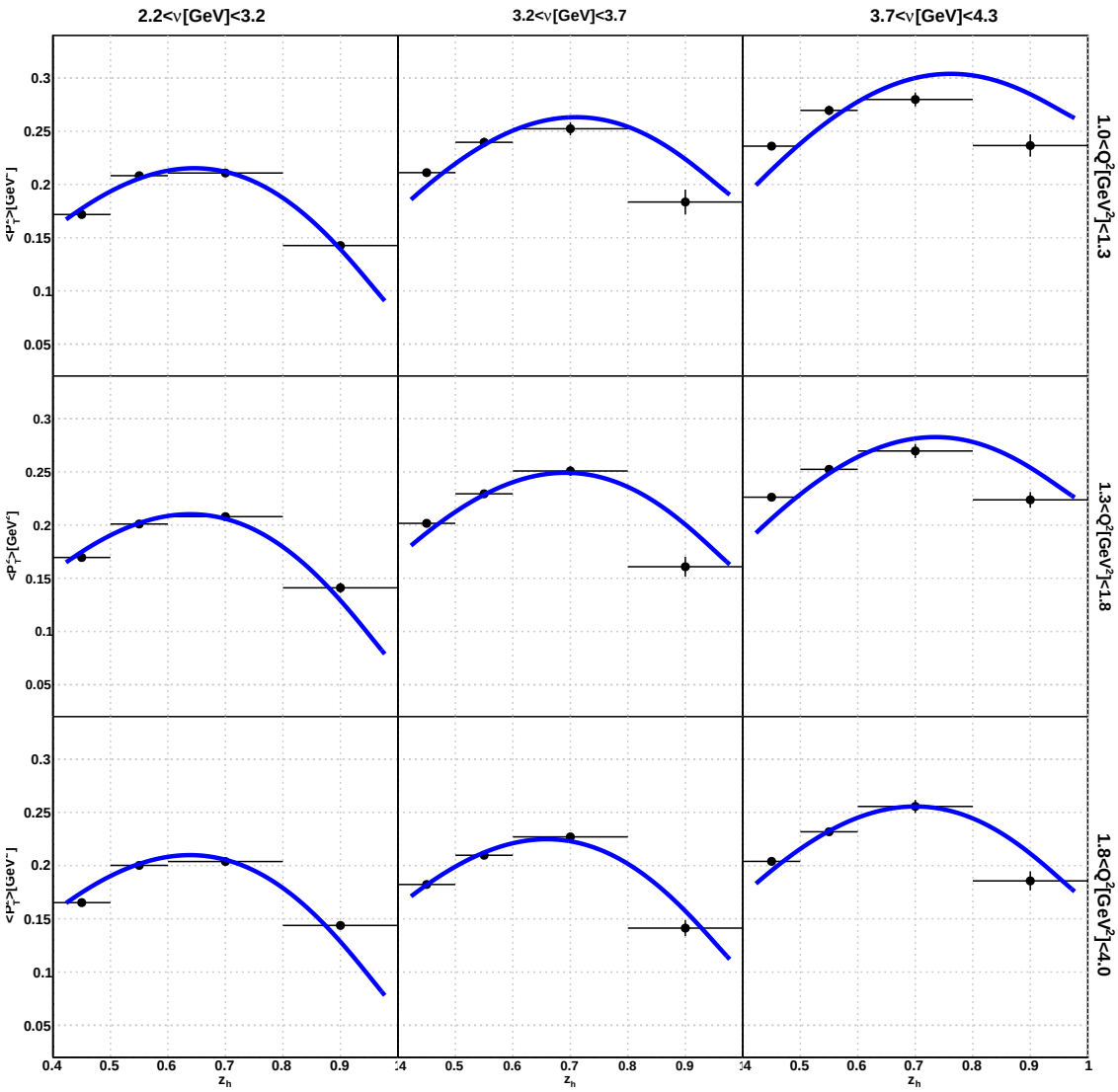

Figure B.69: Fits to Deuterium (Pb) results with $x_f > 0$ cut applied.

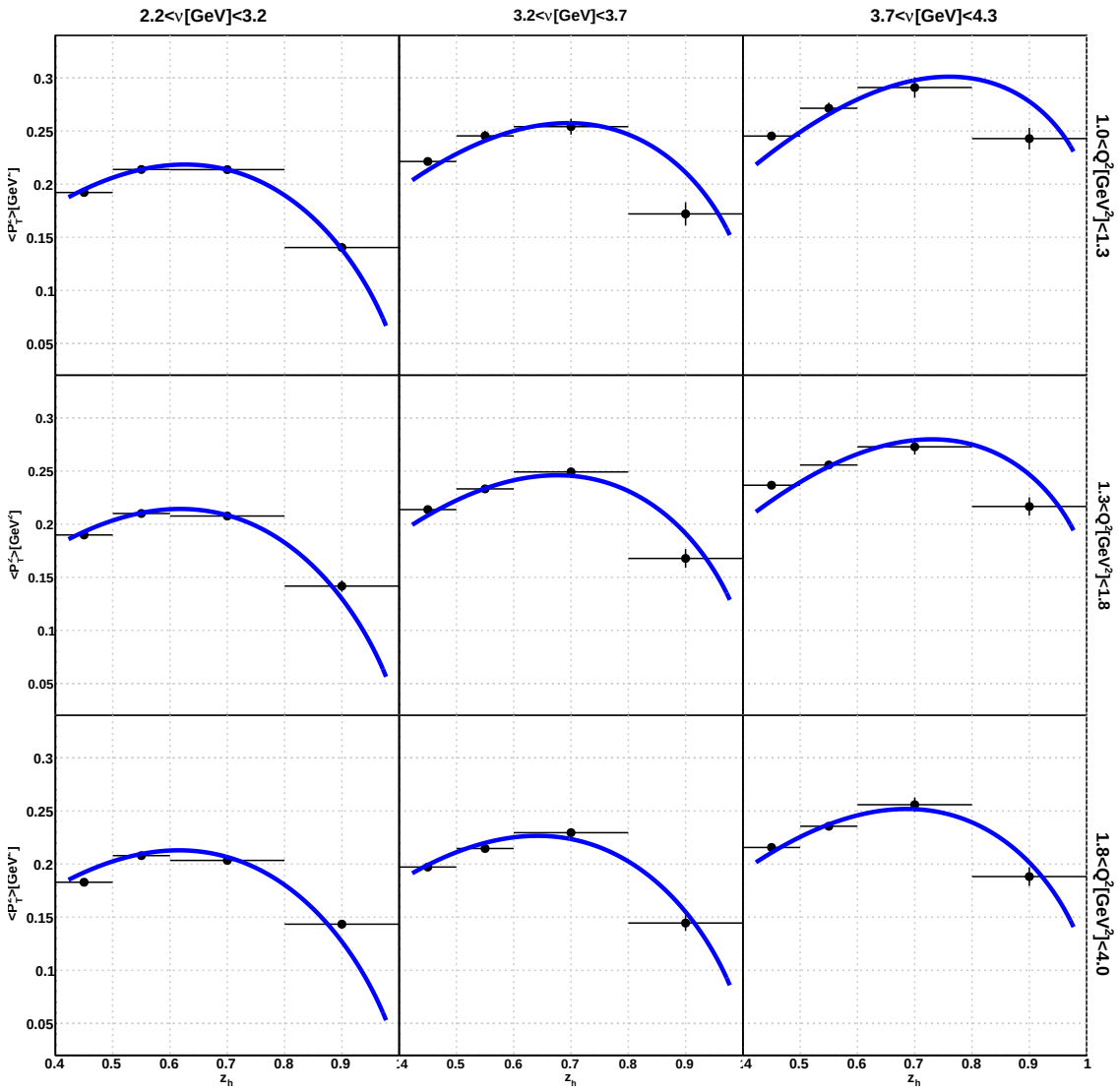

Figure B.70: Fits to Deuterium (C) results with $x_f > 0$ cut not applied.

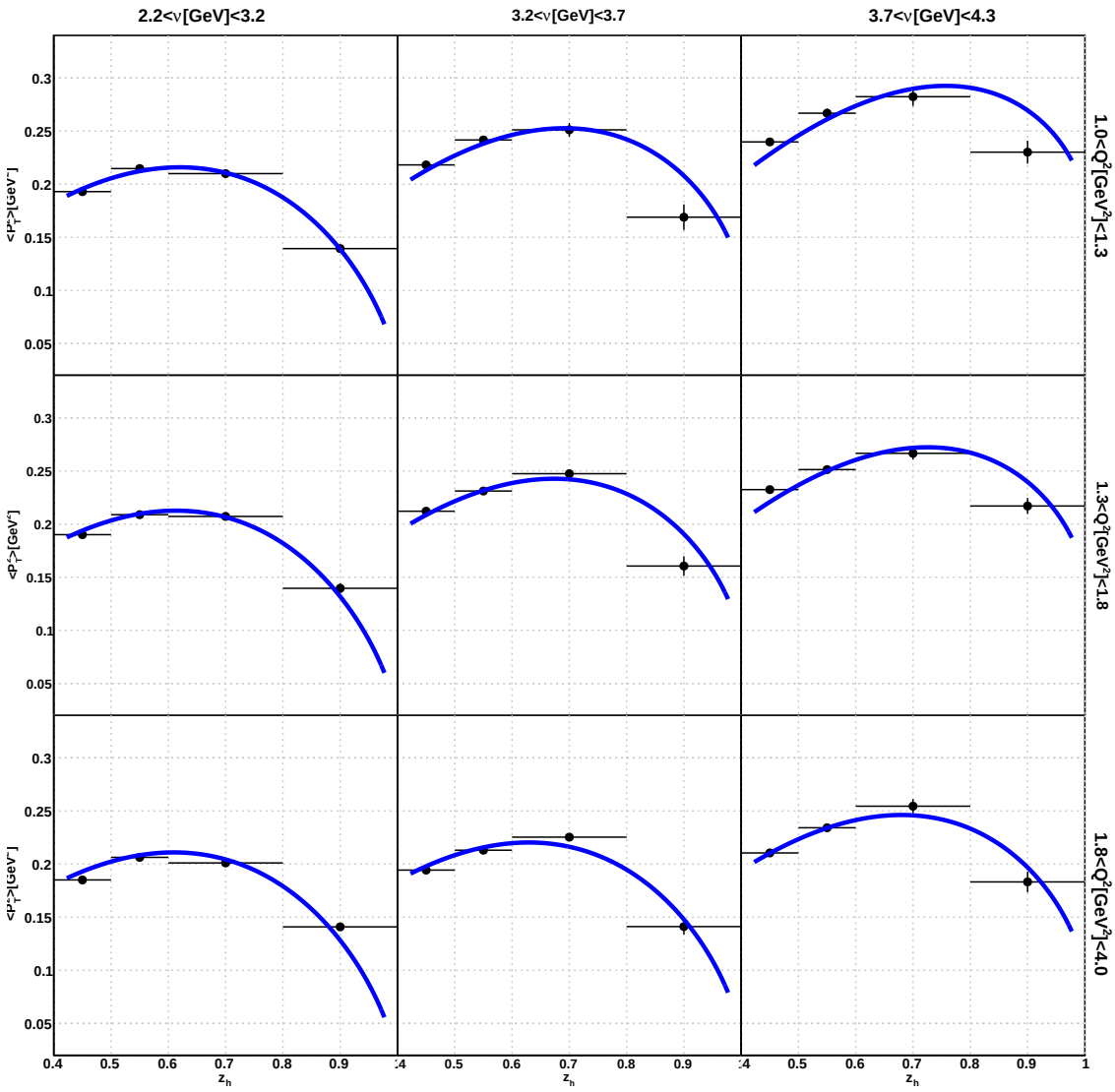

Figure B.71: Fits to Deuterium (Fe) results with $x_f > 0$ cut not applied.

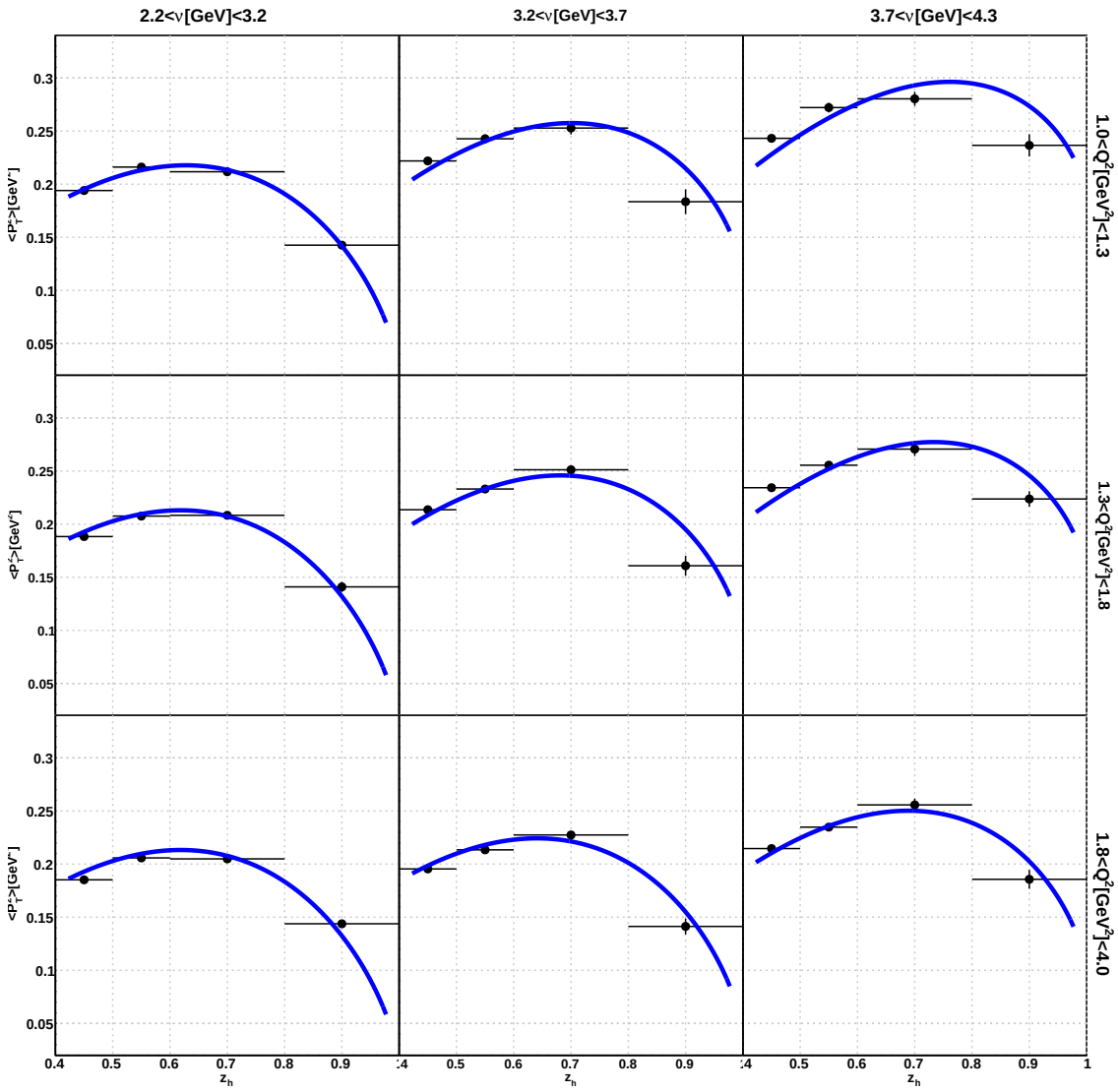

Figure B.72: Fits to Deuterium (Pb) results with $x_f > 0$ cut not applied.

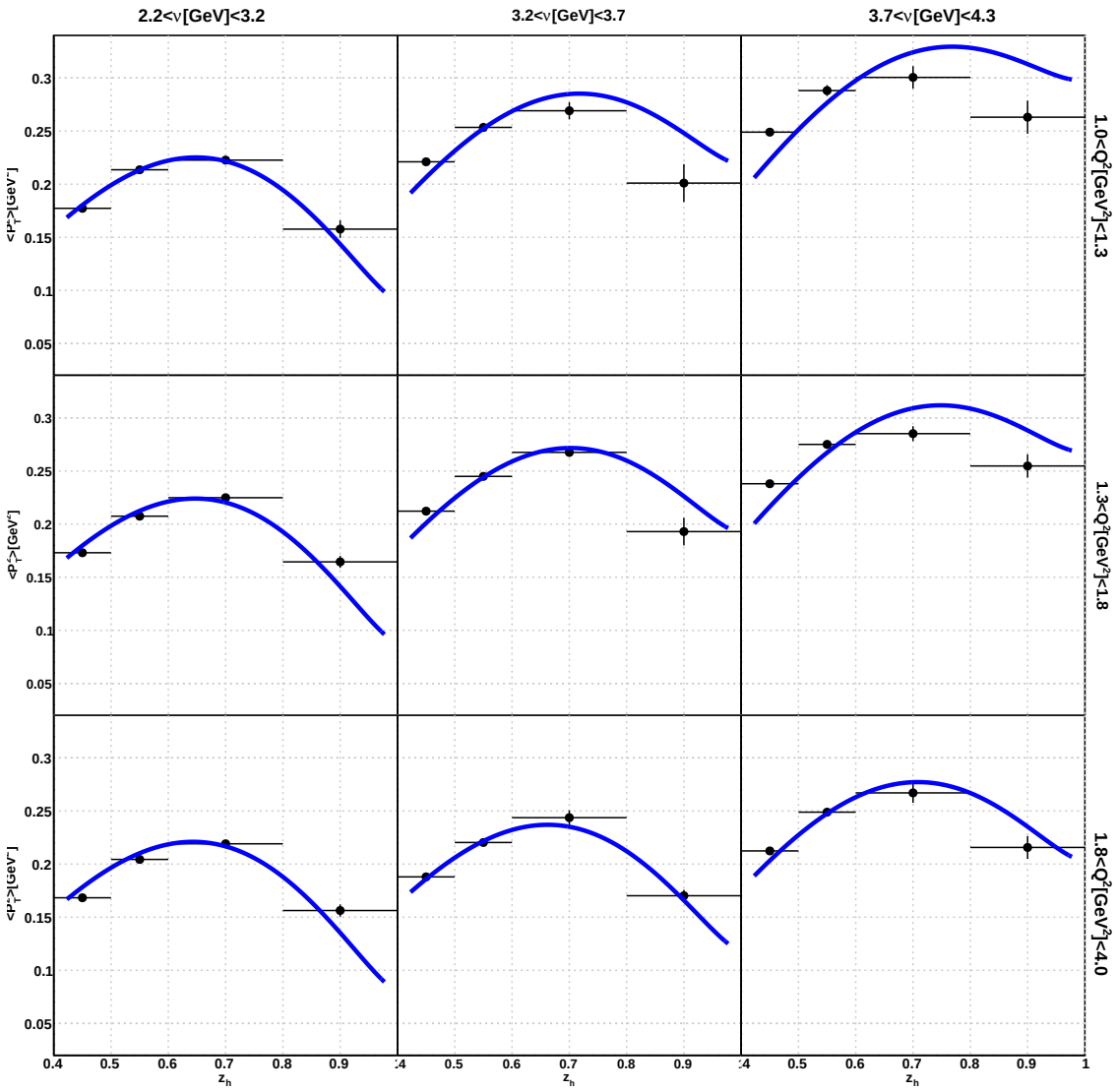

Figure B.73: Fits to C results with $x_f > 0$ cut applied.

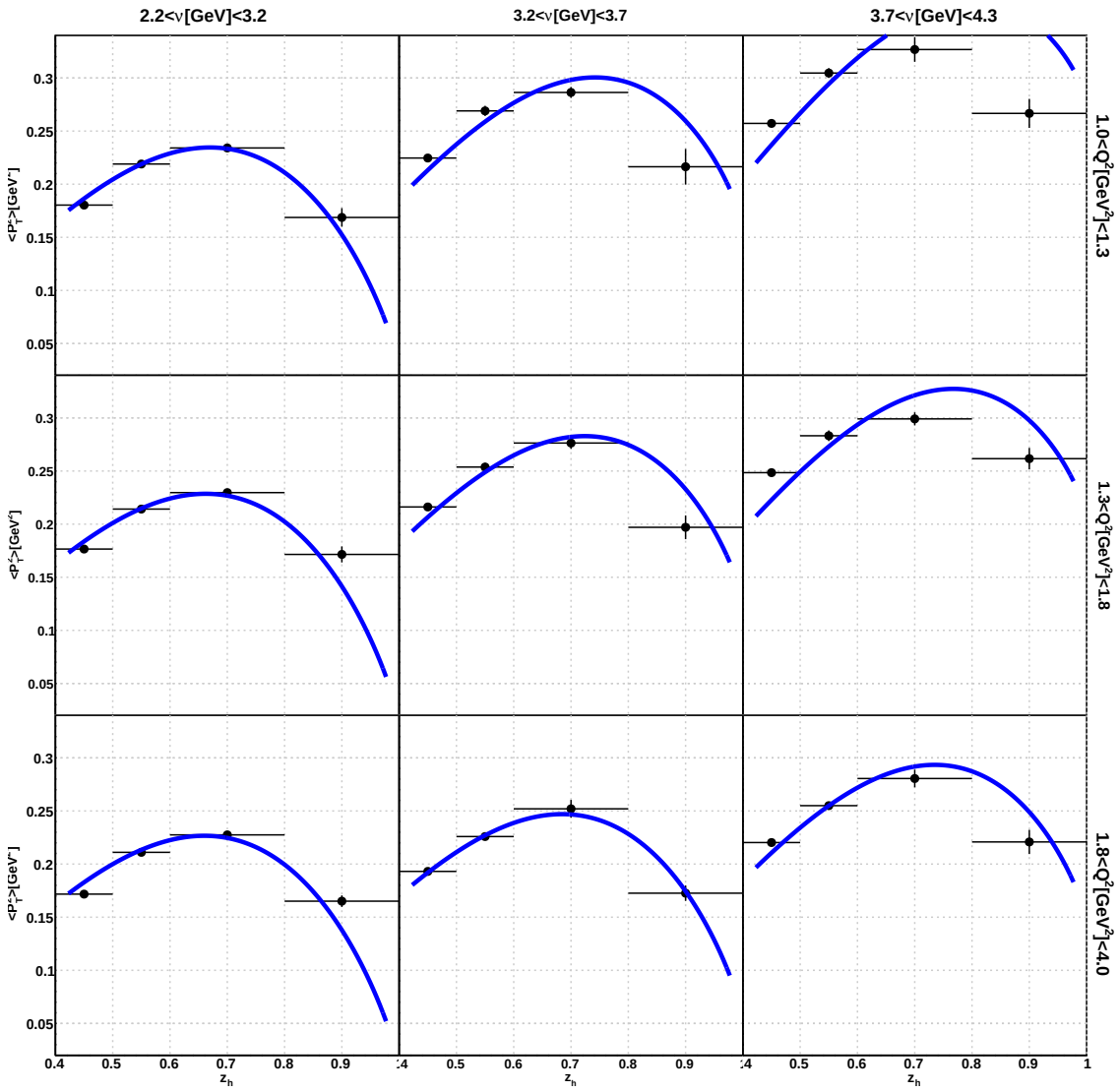

Figure B.74: Fits to Fe results with $x_f > 0$ cut applied.

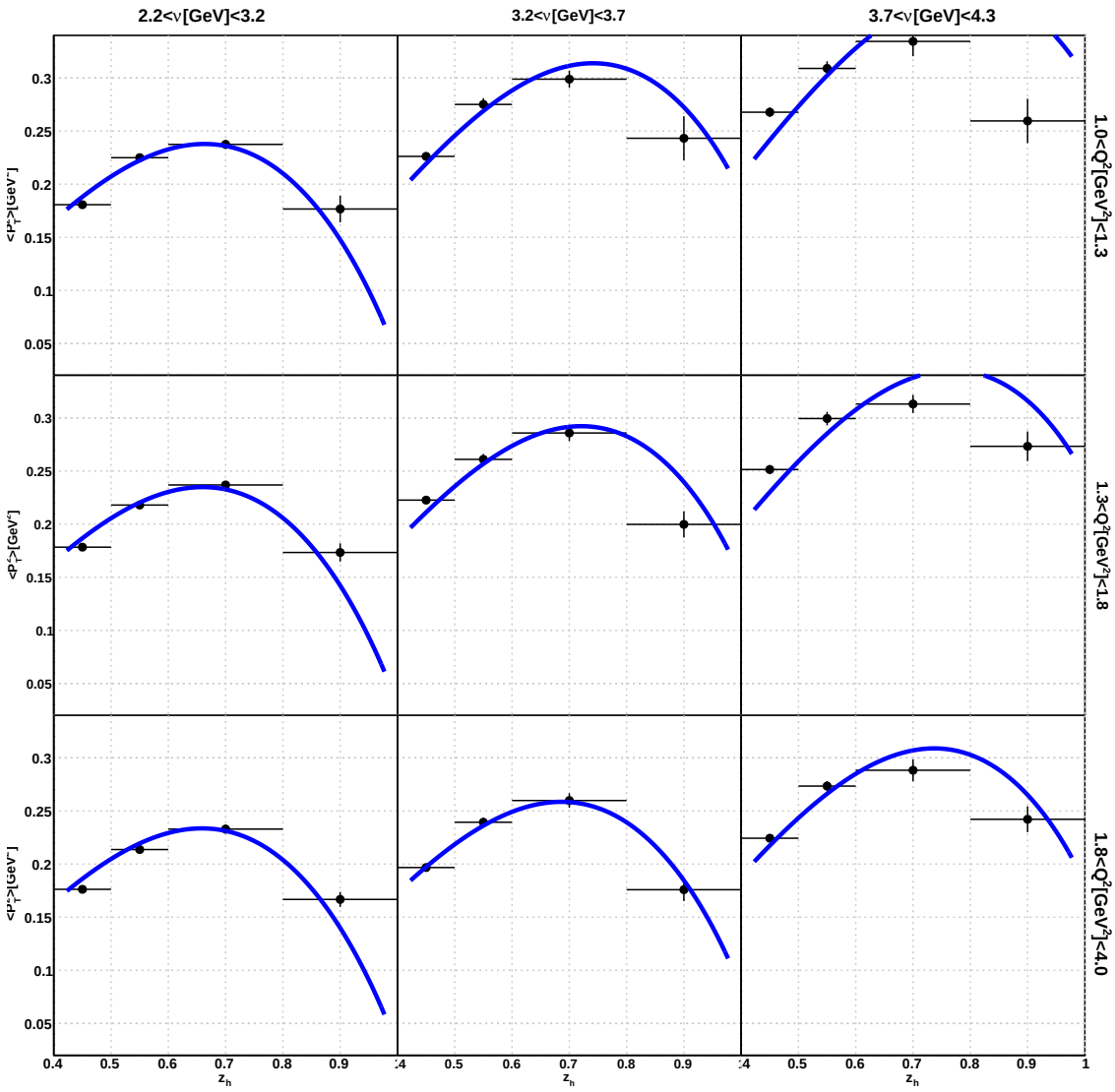

Figure B.75: Fits to Pb results with $x_f > 0$ cut applied.

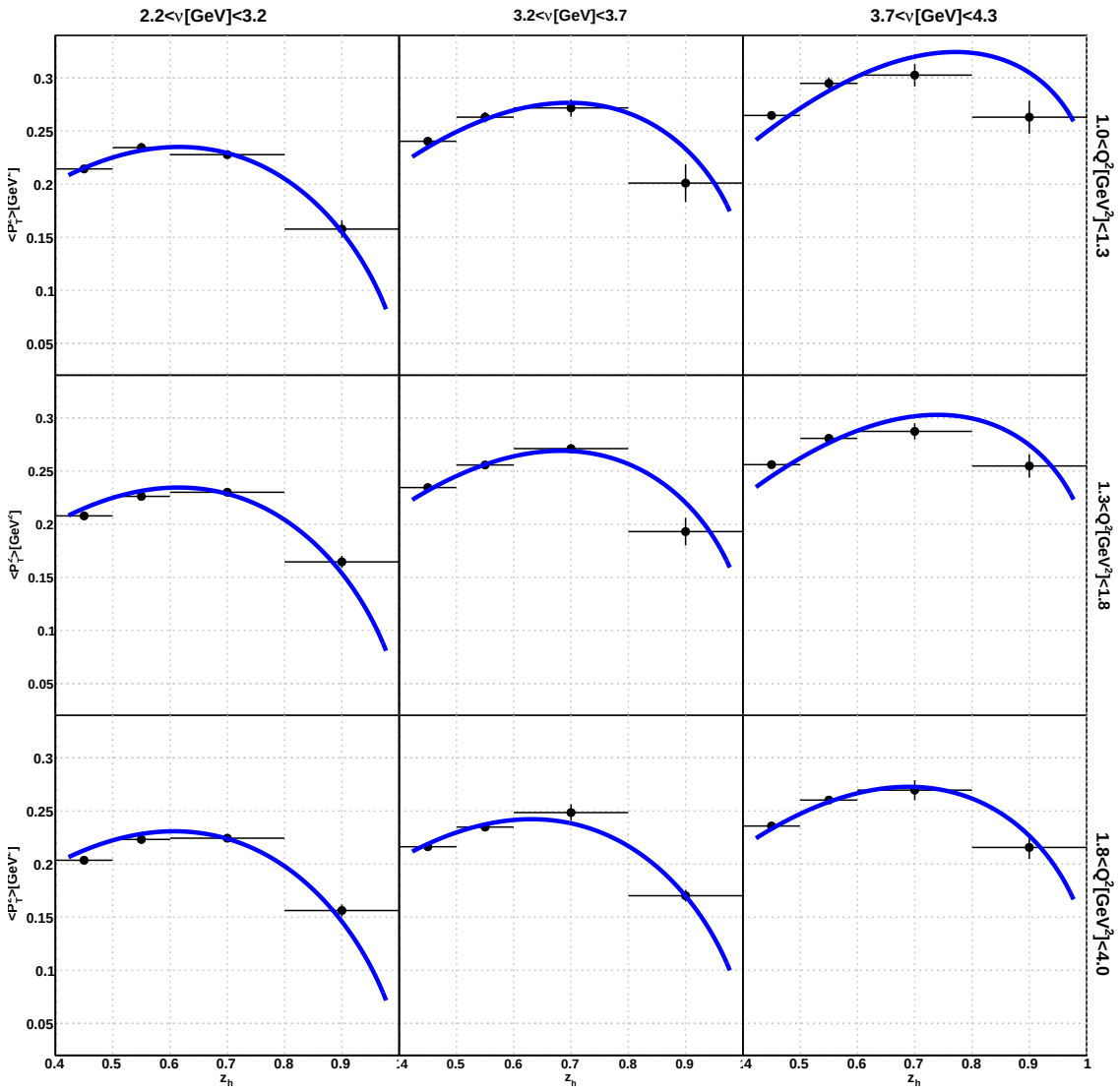

Figure B.76: Fits to C results with $x_f > 0$ cut not applied.

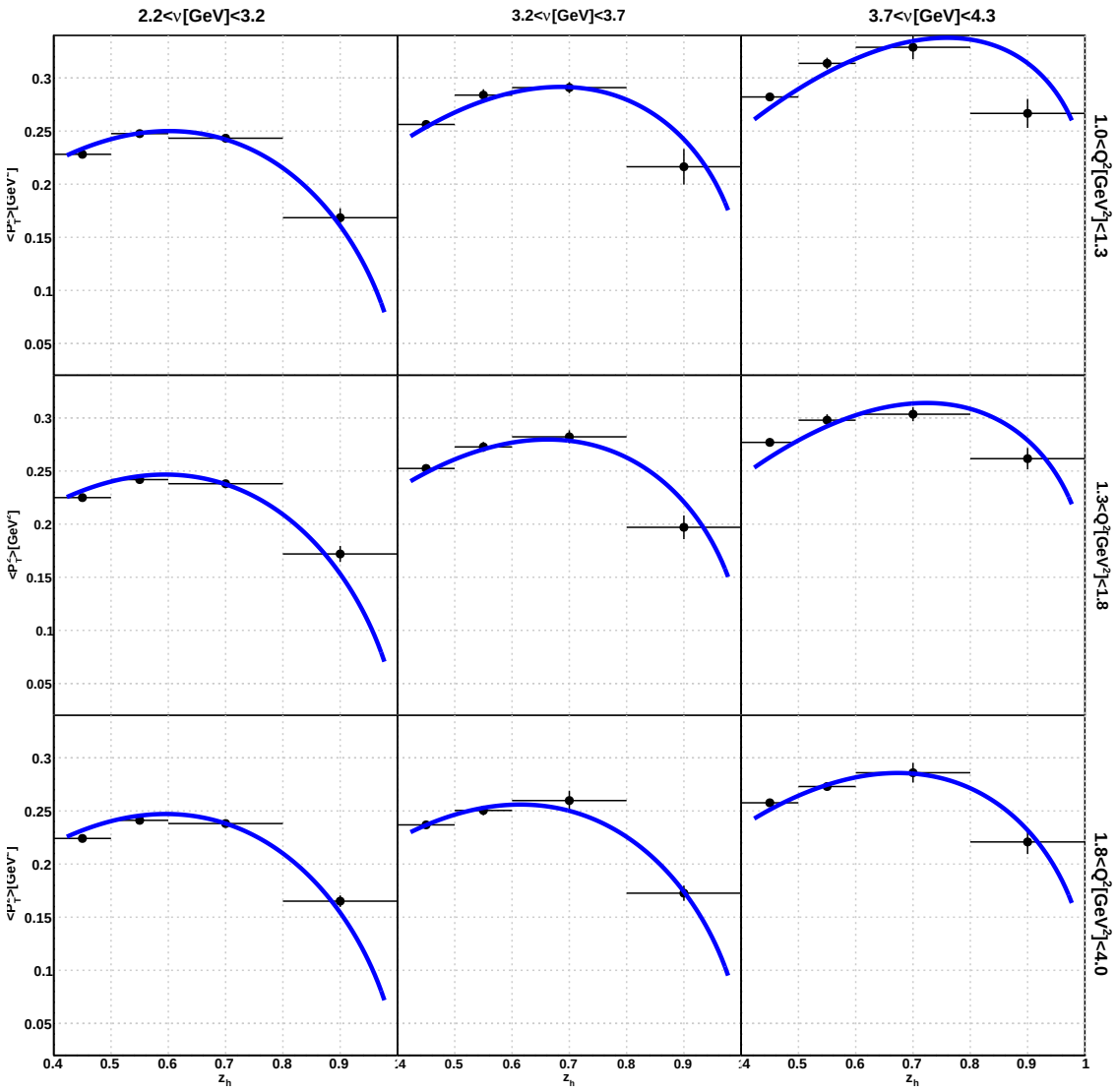

Figure B.77: Fits to Fe results with $x_f > 0$ cut not applied.

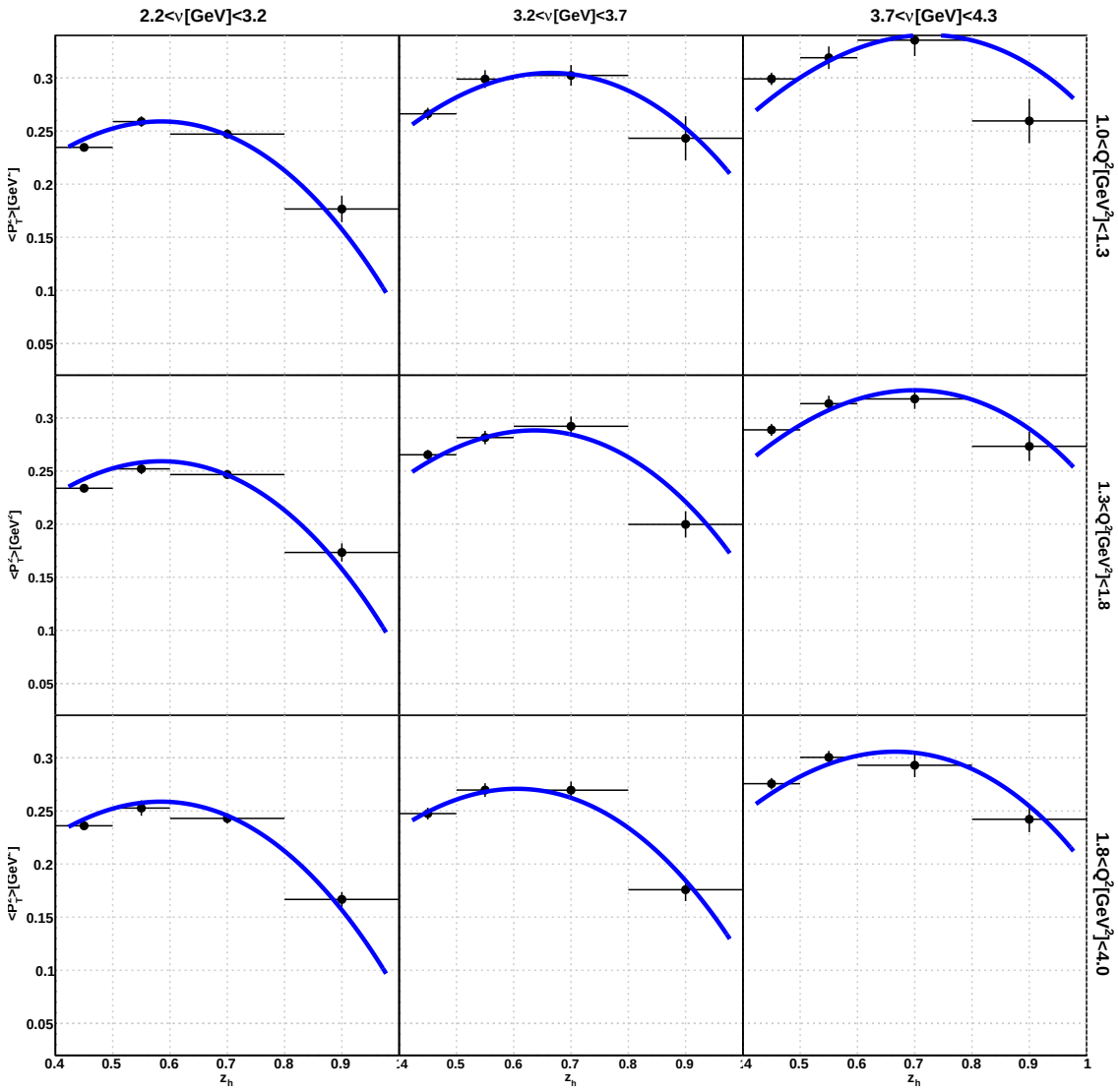

Figure B.78: Fits to Pb results with $x_f > 0$ cut not applied.

B.4.2 Fit With Analytic Function (Hypothesis 2)

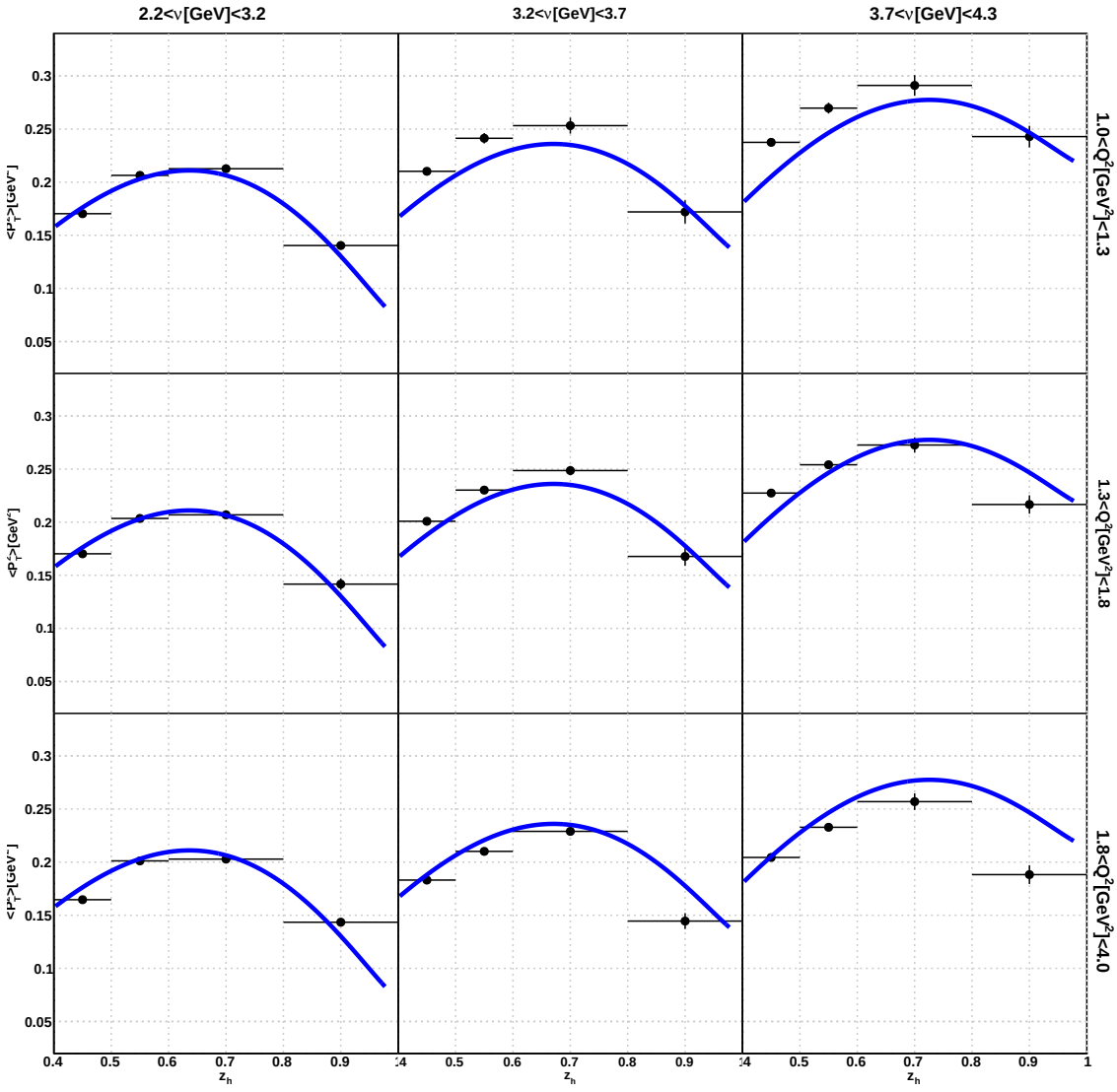

Figure B.79: Fits to Deuterium (C) results with $x_f > 0$ cut applied.

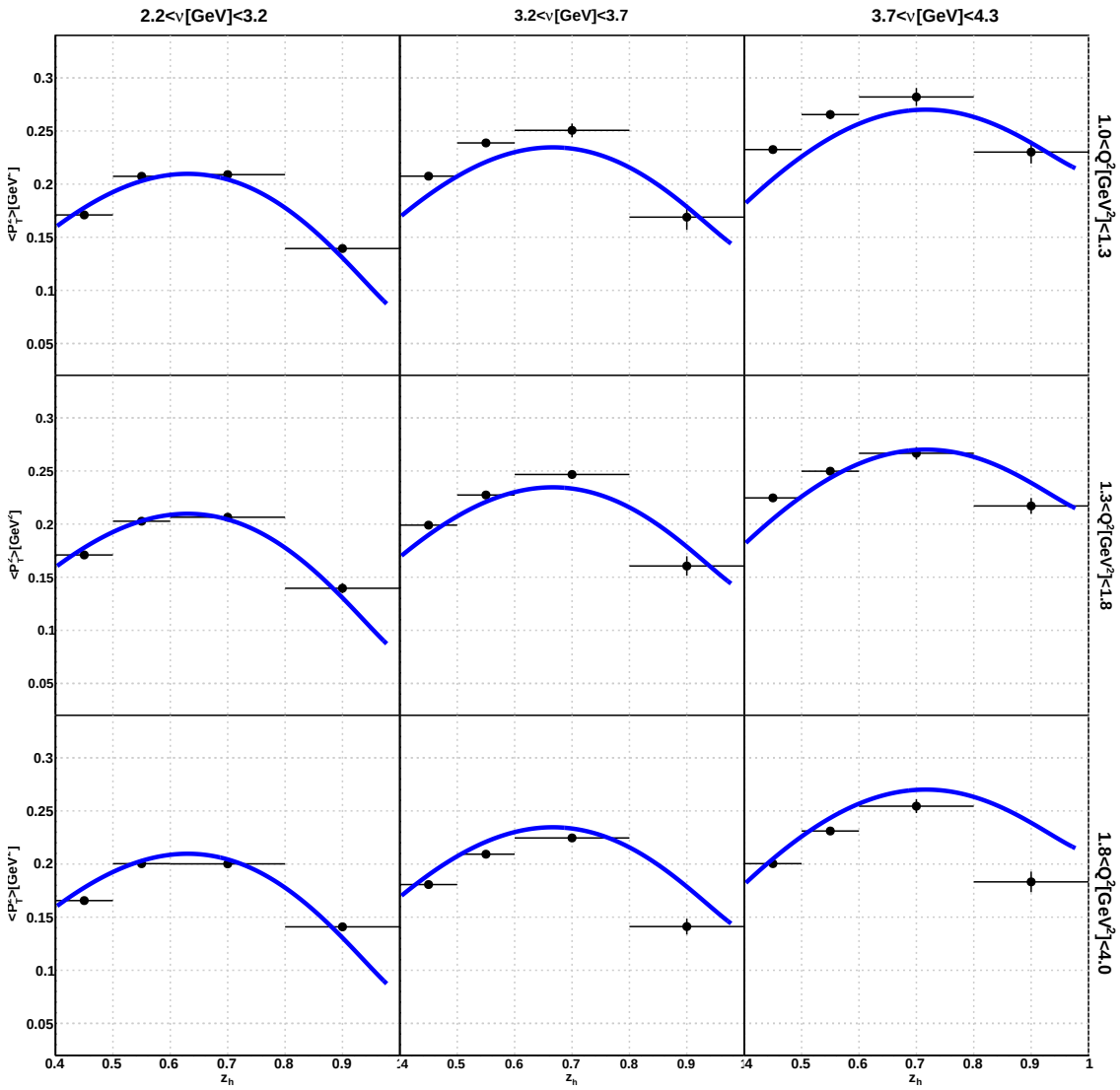

Figure B.80: Fits to Deuterium (Fe) results with $x_f > 0$ cut applied.

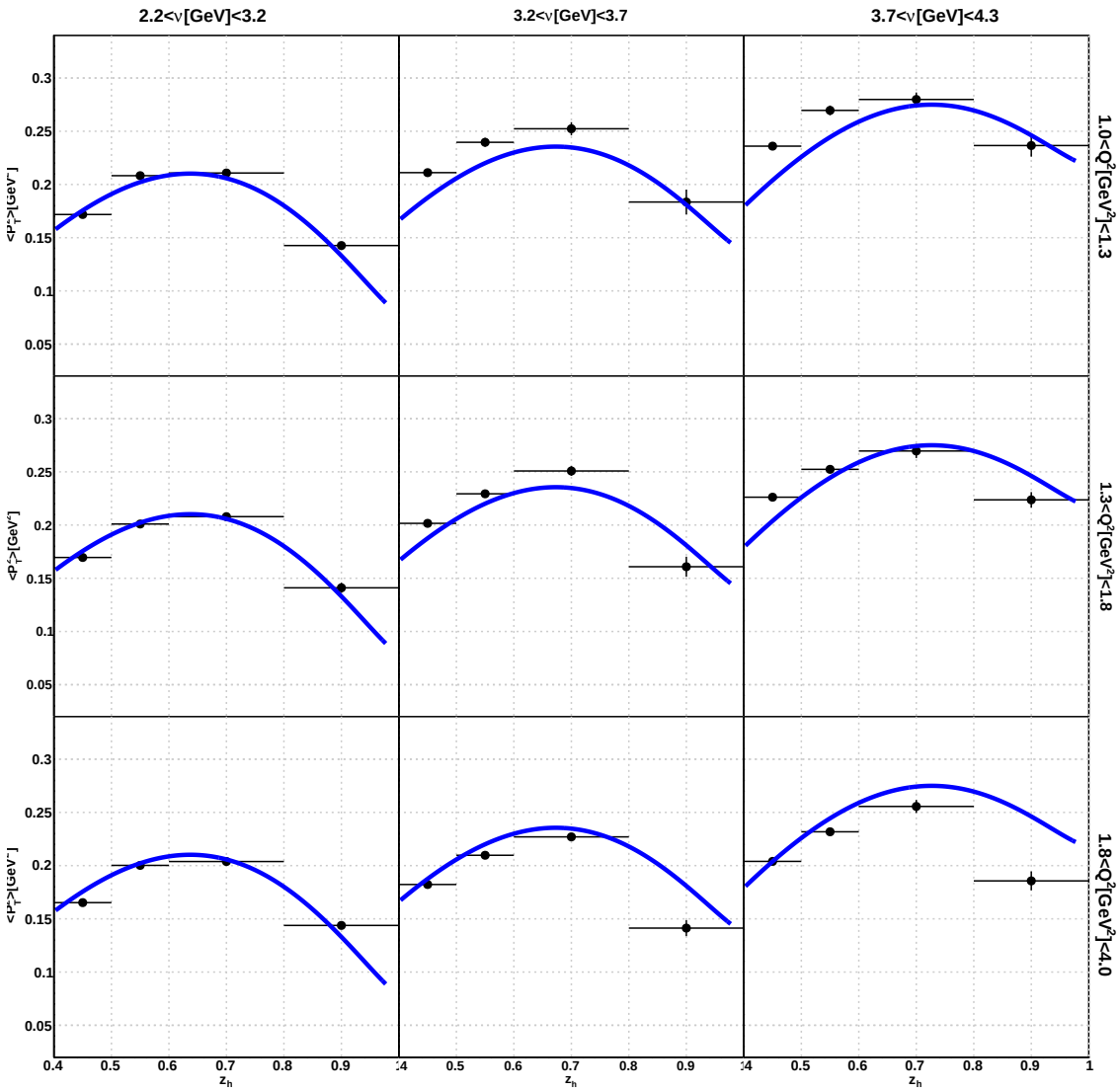

Figure B.81: Fits to Deuterium (Pb) results with $x_f > 0$ cut applied.

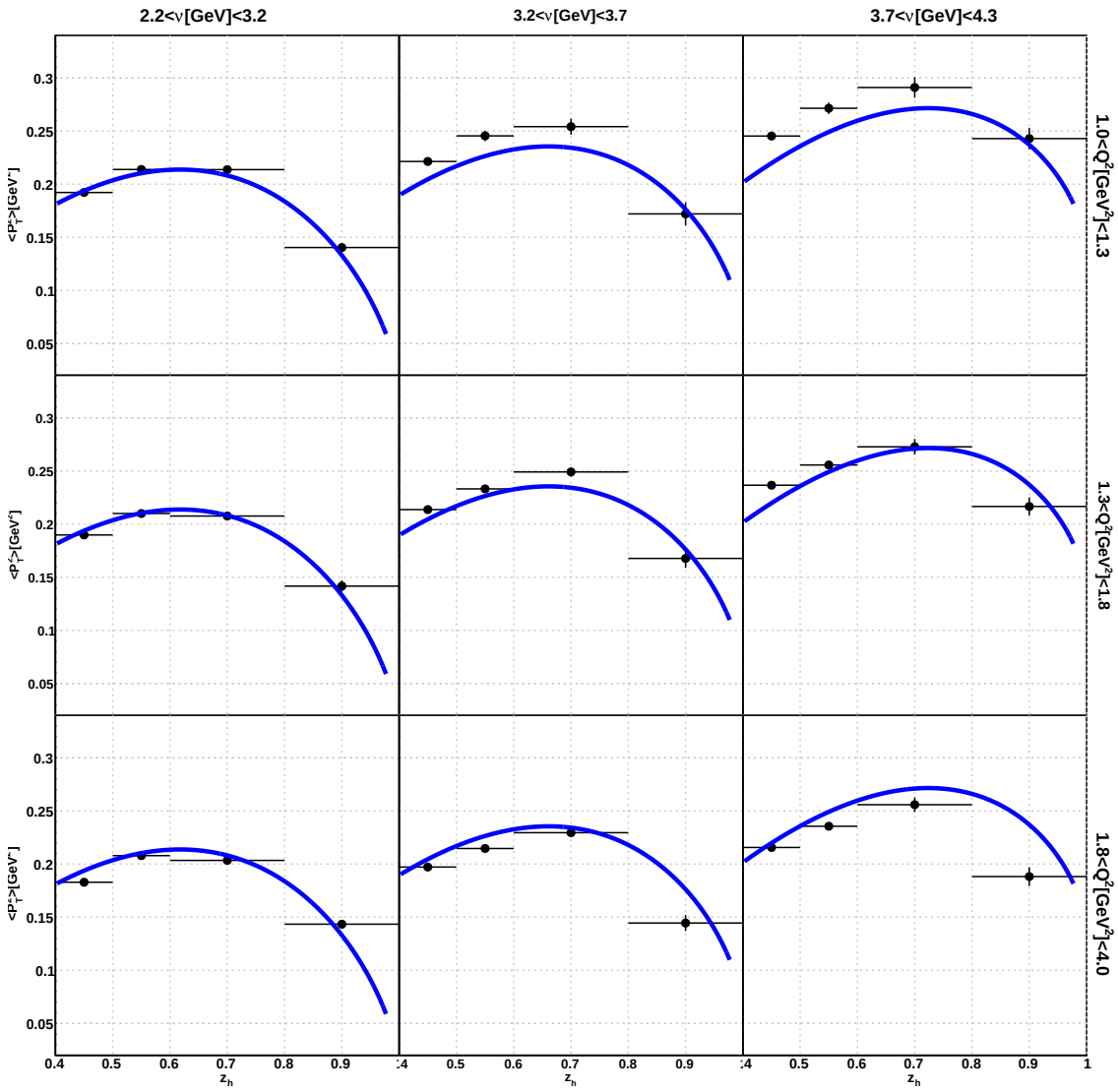

Figure B.82: Fits to Deuterium (C) results with $x_f > 0$ cut not applied.

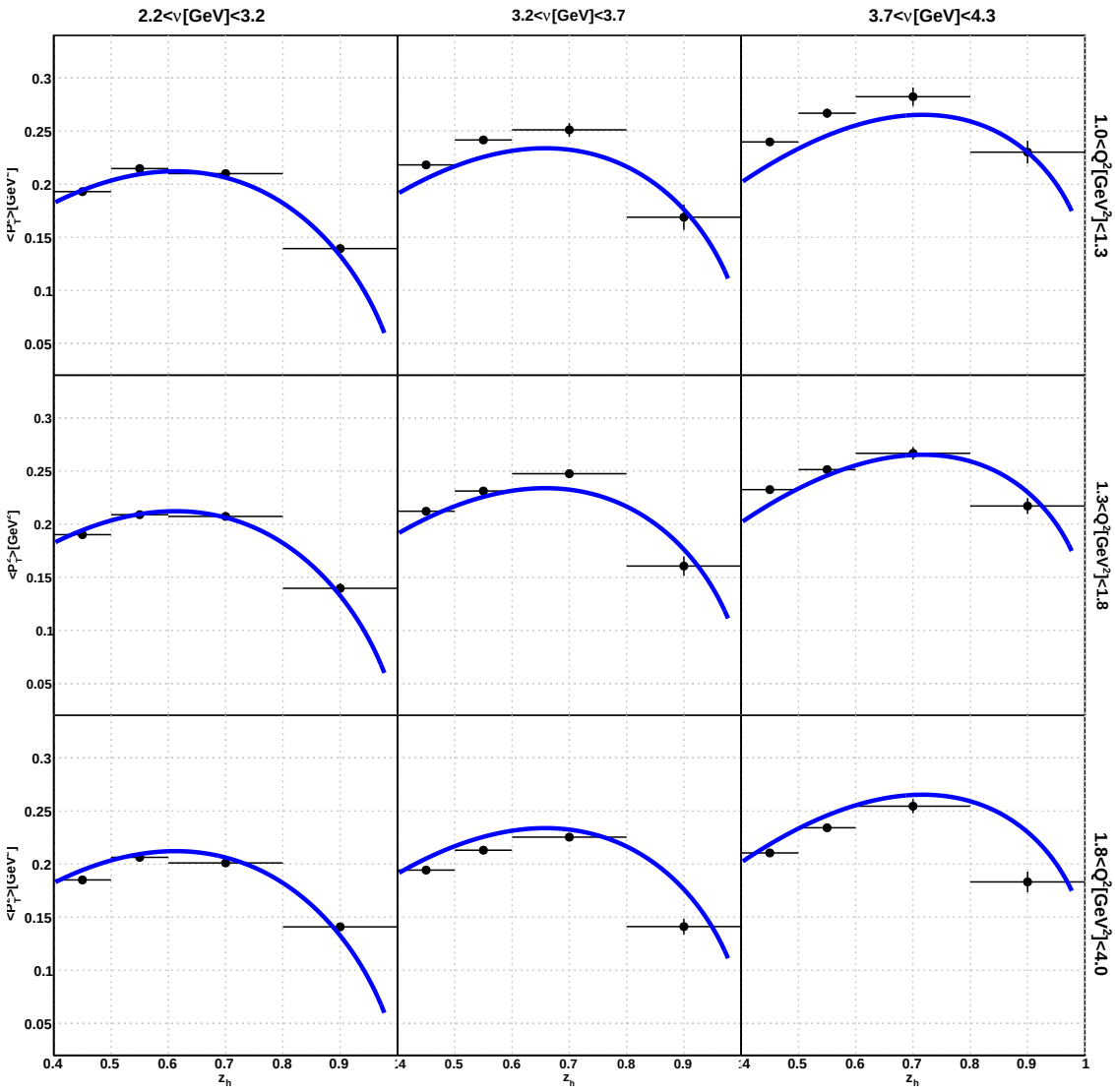

Figure B.83: Fits to Deuterium (Fe) results with $x_f > 0$ cut not applied.

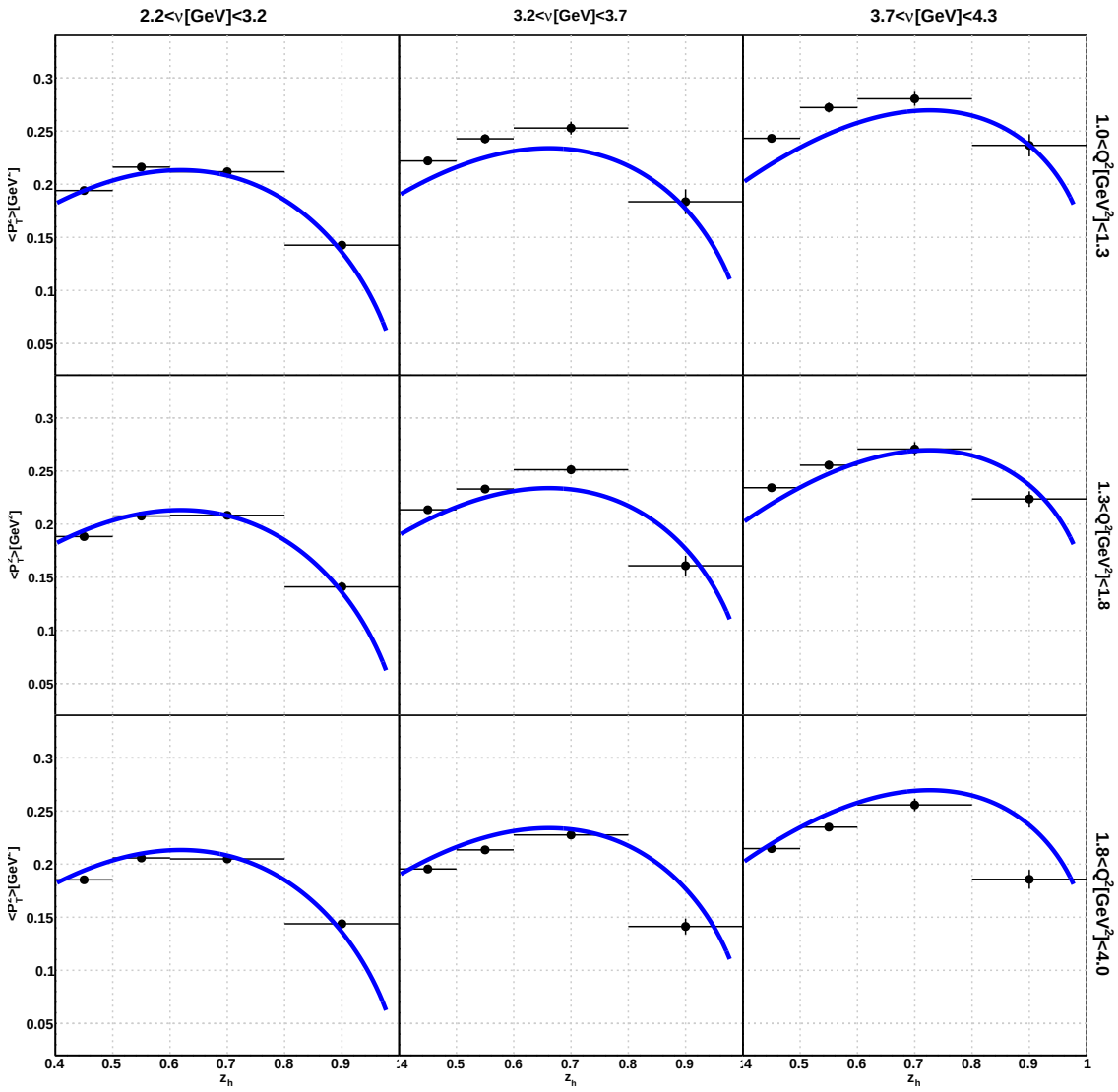

Figure B.84: Fits to Deuterium (Pb) results with $x_f > 0$ cut not applied.

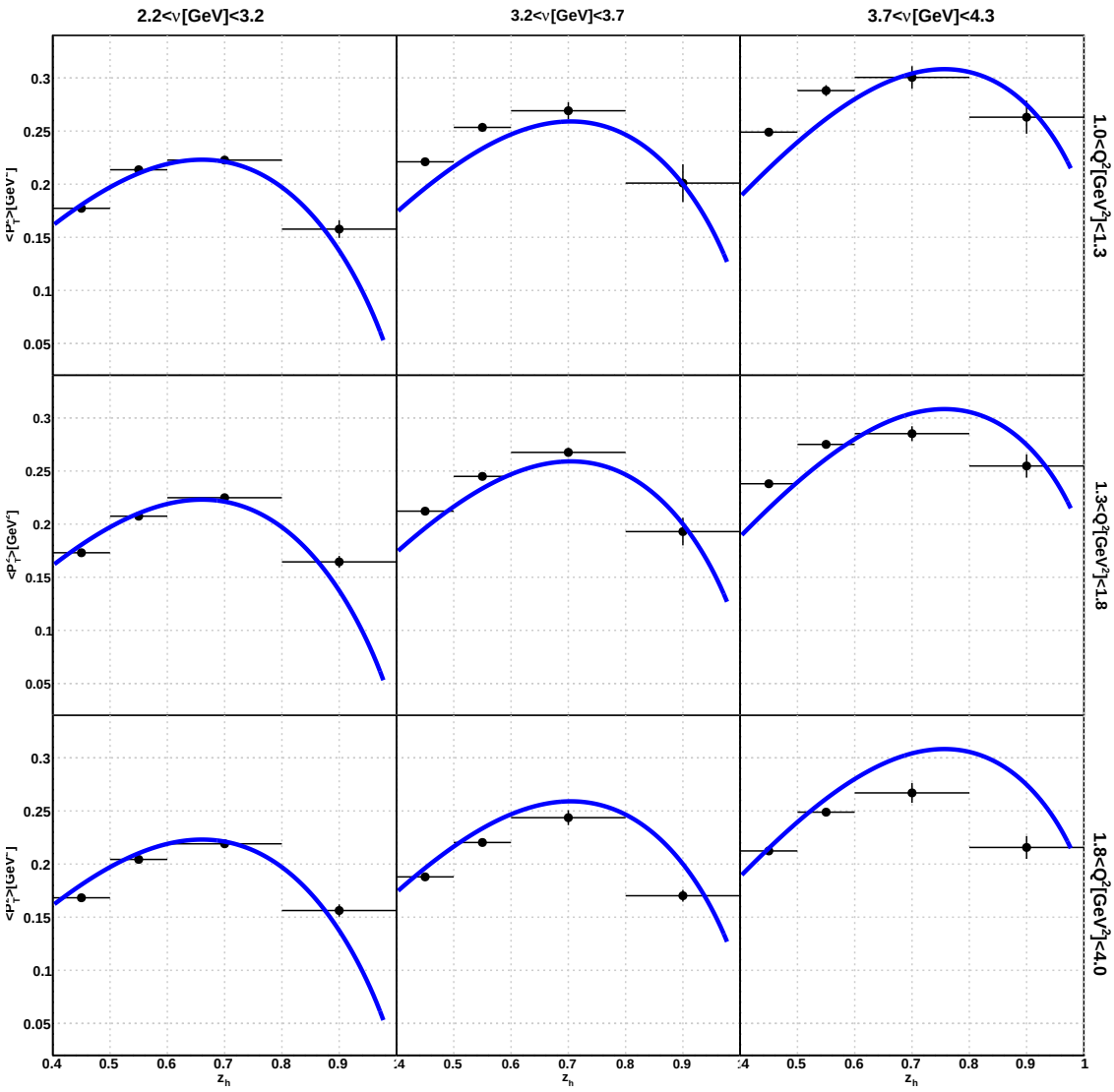

Figure B.85: Fits to C results with $x_f > 0$ cut applied.

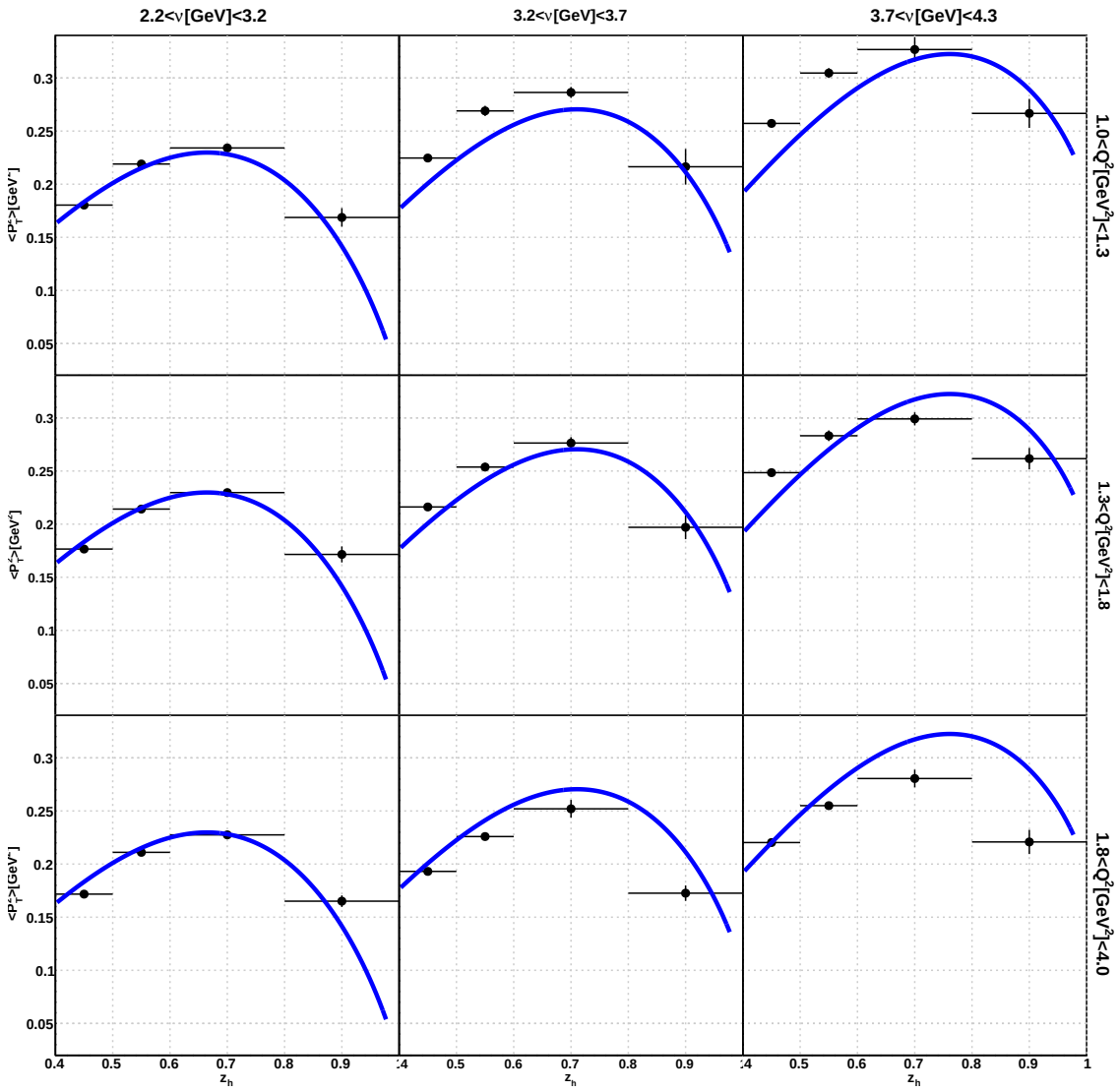

Figure B.86: Fits to Fe results with $x_f > 0$ cut applied.

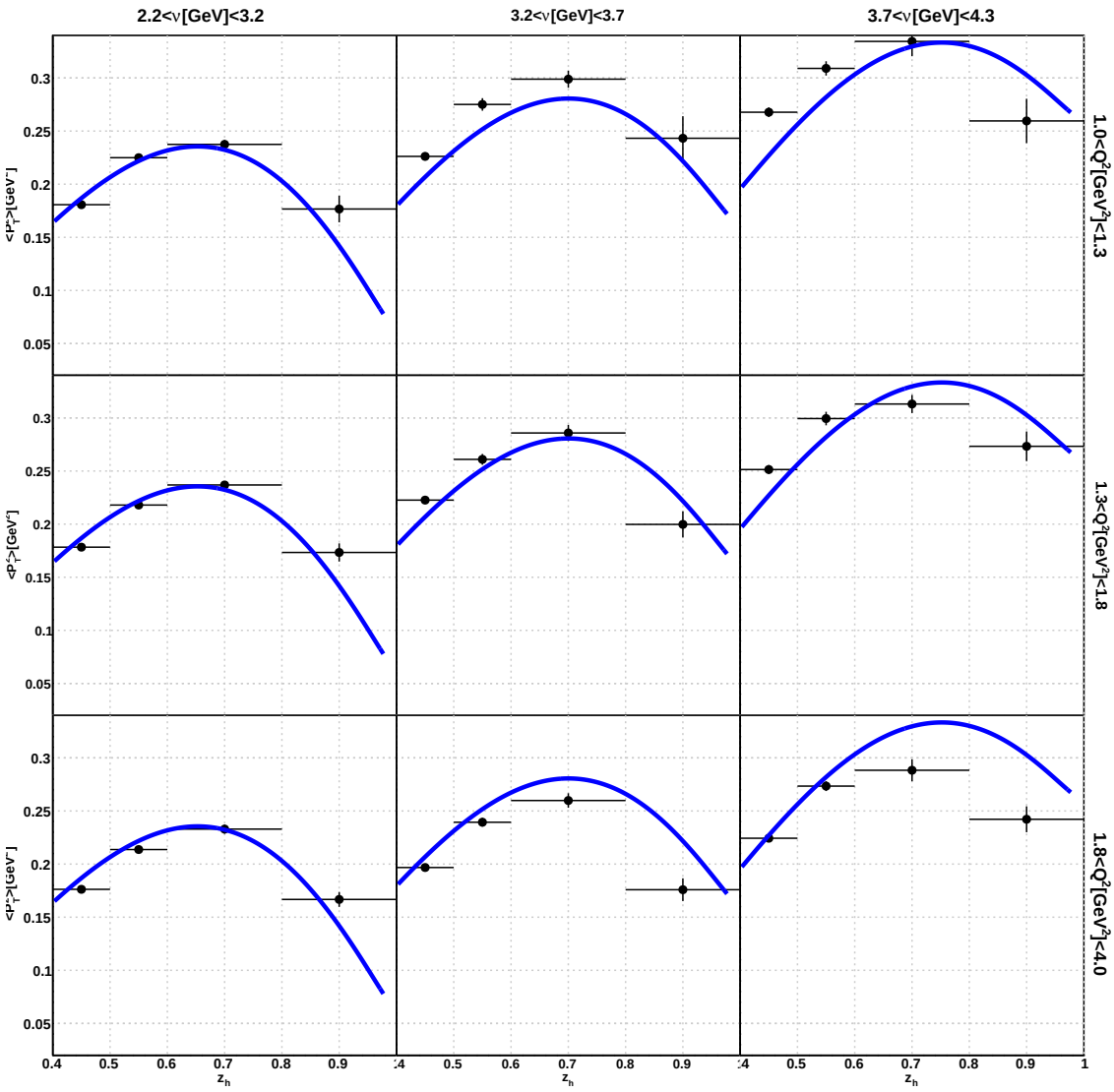

Figure B.87: Fits to Pb results with $x_f > 0$ cut applied.

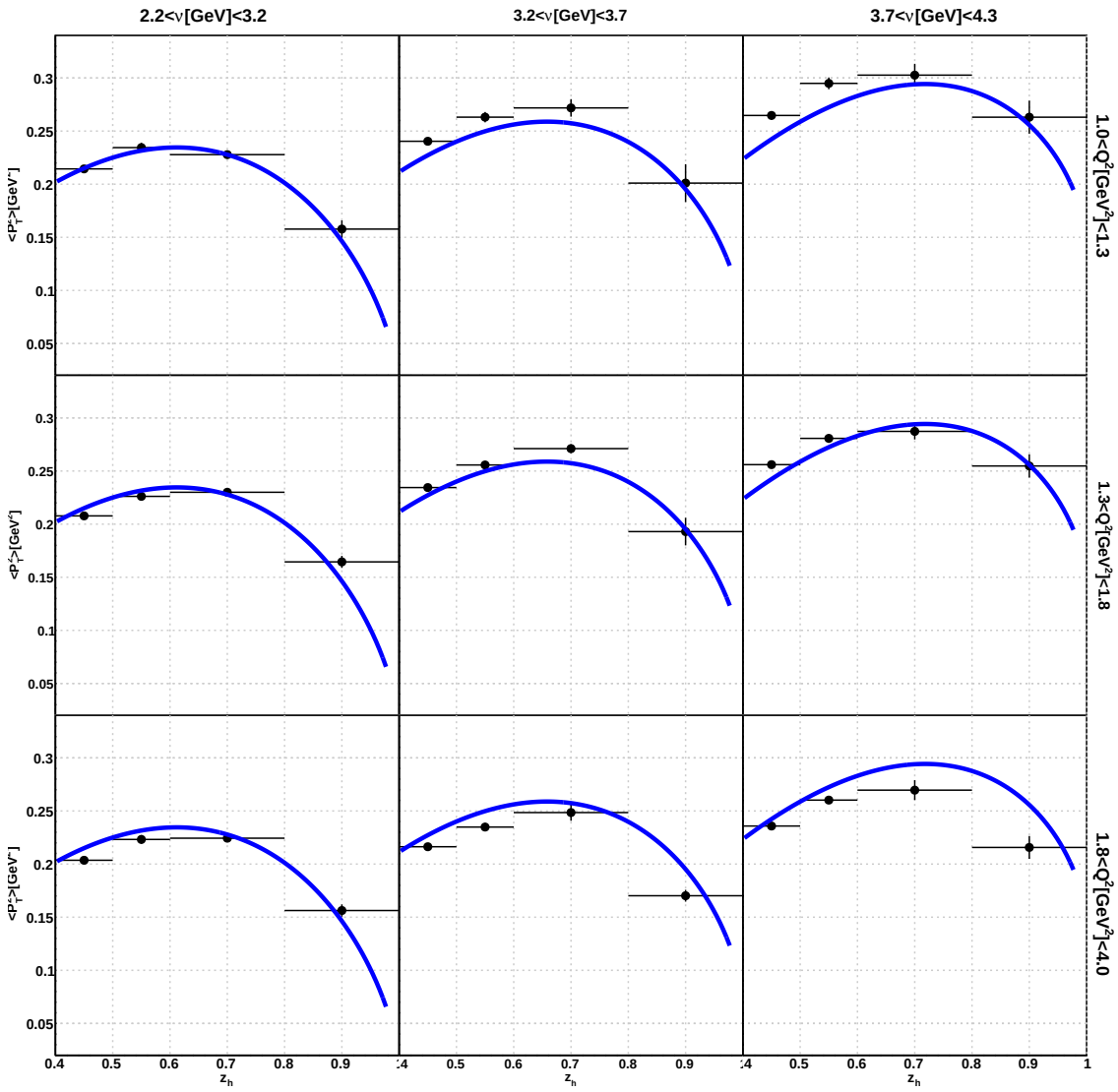

Figure B.88: Fits to C results with $x_f > 0$ cut not applied.

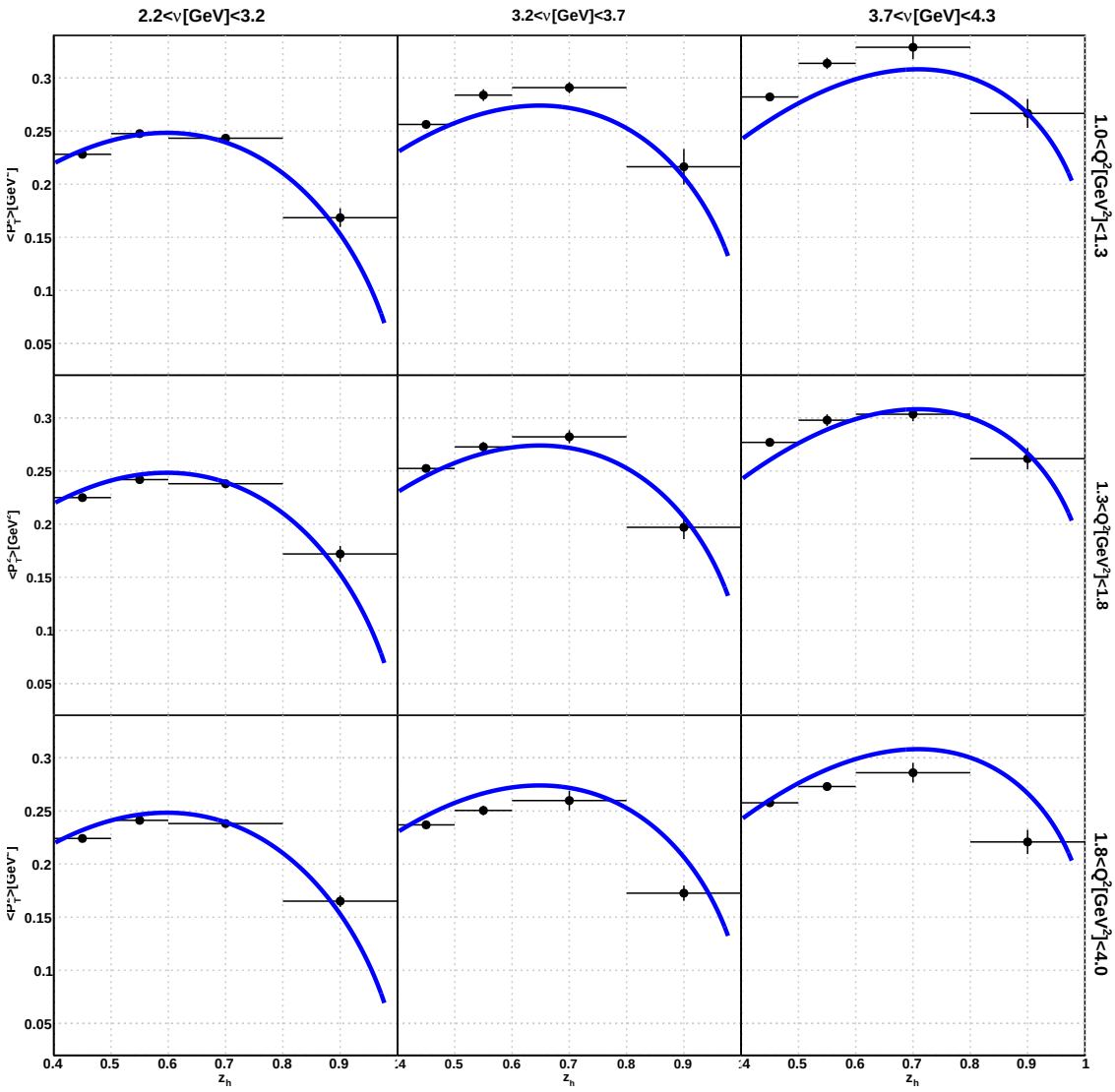

Figure B.89: Fits to Fe results with $x_f > 0$ cut not applied.

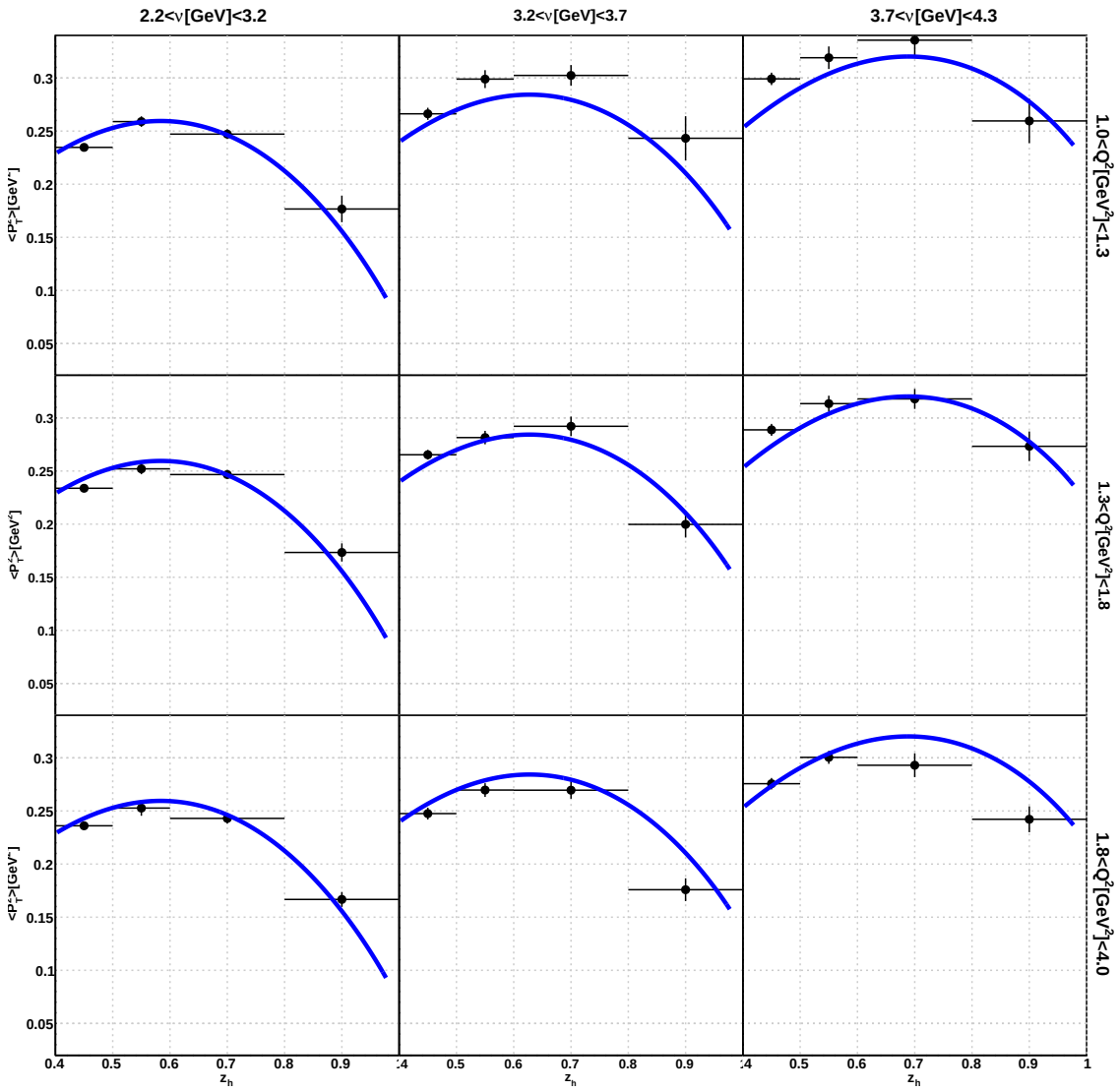

Figure B.90: Fits to Pb results with $x_f > 0$ cut not applied.

B.4.3 Fit With Integral Function (Hypothesis 1)

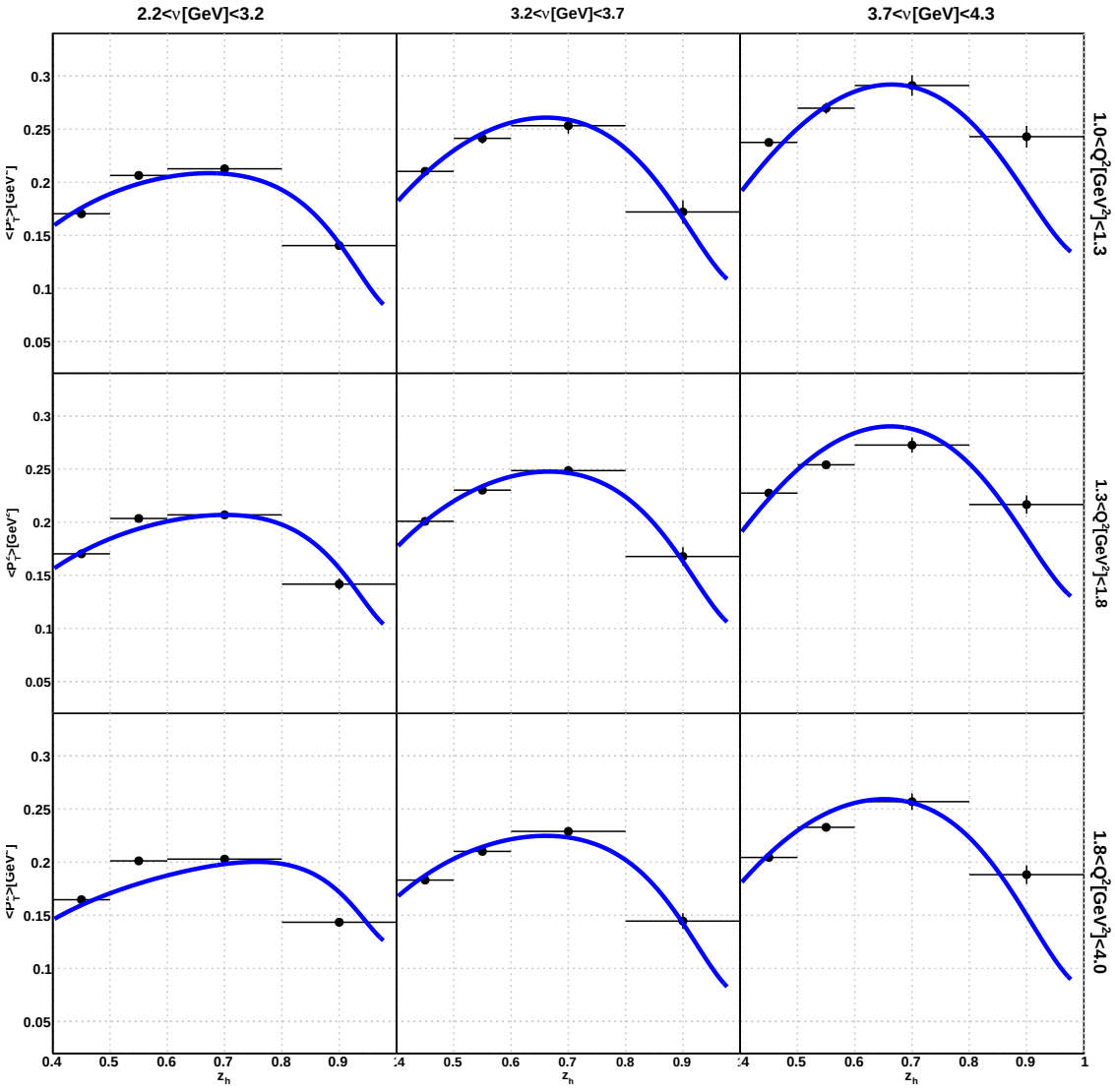

Figure B.91: Fits to Deuterium (C) results with $x_f > 0$ cut applied.

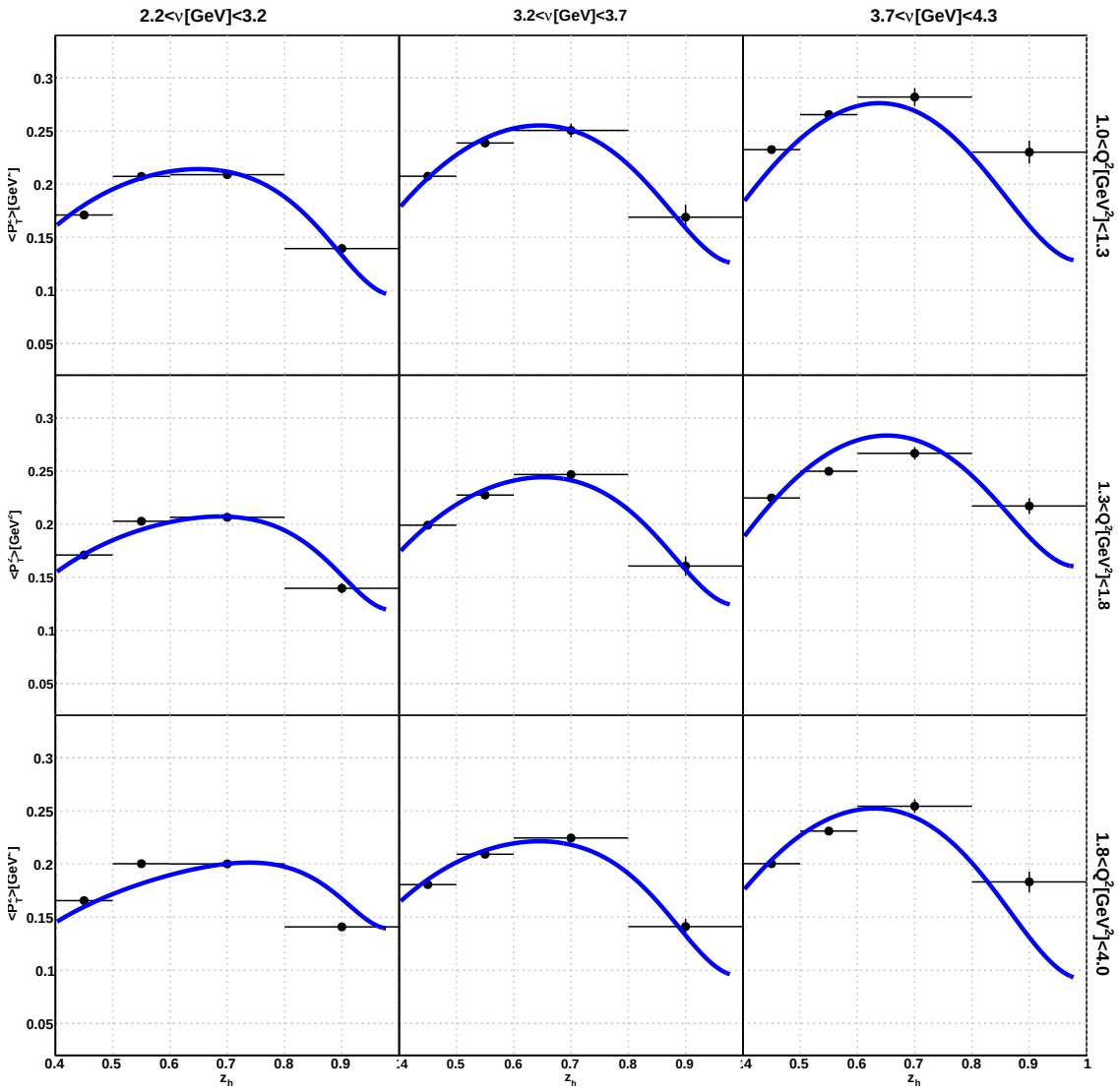

Figure B.92: Fits to Deuterium (Fe) results with $x_f > 0$ cut applied.

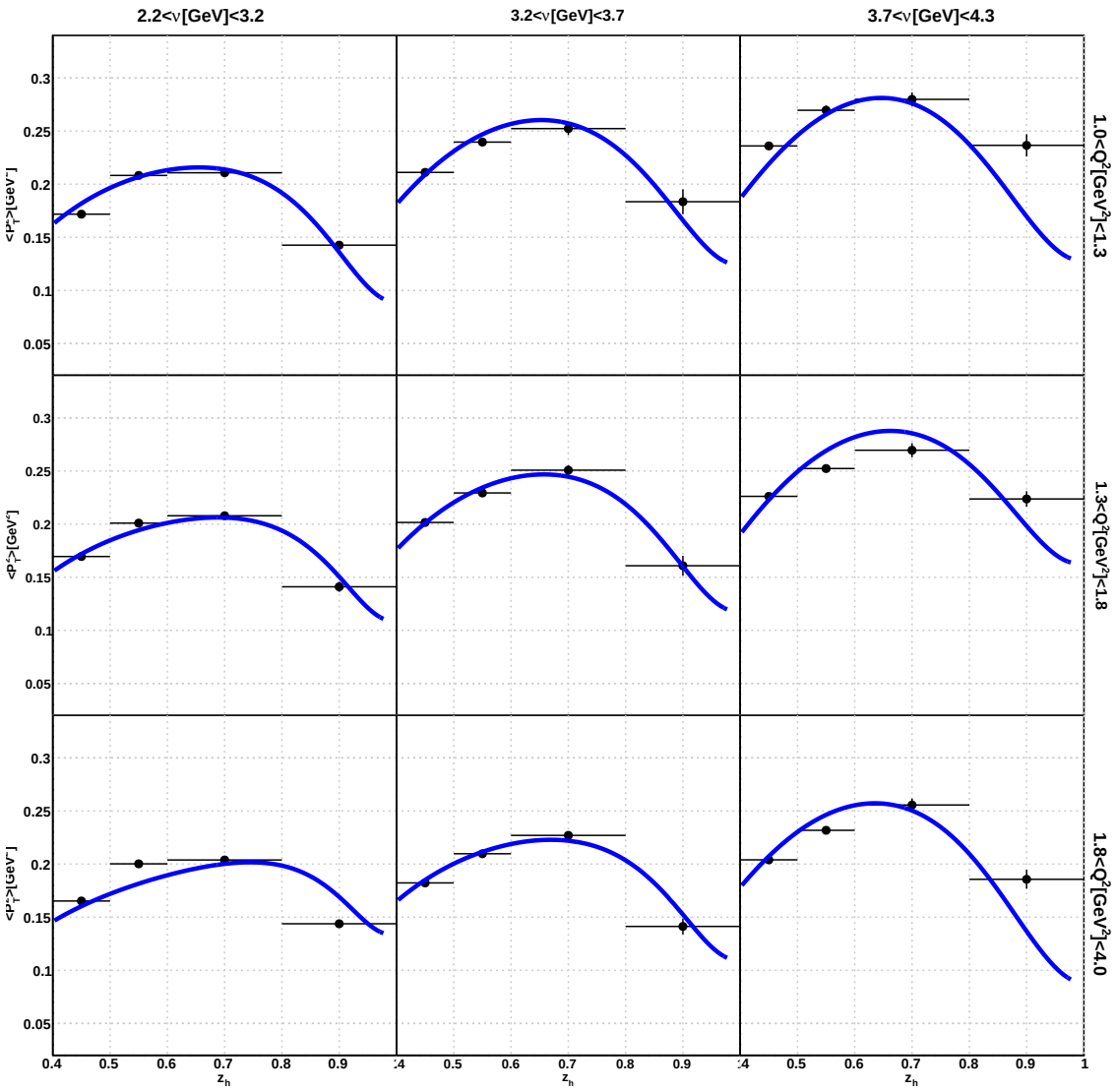

Figure B.93: Fits to Deuterium (Pb) results with $x_f > 0$ cut applied.

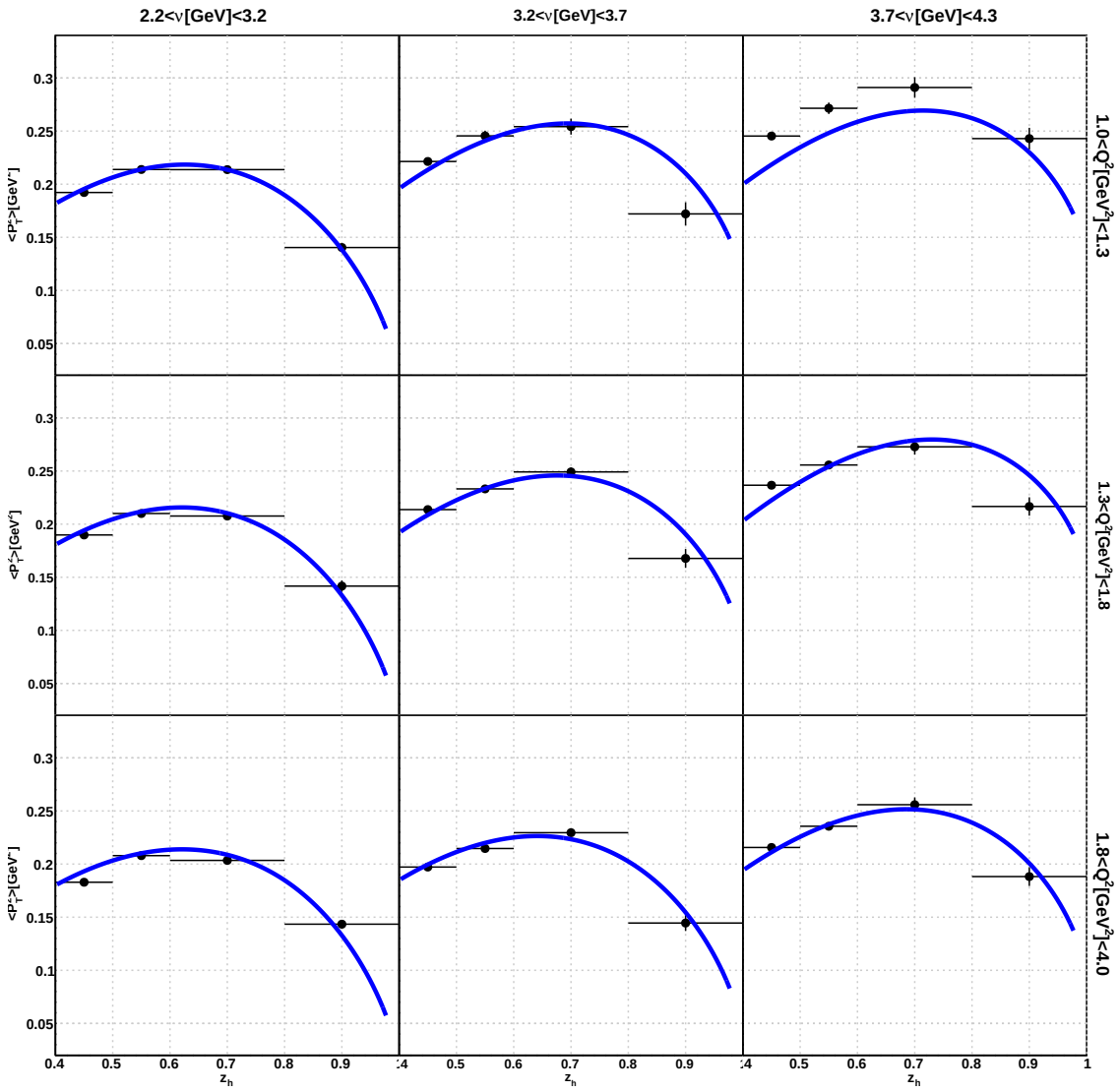

Figure B.94: Fits to Deuterium (C) results with $x_f > 0$ cut not applied.

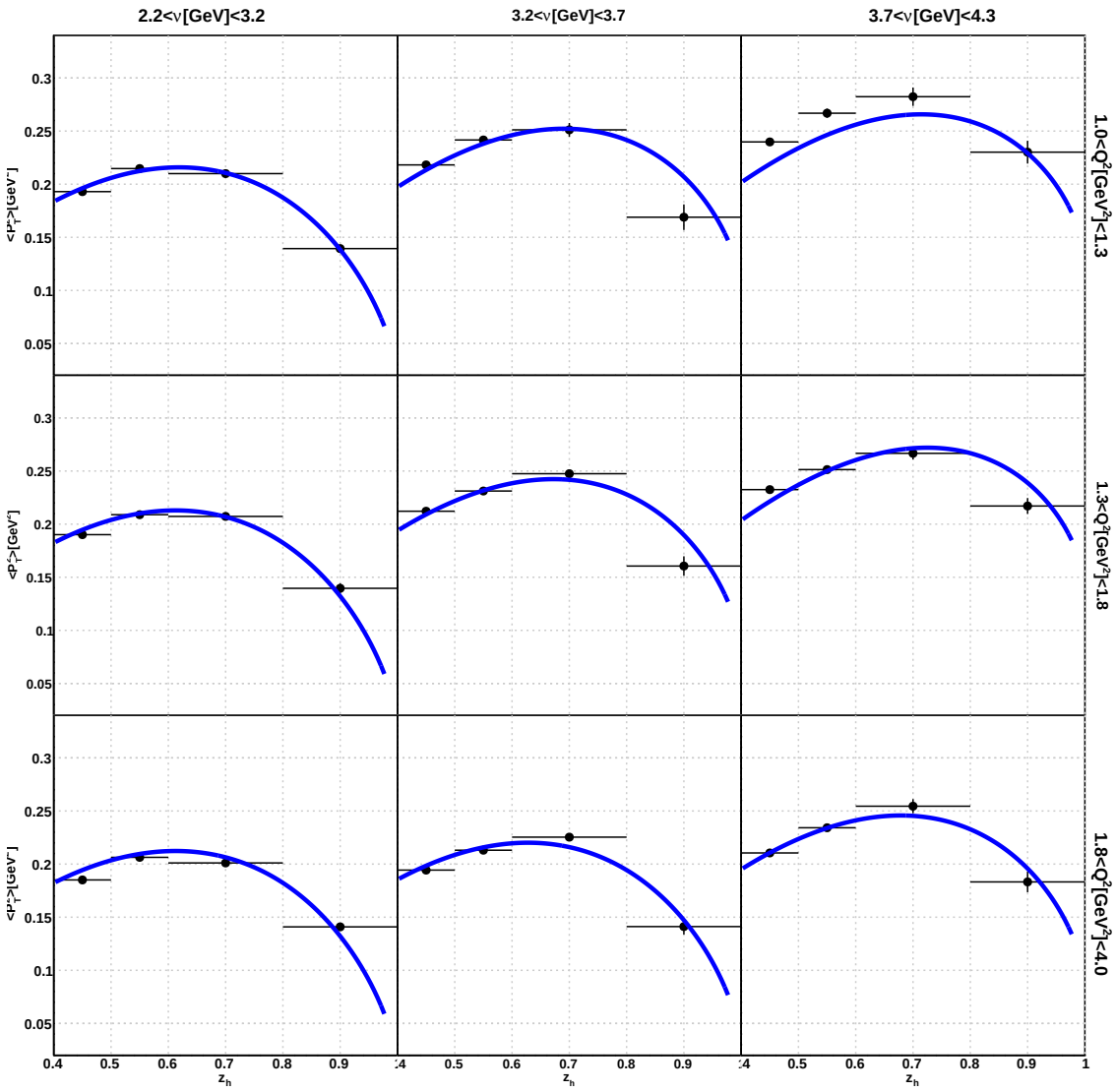

Figure B.95: Fits to Deuterium (Fe) results with $x_f > 0$ cut not applied.

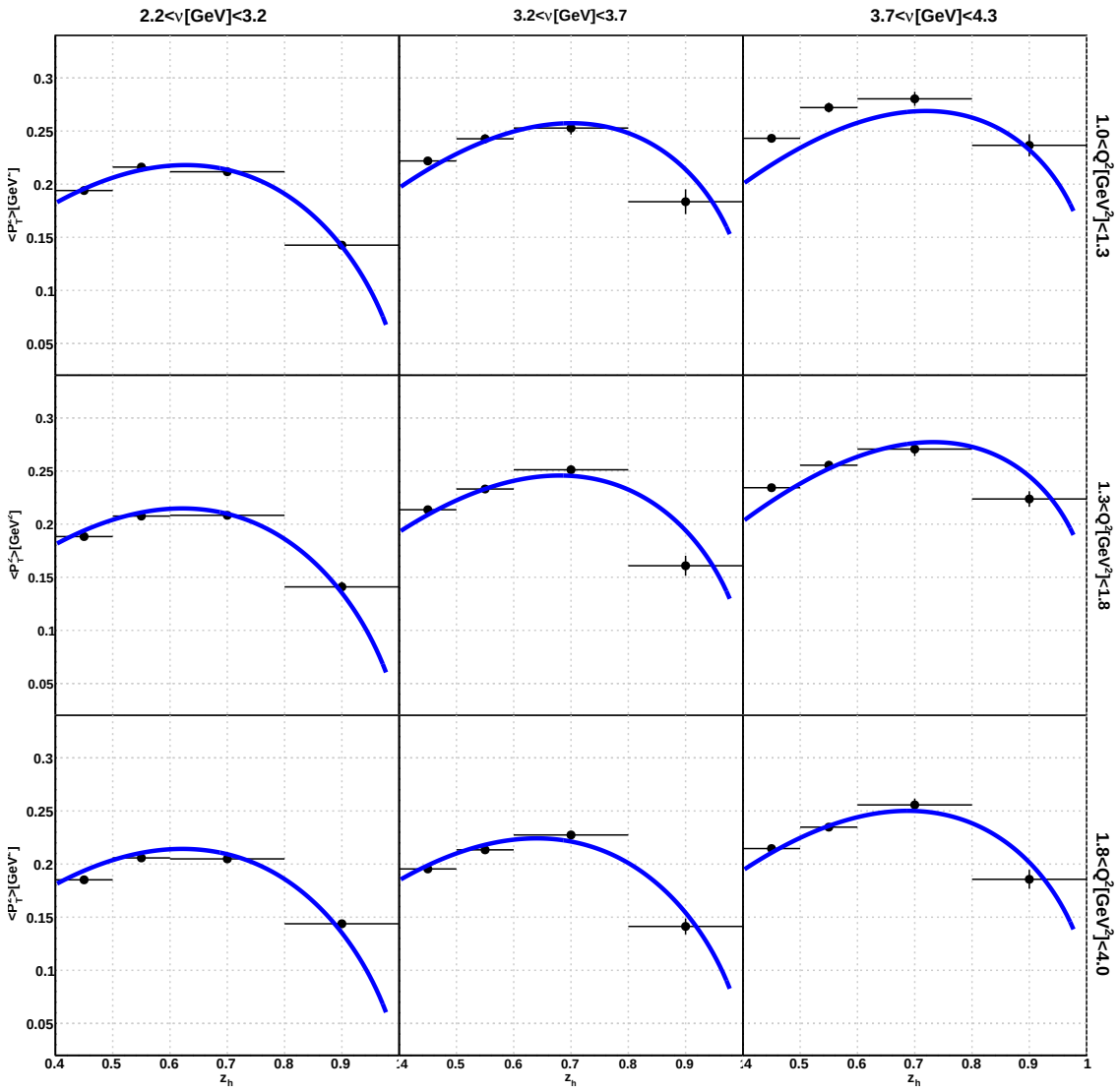

Figure B.96: Fits to Deuterium (Pb) results with $x_f > 0$ cut not applied.

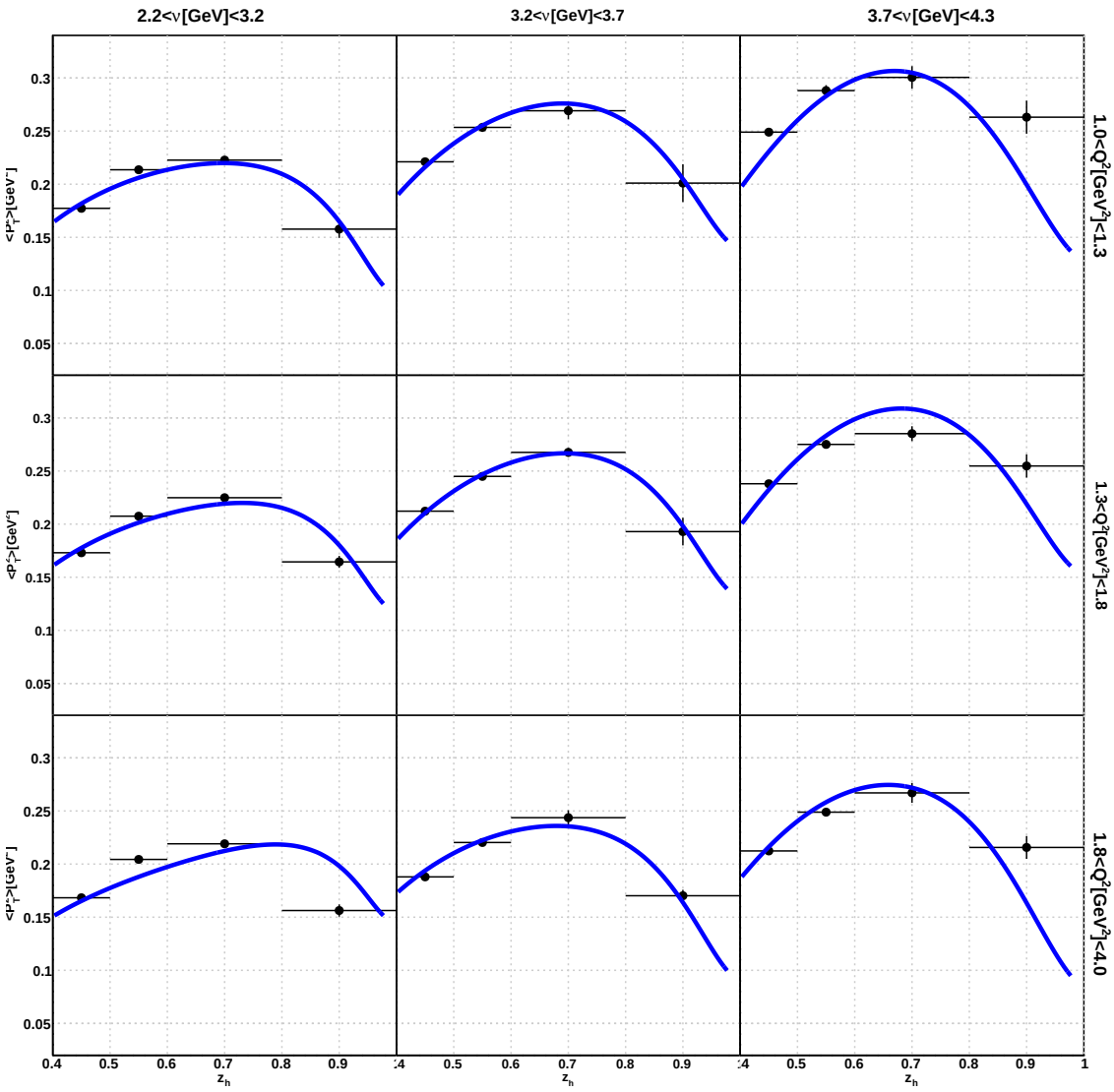

Figure B.97: Fits to C results with $x_f > 0$ cut applied.

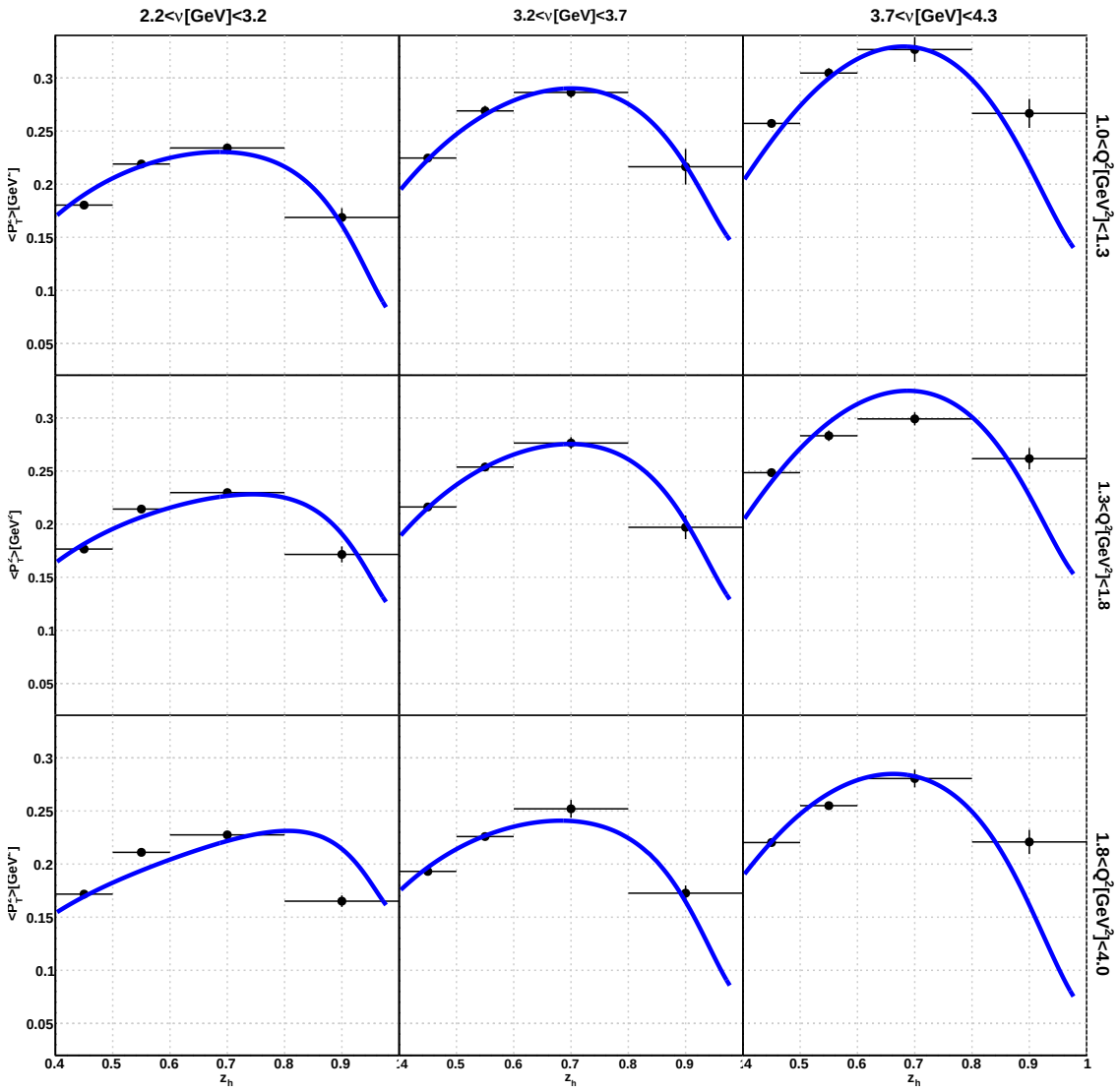

Figure B.98: Fits to Fe results with $x_f > 0$ cut applied.

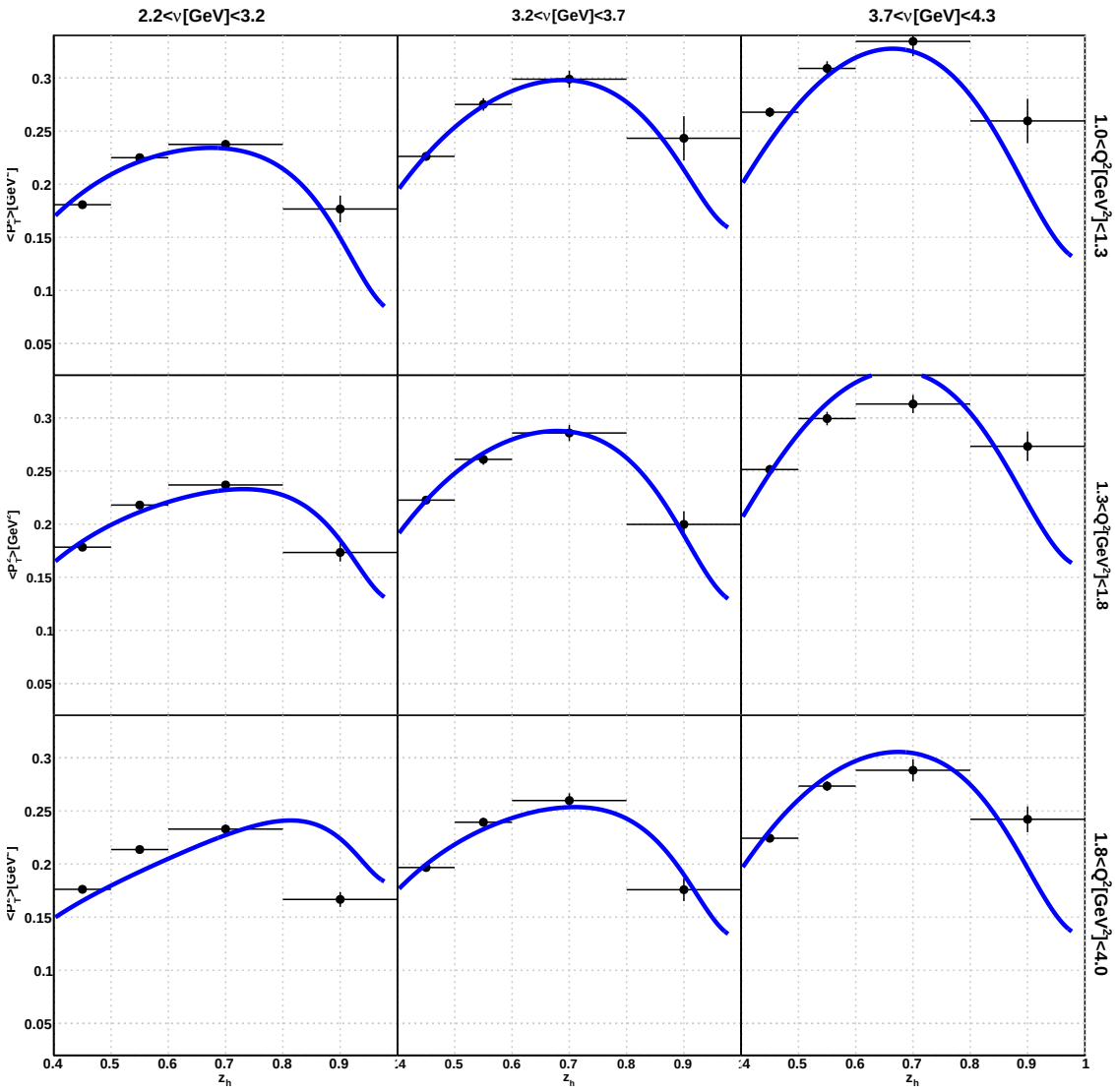

Figure B.99: Fits to Pb results with $x_f > 0$ cut applied.

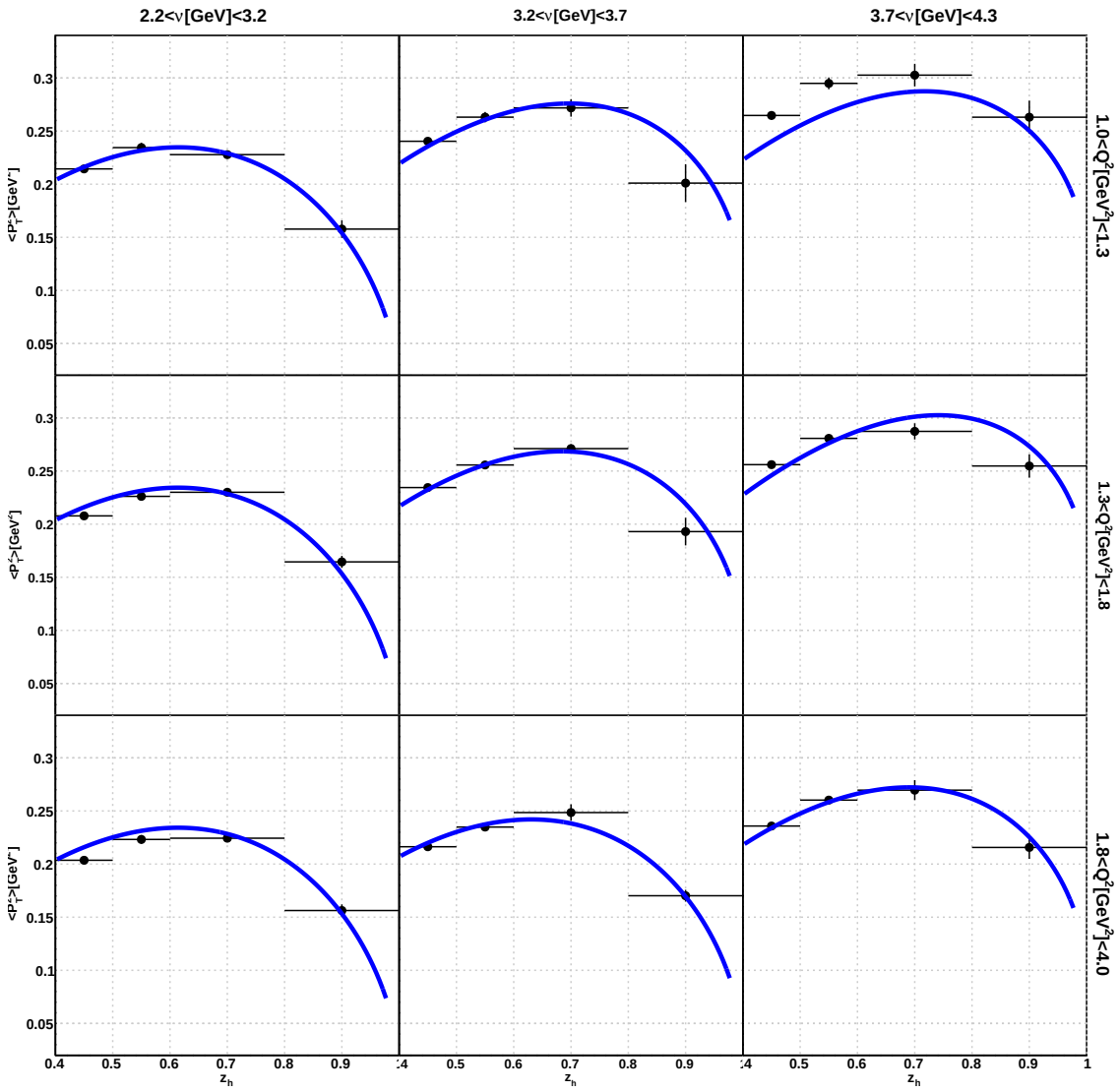

Figure B.100: Fits to C results with $x_f > 0$ cut not applied.

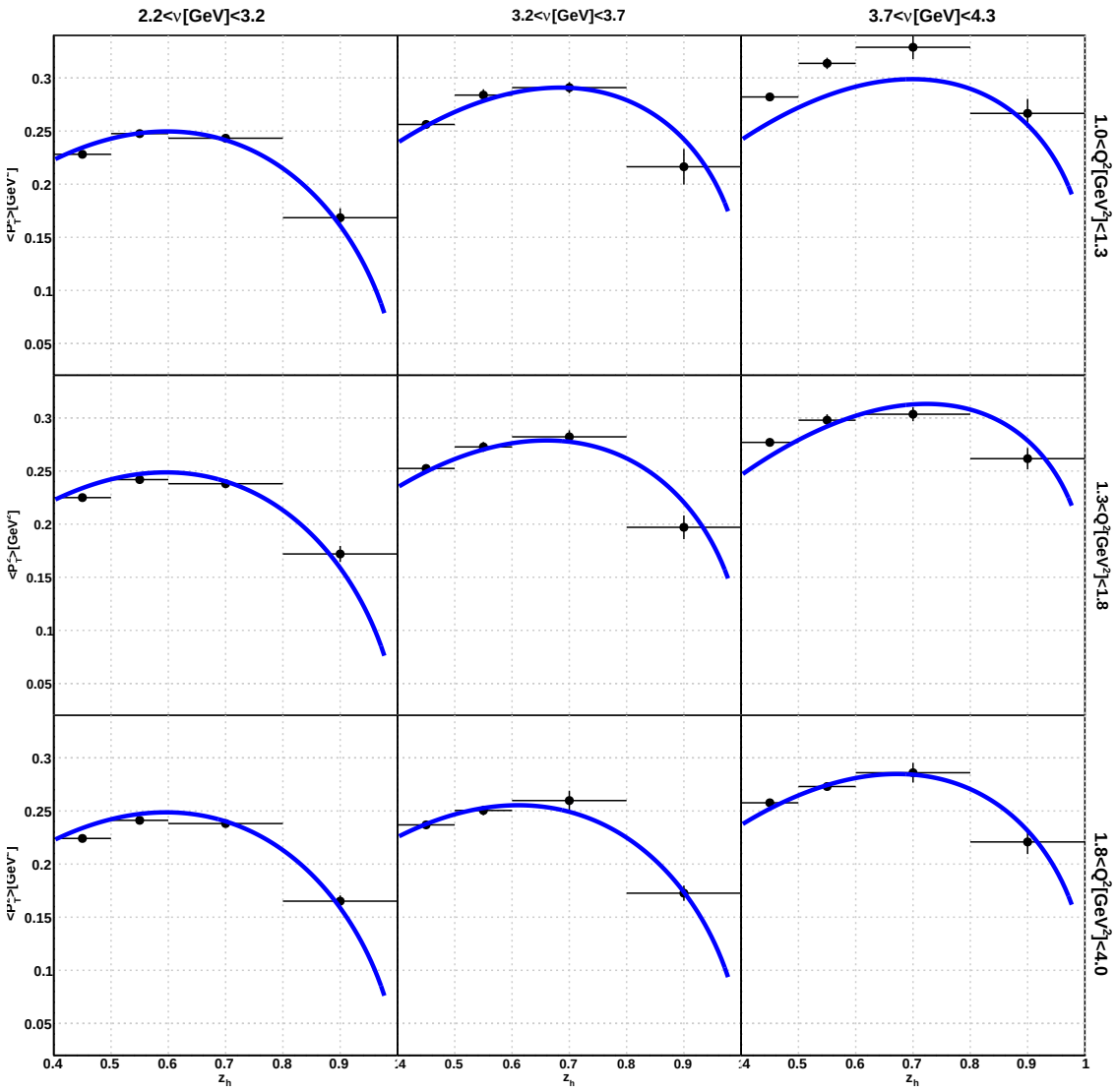

Figure B.101: Fits to Fe results with $x_f > 0$ cut not applied.

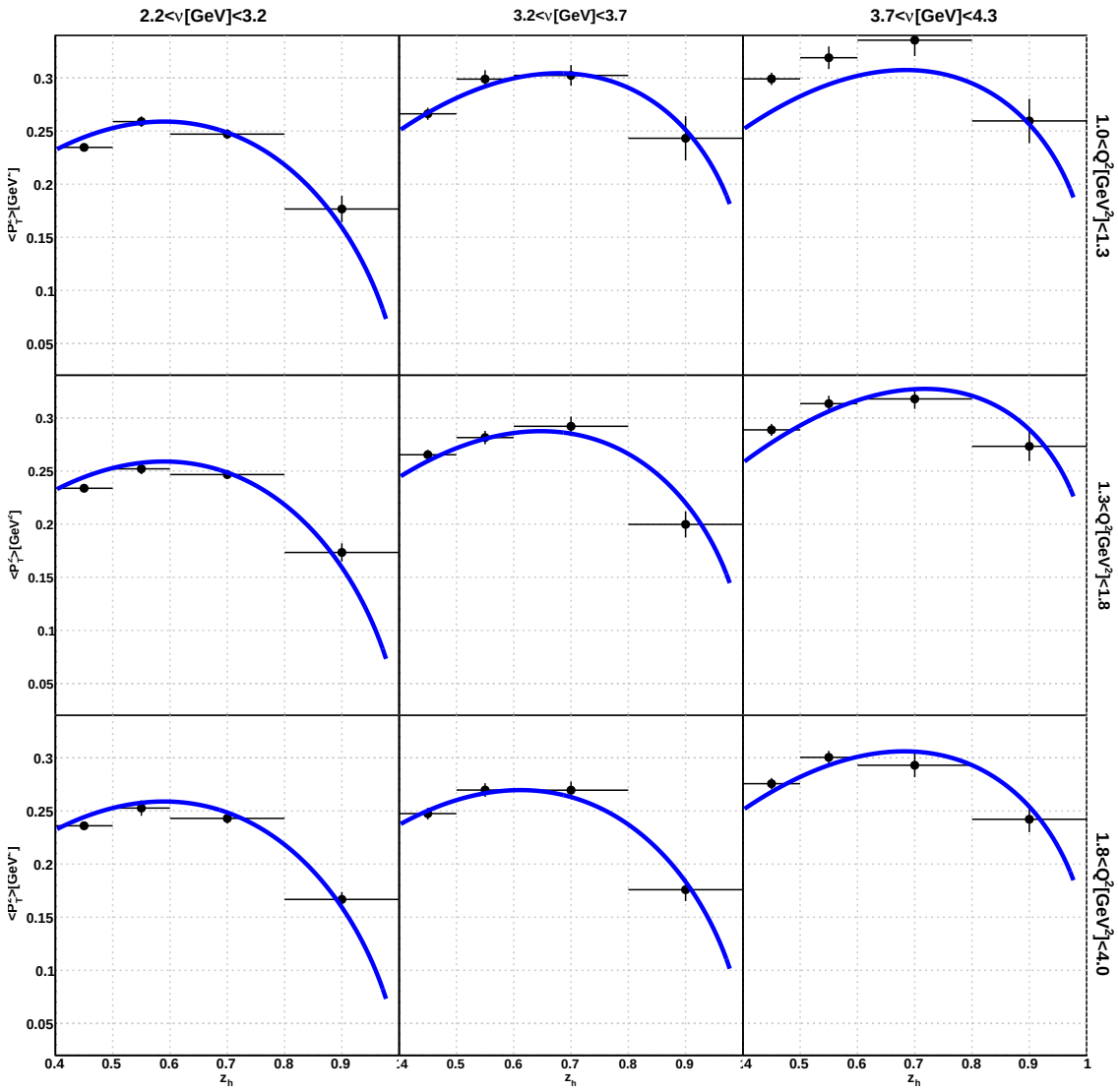

Figure B.102: Fits to Pb results with $x_f > 0$ cut not applied.

B.4.4 Fit With Integral Function (Hypothesis 2)

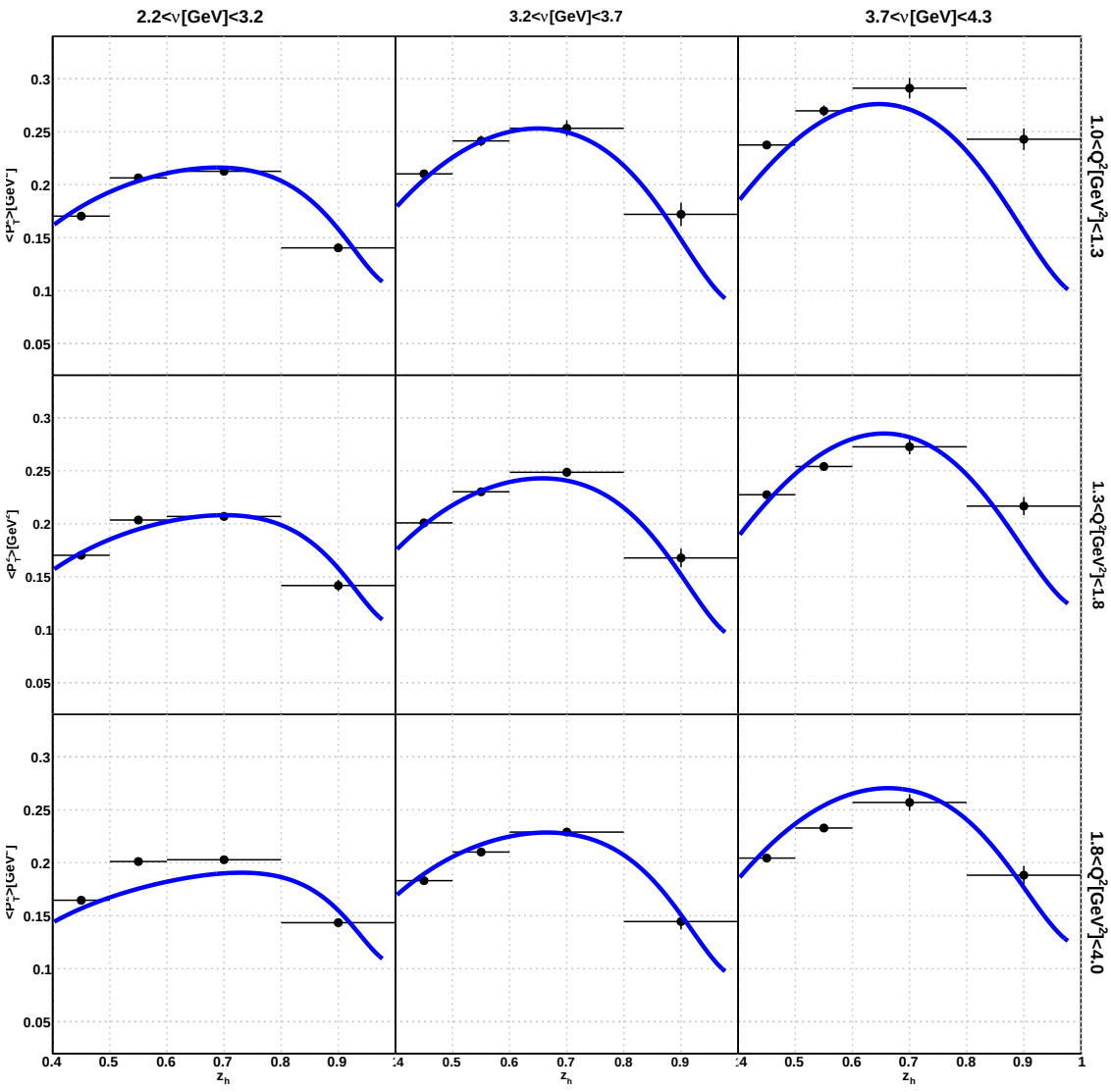

Figure B.103: Fits to Deuterium (C) results with $x_f > 0$ cut applied.

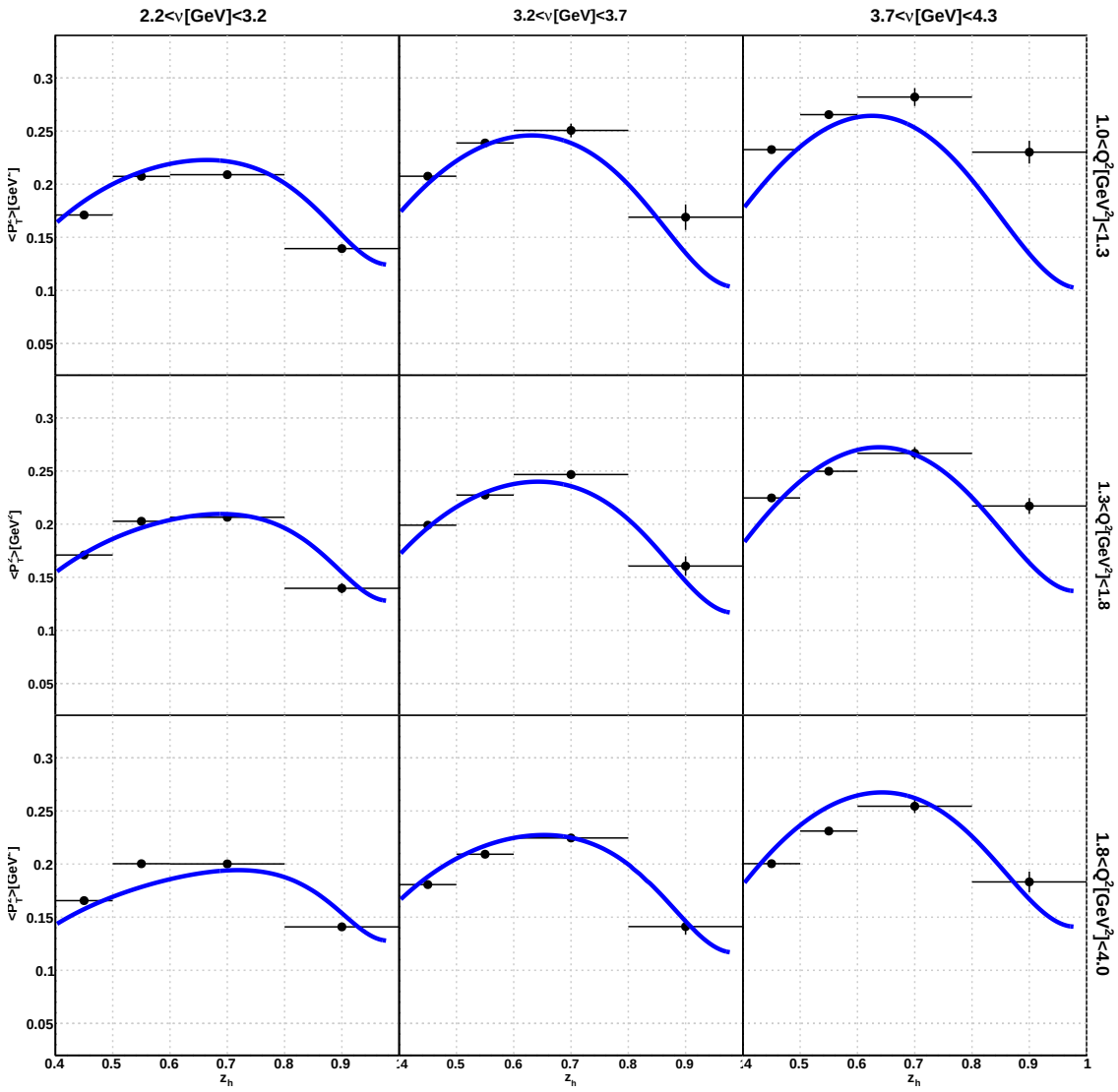

Figure B.104: Fits to Deuterium (Fe) results with $x_f > 0$ cut applied.

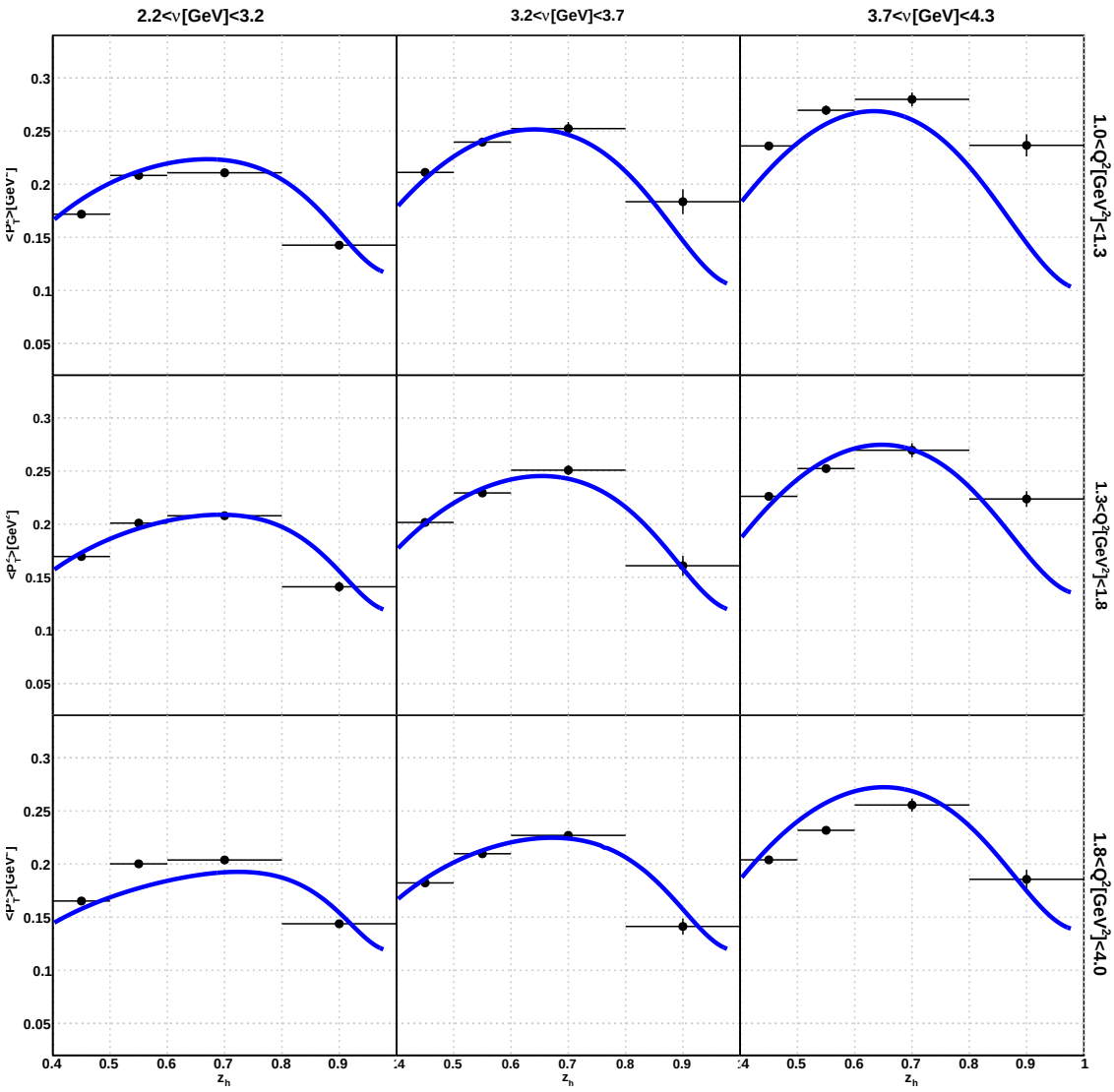

Figure B.105: Fits to Deuterium (Pb) results with $x_f > 0$ cut applied.

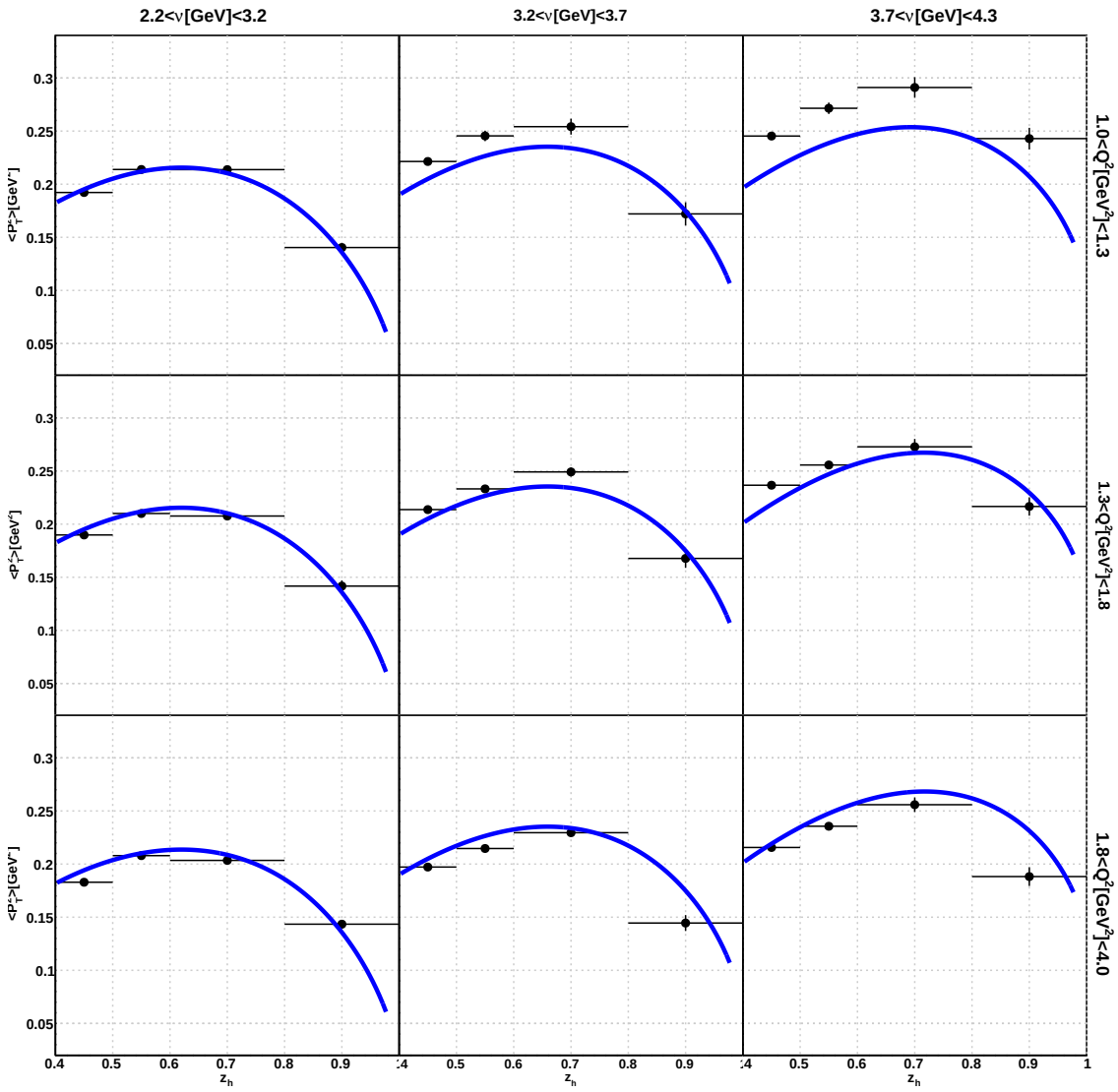

Figure B.106: Fits to Deuterium (C) results with $x_f > 0$ cut not applied.

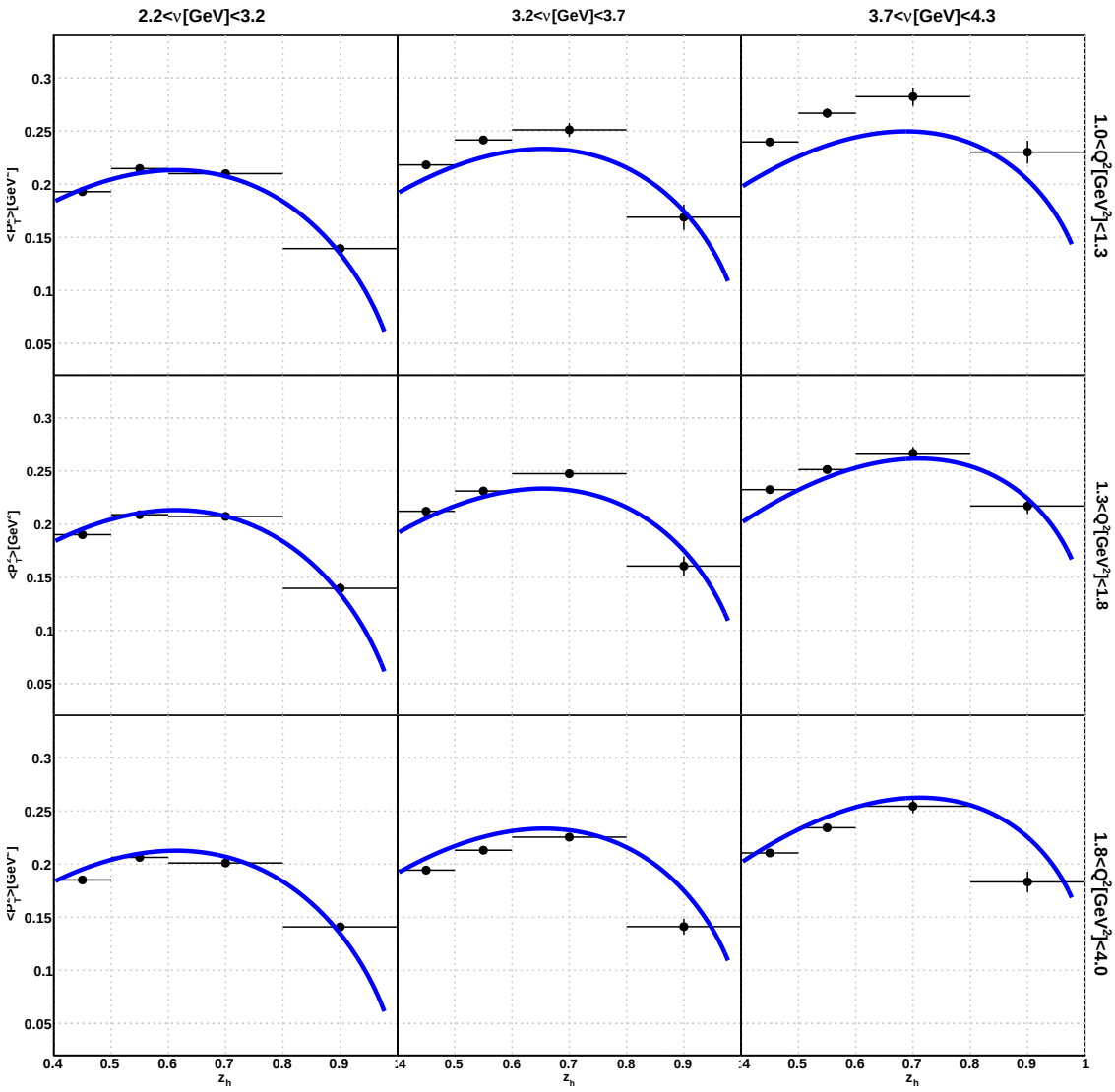

Figure B.107: Fits to Deuterium (Fe) results with $x_f > 0$ cut not applied.

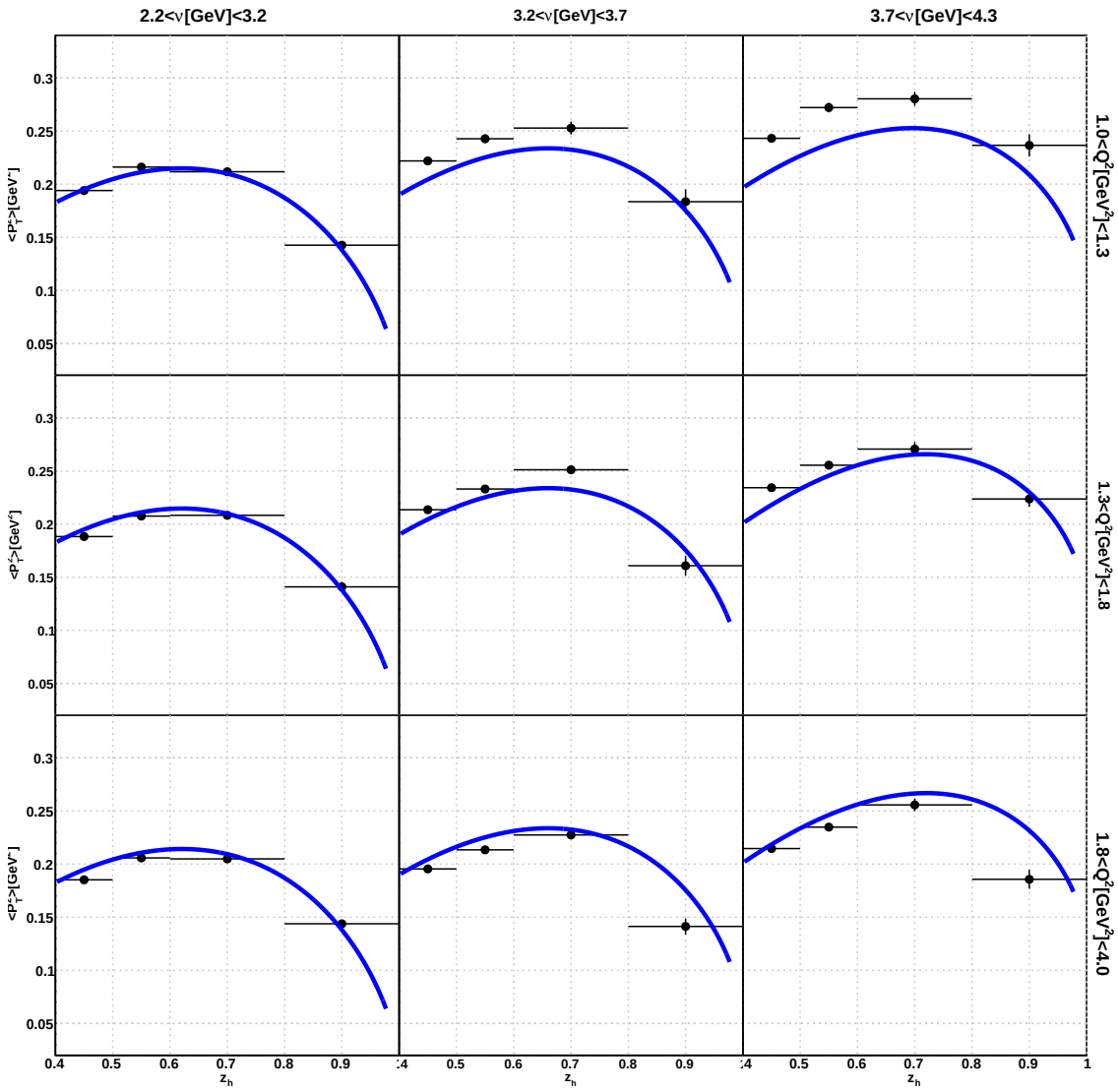

Figure B.108: Fits to Deuterium (Pb) results with $x_f > 0$ cut not applied.

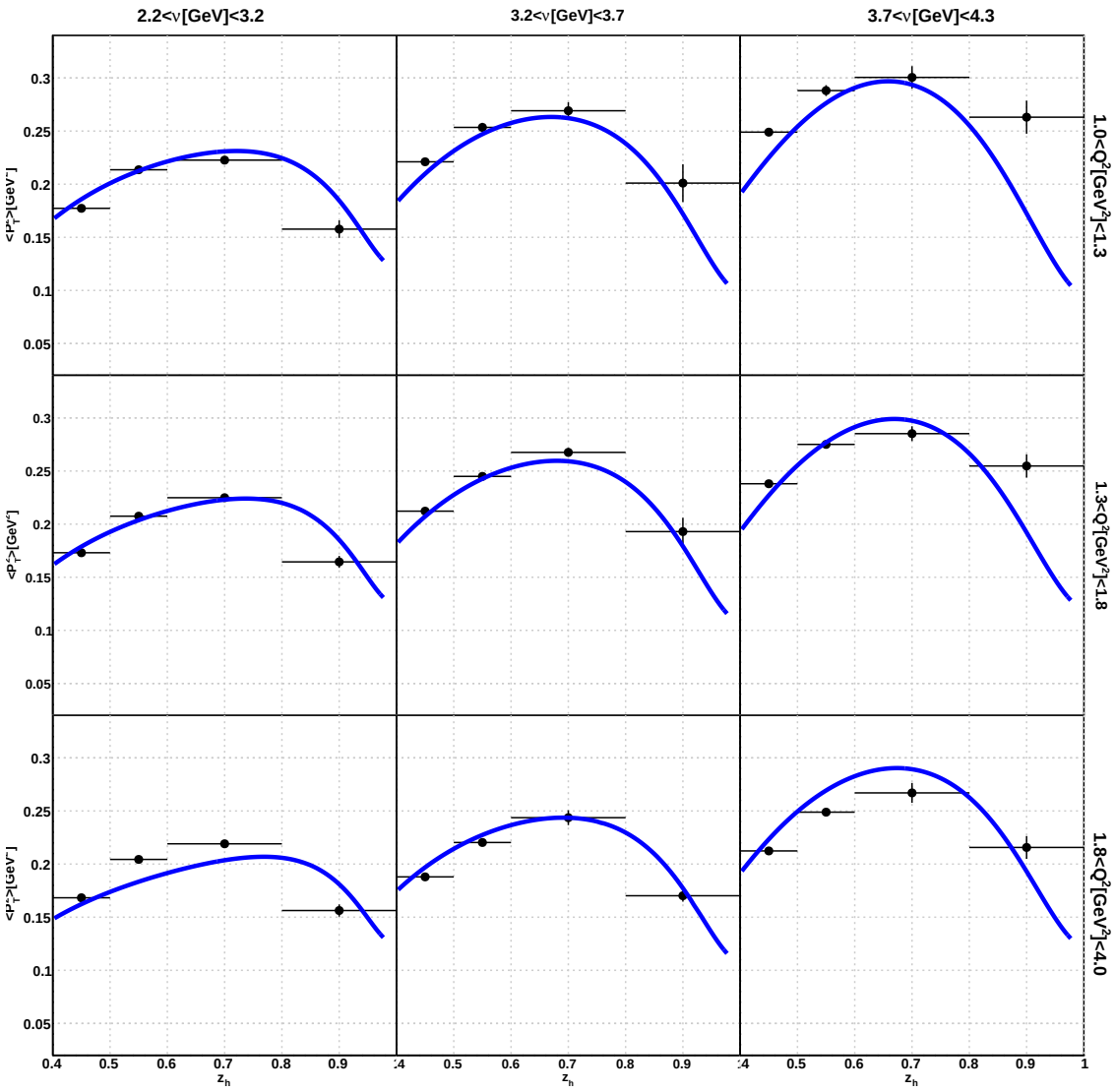

Figure B.109: Fits to C results with $x_f > 0$ cut applied.

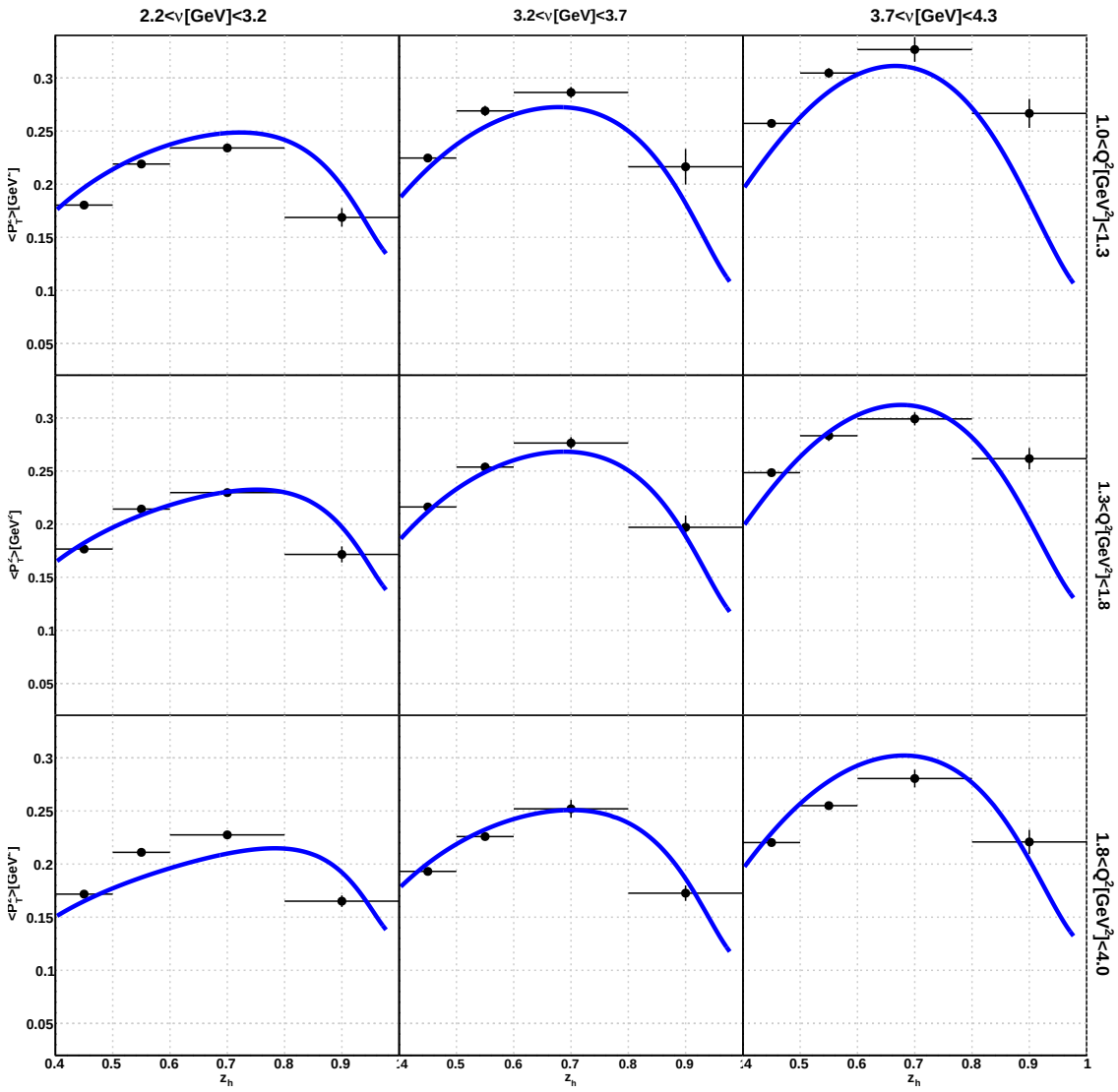

Figure B.110: Fits to Fe results with $x_f > 0$ cut applied.

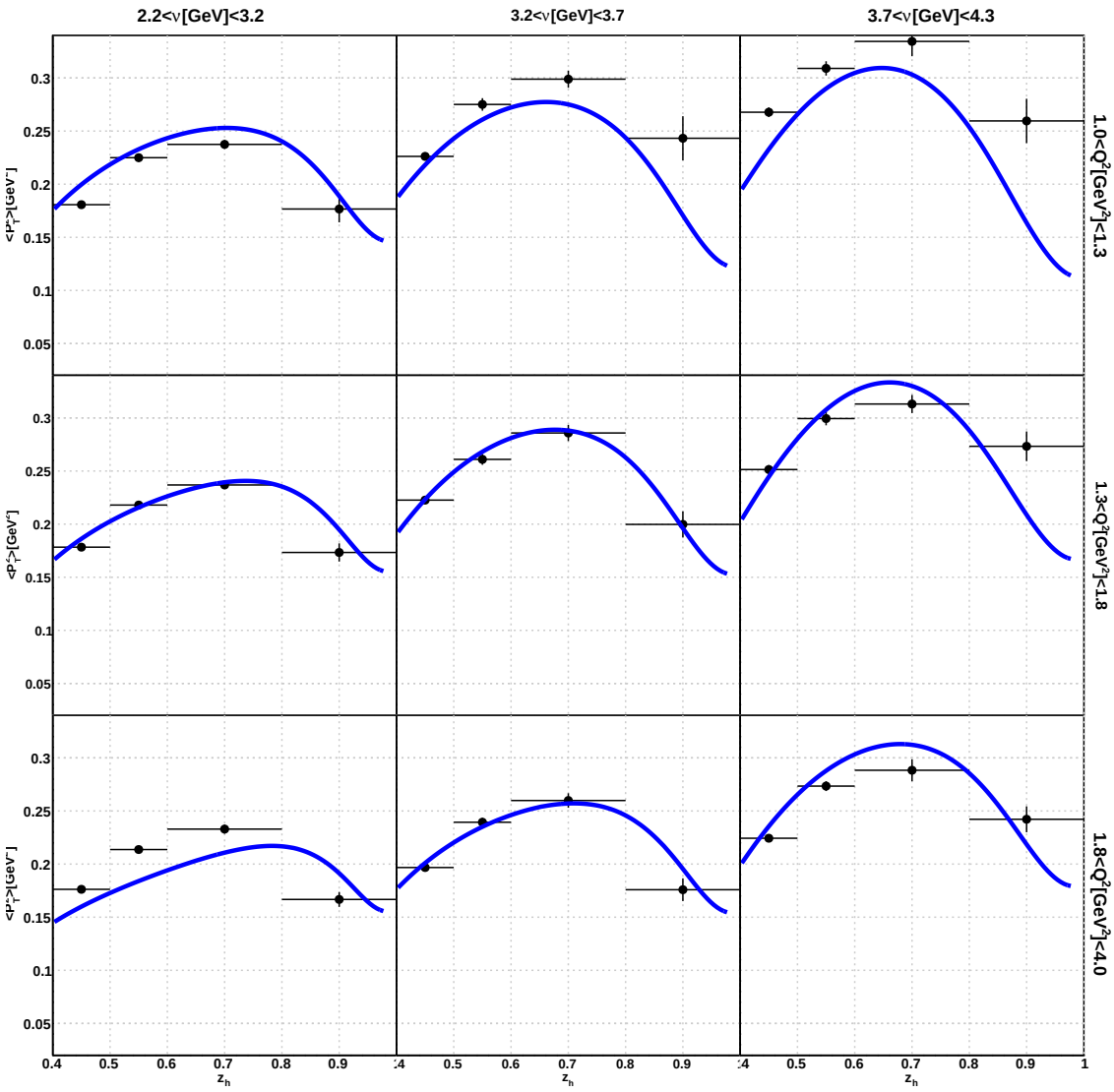

Figure B.111: Fits to Pb results with $x_f > 0$ cut applied.

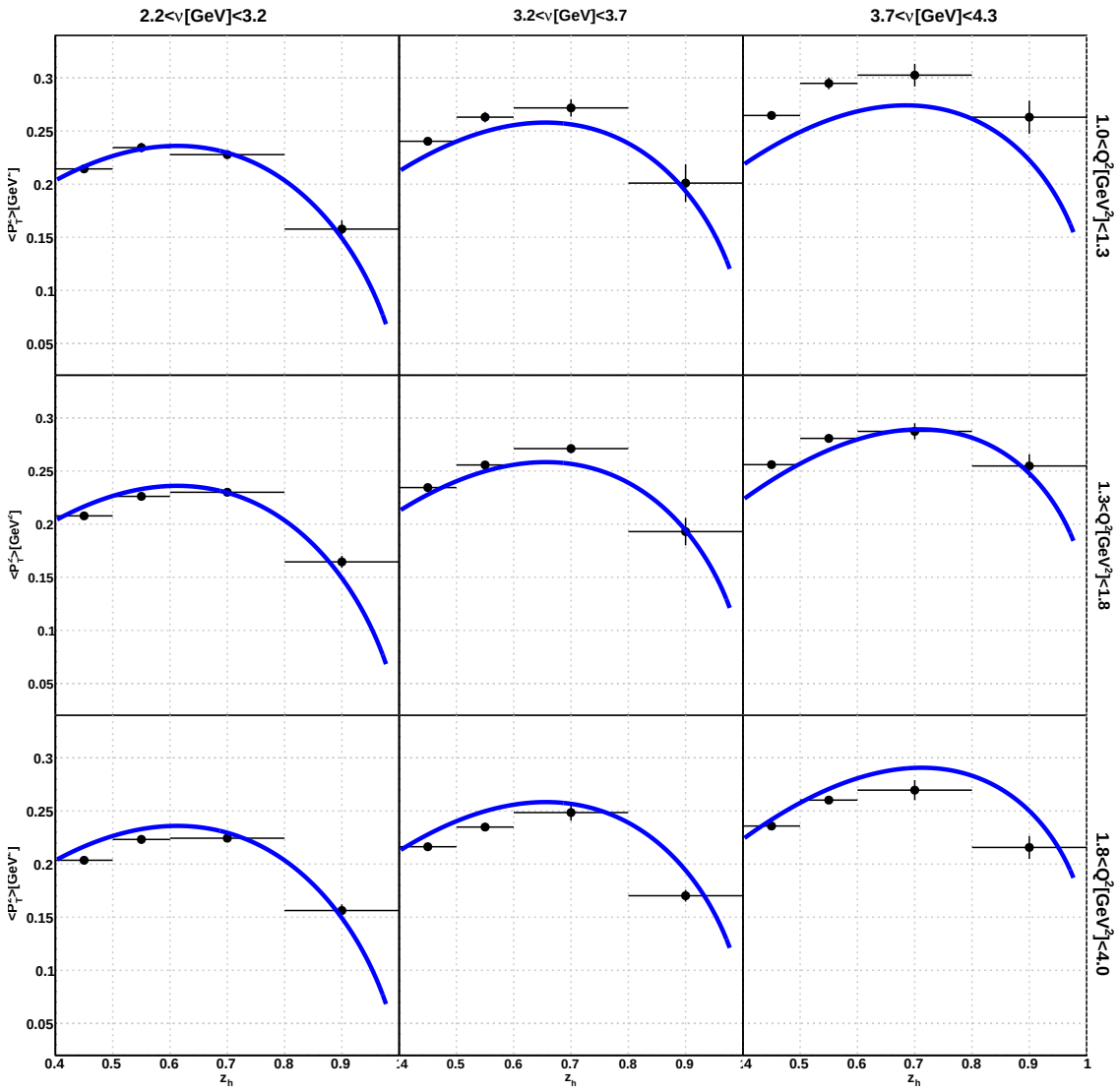

Figure B.112: Fits to C results with $x_f > 0$ cut not applied.

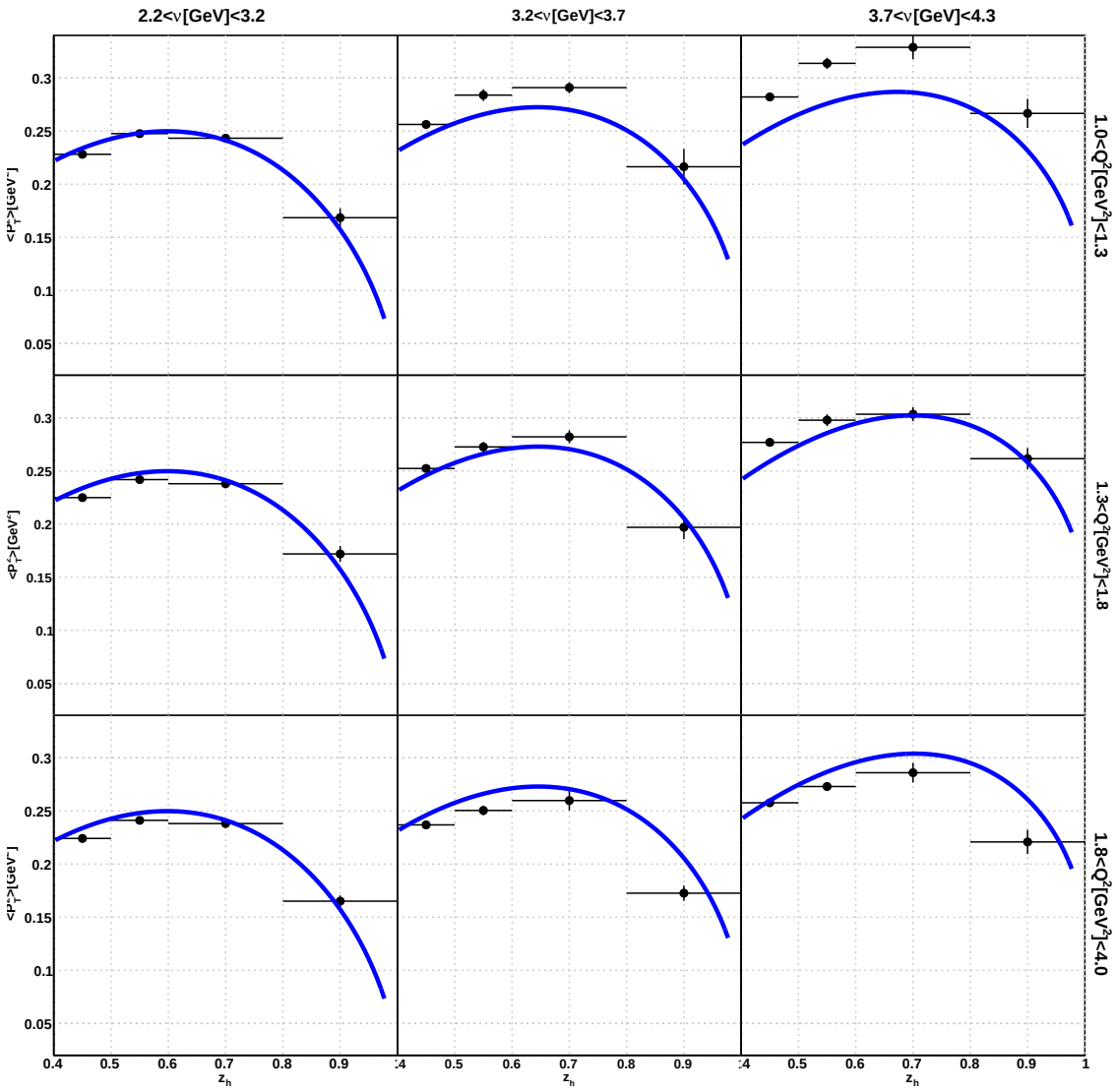

Figure B.113: Fits to Fe results with $x_f > 0$ cut not applied.

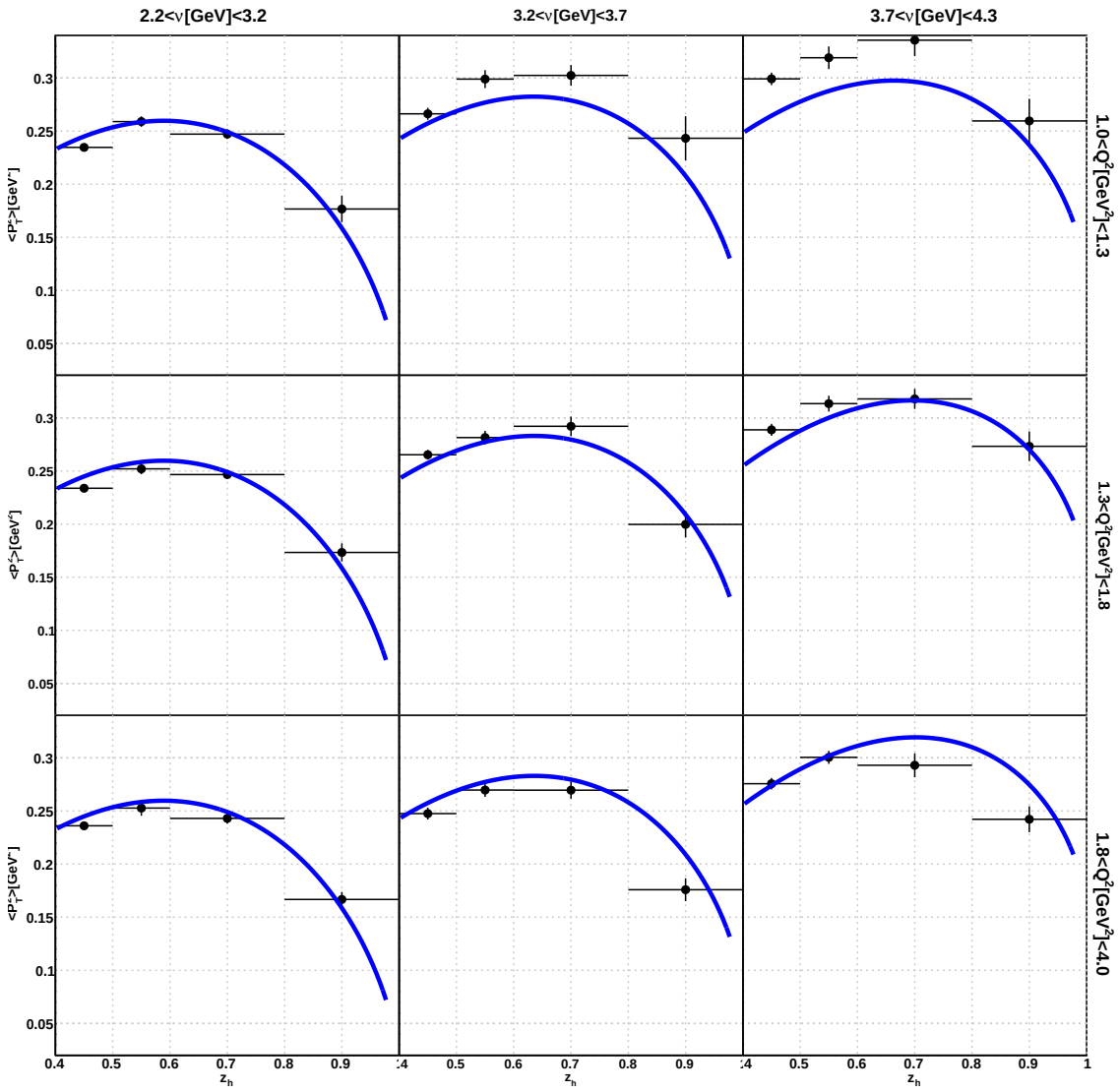

Figure B.114: Fits to Pb results with $x_f > 0$ cut not applied.

Appendix C

Tables

C.1 Average Squared Transverse Momentum

z_h	$\langle P_T^2 \rangle_C$	±Stat.	±Syst.	$\langle P_T^2 \rangle_{Fe}$	±Stat.	±Syst.	$\langle P_T^2 \rangle_{Pb}$	±Stat.	±Syst.
0.1-0.2	0.078	8.3e-05	0.0005	0.082	7.3e-05	0.00044	0.085	0.00011	0.00049
0.2-0.3	0.14	0.0002	0.0011	0.15	0.00018	0.0012	0.16	0.0003	0.0012
0.3-0.4	0.19	0.00037	0.0018	0.21	0.00036	0.002	0.22	0.00058	0.0021
0.4-0.5	0.23	0.00058	0.0035	0.24	0.00056	0.0036	0.26	0.00097	0.0045
0.5-0.6	0.25	0.00097	0.0041	0.26	0.00086	0.0044	0.28	0.0014	0.0048
0.6-0.8	0.25	0.00094	0.0042	0.27	0.00081	0.0045	0.27	0.0015	0.0056
0.8-1	0.18	0.0015	0.0065	0.19	0.0013	0.0076	0.19	0.003	0.0085
z_h	$\langle P_T^2 \rangle_{DC}$	±Stat.	±Syst.	$\langle P_T^2 \rangle_{DFe}$	±Stat.	±Syst.	$\langle P_T^2 \rangle_{DPb}$	±Stat.	±Syst.
0.1-0.2	0.073	7.1e-05	0.00044	0.071	5.8e-05	0.00042	0.072	6.3e-05	0.00044
0.2-0.3	0.13	0.00016	0.001	0.13	0.00013	0.0009	0.13	0.00014	0.001
0.3-0.4	0.17	0.00029	0.0016	0.17	0.00024	0.0015	0.17	0.00026	0.0016
0.4-0.5	0.21	0.00046	0.0025	0.21	0.00037	0.0024	0.21	0.0004	0.0025
0.5-0.6	0.23	0.00067	0.0037	0.23	0.00054	0.0034	0.23	0.00062	0.0037
0.6-0.8	0.23	0.00068	0.0038	0.23	0.00052	0.0035	0.23	0.00056	0.0038
0.8-1	0.16	0.001	0.0039	0.15	0.00074	0.0034	0.16	0.0008	0.0034

Table C.1: Integrated average squared transverse momentum in $[GeV^2]$.

$1 < Q^2[GeV^2] < 1.3$; $2.2 < \nu[GeV] < 3.2$									
z_h	$\langle P_T^2 \rangle_C$	±Stat.	±Syst.	$\langle P_T^2 \rangle_{Fe}$	±Stat.	±Syst.	$\langle P_T^2 \rangle_{Pb}$	±Stat.	±Syst.
0.1-0.2	0.062	0.00017	0.00065	0.063	0.00015	0.00063	0.065	0.00023	0.00064
0.2-0.3	0.13	0.00044	0.001	0.14	0.00039	0.00099	0.14	0.00062	0.0012
0.3-0.4	0.18	0.0009	0.0018	0.19	0.00081	0.0019	0.2	0.0013	0.002
0.4-0.5	0.21	0.0014	0.0025	0.23	0.0013	0.0027	0.23	0.0022	0.0028
0.5-0.6	0.23	0.0028	0.0035	0.25	0.0023	0.0028	0.26	0.0033	0.0037

0.6-0.8	0.23	0.002	0.0031	0.24	0.0018	0.0029	0.25	0.0032	0.0033
0.8-1	0.16	0.0028	0.0077	0.17	0.0026	0.0083	0.18	0.0063	0.011

$1 < Q^2[GeV^2] < 1.3$; $3.2 < \nu[GeV] < 3.7$

z_h	$\langle P_T^2\rangle_C$	±Stat.	±Syst.	$\langle P_T^2\rangle_{Fe}$	±Stat.	±Syst.	$\langle P_T^2\rangle_{Pb}$	±Stat.	±Syst.
0.1-0.2	0.083	0.00027	0.00076	0.086	0.00024	0.0009	0.09	0.00036	0.00099
0.2-0.3	0.15	0.00067	0.0017	0.17	0.00064	0.0022	0.17	0.00098	0.0021
0.3-0.4	0.2	0.0013	0.0021	0.22	0.0013	0.0026	0.22	0.0019	0.0026
0.4-0.5	0.24	0.002	0.003	0.26	0.002	0.0037	0.27	0.0033	0.0046
0.5-0.6	0.26	0.003	0.0039	0.28	0.0028	0.0048	0.3	0.005	0.0068
0.6-0.8	0.27	0.0038	0.0073	0.29	0.0029	0.0044	0.3	0.0052	0.0082
0.8-1	0.2	0.011	0.014	0.22	0.0091	0.014	0.24	0.014	0.015

$1 < Q^2[GeV^2] < 1.3$; $3.7 < \nu[GeV] < 4.3$

z_h	$\langle P_T^2\rangle_C$	±Stat.	±Syst.	$\langle P_T^2\rangle_{Fe}$	±Stat.	±Syst.	$\langle P_T^2\rangle_{Pb}$	±Stat.	±Syst.
0.1-0.2	0.096	0.00031	0.00057	0.1	0.00027	0.00055	0.11	0.00041	0.00067
0.2-0.3	0.16	0.00085	0.002	0.18	0.00077	0.0019	0.19	0.0012	0.0026
0.3-0.4	0.22	0.0015	0.0023	0.23	0.0015	0.0024	0.24	0.0022	0.0028
0.4-0.5	0.26	0.0024	0.0033	0.28	0.0023	0.0032	0.3	0.0039	0.0044
0.5-0.6	0.29	0.0034	0.0044	0.31	0.0034	0.0041	0.32	0.005	0.0094
0.6-0.8	0.3	0.0051	0.0094	0.33	0.0045	0.01	0.34	0.0076	0.013
0.8-1	0.26	0.01	0.012	0.27	0.0087	0.011	0.26	0.014	0.016

$1.3 < Q^2[GeV^2] < 1.8$; $2.2 < \nu[GeV] < 3.2$

z_h	$\langle P_T^2\rangle_C$	±Stat.	±Syst.	$\langle P_T^2\rangle_{Fe}$	±Stat.	±Syst.	$\langle P_T^2\rangle_{Pb}$	±Stat.	±Syst.
0.1-0.2	0.063	0.00015	0.00054	0.065	0.00012	0.00033	0.067	0.0002	0.00057
0.2-0.3	0.13	0.00036	0.00089	0.14	0.00033	0.0013	0.14	0.00054	0.0016
0.3-0.4	0.17	0.00071	0.0016	0.19	0.00065	0.0018	0.2	0.0011	0.0023
0.4-0.5	0.21	0.0011	0.002	0.22	0.0011	0.0021	0.23	0.0019	0.0033
0.5-0.6	0.23	0.0018	0.0033	0.24	0.0015	0.0029	0.25	0.0029	0.0041
0.6-0.8	0.23	0.0015	0.0021	0.24	0.0013	0.0019	0.25	0.0024	0.0036
0.8-1	0.16	0.0017	0.0054	0.17	0.0015	0.0074	0.17	0.0031	0.008

$1.3 < Q^2[GeV^2] < 1.8$; $3.2 < \nu[GeV] < 3.7$

z_h	$\langle P_T^2\rangle_C$	±Stat.	±Syst.	$\langle P_T^2\rangle_{Fe}$	±Stat.	±Syst.	$\langle P_T^2\rangle_{Pb}$	±Stat.	±Syst.
0.1-0.2	0.081	0.00022	0.00095	0.086	0.00019	0.0012	0.089	0.0003	0.0012
0.2-0.3	0.15	0.00055	0.0018	0.16	0.00051	0.0022	0.17	0.00083	0.0024
0.3-0.4	0.2	0.001	0.002	0.21	0.0012	0.0024	0.22	0.0016	0.0029
0.4-0.5	0.23	0.0016	0.0024	0.25	0.0016	0.0029	0.27	0.0026	0.0038
0.5-0.6	0.26	0.0022	0.0031	0.27	0.0021	0.0042	0.28	0.0036	0.0052
0.6-0.8	0.27	0.0024	0.0034	0.28	0.0021	0.0058	0.29	0.0058	0.0071
0.8-1	0.19	0.0051	0.012	0.2	0.0039	0.01	0.2	0.0075	0.0098

$1.3 < Q^2[GeV^2] < 1.8$; $3.7 < \nu[GeV] < 4.3$

z_h	$\langle P_T^2\rangle_C$	±Stat.	±Syst.	$\langle P_T^2\rangle_{Fe}$	±Stat.	±Syst.	$\langle P_T^2\rangle_{Pb}$	±Stat.	±Syst.
0.1-0.2	0.094	0.00027	0.001	0.1	0.00024	0.0013	0.1	0.00037	0.0015
0.2-0.3	0.16	0.00068	0.0021	0.18	0.00067	0.0028	0.18	0.0011	0.0032
0.3-0.4	0.22	0.0012	0.0021	0.23	0.0012	0.0025	0.25	0.0019	0.0029
0.4-0.5	0.26	0.0019	0.003	0.28	0.0018	0.0033	0.29	0.0032	0.0046

0.5-0.6	0.28	0.0026	0.0033	0.3	0.0024	0.005	0.31	0.0044	0.0061
0.6-0.8	0.29	0.0038	0.0066	0.3	0.0033	0.0057	0.32	0.0067	0.0066
0.8-1	0.25	0.007	0.0085	0.26	0.0053	0.0086	0.27	0.0096	0.01

$1.8 < Q^2[GeV^2] < 4$; $2.2 < \nu[GeV] < 3.2$

z_h	$\langle P_T^2\rangle_C$	±Stat.	±Syst.	$\langle P_T^2\rangle_{Fe}$	±Stat.	±Syst.	$\langle P_T^2\rangle_{Pb}$	±Stat.	±Syst.
0.1-0.2	0.066	0.00022	0.00087	0.07	0.00019	0.00093	0.072	0.00031	0.00044
0.2-0.3	0.12	0.00055	0.0017	0.14	0.0005	0.0016	0.14	0.00086	0.0013
0.3-0.4	0.17	0.0011	0.0016	0.19	0.00099	0.0027	0.2	0.0018	0.0016
0.4-0.5	0.2	0.0016	0.0026	0.22	0.0016	0.0025	0.24	0.0028	0.003
0.5-0.6	0.22	0.0024	0.0034	0.24	0.0022	0.0027	0.25	0.0041	0.006
0.6-0.8	0.22	0.0019	0.0017	0.24	0.0018	0.0025	0.24	0.0034	0.0036
0.8-1	0.16	0.0023	0.0053	0.17	0.0022	0.005	0.17	0.0044	0.0055

$1.8 < Q^2[GeV^2] < 4$; $3.2 < \nu[GeV] < 3.7$

z_h	$\langle P_T^2\rangle_C$	±Stat.	±Syst.	$\langle P_T^2\rangle_{Fe}$	±Stat.	±Syst.	$\langle P_T^2\rangle_{Pb}$	±Stat.	±Syst.
0.1-0.2	0.079	0.00021	0.00045	0.084	0.00018	0.00046	0.087	0.0003	0.00068
0.2-0.3	0.14	0.0005	0.0015	0.16	0.00048	0.0016	0.16	0.00081	0.002
0.3-0.4	0.19	0.00092	0.0021	0.21	0.00092	0.0026	0.22	0.0016	0.003
0.4-0.5	0.22	0.0014	0.0034	0.24	0.0014	0.0034	0.25	0.0024	0.005
0.5-0.6	0.23	0.0019	0.0035	0.25	0.0019	0.0041	0.27	0.0034	0.0055
0.6-0.8	0.25	0.002	0.0075	0.26	0.0018	0.0091	0.27	0.0033	0.0073
0.8-1	0.17	0.0032	0.0045	0.17	0.0028	0.0067	0.18	0.0057	0.0091

$1.8 < Q^2[GeV^2] < 4$; $3.7 < \nu[GeV] < 4.3$

z_h	$\langle P_T^2\rangle_C$	±Stat.	±Syst.	$\langle P_T^2\rangle_{Fe}$	±Stat.	±Syst.	$\langle P_T^2\rangle_{Pb}$	±Stat.	±Syst.
0.1-0.2	0.092	0.00026	0.00056	0.098	0.00023	0.00049	0.1	0.00037	0.00065
0.2-0.3	0.16	0.0006	0.0015	0.17	0.00058	0.0014	0.18	0.00097	0.0015
0.3-0.4	0.2	0.001	0.002	0.22	0.001	0.0023	0.24	0.0018	0.0027
0.4-0.5	0.24	0.0016	0.003	0.26	0.0016	0.0032	0.28	0.003	0.0045
0.5-0.6	0.26	0.0023	0.0025	0.27	0.0023	0.0026	0.3	0.004	0.0046
0.6-0.8	0.27	0.0037	0.0087	0.29	0.0026	0.0089	0.29	0.0048	0.01
0.8-1	0.22	0.0039	0.01	0.22	0.0034	0.011	0.24	0.0075	0.0096

$1 < Q^2[GeV^2] < 1.3$; $2.2 < \nu[GeV] < 3.2$

z_h	$\langle P_T^2\rangle_{DC}$	±Stat.	±Syst.	$\langle P_T^2\rangle_{DFe}$	±Stat.	±Syst.	$\langle P_T^2\rangle_{DPb}$	±Stat.	±Syst.
0.1-0.2	0.059	0.00015	0.00065	0.058	0.00012	0.00065	0.058	0.00013	0.00065
0.2-0.3	0.11	0.00036	0.0011	0.11	0.00029	0.00096	0.11	0.00031	0.0011
0.3-0.4	0.16	0.00068	0.0015	0.16	0.00056	0.0016	0.16	0.00059	0.0016
0.4-0.5	0.19	0.0011	0.0021	0.19	0.0009	0.0022	0.19	0.00096	0.0021
0.5-0.6	0.21	0.0017	0.003	0.21	0.0013	0.0024	0.22	0.0016	0.0029
0.6-0.8	0.21	0.0015	0.0032	0.21	0.0011	0.003	0.21	0.0012	0.0031
0.8-1	0.14	0.002	0.0032	0.14	0.0014	0.0034	0.14	0.0015	0.0033

$1 < Q^2[GeV^2] < 1.3$; $3.2 < \nu[GeV] < 3.7$

z_h	$\langle P_T^2\rangle_{DC}$	±Stat.	±Syst.	$\langle P_T^2\rangle_{DFe}$	±Stat.	±Syst.	$\langle P_T^2\rangle_{DPb}$	±Stat.	±Syst.
0.1-0.2	0.077	0.00023	0.0006	0.076	0.00019	0.00057	0.076	0.00021	0.00061
0.2-0.3	0.14	0.00055	0.0014	0.14	0.00047	0.0013	0.14	0.00049	0.0015
0.3-0.4	0.18	0.0012	0.0022	0.18	0.00092	0.0021	0.18	0.00095	0.0021

0.4-0.5	0.22	0.0016	0.0021	0.22	0.0013	0.0024	0.22	0.0014	0.0025
0.5-0.6	0.25	0.0024	0.0043	0.24	0.0019	0.0027	0.24	0.0021	0.0036
0.6-0.8	0.25	0.0033	0.0067	0.25	0.0023	0.006	0.25	0.0024	0.0056
0.8-1	0.17	0.0059	0.0091	0.17	0.0048	0.011	0.18	0.0046	0.011

$1 < Q^2[GeV^2] < 1.3$; $3.7 < \nu[GeV] < 4.3$

z_h	$\langle P_T^2\rangle_{DC}$	±Stat.	±Syst.	$\langle P_T^2\rangle_{DFe}$	±Stat.	±Syst.	$\langle P_T^2\rangle_{DPb}$	±Stat.	±Syst.
0.1-0.2	0.088	0.00026	0.00055	0.087	0.00022	0.00051	0.087	0.00023	0.00061
0.2-0.3	0.15	0.00069	0.0018	0.15	0.0006	0.0017	0.15	0.0006	0.0016
0.3-0.4	0.2	0.0012	0.0022	0.2	0.001	0.0019	0.2	0.0011	0.0021
0.4-0.5	0.25	0.0019	0.003	0.24	0.0016	0.0027	0.24	0.0016	0.0029
0.5-0.6	0.27	0.0026	0.0047	0.27	0.0021	0.0038	0.27	0.0023	0.004
0.6-0.8	0.29	0.0039	0.0089	0.28	0.003	0.0081	0.28	0.0032	0.0058
0.8-1	0.24	0.0066	0.0077	0.23	0.0055	0.0093	0.24	0.0074	0.0074

$1.3 < Q^2[GeV^2] < 1.8$; $2.2 < \nu[GeV] < 3.2$

z_h	$\langle P_T^2\rangle_{DC}$	±Stat.	±Syst.	$\langle P_T^2\rangle_{DFe}$	±Stat.	±Syst.	$\langle P_T^2\rangle_{DPb}$	±Stat.	±Syst.
0.1-0.2	0.06	0.00013	0.00051	0.059	0.0001	0.00048	0.06	0.00011	0.00059
0.2-0.3	0.11	0.0003	0.00091	0.11	0.00024	0.00097	0.11	0.00026	0.00086
0.3-0.4	0.16	0.00054	0.0011	0.16	0.00044	0.0011	0.15	0.00047	0.0012
0.4-0.5	0.19	0.00087	0.0014	0.19	0.00069	0.0014	0.19	0.00074	0.0014
0.5-0.6	0.21	0.0012	0.0019	0.21	0.00096	0.0017	0.21	0.001	0.0024
0.6-0.8	0.21	0.001	0.0021	0.21	0.00077	0.0017	0.21	0.00085	0.0019
0.8-1	0.14	0.0011	0.0053	0.14	0.00076	0.0046	0.14	0.00088	0.0047

$1.3 < Q^2[GeV^2] < 1.8$; $3.2 < \nu[GeV] < 3.7$

z_h	$\langle P_T^2\rangle_{DC}$	±Stat.	±Syst.	$\langle P_T^2\rangle_{DFe}$	±Stat.	±Syst.	$\langle P_T^2\rangle_{DPb}$	±Stat.	±Syst.
0.1-0.2	0.075	0.00019	0.00075	0.075	0.00016	0.00076	0.075	0.00017	0.00077
0.2-0.3	0.13	0.00045	0.0014	0.13	0.00037	0.0015	0.13	0.00039	0.0016
0.3-0.4	0.18	0.00082	0.0019	0.18	0.00069	0.0018	0.18	0.00073	0.0019
0.4-0.5	0.21	0.0014	0.0022	0.21	0.00099	0.0019	0.21	0.0011	0.0023
0.5-0.6	0.23	0.0018	0.0024	0.23	0.0014	0.0024	0.23	0.0015	0.0026
0.6-0.8	0.25	0.0019	0.0039	0.25	0.0014	0.0038	0.25	0.0015	0.004
0.8-1	0.17	0.0029	0.0084	0.16	0.0023	0.0089	0.16	0.0023	0.0092

$1.3 < Q^2[GeV^2] < 1.8$; $3.7 < \nu[GeV] < 4.3$

z_h	$\langle P_T^2\rangle_{DC}$	±Stat.	±Syst.	$\langle P_T^2\rangle_{DFe}$	±Stat.	±Syst.	$\langle P_T^2\rangle_{DPb}$	±Stat.	±Syst.
0.1-0.2	0.087	0.00023	0.00089	0.086	0.00019	0.00086	0.086	0.0002	0.00089
0.2-0.3	0.15	0.00055	0.0017	0.15	0.00047	0.0019	0.15	0.00048	0.0018
0.3-0.4	0.2	0.00094	0.0021	0.2	0.00078	0.0021	0.2	0.00083	0.0023
0.4-0.5	0.24	0.0015	0.0025	0.23	0.0012	0.0022	0.23	0.0013	0.0025
0.5-0.6	0.26	0.0021	0.0031	0.25	0.0016	0.0031	0.26	0.0018	0.0035
0.6-0.8	0.27	0.0028	0.0068	0.27	0.0021	0.0054	0.27	0.0024	0.0061
0.8-1	0.22	0.0052	0.0069	0.22	0.0039	0.0064	0.22	0.0034	0.0065

$1.8 < Q^2[GeV^2] < 4$; $2.2 < \nu[GeV] < 3.2$

z_h	$\langle P_T^2\rangle_{DC}$	±Stat.	±Syst.	$\langle P_T^2\rangle_{DFe}$	±Stat.	±Syst.	$\langle P_T^2\rangle_{DPb}$	±Stat.	±Syst.
0.1-0.2	0.062	0.00019	0.00048	0.061	0.00015	0.00075	0.062	0.00017	0.00048
0.2-0.3	0.11	0.00043	0.0011	0.11	0.00035	0.0013	0.11	0.00038	0.0011

0.3-0.4	0.15	0.00078	0.0012	0.15	0.00063	0.0012	0.15	0.00068	0.0012
0.4-0.5	0.18	0.0012	0.0012	0.19	0.00097	0.002	0.19	0.0011	0.0016
0.5-0.6	0.21	0.0017	0.0015	0.21	0.0013	0.001	0.21	0.0014	0.0011
0.6-0.8	0.2	0.0013	0.003	0.2	0.00099	0.0016	0.2	0.0011	0.0029
0.8-1	0.14	0.0015	0.0037	0.14	0.0011	0.0031	0.14	0.0013	0.0028
$1.8 < Q^2[GeV^2] < 4$; $3.2 < \nu[GeV] < 3.7$									
z_h	$\langle P_T^2\rangle_{DC}$	±Stat.	±Syst.	$\langle P_T^2\rangle_{DFe}$	±Stat.	±Syst.	$\langle P_T^2\rangle_{DPb}$	±Stat.	±Syst.
0.1-0.2	0.072	0.00018	0.00046	0.071	0.00014	0.00044	0.071	0.00015	0.00046
0.2-0.3	0.12	0.00039	0.0015	0.12	0.00031	0.001	0.12	0.00034	0.0011
0.3-0.4	0.16	0.0007	0.0017	0.17	0.00056	0.0016	0.17	0.00061	0.0018
0.4-0.5	0.2	0.001	0.0019	0.19	0.00084	0.0021	0.2	0.0009	0.002
0.5-0.6	0.21	0.0015	0.0022	0.21	0.0012	0.0023	0.21	0.0013	0.0021
0.6-0.8	0.23	0.0014	0.0021	0.23	0.001	0.0034	0.23	0.0011	0.002
0.8-1	0.14	0.0033	0.0067	0.14	0.0015	0.0073	0.14	0.0017	0.0073
$1.8 < Q^2[GeV^2] < 4$; $3.7 < \nu[GeV] < 4.3$									
z_h	$\langle P_T^2\rangle_{DC}$	±Stat.	±Syst.	$\langle P_T^2\rangle_{DFe}$	±Stat.	±Syst.	$\langle P_T^2\rangle_{DPb}$	±Stat.	±Syst.
0.1-0.2	0.082	0.00022	0.00054	0.081	0.00018	0.00049	0.081	0.00019	0.00057
0.2-0.3	0.14	0.00047	0.0012	0.14	0.00039	0.0012	0.14	0.00041	0.0012
0.3-0.4	0.18	0.00081	0.0018	0.18	0.00065	0.0017	0.18	0.0007	0.0017
0.4-0.5	0.22	0.0012	0.0024	0.21	0.001	0.0021	0.21	0.0011	0.0023
0.5-0.6	0.24	0.0018	0.0029	0.23	0.0014	0.0023	0.23	0.0015	0.0026
0.6-0.8	0.26	0.0022	0.0066	0.25	0.0017	0.0064	0.26	0.0018	0.0056
0.8-1	0.19	0.0028	0.0084	0.18	0.0019	0.0095	0.19	0.0022	0.0086

Table C.2: Average squared transverse momentum measurements in $[GeV^2]$.

z_h	$\langle P_T^2\rangle_C$	±Stat.	±Syst.	$\langle P_T^2\rangle_{Fe}$	±Stat.	±Syst.	$\langle P_T^2\rangle_{Pb}$	±Stat.	±Syst.
0.1-0.2	0.035	6e-05	0.00081	0.034	5e-05	0.00087	0.034	7.8e-05	0.00085
0.2-0.3	0.085	0.00013	0.00083	0.085	0.00011	0.00077	0.087	0.00017	0.00079
0.3-0.4	0.15	0.00027	0.0014	0.15	0.00024	0.0014	0.15	0.00037	0.0014
0.4-0.5	0.2	0.00047	0.0033	0.21	0.00043	0.0029	0.21	0.0007	0.0031
0.5-0.6	0.23	0.00086	0.0037	0.24	0.00073	0.0028	0.25	0.0011	0.0039
0.6-0.8	0.25	0.0009	0.004	0.26	0.00075	0.0042	0.27	0.0014	0.0054
0.8-1	0.18	0.0015	0.0065	0.19	0.0013	0.0077	0.19	0.003	0.0086
z_h	$\langle P_T^2\rangle_{DC}$	±Stat.	±Syst.	$\langle P_T^2\rangle_{DFe}$	±Stat.	±Syst.	$\langle P_T^2\rangle_{DPb}$	±Stat.	±Syst.
0.1-0.2	0.035	5.5e-05	0.00071	0.035	4.5e-05	0.00077	0.035	4.8e-05	0.00075
0.2-0.3	0.084	0.00011	0.00085	0.084	9.5e-05	0.0008	0.084	0.0001	0.00085
0.3-0.4	0.14	0.00024	0.0014	0.14	0.00019	0.0013	0.14	0.00021	0.0014
0.4-0.5	0.19	0.00041	0.002	0.19	0.00033	0.0019	0.19	0.00036	0.0021
0.5-0.6	0.22	0.00064	0.0026	0.22	0.00052	0.0024	0.22	0.00059	0.0027
0.6-0.8	0.23	0.00068	0.0033	0.23	0.00052	0.003	0.23	0.00056	0.0034
0.8-1	0.16	0.001	0.004	0.15	0.00074	0.0035	0.16	0.0008	0.0034

Table C.3: Integrated average squared transverse momentum in $[GeV^2]$ with $x_f > 0$.

$1 < Q^2[GeV^2] < 1.3$; $2.2 < \nu[GeV] < 3.2$									
z_h	$\langle P_T^2 \rangle_C$	±Stat.	±Syst.	$\langle P_T^2 \rangle_{Fe}$	±Stat.	±Syst.	$\langle P_T^2 \rangle_{Pb}$	±Stat.	±Syst.
0.1-0.2	0.027	0.00013	0.0012	0.027	0.00011	0.0013	0.027	0.00017	0.0012
0.2-0.3	0.068	0.00027	0.001	0.068	0.00023	0.00097	0.069	0.00036	0.00097
0.3-0.4	0.12	0.0006	0.0013	0.13	0.00051	0.0013	0.12	0.0008	0.0013
0.4-0.5	0.18	0.0011	0.0021	0.18	0.00095	0.0022	0.18	0.0015	0.002
0.5-0.6	0.21	0.0023	0.0028	0.22	0.0018	0.0022	0.22	0.0026	0.003
0.6-0.8	0.22	0.0019	0.0031	0.23	0.0017	0.0029	0.24	0.0029	0.003
0.8-1	0.16	0.0028	0.0077	0.17	0.0027	0.0083	0.18	0.0063	0.011
$1 < Q^2[GeV^2] < 1.3$; $3.2 < \nu[GeV] < 3.7$									
z_h	$\langle P_T^2 \rangle_C$	±Stat.	±Syst.	$\langle P_T^2 \rangle_{Fe}$	±Stat.	±Syst.	$\langle P_T^2 \rangle_{Pb}$	±Stat.	±Syst.
0.1-0.2	0.037	0.00019	0.00061	0.036	0.00016	0.0008	0.036	0.00024	0.00082
0.2-0.3	0.094	0.00041	0.00075	0.095	0.00037	0.00085	0.096	0.00056	0.00077
0.3-0.4	0.16	0.00093	0.0017	0.16	0.00084	0.0017	0.17	0.0012	0.0016
0.4-0.5	0.22	0.0017	0.0029	0.22	0.0015	0.003	0.23	0.0024	0.0029
0.5-0.6	0.25	0.0027	0.0033	0.27	0.0025	0.0041	0.28	0.0041	0.0043
0.6-0.8	0.27	0.0037	0.0071	0.29	0.0028	0.0043	0.3	0.0051	0.0063
0.8-1	0.2	0.011	0.014	0.22	0.0091	0.014	0.24	0.014	0.015
$1 < Q^2[GeV^2] < 1.3$; $3.7 < \nu[GeV] < 4.3$									
z_h	$\langle P_T^2 \rangle_C$	±Stat.	±Syst.	$\langle P_T^2 \rangle_{Fe}$	±Stat.	±Syst.	$\langle P_T^2 \rangle_{Pb}$	±Stat.	±Syst.
0.1-0.2	0.044	0.0002	0.00045	0.043	0.00017	0.00048	0.044	0.00025	0.00043
0.2-0.3	0.11	0.00053	0.0013	0.11	0.00045	0.0011	0.11	0.0007	0.0017
0.3-0.4	0.19	0.0011	0.0017	0.19	0.001	0.0018	0.19	0.0015	0.0019
0.4-0.5	0.25	0.0021	0.0031	0.26	0.0018	0.0029	0.27	0.003	0.0034
0.5-0.6	0.29	0.0032	0.004	0.3	0.0031	0.0034	0.31	0.0046	0.0049
0.6-0.8	0.3	0.005	0.0093	0.33	0.0044	0.011	0.33	0.0075	0.012
0.8-1	0.26	0.01	0.012	0.27	0.0087	0.011	0.26	0.014	0.016
$1.3 < Q^2[GeV^2] < 1.8$; $2.2 < \nu[GeV] < 3.2$									
z_h	$\langle P_T^2 \rangle_C$	±Stat.	±Syst.	$\langle P_T^2 \rangle_{Fe}$	±Stat.	±Syst.	$\langle P_T^2 \rangle_{Pb}$	±Stat.	±Syst.
0.1-0.2	0.027	0.00011	0.0014	0.026	8.6e-05	0.0014	0.026	0.00014	0.0014
0.2-0.3	0.066	0.00021	0.00052	0.066	0.00018	0.00054	0.066	0.00029	0.00058
0.3-0.4	0.12	0.00046	0.00095	0.12	0.0004	0.00076	0.12	0.00066	0.00086
0.4-0.5	0.17	0.00085	0.0012	0.18	0.00077	0.0011	0.18	0.0013	0.0016
0.5-0.6	0.21	0.0015	0.002	0.21	0.0012	0.0015	0.22	0.0022	0.002
0.6-0.8	0.22	0.0014	0.0018	0.23	0.0012	0.0023	0.24	0.0022	0.003
0.8-1	0.16	0.0017	0.0053	0.17	0.0015	0.0074	0.17	0.0031	0.008
$1.3 < Q^2[GeV^2] < 1.8$; $3.2 < \nu[GeV] < 3.7$									
z_h	$\langle P_T^2 \rangle_C$	±Stat.	±Syst.	$\langle P_T^2 \rangle_{Fe}$	±Stat.	±Syst.	$\langle P_T^2 \rangle_{Pb}$	±Stat.	±Syst.
0.1-0.2	0.035	0.00015	0.00069	0.034	0.00013	0.00079	0.034	0.0002	0.00093
0.2-0.3	0.089	0.00033	0.00077	0.089	0.00029	0.00082	0.089	0.00045	0.0008
0.3-0.4	0.16	0.0007	0.0016	0.16	0.00077	0.0017	0.16	0.001	0.0018
0.4-0.5	0.21	0.0013	0.0024	0.22	0.0012	0.0024	0.22	0.0019	0.0027
0.5-0.6	0.24	0.002	0.003	0.25	0.0017	0.0036	0.26	0.0031	0.0041

0.6-0.8	0.27	0.0023	0.0034	0.28	0.002	0.0052	0.29	0.0055	0.0053
0.8-1	0.19	0.0051	0.012	0.2	0.0039	0.01	0.2	0.0075	0.0098

$1.3 < Q^2[GeV^2] < 1.8$; $3.7 < \nu[GeV] < 4.3$

z_h	$\langle P_T^2 \rangle_C$	±Stat.	±Syst.	$\langle P_T^2 \rangle_{Fe}$	±Stat.	±Syst.	$\langle P_T^2 \rangle_{Pb}$	±Stat.	±Syst.
0.1-0.2	0.042	0.00017	0.00053	0.041	0.00015	0.00061	0.041	0.00022	0.00064
0.2-0.3	0.11	0.00042	0.00093	0.11	0.0004	0.0013	0.11	0.00061	0.0012
0.3-0.4	0.18	0.00086	0.0018	0.18	0.00079	0.0019	0.19	0.0012	0.0019
0.4-0.5	0.24	0.0016	0.0029	0.25	0.0015	0.0031	0.25	0.0024	0.0035
0.5-0.6	0.28	0.0025	0.003	0.28	0.0021	0.0045	0.3	0.0039	0.0051
0.6-0.8	0.29	0.0037	0.0059	0.3	0.0032	0.0053	0.31	0.0064	0.0056
0.8-1	0.25	0.007	0.0085	0.26	0.0053	0.0086	0.27	0.0096	0.01

$1.8 < Q^2[GeV^2] < 4$; $2.2 < \nu[GeV] < 3.2$

z_h	$\langle P_T^2 \rangle_C$	±Stat.	±Syst.	$\langle P_T^2 \rangle_{Fe}$	±Stat.	±Syst.	$\langle P_T^2 \rangle_{Pb}$	±Stat.	±Syst.
0.1-0.2	0.026	0.00015	0.0016	0.026	0.00012	0.0016	0.026	0.0002	0.0016
0.2-0.3	0.063	0.0003	0.001	0.064	0.00027	0.001	0.064	0.00044	0.0011
0.3-0.4	0.12	0.00067	0.00098	0.12	0.00057	0.0013	0.12	0.00097	0.0014
0.4-0.5	0.17	0.0012	0.0015	0.17	0.0011	0.0016	0.18	0.0018	0.0017
0.5-0.6	0.2	0.002	0.0026	0.21	0.0017	0.0014	0.21	0.0029	0.0018
0.6-0.8	0.22	0.0018	0.0016	0.23	0.0016	0.0022	0.23	0.0031	0.003
0.8-1	0.16	0.0023	0.0053	0.17	0.0022	0.005	0.17	0.0044	0.0055

$1.8 < Q^2[GeV^2] < 4$; $3.2 < \nu[GeV] < 3.7$

z_h	$\langle P_T^2 \rangle_C$	±Stat.	±Syst.	$\langle P_T^2 \rangle_{Fe}$	±Stat.	±Syst.	$\langle P_T^2 \rangle_{Pb}$	±Stat.	±Syst.
0.1-0.2	0.031	0.00014	0.00089	0.031	0.00011	0.00091	0.03	0.00019	0.001
0.2-0.3	0.077	0.00028	0.0011	0.078	0.00025	0.001	0.078	0.00041	0.0011
0.3-0.4	0.14	0.0006	0.0016	0.14	0.00057	0.0015	0.14	0.0009	0.0015
0.4-0.5	0.19	0.0011	0.0021	0.19	0.00098	0.0017	0.2	0.0017	0.0026
0.5-0.6	0.22	0.0017	0.0022	0.23	0.0015	0.0022	0.24	0.0027	0.0031
0.6-0.8	0.24	0.0019	0.0067	0.25	0.0016	0.0083	0.26	0.003	0.0061
0.8-1	0.17	0.0032	0.0046	0.17	0.0028	0.0067	0.18	0.0057	0.0091

$1.8 < Q^2[GeV^2] < 4$; $3.7 < \nu[GeV] < 4.3$

z_h	$\langle P_T^2 \rangle_C$	±Stat.	±Syst.	$\langle P_T^2 \rangle_{Fe}$	±Stat.	±Syst.	$\langle P_T^2 \rangle_{Pb}$	±Stat.	±Syst.
0.1-0.2	0.037	0.00016	0.00063	0.036	0.00014	0.00066	0.036	0.00022	0.00049
0.2-0.3	0.094	0.00034	0.0011	0.094	0.0003	0.001	0.095	0.00049	0.00095
0.3-0.4	0.16	0.00071	0.0018	0.16	0.00065	0.0018	0.17	0.0011	0.0018
0.4-0.5	0.21	0.0013	0.0026	0.22	0.0012	0.0025	0.22	0.002	0.003
0.5-0.6	0.25	0.002	0.0022	0.25	0.002	0.0021	0.27	0.0032	0.0033
0.6-0.8	0.27	0.0036	0.0087	0.28	0.0024	0.0079	0.29	0.0046	0.0093
0.8-1	0.22	0.0039	0.01	0.22	0.0034	0.011	0.24	0.0075	0.0096

$1 < Q^2[GeV^2] < 1.3$; $2.2 < \nu[GeV] < 3.2$

z_h	$\langle P_T^2 \rangle_{DC}$	±Stat.	±Syst.	$\langle P_T^2 \rangle_{DFe}$	±Stat.	±Syst.	$\langle P_T^2 \rangle_{DPb}$	±Stat.	±Syst.
0.1-0.2	0.028	0.00012	0.0011	0.028	9.4e-05	0.0011	0.028	0.0001	0.0012
0.2-0.3	0.068	0.00023	0.00093	0.068	0.00019	0.00091	0.068	0.00021	0.00095
0.3-0.4	0.12	0.0005	0.0012	0.12	0.00042	0.0012	0.12	0.00044	0.0012
0.4-0.5	0.17	0.00092	0.0019	0.17	0.00076	0.002	0.17	0.00082	0.002

0.5-0.6	0.21	0.0016	0.0028	0.21	0.0013	0.0023	0.21	0.0015	0.0028
0.6-0.8	0.21	0.0014	0.0034	0.21	0.0011	0.0031	0.21	0.0012	0.0033
0.8-1	0.14	0.002	0.0032	0.14	0.0014	0.0034	0.14	0.0015	0.0033

$1 < Q^2[GeV^2] < 1.3$; $3.2 < \nu[GeV] < 3.7$

z_h	$\langle P_T^2\rangle_{DC}$	±Stat.	±Syst.	$\langle P_T^2\rangle_{DFe}$	±Stat.	±Syst.	$\langle P_T^2\rangle_{DPb}$	±Stat.	±Syst.
0.1-0.2	0.037	0.00017	0.00062	0.037	0.00015	0.00067	0.037	0.00015	0.00062
0.2-0.3	0.093	0.00038	0.00079	0.094	0.00032	0.00078	0.093	0.00034	0.00088
0.3-0.4	0.16	0.00093	0.002	0.16	0.00073	0.0018	0.16	0.00076	0.0017
0.4-0.5	0.21	0.0014	0.0024	0.21	0.0012	0.0024	0.21	0.0013	0.0024
0.5-0.6	0.24	0.0023	0.0043	0.24	0.0019	0.0027	0.24	0.002	0.0037
0.6-0.8	0.25	0.0033	0.0068	0.25	0.0023	0.006	0.25	0.0024	0.0057
0.8-1	0.17	0.0059	0.0091	0.17	0.0048	0.011	0.18	0.0046	0.011

$1 < Q^2[GeV^2] < 1.3$; $3.7 < \nu[GeV] < 4.3$

z_h	$\langle P_T^2\rangle_{DC}$	±Stat.	±Syst.	$\langle P_T^2\rangle_{DFe}$	±Stat.	±Syst.	$\langle P_T^2\rangle_{DPb}$	±Stat.	±Syst.
0.1-0.2	0.044	0.00019	0.00039	0.044	0.00016	0.00046	0.044	0.00016	0.00039
0.2-0.3	0.11	0.00049	0.0013	0.11	0.00042	0.0013	0.11	0.00042	0.0011
0.3-0.4	0.18	0.00099	0.0019	0.18	0.00085	0.0017	0.18	0.00089	0.0019
0.4-0.5	0.24	0.0017	0.0029	0.23	0.0015	0.0027	0.24	0.0015	0.0028
0.5-0.6	0.27	0.0025	0.0045	0.27	0.0021	0.0036	0.27	0.0022	0.004
0.6-0.8	0.29	0.0039	0.0089	0.28	0.003	0.0079	0.28	0.0032	0.0057
0.8-1	0.24	0.0066	0.0077	0.23	0.0055	0.0093	0.24	0.0074	0.0074

$1.3 < Q^2[GeV^2] < 1.8$; $2.2 < \nu[GeV] < 3.2$

z_h	$\langle P_T^2\rangle_{DC}$	±Stat.	±Syst.	$\langle P_T^2\rangle_{DFe}$	±Stat.	±Syst.	$\langle P_T^2\rangle_{DPb}$	±Stat.	±Syst.
0.1-0.2	0.027	9.8e-05	0.0011	0.027	7.7e-05	0.0011	0.027	8.4e-05	0.0011
0.2-0.3	0.065	0.00019	0.00049	0.066	0.00015	0.00045	0.065	0.00016	0.00053
0.3-0.4	0.12	0.0004	0.00072	0.12	0.00033	0.0007	0.12	0.00035	0.00081
0.4-0.5	0.17	0.00075	0.0011	0.17	0.00059	0.0012	0.17	0.00064	0.0012
0.5-0.6	0.2	0.0011	0.0016	0.2	0.00091	0.0016	0.2	0.00099	0.0018
0.6-0.8	0.21	0.001	0.002	0.21	0.00076	0.0018	0.21	0.00085	0.0019
0.8-1	0.14	0.0011	0.0053	0.14	0.00076	0.0046	0.14	0.00088	0.0047

$1.3 < Q^2[GeV^2] < 1.8$; $3.2 < \nu[GeV] < 3.7$

z_h	$\langle P_T^2\rangle_{DC}$	±Stat.	±Syst.	$\langle P_T^2\rangle_{DFe}$	±Stat.	±Syst.	$\langle P_T^2\rangle_{DPb}$	±Stat.	±Syst.
0.1-0.2	0.035	0.00014	0.00072	0.035	0.00011	0.00076	0.035	0.00012	0.00068
0.2-0.3	0.088	0.00029	0.00072	0.088	0.00025	0.00069	0.087	0.00026	0.00075
0.3-0.4	0.15	0.00064	0.0017	0.15	0.00054	0.0017	0.15	0.00058	0.0017
0.4-0.5	0.2	0.0013	0.0024	0.2	0.00088	0.002	0.2	0.00096	0.0023
0.5-0.6	0.23	0.0018	0.0024	0.23	0.0014	0.0023	0.23	0.0014	0.0025
0.6-0.8	0.25	0.0019	0.0039	0.25	0.0014	0.0039	0.25	0.0015	0.0043
0.8-1	0.17	0.0029	0.0084	0.16	0.0023	0.0089	0.16	0.0023	0.0092

$1.3 < Q^2[GeV^2] < 1.8$; $3.7 < \nu[GeV] < 4.3$

z_h	$\langle P_T^2\rangle_{DC}$	±Stat.	±Syst.	$\langle P_T^2\rangle_{DFe}$	±Stat.	±Syst.	$\langle P_T^2\rangle_{DPb}$	±Stat.	±Syst.
0.1-0.2	0.043	0.00016	0.00052	0.042	0.00013	0.00058	0.042	0.00014	0.00051
0.2-0.3	0.11	0.00038	0.001	0.11	0.00032	0.0011	0.11	0.00033	0.001
0.3-0.4	0.18	0.00076	0.002	0.18	0.00064	0.002	0.18	0.00068	0.0021

0.4-0.5	0.23	0.0014	0.0027	0.22	0.0011	0.0024	0.23	0.0012	0.0026
0.5-0.6	0.25	0.002	0.003	0.25	0.0016	0.003	0.25	0.0017	0.0033
0.6-0.8	0.27	0.0028	0.0066	0.27	0.0021	0.0054	0.27	0.0024	0.0062
0.8-1	0.22	0.0052	0.0069	0.22	0.0039	0.0064	0.22	0.0034	0.0065
$1.8 < Q^2[GeV^2] < 4$; $2.2 < \nu[GeV] < 3.2$									
z_h	$\langle P_T^2 \rangle_{DC}$	±Stat.	±Syst.	$\langle P_T^2 \rangle_{DFe}$	±Stat.	±Syst.	$\langle P_T^2 \rangle_{DPb}$	±Stat.	±Syst.
0.1-0.2	0.027	0.00014	0.0016	0.027	0.00011	0.0015	0.027	0.00012	0.0015
0.2-0.3	0.062	0.00027	0.0011	0.063	0.00022	0.0011	0.063	0.00023	0.0011
0.3-0.4	0.11	0.00056	0.0011	0.11	0.00046	0.0012	0.11	0.00049	0.0012
0.4-0.5	0.16	0.0011	0.0014	0.17	0.00084	0.0025	0.17	0.0009	0.001
0.5-0.6	0.2	0.0016	0.0016	0.2	0.0012	0.00097	0.2	0.0013	0.0011
0.6-0.8	0.2	0.0013	0.0029	0.2	0.00098	0.0016	0.2	0.0011	0.0028
0.8-1	0.14	0.0015	0.0037	0.14	0.0011	0.0031	0.14	0.0013	0.0028
$1.8 < Q^2[GeV^2] < 4$; $3.2 < \nu[GeV] < 3.7$									
z_h	$\langle P_T^2 \rangle_{DC}$	±Stat.	±Syst.	$\langle P_T^2 \rangle_{DFe}$	±Stat.	±Syst.	$\langle P_T^2 \rangle_{DPb}$	±Stat.	±Syst.
0.1-0.2	0.032	0.00013	0.00078	0.032	0.0001	0.00082	0.032	0.00011	0.00078
0.2-0.3	0.077	0.00025	0.0013	0.077	0.0002	0.001	0.076	0.00022	0.0012
0.3-0.4	0.13	0.00053	0.0017	0.13	0.00043	0.0016	0.13	0.00046	0.0017
0.4-0.5	0.18	0.00092	0.0017	0.18	0.00074	0.0018	0.18	0.0008	0.0017
0.5-0.6	0.21	0.0014	0.0017	0.21	0.0011	0.0021	0.21	0.0012	0.0019
0.6-0.8	0.23	0.0014	0.002	0.22	0.001	0.0032	0.23	0.0011	0.002
0.8-1	0.14	0.0033	0.0067	0.14	0.0015	0.0073	0.14	0.0017	0.0073
$1.8 < Q^2[GeV^2] < 4$; $3.7 < \nu[GeV] < 4.3$									
z_h	$\langle P_T^2 \rangle_{DC}$	±Stat.	±Syst.	$\langle P_T^2 \rangle_{DFe}$	±Stat.	±Syst.	$\langle P_T^2 \rangle_{DPb}$	±Stat.	±Syst.
0.1-0.2	0.038	0.00015	0.00058	0.037	0.00012	0.00063	0.037	0.00013	0.00061
0.2-0.3	0.093	0.00031	0.001	0.092	0.00026	0.00099	0.092	0.00027	0.001
0.3-0.4	0.16	0.00063	0.0017	0.15	0.00051	0.0016	0.16	0.00055	0.0017
0.4-0.5	0.2	0.0011	0.0022	0.2	0.00093	0.0021	0.2	0.001	0.0022
0.5-0.6	0.23	0.0017	0.0027	0.23	0.0014	0.0022	0.23	0.0015	0.0024
0.6-0.8	0.26	0.0022	0.0075	0.25	0.0017	0.0063	0.26	0.0018	0.0058
0.8-1	0.19	0.0028	0.0084	0.18	0.0019	0.0095	0.19	0.0022	0.0086

Table C.4: Average squared transverse momentum measurements in $[GeV^2]$ with $x_f > 0$.

C.2 Transverse Momentum Broadening

z_h	$\Delta P^2_{T_C}$	±Stat.	±Syst.	$\Delta P^2_{T_{Fe}}$	±Stat.	±Syst.	$\Delta P^2_{T_{Pb}}$	±Stat.	±Syst.
0.2-0.3	0.014	0.00025	0.00022	0.028	0.00023	0.00037	0.035	0.00033	0.00042
0.3-0.4	0.018	0.00047	0.00052	0.036	0.00043	0.00081	0.045	0.00064	0.001
0.4-0.5	0.02	0.00074	0.0011	0.04	0.00067	0.0014	0.05	0.001	0.0023
0.5-0.6	0.021	0.0012	0.00073	0.039	0.001	0.0018	0.051	0.0015	0.0023
0.6-0.8	0.018	0.0012	0.0017	0.036	0.00096	0.0029	0.043	0.0016	0.0036
0.8-1	0.022	0.0018	0.003	0.033	0.0015	0.0046	0.037	0.0031	0.0056

Table C.5: Integrated transverse momentum broadening results in $[GeV^2]$.

$1 < Q^2[GeV^2] < 1.3$; $2.2 < \nu[GeV] < 3.2$									
z_h	$\Delta P^2_{T_C}$	±Stat.	±Syst.	$\Delta P^2_{T_{Fe}}$	±Stat.	±Syst.	$\Delta P^2_{T_{Pb}}$	±Stat.	±Syst.
0.2-0.3	0.012	0.00056	0.00032	0.022	0.00049	0.00035	0.027	0.00069	0.00054
0.3-0.4	0.017	0.0011	0.00072	0.033	0.00098	0.00064	0.039	0.0014	0.00091
0.4-0.5	0.022	0.0018	0.00057	0.035	0.0016	0.00077	0.041	0.0024	0.0015
0.5-0.6	0.021	0.0032	0.0011	0.033	0.0026	0.0012	0.043	0.0037	0.0026
0.6-0.8	0.014	0.0025	0.0016	0.033	0.0022	0.0022	0.035	0.0034	0.0027
0.8-1	0.017	0.0034	0.0051	0.029	0.003	0.0077	0.034	0.0065	0.0091
$1 < Q^2[GeV^2] < 1.3$; $3.2 < \nu[GeV] < 3.7$									
z_h	$\Delta P^2_{T_C}$	±Stat.	±Syst.	$\Delta P^2_{T_{Fe}}$	±Stat.	±Syst.	$\Delta P^2_{T_{Pb}}$	±Stat.	±Syst.
0.2-0.3	0.015	0.00087	0.00043	0.03	0.00079	0.00095	0.036	0.0011	0.00075
0.3-0.4	0.018	0.0018	0.0012	0.034	0.0016	0.0007	0.041	0.0022	0.001
0.4-0.5	0.019	0.0025	0.0011	0.038	0.0024	0.0015	0.044	0.0036	0.0024
0.5-0.6	0.018	0.0038	0.0019	0.042	0.0034	0.0031	0.056	0.0054	0.0053
0.6-0.8	0.018	0.0051	0.0034	0.04	0.0037	0.0055	0.05	0.0058	0.0079
0.8-1	0.029	0.012	0.012	0.047	0.01	0.009	0.06	0.015	0.01
$1 < Q^2[GeV^2] < 1.3$; $3.7 < \nu[GeV] < 4.3$									
z_h	$\Delta P^2_{T_C}$	±Stat.	±Syst.	$\Delta P^2_{T_{Fe}}$	±Stat.	±Syst.	$\Delta P^2_{T_{Pb}}$	±Stat.	±Syst.
0.2-0.3	0.015	0.0011	0.00048	0.032	0.00098	0.0009	0.039	0.0014	0.0014
0.3-0.4	0.015	0.0019	0.00066	0.034	0.0018	0.0011	0.042	0.0025	0.0013
0.4-0.5	0.019	0.003	0.0014	0.042	0.0028	0.0014	0.056	0.0042	0.0027
0.5-0.6	0.023	0.0043	0.0025	0.047	0.004	0.0034	0.047	0.0055	0.0081
0.6-0.8	0.012	0.0064	0.0082	0.047	0.0054	0.0062	0.055	0.0082	0.01
0.8-1	0.02	0.012	0.0066	0.036	0.01	0.0047	0.023	0.015	0.012
$1.3 < Q^2[GeV^2] < 1.8$; $2.2 < \nu[GeV] < 3.2$									
z_h	$\Delta P^2_{T_C}$	±Stat.	±Syst.	$\Delta P^2_{T_{Fe}}$	±Stat.	±Syst.	$\Delta P^2_{T_{Pb}}$	±Stat.	±Syst.
0.2-0.3	0.013	0.00047	0.00048	0.023	0.0004	0.0015	0.031	0.0006	0.0014
0.3-0.4	0.019	0.00089	0.0008	0.034	0.00079	0.0012	0.044	0.0012	0.0017
0.4-0.5	0.018	0.0014	0.00073	0.035	0.0013	0.0012	0.045	0.002	0.0028
0.5-0.6	0.016	0.0022	0.0016	0.033	0.0018	0.0015	0.044	0.0031	0.0023

0.6-0.8	0.022	0.0018	0.0014	0.031	0.0015	0.002	0.038	0.0025	0.0023
0.8-1	0.023	0.002	0.0022	0.032	0.0017	0.0029	0.032	0.0032	0.0045
$1.3 < Q^2[GeV^2] < 1.8$; $3.2 < \nu[GeV] < 3.7$									
z_h	$\Delta P^2_{T_C}$	±Stat.	±Syst.	$\Delta P^2_{T_{Fe}}$	±Stat.	±Syst.	$\Delta P^2_{T_{Pb}}$	±Stat.	±Syst.
0.2-0.3	0.015	0.00071	0.00048	0.03	0.00063	0.00078	0.038	0.00092	0.00084
0.3-0.4	0.018	0.0013	0.00027	0.035	0.0014	0.00093	0.045	0.0018	0.0011
0.4-0.5	0.021	0.0021	0.00068	0.04	0.0018	0.0012	0.052	0.0028	0.002
0.5-0.6	0.023	0.0029	0.0022	0.042	0.0025	0.0035	0.048	0.0039	0.004
0.6-0.8	0.022	0.003	0.0035	0.035	0.0025	0.007	0.041	0.006	0.0082
0.8-1	0.025	0.0059	0.0062	0.036	0.0045	0.004	0.039	0.0079	0.0063
$1.3 < Q^2[GeV^2] < 1.8$; $3.7 < \nu[GeV] < 4.3$									
z_h	$\Delta P^2_{T_C}$	±Stat.	±Syst.	$\Delta P^2_{T_{Fe}}$	±Stat.	±Syst.	$\Delta P^2_{T_{Pb}}$	±Stat.	±Syst.
0.2-0.3	0.015	0.00087	0.00061	0.03	0.00082	0.001	0.038	0.0012	0.0016
0.3-0.4	0.017	0.0015	0.00056	0.033	0.0014	0.00066	0.047	0.0021	0.0011
0.4-0.5	0.019	0.0024	0.00069	0.044	0.0022	0.0014	0.054	0.0034	0.0028
0.5-0.6	0.025	0.0034	0.0015	0.047	0.0029	0.0036	0.058	0.0047	0.004
0.6-0.8	0.015	0.0048	0.0034	0.037	0.0039	0.0037	0.047	0.0071	0.0056
0.8-1	0.038	0.0087	0.0027	0.045	0.0066	0.0039	0.05	0.01	0.006
$1.8 < Q^2[GeV^2] < 4$; $2.2 < \nu[GeV] < 3.2$									
z_h	$\Delta P^2_{T_C}$	±Stat.	±Syst.	$\Delta P^2_{T_{Fe}}$	±Stat.	±Syst.	$\Delta P^2_{T_{Pb}}$	±Stat.	±Syst.
0.2-0.3	0.014	0.0007	0.0017	0.027	0.00061	0.00039	0.035	0.00094	0.00035
0.3-0.4	0.019	0.0013	0.00079	0.037	0.0012	0.0024	0.048	0.0019	0.00056
0.4-0.5	0.021	0.002	0.0017	0.039	0.0019	0.0038	0.051	0.003	0.0032
0.5-0.6	0.015	0.0029	0.0023	0.035	0.0025	0.0021	0.047	0.0043	0.0054
0.6-0.8	0.021	0.0023	0.0031	0.037	0.002	0.0036	0.038	0.0036	0.0034
0.8-1	0.013	0.0027	0.0045	0.024	0.0024	0.0052	0.023	0.0045	0.0047
$1.8 < Q^2[GeV^2] < 4$; $3.2 < \nu[GeV] < 3.7$									
z_h	$\Delta P^2_{T_C}$	±Stat.	±Syst.	$\Delta P^2_{T_{Fe}}$	±Stat.	±Syst.	$\Delta P^2_{T_{Pb}}$	±Stat.	±Syst.
0.2-0.3	0.017	0.00063	0.0003	0.033	0.00057	0.00058	0.039	0.00088	0.00089
0.3-0.4	0.024	0.0012	0.00059	0.041	0.0011	0.0011	0.05	0.0017	0.0015
0.4-0.5	0.019	0.0017	0.0017	0.043	0.0016	0.0014	0.052	0.0026	0.0033
0.5-0.6	0.02	0.0024	0.0015	0.037	0.0022	0.002	0.056	0.0036	0.0036
0.6-0.8	0.019	0.0024	0.0059	0.034	0.002	0.0059	0.042	0.0035	0.0064
0.8-1	0.026	0.0046	0.0028	0.031	0.0031	0.0037	0.035	0.0059	0.0072
$1.8 < Q^2[GeV^2] < 4$; $3.7 < \nu[GeV] < 4.3$									
z_h	$\Delta P^2_{T_C}$	±Stat.	±Syst.	$\Delta P^2_{T_{Fe}}$	±Stat.	±Syst.	$\Delta P^2_{T_{Pb}}$	±Stat.	±Syst.
0.2-0.3	0.018	0.00076	0.00034	0.035	0.0007	0.00047	0.045	0.0011	0.00042
0.3-0.4	0.018	0.0013	0.00028	0.041	0.0012	0.0008	0.056	0.002	0.0013
0.4-0.5	0.02	0.002	0.00092	0.047	0.0019	0.0012	0.061	0.0032	0.0028
0.5-0.6	0.025	0.0029	0.0013	0.039	0.0027	0.0014	0.066	0.0043	0.003
0.6-0.8	0.014	0.0043	0.0026	0.032	0.0031	0.0031	0.037	0.0051	0.0048
0.8-1	0.027	0.0049	0.0026	0.038	0.0039	0.0015	0.057	0.0078	0.0059

Table C.6: Transverse momentum broadening measurements in $[GeV^2]$.

z_h	$\Delta P^2_{T_C}$	±Stat.	±Syst.	$\Delta P^2_{T_{Fe}}$	±Stat.	±Syst.	$\Delta P^2_{T_{Pb}}$	±Stat.	±Syst.
0.2-0.3	0.00085	0.00017	0.00018	0.0018	0.00015	0.00016	0.0025	0.0002	0.0002
0.3-0.4	0.0036	0.00036	0.0002	0.0074	0.00031	0.00041	0.0089	0.00043	0.00023
0.4-0.5	0.0083	0.00062	0.0017	0.015	0.00054	0.0013	0.018	0.00078	0.0013
0.5-0.6	0.011	0.0011	0.0018	0.022	0.00089	0.0011	0.03	0.0013	0.002
0.6-0.8	0.015	0.0011	0.0022	0.03	0.00091	0.0034	0.036	0.0015	0.0042
0.8-1	0.022	0.0018	0.0029	0.033	0.0015	0.0048	0.037	0.0031	0.0059

Table C.7: Integrated transverse momentum broadening results in $[GeV^2]$ with $x_f > 0$.

$1 < Q^2[GeV^2] < 1.3$; $2.2 < \nu[GeV] < 3.2$									
z_h	$\Delta P^2_{T_C}$	±Stat.	±Syst.	$\Delta P^2_{T_{Fe}}$	±Stat.	±Syst.	$\Delta P^2_{T_{Pb}}$	±Stat.	±Syst.
0.2-0.3	0.00017	0.00035	0.00016	0.00075	0.0003	0.0001	0.0013	0.00041	0.00011
0.3-0.4	0.0015	0.00078	0.0005	0.0051	0.00066	0.00033	0.0044	0.00091	0.00034
0.4-0.5	0.0069	0.0014	0.00034	0.0093	0.0012	0.00047	0.0089	0.0017	0.0008
0.5-0.6	0.0072	0.0028	0.00065	0.012	0.0022	0.001	0.017	0.003	0.0014
0.6-0.8	0.01	0.0024	0.001	0.025	0.002	0.002	0.027	0.0031	0.0023
0.8-1	0.017	0.0034	0.0052	0.029	0.003	0.0077	0.034	0.0065	0.0092
$1 < Q^2[GeV^2] < 1.3$; $3.2 < \nu[GeV] < 3.7$									
z_h	$\Delta P^2_{T_C}$	±Stat.	±Syst.	$\Delta P^2_{T_{Fe}}$	±Stat.	±Syst.	$\Delta P^2_{T_{Pb}}$	±Stat.	±Syst.
0.2-0.3	0.00036	0.00056	0.00033	0.0016	0.00049	0.00029	0.0024	0.00065	0.00024
0.3-0.4	0.0053	0.0013	0.0011	0.0072	0.0011	0.00029	0.0087	0.0014	0.00076
0.4-0.5	0.011	0.0022	0.00061	0.017	0.0019	0.00083	0.015	0.0027	0.0011
0.5-0.6	0.012	0.0035	0.0021	0.03	0.0031	0.0021	0.035	0.0046	0.0025
0.6-0.8	0.016	0.0049	0.0035	0.036	0.0036	0.0055	0.047	0.0056	0.0074
0.8-1	0.029	0.012	0.012	0.047	0.01	0.009	0.06	0.015	0.01
$1 < Q^2[GeV^2] < 1.3$; $3.7 < \nu[GeV] < 4.3$									
z_h	$\Delta P^2_{T_C}$	±Stat.	±Syst.	$\Delta P^2_{T_{Fe}}$	±Stat.	±Syst.	$\Delta P^2_{T_{Pb}}$	±Stat.	±Syst.
0.2-0.3	0.00051	0.00072	0.00034	0.0029	0.00062	0.00056	0.0031	0.00081	0.00077
0.3-0.4	0.0043	0.0015	0.00028	0.01	0.0013	0.0004	0.011	0.0017	0.00042
0.4-0.5	0.011	0.0027	0.001	0.025	0.0024	0.00072	0.032	0.0034	0.00091
0.5-0.6	0.018	0.0041	0.0017	0.039	0.0038	0.0027	0.039	0.0051	0.0028
0.6-0.8	0.0094	0.0063	0.0082	0.045	0.0053	0.0058	0.055	0.0081	0.0087
0.8-1	0.02	0.012	0.0067	0.036	0.01	0.0046	0.023	0.015	0.012
$1.3 < Q^2[GeV^2] < 1.8$; $2.2 < \nu[GeV] < 3.2$									
z_h	$\Delta P^2_{T_C}$	±Stat.	±Syst.	$\Delta P^2_{T_{Fe}}$	±Stat.	±Syst.	$\Delta P^2_{T_{Pb}}$	±Stat.	±Syst.
0.2-0.3	0.00074	0.00028	7.1e-05	0.0006	0.00024	0.00011	0.00099	0.00034	0.00018
0.3-0.4	0.0021	0.00061	0.00051	0.0041	0.00052	0.00022	0.0051	0.00075	0.00036
0.4-0.5	0.0028	0.0011	0.00024	0.0056	0.00097	0.00055	0.0088	0.0014	0.001
0.5-0.6	0.004	0.0019	0.00051	0.011	0.0015	0.0004	0.017	0.0024	0.00096
0.6-0.8	0.018	0.0017	0.0013	0.023	0.0014	0.0022	0.029	0.0023	0.0023
0.8-1	0.023	0.002	0.0021	0.032	0.0017	0.0029	0.032	0.0032	0.0045

$1.3 < Q^2[GeV^2] < 1.8$; $3.2 < \nu[GeV] < 3.7$									
z_h	$\Delta P^2_{T_C}$	±Stat.	±Syst.	$\Delta P^2_{T_{Fe}}$	±Stat.	±Syst.	$\Delta P^2_{T_{Pb}}$	±Stat.	±Syst.
0.2-0.3	0.0011	0.00044	9.4e-05	0.0013	0.00038	0.00019	0.0019	0.00052	7.3e-05
0.3-0.4	0.0034	0.00095	0.00028	0.006	0.00094	0.0006	0.0074	0.0012	0.00053
0.4-0.5	0.011	0.0018	0.00065	0.017	0.0015	0.00051	0.021	0.0021	0.00074
0.5-0.6	0.015	0.0027	0.0017	0.026	0.0022	0.0027	0.032	0.0034	0.0021
0.6-0.8	0.019	0.003	0.0033	0.03	0.0024	0.0064	0.035	0.0057	0.0071
0.8-1	0.025	0.0059	0.0063	0.036	0.0045	0.0042	0.039	0.0079	0.0063
$1.3 < Q^2[GeV^2] < 1.8$; $3.7 < \nu[GeV] < 4.3$									
z_h	$\Delta P^2_{T_C}$	±Stat.	±Syst.	$\Delta P^2_{T_{Fe}}$	±Stat.	±Syst.	$\Delta P^2_{T_{Pb}}$	±Stat.	±Syst.
0.2-0.3	0.0013	0.00056	0.00022	0.0023	0.00052	0.00038	0.0023	0.00069	0.00052
0.3-0.4	0.0044	0.0011	0.00038	0.0081	0.001	0.00036	0.013	0.0014	0.00032
0.4-0.5	0.011	0.0021	0.00078	0.024	0.0018	0.00076	0.025	0.0026	0.001
0.5-0.6	0.021	0.0032	0.001	0.033	0.0026	0.0028	0.047	0.0042	0.0025
0.6-0.8	0.013	0.0047	0.0035	0.032	0.0038	0.0043	0.044	0.0068	0.0054
0.8-1	0.038	0.0087	0.0027	0.045	0.0066	0.004	0.05	0.01	0.0067
$1.8 < Q^2[GeV^2] < 4$; $2.2 < \nu[GeV] < 3.2$									
z_h	$\Delta P^2_{T_C}$	±Stat.	±Syst.	$\Delta P^2_{T_{Fe}}$	±Stat.	±Syst.	$\Delta P^2_{T_{Pb}}$	±Stat.	±Syst.
0.2-0.3	0.00017	0.0004	0.00014	0.001	0.00034	0.00013	0.00096	0.0005	5.2e-05
0.3-0.4	0.0023	0.00087	0.00069	0.0048	0.00073	0.00019	0.0039	0.0011	0.00049
0.4-0.5	0.0037	0.0016	0.0014	0.0061	0.0013	0.0015	0.011	0.002	0.0012
0.5-0.6	0.0032	0.0026	0.0018	0.011	0.0021	0.00093	0.013	0.0032	0.0013
0.6-0.8	0.016	0.0022	0.0035	0.027	0.0018	0.0033	0.029	0.0033	0.0037
0.8-1	0.013	0.0027	0.0045	0.024	0.0024	0.0052	0.023	0.0045	0.0047
$1.8 < Q^2[GeV^2] < 4$; $3.2 < \nu[GeV] < 3.7$									
z_h	$\Delta P^2_{T_C}$	±Stat.	±Syst.	$\Delta P^2_{T_{Fe}}$	±Stat.	±Syst.	$\Delta P^2_{T_{Pb}}$	±Stat.	±Syst.
0.2-0.3	0.00062	0.00038	0.00022	0.0013	0.00032	4.9e-05	0.0019	0.00047	0.00027
0.3-0.4	0.005	0.0008	0.00044	0.0068	0.00071	0.00047	0.0071	0.001	0.00052
0.4-0.5	0.0048	0.0014	0.00075	0.012	0.0012	0.00033	0.014	0.0018	0.0011
0.5-0.6	0.01	0.0022	0.00088	0.017	0.0019	0.00037	0.03	0.0029	0.0015
0.6-0.8	0.015	0.0023	0.0053	0.027	0.0019	0.0052	0.033	0.0032	0.0051
0.8-1	0.026	0.0046	0.0029	0.031	0.0031	0.0039	0.035	0.0059	0.0072
$1.8 < Q^2[GeV^2] < 4$; $3.7 < \nu[GeV] < 4.3$									
z_h	$\Delta P^2_{T_C}$	±Stat.	±Syst.	$\Delta P^2_{T_{Fe}}$	±Stat.	±Syst.	$\Delta P^2_{T_{Pb}}$	±Stat.	±Syst.
0.2-0.3	0.0011	0.00046	0.00011	0.0021	0.0004	0.00017	0.0029	0.00056	0.00016
0.3-0.4	0.0028	0.00095	0.00025	0.0077	0.00082	0.0003	0.011	0.0012	0.00043
0.4-0.5	0.008	0.0017	0.00056	0.02	0.0015	0.00062	0.02	0.0022	0.001
0.5-0.6	0.016	0.0027	0.00083	0.024	0.0024	0.00061	0.042	0.0036	0.0017
0.6-0.8	0.01	0.0042	0.0028	0.026	0.003	0.0024	0.033	0.0049	0.004
0.8-1	0.027	0.0049	0.0026	0.038	0.0039	0.002	0.057	0.0078	0.006

Table C.8: Transverse momentum broadening measurements in $[GeV^2]$ with $x_f > 0$.

C.3 Intrinsic Parton Momentum

C.3.1 Fit With Analytic Function

Target	χ^2_{ndf}	$Q^2[GeV^2]$	$\nu[GeV]$	$\langle k_\perp^2\rangle[GeV^2]$	$\delta\langle k_\perp^2\rangle[GeV^2]$
DC	12.9	1-1.3	2.2-3.2	0.0653	±0.0217
		1-1.3	3.2-3.7	0.166	±0.0229
		1-1.3	3.7-4.26	0.256	±0.0227
		1.3-1.8	2.2-3.2	0.0531	±0.0221
		1.3-1.8	3.2-3.7	0.139	±0.0223
		1.3-1.8	3.7-4.26	0.212	±0.0222
		1.8-4	2.2-3.2	0.0531	±0.0217
		1.8-4	3.2-3.7	0.0902	±0.0223
		1.8-4	3.7-4.26	0.157	±0.0221

Table C.9: Deuterium (C) global fit with Hypothesis 1. x_f cut applied.

Target	χ^2_{ndf}	$Q^2[GeV^2]$	$\nu[GeV]$	$\langle k_\perp^2\rangle[GeV^2]$	$\delta\langle k_\perp^2\rangle[GeV^2]$
DFe	11.2	1-1.3	2.2-3.2	0.0809	±0.0157
		1-1.3	3.2-3.7	0.18	±0.0167
		1-1.3	3.7-4.26	0.261	±0.017
		1.3-1.8	2.2-3.2	0.0725	±0.016
		1.3-1.8	3.2-3.7	0.153	±0.0163
		1.3-1.8	3.7-4.26	0.22	±0.0163
		1.8-4	2.2-3.2	0.0711	±0.0156
		1.8-4	3.2-3.7	0.099	±0.0162
		1.8-4	3.7-4.26	0.167	±0.0162

Table C.10: Deuterium (Fe) global fit with Hypothesis 1. x_f cut applied.

Target	χ^2_{ndf}	$Q^2[GeV^2]$	$\nu[GeV]$	$\langle k_\perp^2\rangle[GeV^2]$	$\delta\langle k_\perp^2\rangle[GeV^2]$
DPb	14.9	1-1.3	2.2-3.2	0.0782	±0.0189
		1-1.3	3.2-3.7	0.183	±0.0201
		1-1.3	3.7-4.26	0.258	±0.02
		1.3-1.8	2.2-3.2	0.0659	±0.0193
		1.3-1.8	3.2-3.7	0.154	±0.0195
		1.3-1.8	3.7-4.26	0.22	±0.0194
		1.8-4	2.2-3.2	0.0651	±0.0187
		1.8-4	3.2-3.7	0.101	±0.0195
		1.8-4	3.7-4.26	0.167	±0.0193

Table C.11: Deuterium (Pb) global fit with Hypothesis 1. x_f cut applied.

Target	χ^2_{ndf}	$Q^2[GeV^2]$	$\nu[GeV]$	$\langle k_\perp^2 \rangle [GeV^2]$	$\delta\langle k_\perp^2 \rangle [GeV^2]$
DC	7.6	1-1.3	2.2-3.2	0.0243	±0.00477
		1-1.3	3.2-3.7	0.114	±0.00788
		1-1.3	3.7-4.26	0.196	±0.00867
		1.3-1.8	2.2-3.2	0.0135	±0.00454
		1.3-1.8	3.2-3.7	0.0893	±0.00614
		1.3-1.8	3.7-4.26	0.158	±0.00714
		1.8-4	2.2-3.2	0.01	±0.0195
		1.8-4	3.2-3.7	0.0445	±0.00502
		1.8-4	3.7-4.26	0.102	±0.00687

Table C.12: Deuterium (C) global fit with Hypothesis 1. x_f cut not applied.

Target	χ^2_{ndf}	$Q^2[GeV^2]$	$\nu[GeV]$	$\langle k_\perp^2 \rangle [GeV^2]$	$\delta\langle k_\perp^2 \rangle [GeV^2]$
DFe	6.17	1-1.3	2.2-3.2	0.023	±0.00415
		1-1.3	3.2-3.7	0.108	±0.00696
		1-1.3	3.7-4.26	0.184	±0.00793
		1.3-1.8	2.2-3.2	0.0145	±0.00365
		1.3-1.8	3.2-3.7	0.0871	±0.00546
		1.3-1.8	3.7-4.26	0.148	±0.00609
		1.8-4	2.2-3.2	0.01	±0.0614
		1.8-4	3.2-3.7	0.0343	±0.00503
		1.8-4	3.7-4.26	0.0947	±0.00617

Table C.13: Deuterium (Fe) global fit with Hypothesis 1. x_f cut not applied.

Target	χ^2_{ndf}	$Q^2[GeV^2]$	$\nu[GeV]$	$\langle k_\perp^2 \rangle [GeV^2]$	$\delta\langle k_\perp^2 \rangle [GeV^2]$
DPb	7.55	1-1.3	2.2-3.2	0.0223	±0.00454
		1-1.3	3.2-3.7	0.112	±0.0074
		1-1.3	3.7-4.26	0.185	±0.00775
		1.3-1.8	2.2-3.2	0.01	±0.0155
		1.3-1.8	3.2-3.7	0.0878	±0.00596
		1.3-1.8	3.7-4.26	0.151	±0.00658
		1.8-4	2.2-3.2	0.0106	±0.00672
		1.8-4	3.2-3.7	0.0383	±0.0046
		1.8-4	3.7-4.26	0.0971	±0.00635

Table C.14: Deuterium (Pb) global fit with Hypothesis 1. x_f cut not applied.

Target	χ^2_{ndf}	$Q^2[GeV^2]$	$\nu[GeV]$	$\langle k_\perp^2 \rangle [GeV^2]$	$\delta\langle k_\perp^2 \rangle [GeV^2]$
DC	18	1-1.3	2.2-3.2	0.0715	±0.0184
		1-1.3	3.2-3.7	0.13	±0.0188
		1-1.3	3.7-4.26	0.215	±0.0184
		1.3-1.8	2.2-3.2	0.0715	±0.0184
		1.3-1.8	3.2-3.7	0.13	±0.0188
		1.3-1.8	3.7-4.26	0.215	±0.0184
		1.8-4	2.2-3.2	0.0715	±0.0184
		1.8-4	3.2-3.7	0.13	±0.0188
		1.8-4	3.7-4.26	0.215	±0.0184

Table C.15: Deuterium (C) global fit with Hypothesis 2. x_f cut applied.

Target	χ^2_{ndf}	$Q^2[GeV^2]$	$\nu[GeV]$	$\langle k_\perp^2 \rangle [GeV^2]$	$\delta\langle k_\perp^2 \rangle [GeV^2]$
DFe	17.7	1-1.3	2.2-3.2	0.0779	±0.0149
		1-1.3	3.2-3.7	0.137	±0.0151
		1-1.3	3.7-4.26	0.211	±0.015
		1.3-1.8	2.2-3.2	0.0779	±0.0149
		1.3-1.8	3.2-3.7	0.137	±0.0151
		1.3-1.8	3.7-4.26	0.211	±0.015
		1.8-4	2.2-3.2	0.0779	±0.0149
		1.8-4	3.2-3.7	0.137	±0.0151
		1.8-4	3.7-4.26	0.211	±0.015

Table C.16: Deuterium (Fe) global fit with Hypothesis 2. x_f cut applied.

Target	χ^2_{ndf}	$Q^2[GeV^2]$	$\nu[GeV]$	$\langle k_\perp^2 \rangle [GeV^2]$	$\delta\langle k_\perp^2 \rangle [GeV^2]$
DPb	20.9	1-1.3	2.2-3.2	0.0788	±0.0163
		1-1.3	3.2-3.7	0.138	±0.0168
		1-1.3	3.7-4.26	0.218	±0.0164
		1.3-1.8	2.2-3.2	0.0788	±0.0163
		1.3-1.8	3.2-3.7	0.138	±0.0168
		1.3-1.8	3.7-4.26	0.218	±0.0164
		1.8-4	2.2-3.2	0.0788	±0.0163
		1.8-4	3.2-3.7	0.138	±0.0168
		1.8-4	3.7-4.26	0.218	±0.0164

Table C.17: Deuterium (Pb) global fit with Hypothesis 2. x_f cut applied.

Target	χ^2_{ndf}	$Q^2[GeV^2]$	$\nu[GeV]$	$\langle k_\perp^2 \rangle [GeV^2]$	$\delta\langle k_\perp^2 \rangle [GeV^2]$
DC	12.7	1-1.3	2.2-3.2	0.01	±0.0549
		1-1.3	3.2-3.7	0.0633	±0.0104
		1-1.3	3.7-4.26	0.138	±0.0107
		1.3-1.8	2.2-3.2	0.01	±0.0549
		1.3-1.8	3.2-3.7	0.0633	±0.0104
		1.3-1.8	3.7-4.26	0.138	±0.0107
		1.8-4	2.2-3.2	0.01	±0.0549
		1.8-4	3.2-3.7	0.0633	±0.0104
		1.8-4	3.7-4.26	0.138	±0.0107

Table C.18: Deuterium (C) global fit with Hypothesis 2. x_f cut not applied.

Target	χ^2_{ndf}	$Q^2[GeV^2]$	$\nu[GeV]$	$\langle k_\perp^2 \rangle [GeV^2]$	$\delta\langle k_\perp^2 \rangle [GeV^2]$
DFe	12.4	1-1.3	2.2-3.2	0.01	±0.277
		1-1.3	3.2-3.7	0.0637	±0.025
		1-1.3	3.7-4.26	0.13	±0.0251
		1.3-1.8	2.2-3.2	0.01	±0.277
		1.3-1.8	3.2-3.7	0.0637	±0.025
		1.3-1.8	3.7-4.26	0.13	±0.0251
		1.8-4	2.2-3.2	0.01	±0.277
		1.8-4	3.2-3.7	0.0637	±0.025
		1.8-4	3.7-4.26	0.13	±0.0251

Table C.19: Deuterium (Fe) global fit with Hypothesis 2. x_f cut not applied.

Target	χ^2_{ndf}	$Q^2[GeV^2]$	$\nu[GeV]$	$\langle k_\perp^2 \rangle [GeV^2]$	$\delta\langle k_\perp^2 \rangle [GeV^2]$
DPb	13.8	1-1.3	2.2-3.2	0.01	±0.0272
		1-1.3	3.2-3.7	0.0604	±0.00327
		1-1.3	3.7-4.26	0.134	±0.00396
		1.3-1.8	2.2-3.2	0.01	±0.0272
		1.3-1.8	3.2-3.7	0.0604	±0.00327
		1.3-1.8	3.7-4.26	0.134	±0.00396
		1.8-4	2.2-3.2	0.01	±0.0272
		1.8-4	3.2-3.7	0.0604	±0.00327
		1.8-4	3.7-4.26	0.134	±0.00396

Table C.20: Deuterium (Pb) global fit with Hypothesis 2. x_f cut not applied.

Target	χ^2_{ndf}	$Q^2[GeV^2]$	$\nu[GeV]$	$\langle k_\perp^2 \rangle [GeV^2]$	$\delta\langle k_\perp^2 \rangle [GeV^2]$
C	3.53	1-1.3	2.2-3.2	0.0348	±0.0655
		1-1.3	3.2-3.7	0.131	±0.0723
		1-1.3	3.7-4.26	0.22	±0.0715
		1.3-1.8	2.2-3.2	0.0332	±0.0649
		1.3-1.8	3.2-3.7	0.115	±0.0724
		1.3-1.8	3.7-4.26	0.182	±0.0719
		1.8-4	2.2-3.2	0.0236	±0.161
		1.8-4	3.2-3.7	0.0533	±0.0686
		1.8-4	3.7-4.26	0.123	±0.0714

Table C.21: C global fit with Hypothesis 1. x_f cut not applied.

Target	χ^2_{ndf}	$Q^2[GeV^2]$	$\nu[GeV]$	$\langle k_\perp^2 \rangle [GeV^2]$	$\delta\langle k_\perp^2 \rangle [GeV^2]$
Fe	3.71	1-1.3	2.2-3.2	0.0194	±0.00616
		1-1.3	3.2-3.7	0.12	±0.00863
		1-1.3	3.7-4.26	0.208	±0.0102
		1.3-1.8	2.2-3.2	0.01	±0.201
		1.3-1.8	3.2-3.7	0.0936	±0.00807
		1.3-1.8	3.7-4.26	0.165	±0.00841
		1.8-4	2.2-3.2	0.0114	±0.00552
		1.8-4	3.2-3.7	0.0357	±0.00771
		1.8-4	3.7-4.26	0.107	±0.00824

Table C.22: Fe global fit with Hypothesis 1. x_f cut not applied.

Target	χ^2_{ndf}	$Q^2[GeV^2]$	$\nu[GeV]$	$\langle k_\perp^2 \rangle [GeV^2]$	$\delta\langle k_\perp^2 \rangle [GeV^2]$
Pb	2.54	1-1.3	2.2-3.2	0.0761	±0.0393
		1-1.3	3.2-3.7	0.193	±0.0407
		1-1.3	3.7-4.26	0.268	±0.0341
		1.3-1.8	2.2-3.2	0.0763	±0.0439
		1.3-1.8	3.2-3.7	0.154	±0.0404
		1.3-1.8	3.7-4.26	0.239	±0.0373
		1.8-4	2.2-3.2	0.0751	±0.041
		1.8-4	3.2-3.7	0.109	±0.0404
		1.8-4	3.7-4.26	0.196	±0.0387

Table C.23: Pb global fit with Hypothesis 1. x_f cut not applied.

Target	χ^2_{ndf}	$Q^2[GeV^2]$	$\nu[GeV]$	$\langle k_\perp^2 \rangle [GeV^2]$	$\delta\langle k_\perp^2 \rangle [GeV^2]$
C	12.6	1-1.3	2.2-3.2	0.0908	±0.00814
		1-1.3	3.2-3.7	0.22	±0.0176
		1-1.3	3.7-4.26	0.3	±0.00123
		1.3-1.8	2.2-3.2	0.0881	±0.0063
		1.3-1.8	3.2-3.7	0.193	±0.0127
		1.3-1.8	3.7-4.26	0.269	±0.0131
		1.8-4	2.2-3.2	0.0806	±0.00623
		1.8-4	3.2-3.7	0.118	±0.00824
		1.8-4	3.7-4.26	0.204	±0.0169

Table C.24: C global fit with Hypothesis 1. x_f cut applied.

Target	χ^2_{ndf}	$Q^2[GeV^2]$	$\nu[GeV]$	$\langle k_\perp^2 \rangle [GeV^2]$	$\delta\langle k_\perp^2 \rangle [GeV^2]$
Fe	15.2	1-1.3	2.2-3.2	0.0281	±0.00391
		1-1.3	3.2-3.7	0.16	±0.00892
		1-1.3	3.7-4.26	0.278	±0.01
		1.3-1.8	2.2-3.2	0.0145	±0.00199
		1.3-1.8	3.2-3.7	0.127	±0.0071
		1.3-1.8	3.7-4.26	0.207	±0.00871
		1.8-4	2.2-3.2	0.0101	±0.000231
		1.8-4	3.2-3.7	0.0552	±0.00593
		1.8-4	3.7-4.26	0.147	±0.00717

Table C.25: Fe global fit with Hypothesis 1. x_f cut applied.

Target	χ^2_{ndf}	$Q^2[GeV^2]$	$\nu[GeV]$	$\langle k_\perp^2 \rangle [GeV^2]$	$\delta\langle k_\perp^2 \rangle [GeV^2]$
Pb	9.93	1-1.3	2.2-3.2	0.0356	±0.0137
		1-1.3	3.2-3.7	0.19	±0.0157
		1-1.3	3.7-4.26	0.3	±0.016
		1.3-1.8	2.2-3.2	0.0288	±0.0132
		1.3-1.8	3.2-3.7	0.149	±0.0147
		1.3-1.8	3.7-4.26	0.243	±0.0155
		1.8-4	2.2-3.2	0.0259	±0.0132
		1.8-4	3.2-3.7	0.0811	±0.0141
		1.8-4	3.7-4.26	0.18	±0.0148

Table C.26: Pb global fit with Hypothesis 1. x_f cut applied.

Target	χ^2_{ndf}	$Q^2[GeV^2]$	$\nu[GeV]$	$\langle k_\perp^2 \rangle [GeV^2]$	$\delta\langle k_\perp^2 \rangle [GeV^2]$
C	8.05	1-1.3	2.2-3.2	0.01	±0.0361
		1-1.3	3.2-3.7	0.0703	±0.00437
		1-1.3	3.7-4.26	0.145	±0.00521
		1.3-1.8	2.2-3.2	0.01	±0.0361
		1.3-1.8	3.2-3.7	0.0703	±0.00437
		1.3-1.8	3.7-4.26	0.145	±0.00521
		1.8-4	2.2-3.2	0.01	±0.0361
		1.8-4	3.2-3.7	0.0703	±0.00437
		1.8-4	3.7-4.26	0.145	±0.00521

Table C.27: C global fit with Hypothesis 2. x_f cut not applied.

Target	χ^2_{ndf}	$Q^2[GeV^2]$	$\nu[GeV]$	$\langle k_\perp^2 \rangle [GeV^2]$	$\delta\langle k_\perp^2 \rangle [GeV^2]$
Fe	8.05	1-1.3	2.2-3.2	0.01	±0.0236
		1-1.3	3.2-3.7	0.0762	±0.0048
		1-1.3	3.7-4.26	0.15	±0.00523
		1.3-1.8	2.2-3.2	0.01	±0.0236
		1.3-1.8	3.2-3.7	0.0762	±0.0048
		1.3-1.8	3.7-4.26	0.15	±0.00523
		1.8-4	2.2-3.2	0.01	±0.0236
		1.8-4	3.2-3.7	0.0762	±0.0048
		1.8-4	3.7-4.26	0.15	±0.00523

Table C.28: Fe global fit with Hypothesis 2. x_f cut not applied.

Target	χ^2_{ndf}	$Q^2[GeV^2]$	$\nu[GeV]$	$\langle k_\perp^2 \rangle [GeV^2]$	$\delta\langle k_\perp^2 \rangle [GeV^2]$
Pb	3.77	1-1.3	2.2-3.2	0.0688	±0.0506
		1-1.3	3.2-3.7	0.136	±0.0507
		1-1.3	3.7-4.26	0.219	±0.0503
		1.3-1.8	2.2-3.2	0.0688	±0.0506
		1.3-1.8	3.2-3.7	0.136	±0.0507
		1.3-1.8	3.7-4.26	0.219	±0.0503
		1.8-4	2.2-3.2	0.0688	±0.0506
		1.8-4	3.2-3.7	0.136	±0.0507
		1.8-4	3.7-4.26	0.219	±0.0503

Table C.29: Pb global fit with Hypothesis 2. x_f cut not applied.

Target	χ^2_{ndf}	$Q^2[GeV^2]$	$\nu[GeV]$	$\langle k_\perp^2 \rangle [GeV^2]$	$\delta\langle k_\perp^2 \rangle [GeV^2]$
C	18.5	1-1.3	2.2-3.2	0.01	±0.0666
		1-1.3	3.2-3.7	0.0873	±0.217
		1-1.3	3.7-4.26	0.18	±0.0973
		1.3-1.8	2.2-3.2	0.01	±0.0666
		1.3-1.8	3.2-3.7	0.0873	±0.217
		1.3-1.8	3.7-4.26	0.18	±0.0973
		1.8-4	2.2-3.2	0.01	±0.0666
		1.8-4	3.2-3.7	0.0873	±0.217
		1.8-4	3.7-4.26	0.18	±0.0973

Table C.30: C global fit with Hypothesis 2. x_f cut applied.

Target	χ^2_{ndf}	$Q^2[GeV^2]$	$\nu[GeV]$	$\langle k_\perp^2 \rangle [GeV^2]$	$\delta\langle k_\perp^2 \rangle [GeV^2]$
Fe	22.9	1-1.3	2.2-3.2	0.01	±0.0331
		1-1.3	3.2-3.7	0.0961	±0.00407
		1-1.3	3.7-4.26	0.192	±0.00465
		1.3-1.8	2.2-3.2	0.01	±0.0331
		1.3-1.8	3.2-3.7	0.0961	±0.00407
		1.3-1.8	3.7-4.26	0.192	±0.00465
		1.8-4	2.2-3.2	0.01	±0.0331
		1.8-4	3.2-3.7	0.0961	±0.00407
		1.8-4	3.7-4.26	0.192	±0.00465

Table C.31: Fe global fit with Hypothesis 2. x_f cut applied.

Target	χ^2_{ndf}	$Q^2[GeV^2]$	$\nu[GeV]$	$\langle k_\perp^2 \rangle [GeV^2]$	$\delta\langle k_\perp^2 \rangle [GeV^2]$
Pb	13.5	1-1.3	2.2-3.2	0.0607	±0.0336
		1-1.3	3.2-3.7	0.159	±0.0336
		1-1.3	3.7-4.26	0.259	±0.0332
		1.3-1.8	2.2-3.2	0.0607	±0.0336
		1.3-1.8	3.2-3.7	0.159	±0.0336
		1.3-1.8	3.7-4.26	0.259	±0.0332
		1.8-4	2.2-3.2	0.0607	±0.0336
		1.8-4	3.2-3.7	0.159	±0.0336
		1.8-4	3.7-4.26	0.259	±0.0332

Table C.32: Pb global fit with Hypothesis 2. x_f cut applied.

C.3.2 Fit With Numerical Integration

Target	χ^2_{ndf}	$Q^2[GeV^2]$	$\nu[GeV]$	$\langle k_\perp^2\rangle[GeV^2]$	$\delta\langle k_\perp^2\rangle[GeV^2]$
DC	14.3	1-1.3	2.2-3.2	0.0779	±0.00768
		1-1.3	3.2-3.7	0.115	±0.0192
		1-1.3	3.7-4.26	0.3	±0.00878
		1.3-1.8	2.2-3.2	0.0978	±0.0062
		1.3-1.8	3.2-3.7	0.0999	±0.00984
		1.3-1.8	3.7-4.26	0.127	±0.0125
		1.8-4	2.2-3.2	0.121	±0.00575
		1.8-4	3.2-3.7	0.0754	±0.00831
		1.8-4	3.7-4.26	0.0826	±0.0108

Table C.33: Deuterium (C) global fit with Hypothesis 1. x_f cut applied.

Target	χ^2_{ndf}	$Q^2[GeV^2]$	$\nu[GeV]$	$\langle k_\perp^2\rangle[GeV^2]$	$\delta\langle k_\perp^2\rangle[GeV^2]$
DFe	19.2	1-1.3	2.2-3.2	0.0972	±0.00701
		1-1.3	3.2-3.7	0.167	±0.0267
		1-1.3	3.7-4.26	0.3	±0.006
		1.3-1.8	2.2-3.2	0.121	±0.00541
		1.3-1.8	3.2-3.7	0.126	±0.00864
		1.3-1.8	3.7-4.26	0.173	±0.0124
		1.8-4	2.2-3.2	0.141	±0.00463
		1.8-4	3.2-3.7	0.0961	±0.00766
		1.8-4	3.7-4.26	0.0931	±0.00929

Table C.34: Deuterium (Fe) global fit with Hypothesis 1. x_f cut applied.

Target	χ^2_{ndf}	$Q^2[GeV^2]$	$\nu[GeV]$	$\langle k_\perp^2\rangle[GeV^2]$	$\delta\langle k_\perp^2\rangle[GeV^2]$
DPb	18	1-1.3	2.2-3.2	0.0902	±0.00565
		1-1.3	3.2-3.7	0.162	±0.0238
		1-1.3	3.7-4.26	0.3	±0.00647
		1.3-1.8	2.2-3.2	0.11	±0.00441
		1.3-1.8	3.2-3.7	0.119	±0.00751
		1.3-1.8	3.7-4.26	0.176	±0.0105
		1.8-4	2.2-3.2	0.135	±0.00395
		1.8-4	3.2-3.7	0.111	±0.000223
		1.8-4	3.7-4.26	0.0893	±0.00772

Table C.35: Deuterium (Pb) global fit with Hypothesis 1. x_f cut applied.

Target	χ^2_{ndf}	$Q^2[GeV^2]$	$\nu[GeV]$	$\langle k_\perp^2 \rangle [GeV^2]$	$\delta\langle k_\perp^2 \rangle [GeV^2]$
DC	9.63	1-1.3	2.2-3.2	0.0167	±0.00423
		1-1.3	3.2-3.7	0.119	±0.0152
		1-1.3	3.7-4.26	0.3	±0.00645
		1.3-1.8	2.2-3.2	0.01	±0.00118
		1.3-1.8	3.2-3.7	0.0811	±0.00604
		1.3-1.8	3.7-4.26	0.156	±0.00841
		1.8-4	2.2-3.2	0.01	±0.000998
		1.8-4	3.2-3.7	0.0367	±0.00443
		1.8-4	3.7-4.26	0.0937	±0.00649

Table C.36: Deuterium (C) global fit with Hypothesis 1. x_f cut not applied.

Target	χ^2_{ndf}	$Q^2[GeV^2]$	$\nu[GeV]$	$\langle k_\perp^2 \rangle [GeV^2]$	$\delta\langle k_\perp^2 \rangle [GeV^2]$
DFe	7.96	1-1.3	2.2-3.2	0.0177	±0.00382
		1-1.3	3.2-3.7	0.115	±0.0109
		1-1.3	3.7-4.26	0.3	±0.00668
		1.3-1.8	2.2-3.2	0.01	±0.00364
		1.3-1.8	3.2-3.7	0.0811	±0.00518
		1.3-1.8	3.7-4.26	0.146	±0.00686
		1.8-4	2.2-3.2	0.01	±0.000681
		1.8-4	3.2-3.7	0.0286	±0.00523
		1.8-4	3.7-4.26	0.0885	±0.00592

Table C.37: Deuterium (Fe) global fit with Hypothesis 1. x_f cut not applied.

Target	χ^2_{ndf}	$Q^2[GeV^2]$	$\nu[GeV]$	$\langle k_\perp^2 \rangle [GeV^2]$	$\delta\langle k_\perp^2 \rangle [GeV^2]$
DPb	9.58	1-1.3	2.2-3.2	0.0176	±0.00397
		1-1.3	3.2-3.7	0.122	±0.0125
		1-1.3	3.7-4.26	0.3	±0.00597
		1.3-1.8	2.2-3.2	0.01	±0.000877
		1.3-1.8	3.2-3.7	0.0826	±0.00558
		1.3-1.8	3.7-4.26	0.151	±0.00753
		1.8-4	2.2-3.2	0.01	±0.00116
		1.8-4	3.2-3.7	0.0333	±0.0041
		1.8-4	3.7-4.26	0.0918	±0.00598

Table C.38: Deuterium (Pb) global fit with Hypothesis 1. x_f cut not applied.

Target	χ^2_{ndf}	$Q^2[GeV^2]$	$\nu[GeV]$	$\langle k_\perp^2\rangle[GeV^2]$	$\delta\langle k_\perp^2\rangle[GeV^2]$
DC	17.1	1-1.3	2.2-3.2	0.105	±0.00548
		1-1.3	3.2-3.7	0.0925	±0.00753
		1-1.3	3.7-4.26	0.123	±0.00882
		1.3-1.8	2.2-3.2	0.105	±0.00548
		1.3-1.8	3.2-3.7	0.0925	±0.00753
		1.3-1.8	3.7-4.26	0.123	±0.00882
		1.8-4	2.2-3.2	0.105	±0.00548
		1.8-4	3.2-3.7	0.0925	±0.00753
		1.8-4	3.7-4.26	0.123	±0.00882

Table C.39: Deuterium (C) global fit with Hypothesis 2. x_f cut applied.

Target	χ^2_{ndf}	$Q^2[GeV^2]$	$\nu[GeV]$	$\langle k_\perp^2\rangle[GeV^2]$	$\delta\langle k_\perp^2\rangle[GeV^2]$
DFe	24	1-1.3	2.2-3.2	0.13	±0.00606
		1-1.3	3.2-3.7	0.119	±0.00774
		1-1.3	3.7-4.26	0.144	±0.0107
		1.3-1.8	2.2-3.2	0.13	±0.00606
		1.3-1.8	3.2-3.7	0.119	±0.00774
		1.3-1.8	3.7-4.26	0.144	±0.0107
		1.8-4	2.2-3.2	0.13	±0.00606
		1.8-4	3.2-3.7	0.119	±0.00774
		1.8-4	3.7-4.26	0.144	±0.0107

Table C.40: Deuterium (Fe) global fit with Hypothesis 2. x_f cut applied.

Target	χ^2_{ndf}	$Q^2[GeV^2]$	$\nu[GeV]$	$\langle k_\perp^2\rangle[GeV^2]$	$\delta\langle k_\perp^2\rangle[GeV^2]$
DPb	22.6	1-1.3	2.2-3.2	0.119	±0.00447
		1-1.3	3.2-3.7	0.12	±0.00596
		1-1.3	3.7-4.26	0.14	±0.00717
		1.3-1.8	2.2-3.2	0.119	±0.00447
		1.3-1.8	3.2-3.7	0.12	±0.00596
		1.3-1.8	3.7-4.26	0.14	±0.00717
		1.8-4	2.2-3.2	0.119	±0.00447
		1.8-4	3.2-3.7	0.12	±0.00596
		1.8-4	3.7-4.26	0.14	±0.00717

Table C.41: Deuterium (Pb) global fit with Hypothesis 2. x_f cut applied.

Target	χ^2_{ndf}	$Q^2[GeV^2]$	$\nu[GeV]$	$\langle k_\perp^2 \rangle [GeV^2]$	$\delta\langle k_\perp^2 \rangle [GeV^2]$
DC	14.8	1-1.3	2.2-3.2	0.01	±0.00053
		1-1.3	3.2-3.7	0.0583	±0.00341
		1-1.3	3.7-4.26	0.128	±0.00459
		1.3-1.8	2.2-3.2	0.01	±0.00053
		1.3-1.8	3.2-3.7	0.0583	±0.00341
		1.3-1.8	3.7-4.26	0.128	±0.00459
		1.8-4	2.2-3.2	0.01	±0.00053
		1.8-4	3.2-3.7	0.0583	±0.00341
		1.8-4	3.7-4.26	0.128	±0.00459

Table C.42: Deuterium (C) global fit with Hypothesis 2. x_f cut not applied.

Target	χ^2_{ndf}	$Q^2[GeV^2]$	$\nu[GeV]$	$\langle k_\perp^2 \rangle [GeV^2]$	$\delta\langle k_\perp^2 \rangle [GeV^2]$
DFe	14.6	1-1.3	2.2-3.2	0.01	±0.000523
		1-1.3	3.2-3.7	0.06	±0.00331
		1-1.3	3.7-4.26	0.122	±0.00411
		1.3-1.8	2.2-3.2	0.01	±0.000523
		1.3-1.8	3.2-3.7	0.06	±0.00331
		1.3-1.8	3.7-4.26	0.122	±0.00411
		1.8-4	2.2-3.2	0.01	±0.000523
		1.8-4	3.2-3.7	0.06	±0.00331
		1.8-4	3.7-4.26	0.122	±0.00411

Table C.43: Deuterium (Fe) global fit with Hypothesis 2. x_f cut not applied.

Target	χ^2_{ndf}	$Q^2[GeV^2]$	$\nu[GeV]$	$\langle k_\perp^2 \rangle [GeV^2]$	$\delta\langle k_\perp^2 \rangle [GeV^2]$
DPb	16.3	1-1.3	2.2-3.2	0.01	±0.000471
		1-1.3	3.2-3.7	0.0562	±0.00323
		1-1.3	3.7-4.26	0.125	±0.0023
		1.3-1.8	2.2-3.2	0.01	±0.000471
		1.3-1.8	3.2-3.7	0.0562	±0.00323
		1.3-1.8	3.7-4.26	0.125	±0.0023
		1.8-4	2.2-3.2	0.01	±0.000471
		1.8-4	3.2-3.7	0.0562	±0.00323
		1.8-4	3.7-4.26	0.125	±0.0023

Table C.44: Deuterium (Pb) global fit with Hypothesis 2. x_f cut not applied.

Target	χ^2_{ndf}	$Q^2[GeV^2]$	$\nu[GeV]$	$\langle k_\perp^2 \rangle [GeV^2]$	$\delta\langle k_\perp^2 \rangle [GeV^2]$
C	5.67	1-1.3	2.2-3.2	0.011	±0.00877
		1-1.3	3.2-3.7	0.122	±0.0164
		1-1.3	3.7-4.26	0.3	±0.00854
		1.3-1.8	2.2-3.2	0.01	±0.0162
		1.3-1.8	3.2-3.7	0.0912	±0.00647
		1.3-1.8	3.7-4.26	0.167	±0.0103
		1.8-4	2.2-3.2	0.01	±0.000787
		1.8-4	3.2-3.7	0.0299	±0.0061
		1.8-4	3.7-4.26	0.099	±0.00758

Table C.45: C global fit with Hypothesis 1. x_f cut not applied.

Target	χ^2_{ndf}	$Q^2[GeV^2]$	$\nu[GeV]$	$\langle k_\perp^2 \rangle [GeV^2]$	$\delta\langle k_\perp^2 \rangle [GeV^2]$
Fe	6.33	1-1.3	2.2-3.2	0.0126	±0.00558
		1-1.3	3.2-3.7	0.134	±0.0162
		1-1.3	3.7-4.26	0.3	±0.00717
		1.3-1.8	2.2-3.2	0.01	±0.00104
		1.3-1.8	3.2-3.7	0.0862	±0.00763
		1.3-1.8	3.7-4.26	0.167	±0.0104
		1.8-4	2.2-3.2	0.01	±0.00156
		1.8-4	3.2-3.7	0.0283	±0.0072
		1.8-4	3.7-4.26	0.0997	±0.00782

Table C.46: Fe global fit with Hypothesis 1. x_f cut not applied.

Target	χ^2_{ndf}	$Q^2[GeV^2]$	$\nu[GeV]$	$\langle k_\perp^2 \rangle [GeV^2]$	$\delta\langle k_\perp^2 \rangle [GeV^2]$
Pb	3.57	1-1.3	2.2-3.2	0.01	±0.00624
		1-1.3	3.2-3.7	0.156	±0.0309
		1-1.3	3.7-4.26	0.3	±0.018
		1.3-1.8	2.2-3.2	0.01	±0.00455
		1.3-1.8	3.2-3.7	0.0848	±0.01
		1.3-1.8	3.7-4.26	0.183	±0.0156
		1.8-4	2.2-3.2	0.01	±0.00421
		1.8-4	3.2-3.7	0.0396	±0.00942
		1.8-4	3.7-4.26	0.127	±0.0105

Table C.47: Pb global fit with Hypothesis 1. x_f cut not applied.

Target	χ^2_{ndf}	$Q^2[GeV^2]$	$\nu[GeV]$	$\langle k_\perp^2 \rangle [GeV^2]$	$\delta\langle k_\perp^2 \rangle [GeV^2]$
C	10.2	1-1.3	2.2-3.2	0.0963	±0.00953
		1-1.3	3.2-3.7	0.207	±0.0522
		1-1.3	3.7-4.26	0.3	±0.0116
		1.3-1.8	2.2-3.2	0.117	±0.00656
		1.3-1.8	3.2-3.7	0.132	±0.0112
		1.3-1.8	3.7-4.26	0.162	±0.0165
		1.8-4	2.2-3.2	0.145	±0.00569
		1.8-4	3.2-3.7	0.0908	±0.0097
		1.8-4	3.7-4.26	0.0857	±0.0125

Table C.48: C global fit with Hypothesis 1. x_f cut applied.

Target	χ^2_{ndf}	$Q^2[GeV^2]$	$\nu[GeV]$	$\langle k_\perp^2 \rangle [GeV^2]$	$\delta\langle k_\perp^2 \rangle [GeV^2]$
Fe	13.9	1-1.3	2.2-3.2	0.0711	±0.00917
		1-1.3	3.2-3.7	0.197	±0.043
		1-1.3	3.7-4.26	0.3	±0.0109
		1.3-1.8	2.2-3.2	0.116	±0.00608
		1.3-1.8	3.2-3.7	0.118	±0.0111
		1.3-1.8	3.7-4.26	0.148	±0.0151
		1.8-4	2.2-3.2	0.152	±0.00519
		1.8-4	3.2-3.7	0.0727	±0.00957
		1.8-4	3.7-4.26	0.0619	±0.0122

Table C.49: Fe global fit with Hypothesis 1. x_f cut applied.

Target	χ^2_{ndf}	$Q^2[GeV^2]$	$\nu[GeV]$	$\langle k_\perp^2 \rangle [GeV^2]$	$\delta\langle k_\perp^2 \rangle [GeV^2]$
Pb	11.8	1-1.3	2.2-3.2	0.0804	±0.00919
		1-1.3	3.2-3.7	0.3	±0.0576
		1-1.3	3.7-4.26	0.3	±0.0134
		1.3-1.8	2.2-3.2	0.129	±0.00651
		1.3-1.8	3.2-3.7	0.127	±0.0113
		1.3-1.8	3.7-4.26	0.172	±0.0179
		1.8-4	2.2-3.2	0.184	±0.00544
		1.8-4	3.2-3.7	0.132	±0.0093
		1.8-4	3.7-4.26	0.134	±0.0114

Table C.50: Pb global fit with Hypothesis 1. x_f cut applied.

Target	χ^2_{ndf}	$Q^2[GeV^2]$	$\nu[GeV]$	$\langle k_\perp^2 \rangle [GeV^2]$	$\delta\langle k_\perp^2 \rangle [GeV^2]$
C	10.1	1-1.3	2.2-3.2	0.01	±0.000693
		1-1.3	3.2-3.7	0.0654	±0.00428
		1-1.3	3.7-4.26	0.134	±0.0055
		1.3-1.8	2.2-3.2	0.01	±0.000693
		1.3-1.8	3.2-3.7	0.0654	±0.00428
		1.3-1.8	3.7-4.26	0.134	±0.0055
		1.8-4	2.2-3.2	0.01	±0.000693
		1.8-4	3.2-3.7	0.0654	±0.00428
		1.8-4	3.7-4.26	0.134	±0.0055

Table C.51: C global fit with Hypothesis 2. x_f cut not applied.

Target	χ^2_{ndf}	$Q^2[GeV^2]$	$\nu[GeV]$	$\langle k_\perp^2 \rangle [GeV^2]$	$\delta\langle k_\perp^2 \rangle [GeV^2]$
Fe	10.6	1-1.3	2.2-3.2	0.01	±0.000571
		1-1.3	3.2-3.7	0.0698	±0.00468
		1-1.3	3.7-4.26	0.138	±0.00558
		1.3-1.8	2.2-3.2	0.01	±0.000571
		1.3-1.8	3.2-3.7	0.0698	±0.00468
		1.3-1.8	3.7-4.26	0.138	±0.00558
		1.8-4	2.2-3.2	0.01	±0.000571
		1.8-4	3.2-3.7	0.0698	±0.00468
		1.8-4	3.7-4.26	0.138	±0.00558

Table C.52: Fe global fit with Hypothesis 2. x_f cut not applied.

Target	χ^2_{ndf}	$Q^2[GeV^2]$	$\nu[GeV]$	$\langle k_\perp^2 \rangle [GeV^2]$	$\delta\langle k_\perp^2 \rangle [GeV^2]$
Pb	4.93	1-1.3	2.2-3.2	0.01	±0.00136
		1-1.3	3.2-3.7	0.0722	±0.00653
		1-1.3	3.7-4.26	0.153	±0.00815
		1.3-1.8	2.2-3.2	0.01	±0.00136
		1.3-1.8	3.2-3.7	0.0722	±0.00653
		1.3-1.8	3.7-4.26	0.153	±0.00815
		1.8-4	2.2-3.2	0.01	±0.00136
		1.8-4	3.2-3.7	0.0722	±0.00653
		1.8-4	3.7-4.26	0.153	±0.00815

Table C.53: Pb global fit with Hypothesis 2. x_f cut not applied.

Target	χ^2_{ndf}	$Q^2[GeV^2]$	$\nu[GeV]$	$\langle k_\perp^2 \rangle [GeV^2]$	$\delta\langle k_\perp^2 \rangle [GeV^2]$
C	13.9	1-1.3	2.2-3.2	0.124	±0.00303
		1-1.3	3.2-3.7	0.108	±0.00488
		1-1.3	3.7-4.26	0.123	±0.00549
		1.3-1.8	2.2-3.2	0.124	±0.00303
		1.3-1.8	3.2-3.7	0.108	±0.00488
		1.3-1.8	3.7-4.26	0.123	±0.00549
		1.8-4	2.2-3.2	0.124	±0.00303
		1.8-4	3.2-3.7	0.108	±0.00488
		1.8-4	3.7-4.26	0.123	±0.00549

Table C.54: C global fit with Hypothesis 2. x_f cut applied.

Target	χ^2_{ndf}	$Q^2[GeV^2]$	$\nu[GeV]$	$\langle k_\perp^2 \rangle [GeV^2]$	$\delta\langle k_\perp^2 \rangle [GeV^2]$
Fe	21	1-1.3	2.2-3.2	0.129	±0.00456
		1-1.3	3.2-3.7	0.108	±0.00696
		1-1.3	3.7-4.26	0.123	±0.00835
		1.3-1.8	2.2-3.2	0.129	±0.00456
		1.3-1.8	3.2-3.7	0.108	±0.00696
		1.3-1.8	3.7-4.26	0.123	±0.00835
		1.8-4	2.2-3.2	0.129	±0.00456
		1.8-4	3.2-3.7	0.108	±0.00696
		1.8-4	3.7-4.26	0.123	±0.00835

Table C.55: Fe global fit with Hypothesis 2. x_f cut applied.

Target	χ^2_{ndf}	$Q^2[GeV^2]$	$\nu[GeV]$	$\langle k_\perp^2 \rangle [GeV^2]$	$\delta\langle k_\perp^2 \rangle [GeV^2]$
Pb	15	1-1.3	2.2-3.2	0.157	±0.0062
		1-1.3	3.2-3.7	0.156	±0.00929
		1-1.3	3.7-4.26	0.182	±0.0118
		1.3-1.8	2.2-3.2	0.157	±0.0062
		1.3-1.8	3.2-3.7	0.156	±0.00929
		1.3-1.8	3.7-4.26	0.182	±0.0118
		1.8-4	2.2-3.2	0.157	±0.0062
		1.8-4	3.2-3.7	0.156	±0.00929
		1.8-4	3.7-4.26	0.182	±0.0118

Table C.56: Pb global fit with Hypothesis 2. x_f cut applied.

Bibliography

[1] Mark Thomson. *Modern particle physics*. New York: Cambridge University Press, 2013. ISBN: 978-1-107-03426-6.

[2] R.Keith Ellis, W.James Stirling, and B.R. Webber. *QCD and collider physics*. Vol. 8. Cambridge University Press, Feb. 2011. ISBN: 978-0-511-82328-2, 978-0-521-54589-1.

[3] John Collins. *Foundations of perturbative QCD*. Vol. 32. Cambridge University Press, Nov. 2013. ISBN: 978-1-107-64525-7, 978-1-107-64525-7, 978-0-521-85533-4, 978-1-139-09782-6.

[4] R.P. Feynman. "The behavior of hadron collisions at extreme energies". In: *Conf. Proc. C* 690905 (1969), pp. 237–258.

[5] V. N. Gribov and L. N. Lipatov. "Deep inelastic e p scattering in perturbation theory". In: *Sov. J. Nucl. Phys.* 15 (1972), pp. 438–450.

[6] Guido Altarelli and G. Parisi. "Asymptotic Freedom in Parton Language". In: *Nucl. Phys. B* 126 (1977), pp. 298–318. DOI: 10.1016/0550-3213(77)90384-4.

[7] Yuri L. Dokshitzer. "Calculation of the Structure Functions for Deep Inelastic Scattering and e+ e- Annihilation by Perturbation Theory in Quantum Chromodynamics." In: *Sov. Phys. JETP* 46 (1977), pp. 641–653.

[8] Alessandro Bacchetta et al. "Semi-inclusive deep inelastic scattering at small transverse momentum". In: *JHEP* 02 (2007), p. 093. DOI: 10.1088/1126-6708/2007/02/093. arXiv: hep-ph/0611265.

[9] V. Barone et al. "Phenomenological analysis of azimuthal asymmetries in unpolarized semi-inclusive deep inelastic scattering". In: *Phys. Rev. D* 91.7 (2015), p. 074019. DOI: 10.1103/PhysRevD.91.074019. arXiv: 1502.04214 [hep-ph].

[10] Xiang-dong Ji, Jian-ping Ma, and Feng Yuan. "QCD factorization for semi-inclusive deep-inelastic scattering at low transverse momentum". In: *Phys. Rev. D* 71 (2005), p. 034005. DOI: 10.1103/PhysRevD.71.034005. arXiv: hep-ph/0404183.

[11] M. Boglione, S. Melis, and A. Prokudin. "Partonic Transverse Motion in Unpolarized Semi-Inclusive Deep Inelastic Scattering Processes". In: *Phys. Rev. D* 84 (2011), p. 034033. DOI: 10.1103/PhysRevD.84.034033. arXiv: 1106.6177 [hep-ph].

[12] B. Z. Kopeliovich et al. "Novel mechanism for suppression of heavy flavored mesons in heavy ion collisions". In: *J. Phys. Conf. Ser.* 1137.1 (2018). Ed. by Fernando Bar˜ao et al., p. 012047. DOI: 10.1088/1742-6596/1137/1/012047.

[13] B.Z. Kopeliovich et al. "Nuclear hadronization: Within or without?" In: *Nucl. Phys. A* 740 (2004), pp. 211–245. DOI: 10.1016/j.nuclphysa.2004.04.110. arXiv: hep-ph/0311220.

[14] A. Casher, H. Neuberger, and S. Nussinov. "Chromoelectric-flux-tube model of particle production". In: *Phys. Rev. D* 20 (1 1979), pp. 179–188. DOI: 10.1103/PhysRevD.20.179. URL: https://link.aps.org/doi/10.1103/PhysRevD.20.179.

[15] S. Domdey et al. "Transverse Momentum Broadening in Semi-inclusive DIS on Nuclei". In: *Nucl. Phys. A* 825 (2009), pp. 200–211. DOI: 10.1016/j.nuclphysa.2009.04.009. arXiv: 0812.2838 [hep-ph].

[16] B.A. Mecking et al. "The CEBAF Large Acceptance Spectrometer (CLAS)". In: *Nucl. Instrum. Meth. A* 503 (2003), pp. 513–553. DOI: 10.1016/S0168-9002(03)01001-5.

[17] M.D. Mestayer et al. "The CLAS drift chamber system". In: *Nucl. Instrum. Meth. A* 449 (2000), pp. 81–111. DOI: 10.1016/S0168-9002(00)00151-0.

[18] G. Adams et al. "The CLAS Cherenkov detector". In: *Nucl. Instrum. Meth. A* 465 (2001), pp. 414–427. DOI: 10.1016/S0168-9002(00)01313-9.

[19] E.S. Smith et al. "The time-of-flight system for CLAS". In: *Nucl. Instrum. Meth. A* 432 (1999), pp. 265–298. DOI: 10.1016/S0168-9002(99)00484-2.

[20] H. Hakobyan et al. "A double-target system for precision measurements of nuclear medium effects". In: *Nuclear Instruments and Methods in Physics Research Section A: Accelerators, Spectrometers, Detectors and Associated Equipment* 592.3 (2008), pp. 218 –223. ISSN: 0168-9002. DOI: https://doi.org/10.1016/j.nima.2008.04.055.

[21] Sebastian Morán. "Charged-pion Multiplicity Ratio Measurement with EG2 Data". CLAS Analysis Note. 2021.

[22] Taisiya Mineeva. "Hadronization Studies via π^0 Electroproduction off D, C, Fe, and Pb". PhD thesis. Connecticut U., 2013.

[23] Lorenzo Zana. "Search for the onset of color transparency through rho electroproduction on nuclei". PhD thesis. New Hampshire U., 2010.

[24] Taisiya Mineeva. "Neutral Pion Multiplicity Ratios from SIDIS Lepton-nuclear Scattering". CLAS Analysis Note. 2020.

[25] H. Egiyan et al. "Single pi+ electroproduction on the proton in the first and second resonance regions at 0.25-GeV**2 < Q**2 < 0.65-GeV**2 using CLAS". In: *Phys. Rev. C* 73 (2006), p. 025204. DOI: 10.1103/PhysRevC.73.025204. arXiv: nucl-ex/0601007.

[26] Raphael Dupré. "Quark Fragmentation and Hadron Formation in Nuclear Matter". PhD thesis. Université de Lyon, 2011.

[27] Hayk Hakobyan. "Observation of Quark Propagation Pattern in Nuclear Medium". PhD thesis. Yerevan State University, 2008.

[28] I. Akushevich, N. Shumeiko, and A. Soroko. "Radiative effects in the processes of hadron electroproduction". In: *Eur. Phys. J. C* 10 (1999), pp. 681–687. DOI: 10.1007/s100520050606. arXiv: hep-ph/9903325.

[29] I. Akushevich, A. Ilyichev, and M. Osipenko. "Complete lowest order radiative corrections to five-fold differential cross-section of hadron leptoproduction". In: *Phys. Lett. B* 672 (2009), pp. 35–44. DOI: 10.1016/j.physletb.2008.12.058. arXiv: 0711.4789 [hep-ph].

[30] CERN. *TH1 Class Definition*. 2011. URL: https://root.cern/root/html530/src/TH1.cxx.html.

[31] William K. Brooks and Jorge A. López. "Estimating the Color Lifetime of Energetic Quarks". In: *Phys. Lett. B* 816 (2021), p. 136171. DOI: 10.1016/j.physletb.2021.136171. arXiv: 2004.07236 [hep-ph].